

## NRC Publications Archive Archives des publications du CNRC

### Accurate measurements of the collision stopping powers for 5 to 30 MeV electrons MacPherson, M. S.

For the publisher's version, please access the DOI link below. / Pour consulter la version de l'éditeur, utilisez le lien DOI ci-dessous.

#### **Publisher's version / Version de l'éditeur:**

<https://doi.org/10.4224/40000364>

*Report (National Research Council of Canada. Institute for National Measurement Standards. Ionizing Radiation Standards); no. PIRS-0626, 1998-09*

#### **NRC Publications Archive Record / Notice des Archives des publications du CNRC :**

<https://nrc-publications.canada.ca/eng/view/object/?id=bcf26036-6ec7-4520-bc5c-201387404393>

<https://publications-cnrc.canada.ca/fra/voir/objet/?id=bcf26036-6ec7-4520-bc5c-201387404393>

Access and use of this website and the material on it are subject to the Terms and Conditions set forth at

<https://nrc-publications.canada.ca/eng/copyright>

READ THESE TERMS AND CONDITIONS CAREFULLY BEFORE USING THIS WEBSITE.

L'accès à ce site Web et l'utilisation de son contenu sont assujettis aux conditions présentées dans le site

<https://publications-cnrc.canada.ca/fra/droits>

LISEZ CES CONDITIONS ATTENTIVEMENT AVANT D'UTILISER CE SITE WEB.

**Questions?** Contact the NRC Publications Archive team at

PublicationsArchive-ArchivesPublications@nrc-cnrc.gc.ca. If you wish to email the authors directly, please see the first page of the publication for their contact information.

**Vous avez des questions?** Nous pouvons vous aider. Pour communiquer directement avec un auteur, consultez la première page de la revue dans laquelle son article a été publié afin de trouver ses coordonnées. Si vous n'arrivez pas à les repérer, communiquez avec nous à PublicationsArchive-ArchivesPublications@nrc-cnrc.gc.ca.

# Corrections to report PIRS-0626 on electron stopping powers

Frédéric Tessier<sup>1</sup>, and Carl K. Ross<sup>2</sup>

*Ionizing Radiation Standards, Metrology, National Research Council Canada, Ottawa,  
Ontario K1A 0R6 Canada*

<sup>1</sup>Corresponding author: Frederic.Tessier@nrc-cnrc.gc.ca

<sup>2</sup>Retired

February 6, 2019

## Abstract

NRC Report PIRS-0626 gives measured values of the electronic stopping powers for several elements and compounds. The general conclusion of the report is that the measured data are in good agreement with the calculated values tabulated in ICRU Report 37. Unfortunately, the curves that are stated to represent ICRU 37 data for all of the elemental materials are not correct. Instead, they correspond to the stopping power calculated using the density effect correction of Sternheimer and Peirels. In some cases, the differences are substantial enough to suggest that the stopping powers may not be as well-known as thought. We have reviewed the data files and analysis underlying the results presented in PIRS-0626. The essence of that work was to determine a correction to the stopping power used by the EGS4 Monte Carlo code so that the measured and calculated spectra of electrons passing through thin absorbers agree. We have determined that the EGS4 calculations did indeed use the ICRU 37 stopping powers so the reported corrections are with respect to these stopping powers. However, when the plots reporting the revised stopping powers were prepared, the corrections were added to the Sternheimer-Peirels data set rather than that of ICRU Report 37. Corrected figures are presented for all the elemental materials. The figures in PIRS-0626 for the composite materials are correct. The main conclusion of PIRS-0626 regarding the agreement between the measured stopping powers and the values tabulated in ICRU Report 37 remains unchanged.

# 1 Introduction

NRC Report PIRS-0626 [1] describes how a large NaI detector was used to measure electronic stopping powers. Monoenergetic electrons were directed at a thin slab of material and the NaI detector was used to measure the transmitted electron spectrum. The measured spectrum was compared to the spectrum calculated using the EGS4 Monte Carlo code [2] and some reasonable model for the electron stopping power. Any difference between the measured and calculated spectra was used to establish a revised value for the stopping power.

PIRS-0626 presents several graphs that purport to show how the measured stopping powers compare to values tabulated in ICRU Report 37 [3]. In general, there is good agreement between the measured data and the plotted curves, usually within the combined standard uncertainty.

Unfortunately, the curves in the plots for the elemental materials do not correspond to the tables in ICRU Report 37. Instead, they represent the stopping powers obtained using an approximation by Sternheimer and Peierls [4] for the density effect. In some cases, the differences are substantial.

We had access to the original data and analysis that was used to generate the results shown in PIRS-0626. After extensive review, we have determined that, indeed, ICRU 37 stopping powers were used with the EGS4 code to generate the reported corrections to the stopping powers. These corrections are denoted by  $\kappa$  in PIRS-0626. However, when generating the final plots,  $\kappa$  was added to the stopping power data calculated with the Sternheimer-Peierls approximation rather than the tables of ICRU Report 37. We have corrected this error and produced revised plots for the elemental materials. Note that the plots for water and the A-150 and C-552 compounds in PIRS-0626 are correct.

## 2 Revised plots

The following plots present the measured stopping power data, the stopping power calculated using the Sternheimer and Peierls approximation and the stopping power as tabulated in ICRU Report 37. The latter were obtained using the ESTAR.f Fortran program (version 1.2, 1999) provided by the National Institute of Standards and Technology [5]. The dashed curves labelled SP71 are identical to those shown in PIRS-0626, but in that report they are mislabelled as ICRU37.

# Beryllium

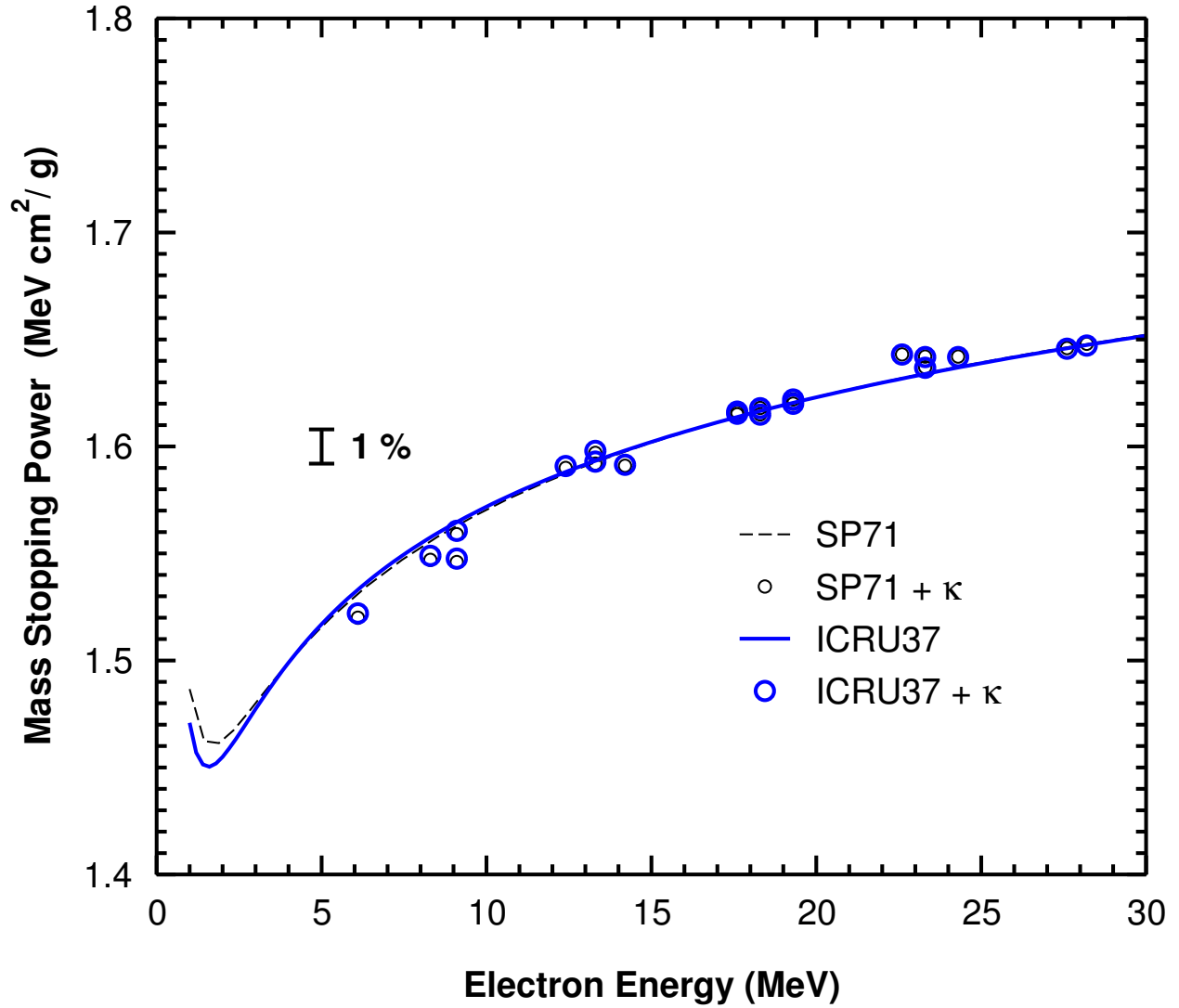


**FIGURE 1** Electronic stopping power data for beryllium. The dashed line is the SP71 data, and the small circles show the correction  $\kappa$  added to SP71 data (as reported in PIRS-0626). The solid line is the ICRU Report 37 data, and the larger circles show the correction  $\kappa$  added to this ICRU37 data. For beryllium, the two approximations for the density effect give similar results.

## Graphite, using bulk density

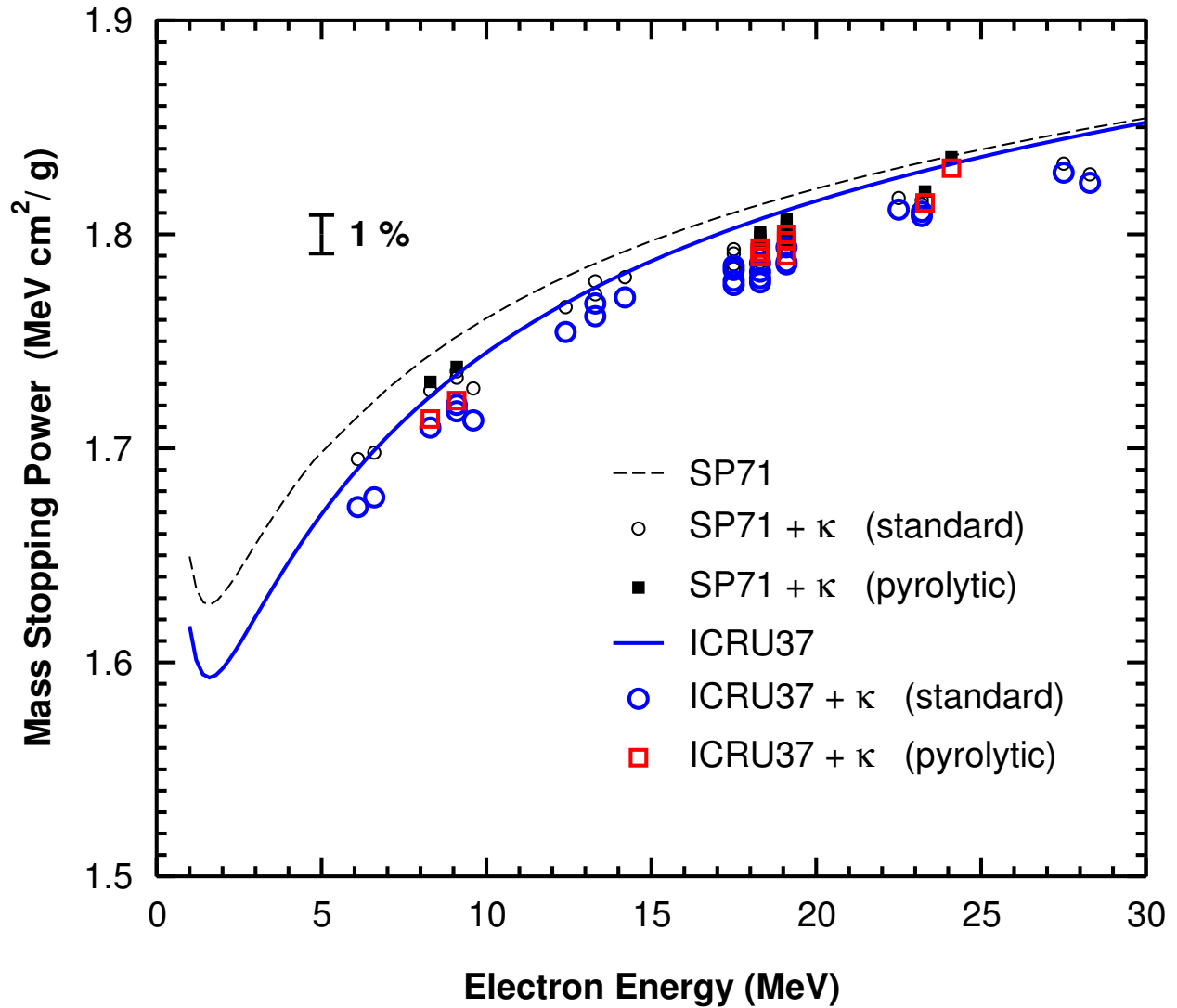


**FIGURE 2** Electronic stopping power data for carbon in the form of graphite. The circles show the measured results for ordinary graphite with a density of 1.7 g/cm<sup>3</sup> while the squares are measured results for pyrolytic graphite with a density of 2.2 g/cm<sup>3</sup>. The curves were calculated using the bulk density of 1.7 g/cm<sup>3</sup>.

## Graphite, using grain density

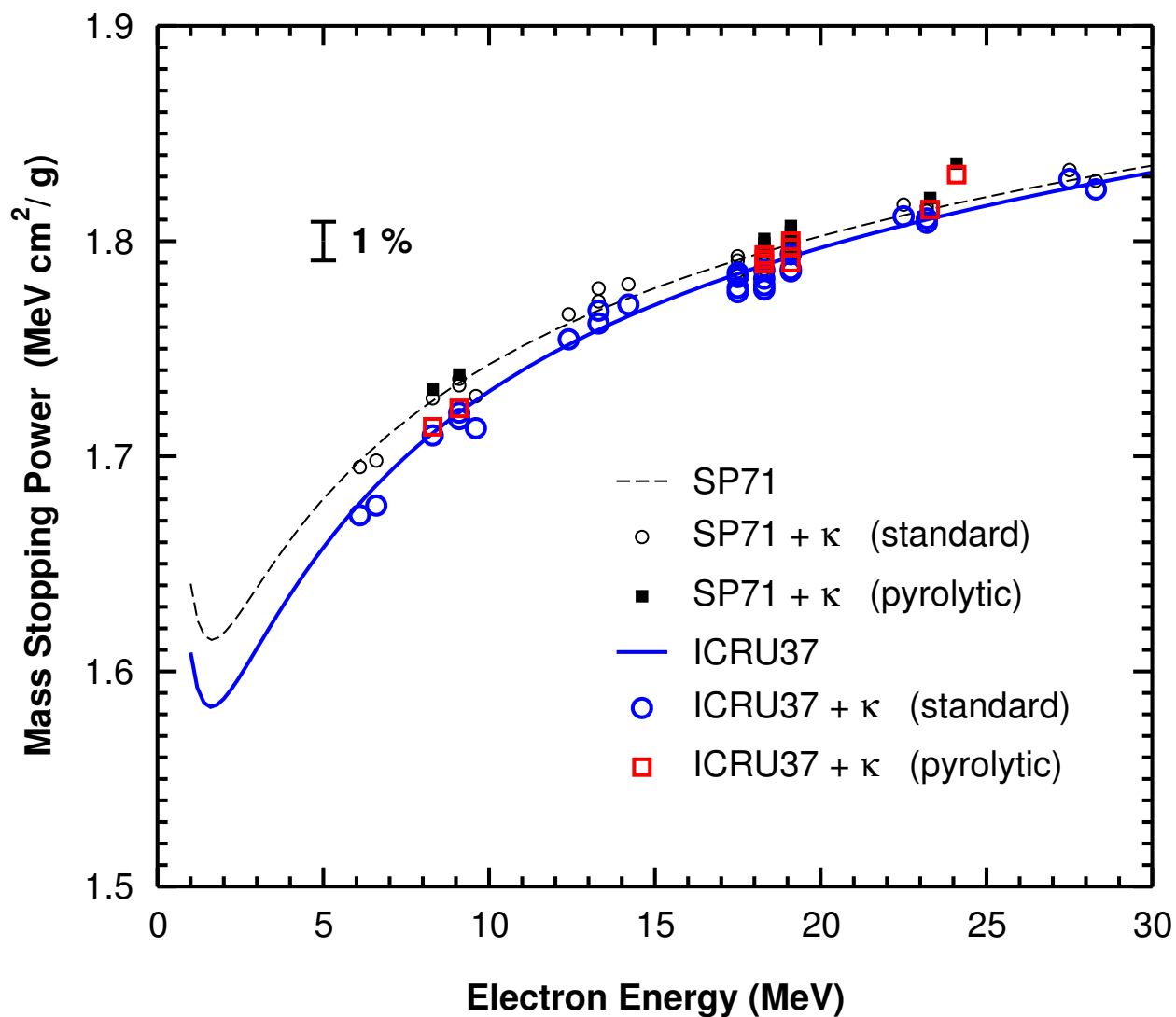


**FIGURE 3** Electronic stopping power data for carbon in the form of graphite. The circles show the measured results for ordinary graphite with a density of 1.7 g/cm<sup>3</sup> while the squares are measured results for pyrolytic graphite with a density of 2.2 g/cm<sup>3</sup>. The curves were calculated using the graphite grain density of 2.265 g/cm<sup>3</sup>.

# Aluminum

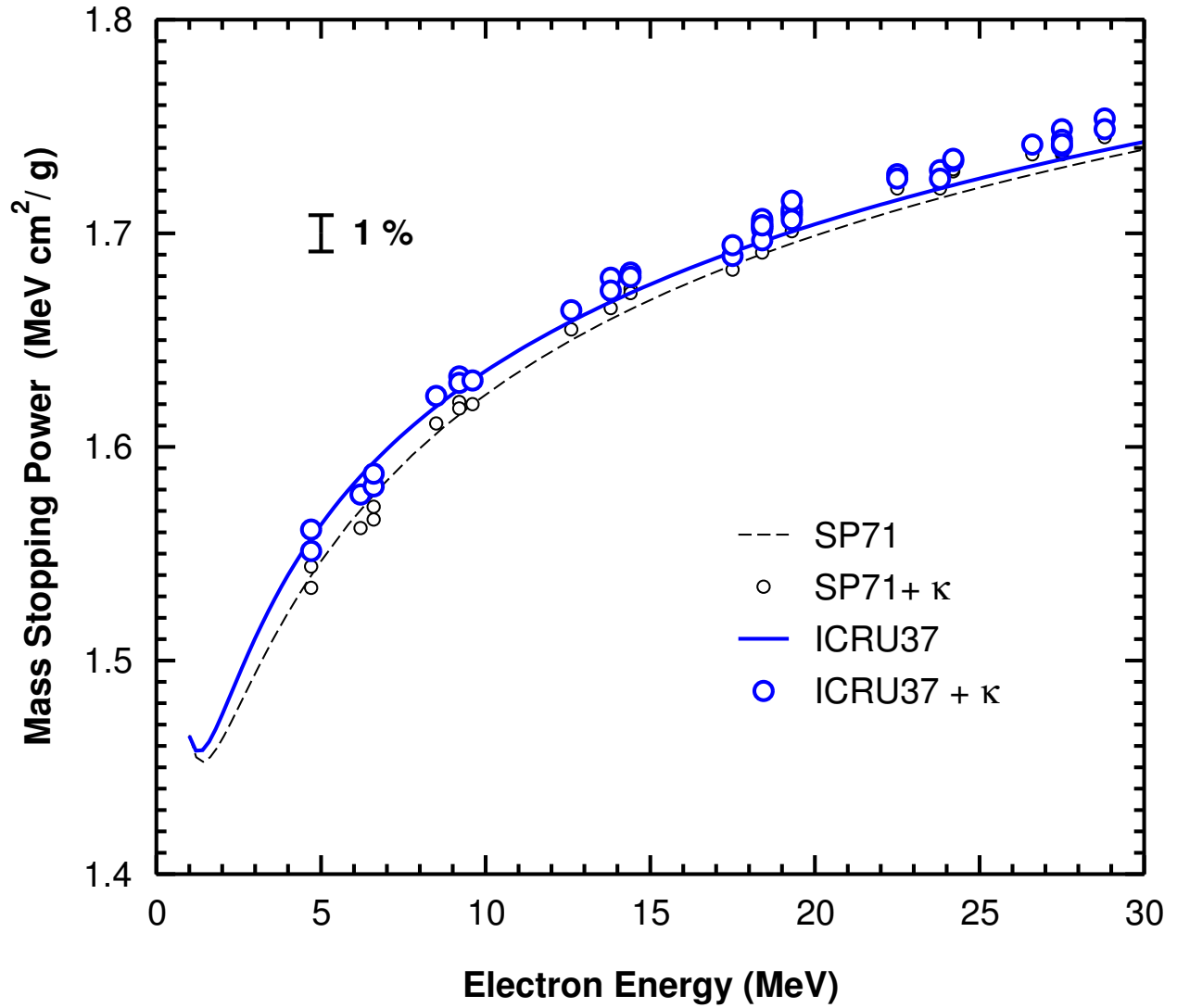


**FIGURE 4** Electronic stopping power data for aluminum. The dashed line is the SP71 data, and the small circles show the correction  $\kappa$  added to SP71 data (as reported in PIRS-0626). The solid line is the ICRU Report 37 data, and the larger circles show the correction  $\kappa$  added to this ICRU37 data.

# Copper

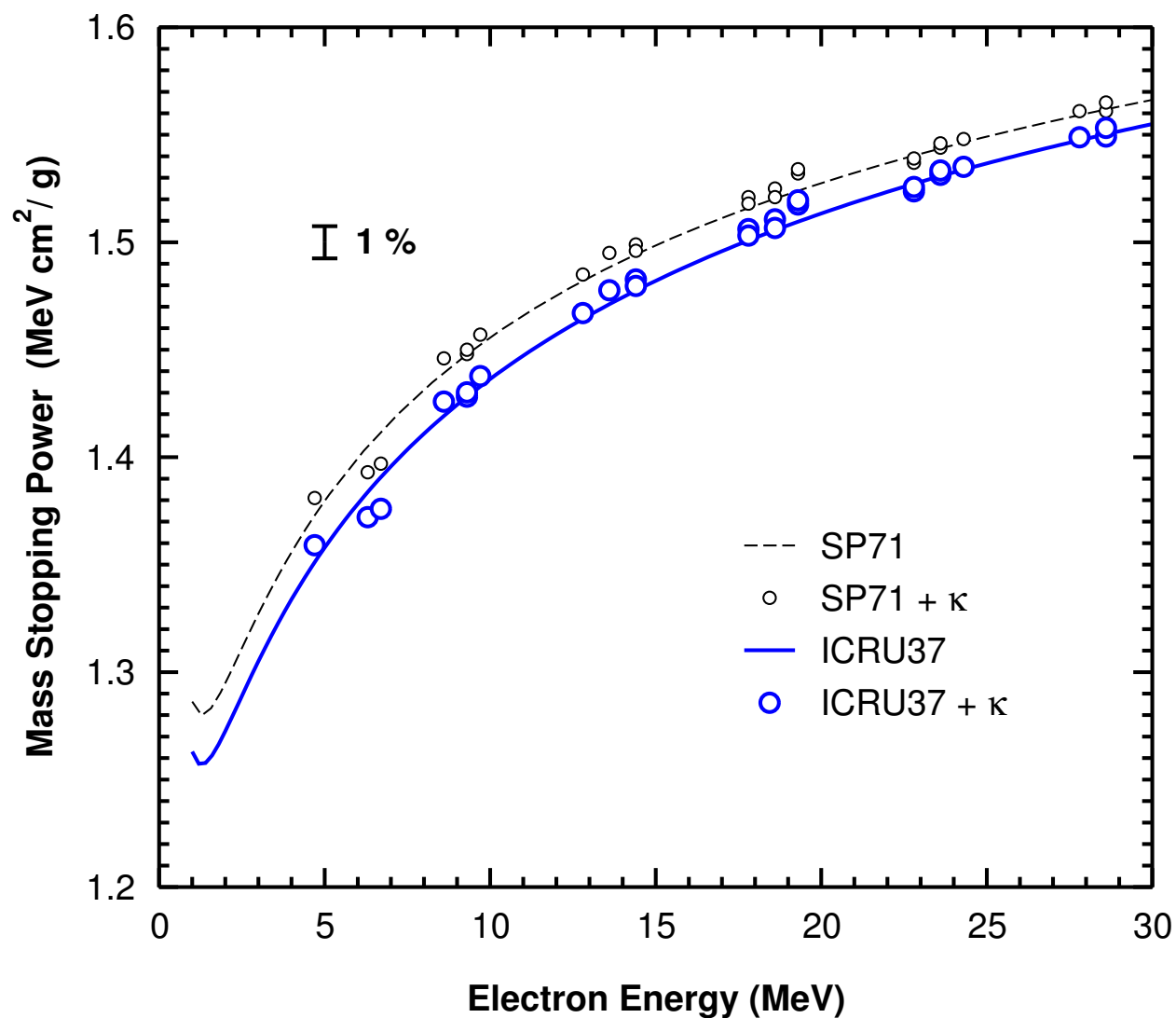


**FIGURE 5** Electronic stopping power data for copper. The dashed line is the SP71 data, and the small circles show the correction  $\kappa$  added to SP71 data (as reported in PIRS-0626). The solid line is the ICRU Report 37 data, and the larger circles show the correction  $\kappa$  added to this ICRU37 data.



# Tantalum

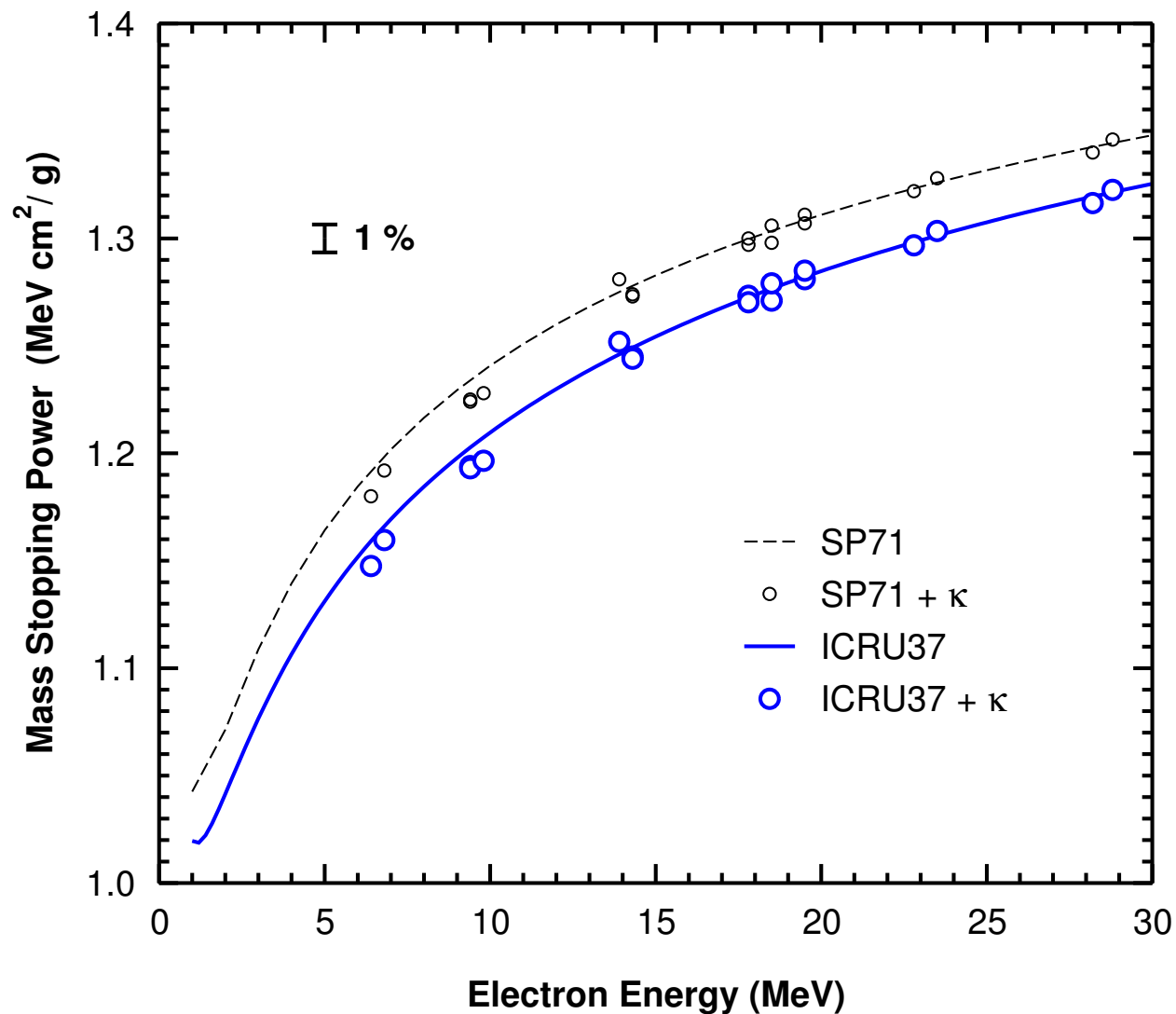


**FIGURE 6** Electronic stopping power data for tantalum. The dashed line is the SP71 data, and the small circles show the correction  $\kappa$  added to SP71 data (as reported in PIRS-0626). The solid line is the ICRU Report 37 data, and the larger circles show the correction  $\kappa$  added to this ICRU37 data.

### 3 Conclusions

We have presented revised plots of the stopping power data shown in PIRS-0626. Because the stopping power correction,  $\kappa$ , was calculated using the data of ICRU Report 37 the main conclusions of that Report remain unchanged. However, the measured total stopping powers can now be read correctly off the graphs.

Since the work described in PIRS-0626 an improved version of EGS4, referred to as EGSnrc, has been developed [6]. Efforts are underway to determine how the analysis of PIRS-0626 would be affected if EGSnrc were to be used rather than EGS4.

### References

- [1] M. S. MacPherson. Accurate measurements of the collision stopping powers for 5 to 30 MeV electrons. NRC Report PIRS-0626, National Research Council, Ottawa, Canada, 1998.
- [2] W. R. Nelson, H. Hirayama, and D. W. O. Rogers. The EGS4 Code System. SLAC Report 265, Stanford University, Stanford, California, 1985.
- [3] ICRU. Stopping powers for electrons and positrons. ICRU Report 37, International Commission on Radiation Units and Measurements, Bethesda, MD, 1984.
- [4] R. M. Sternheimer and R. F. Peierls. General expression for the density effect for the ionization loss of charged particles. *Physical Review B*, 3(11):3681–3692, June 1971.
- [5] M. J. Berger. NIST: Download Your Own Copies of ESTAR, PSTAR, and ASTAR. <https://physics.nist.gov/PhysRefData/Star/Text/download.html>. Accessed: 5 February 2019.
- [6] I. Kawrakow. Accurate condensed history Monte Carlo simulation of electron transport. I. EGSnrc, the new EGS4 version. *Medical Physics*, 27(3):485–498, March 2000.

PhD Thesis

Accurate Measurements of the Collision Stopping  
Powers for 5 to 30 MeV Electrons

Miller S. MacPherson

September, 1998

PIRS-0626

Ionizing Radiation Standards  
Institute for National Measurement Standards  
National Research Council  
Ottawa, Ontario K1A 0R6 Canada

Telephone: 613-993-9352  
Fax: 613-952-9865  
E-mail: [carl.ross@nrc.ca](mailto:carl.ross@nrc.ca)



# Abstract

Accurate knowledge of electron stopping powers is crucial for accurate radiation dosimetry and radiation transport calculations. Current values for stopping powers are based on a theoretical model, with estimated uncertainties of 0.5-1% ( $1\sigma$ ) for electron energies greater than 100 keV. This work presents the first measurements of electron collision stopping powers capable of testing the theoretical values within these stated uncertainties.

A large NaI spectrometer was used to measure the change in electron energy when an absorbing disk of known thickness was placed in an electron beam. Monte Carlo simulations of the experiment were performed to account for the effects of surrounding materials. Energy differences between the calculated and measured spectra were used to determine corrections to the soft collision component of the theoretical stopping powers employed by the Monte Carlo simulations.

Four different elemental materials were studied: Be, Al, Cu, and Ta. This provided a wide range of atomic numbers and densities over which to test the theory. In addition, stopping powers were measured for graphite (both standard and pyrolytic), A-150 tissue equivalent plastic, C-552 air equivalent plastic, and water. The incident electron energies ranged from 5 to 30 MeV. Generally, the measured stopping powers agree with the theoretical values within the experimental uncertainties, which range from 0.4% to 0.7% ( $1\sigma$ ). Aluminum, however, exhibits a 0.7% discrepancy at higher electron energies. Furthermore, these measurements have established that the grain density stopping power is appropriate for graphite, contrary to the recommendations of ICRU Report 37. This removes a 0.2% uncertainty in air kerma calibrations, and impacts on dosimetric quantities determined *via* graphite calorimetry, such as  $\epsilon G$  for Fricke dosimetry and  $(W/e)_{\text{air}}$  for ion chamber measurements.

## Acknowledgments

I was very fortunate to be teamed up with Dr. Carl Ross as my thesis advisor. His experience, judgement, and support were invaluable throughout this project. I am also grateful to Dr. Dave Rogers, who provided a great deal of guidance and insight over the years.

My colleagues and co-workers at the Ionizing Radiation Standards group of the National Research Council have been exceedingly helpful, and I thank all of them for sharing their talents, humour, and criticisms. In particular, I would like to thank Leo Heistek, David Marchington, and Matt Kosaki, whose helpfulness and technical expertise made this project possible. I would also like to thank my fellow graduate students at NRC: George Ding, Andrew Weber, Jiansu Wei, Daryoush Sheikh Bagheri, Geoff Zhang, and Ria Corsten.

I am grateful to the physicians and staff of the Ottawa and Montreal General Hospitals, for enabling me to continue my studies.

I would like to thank my family, especially my parents, who have always given me unwavering and unconditional support. This thesis is ultimately a product of their sacrifices.

Always, and above all, there was Jessie, my wife and best friend. I dedicate this thesis to her.

# Contents

<b>1</b>	<b>Introduction</b>	<b>1</b>
1.1	Stopping Power . . . . .	2
1.1.1	Radiative Stopping Power . . . . .	3
1.1.2	Collision Stopping Power . . . . .	4
1.1.3	Restricted Stopping Power . . . . .	7
1.2	The Need for Accurate Stopping Power Measurements . . . . .	8
1.2.1	Theoretical Problems . . . . .	8
1.2.2	Historical Changes . . . . .	8
1.2.3	Lack of Experimental Confirmation . . . . .	9
1.3	Guide to the Thesis . . . . .	10
<b>2</b>	<b>A Detailed Study of a Proposal for the Measurement of Electron Collision Stopping Powers</b>	<b>12</b>
2.1	Introduction . . . . .	12
2.2	Revised Formalism . . . . .	14
2.3	Sensitivity to Monte Carlo Uncertainties . . . . .	23
2.3.1	Dependence on $S_{\text{rad}}$ . . . . .	23
2.3.2	Role of the Møller Cross Section . . . . .	32
2.3.3	Dependence on Path Length . . . . .	32
2.4	Preliminary Experimental Considerations . . . . .	36
2.4.1	Simulated NaI Spectra . . . . .	36
2.4.2	Uncertainty Verification . . . . .	38
2.4.3	Counting Statistics . . . . .	41
2.4.4	Range of Fit . . . . .	41
2.4.5	Binning Requirements . . . . .	44
2.4.6	Sensitivity of the Method . . . . .	44
2.5	Conclusions . . . . .	47

<b>3</b>	<b>A Magnetic Spectrometer for Electron Energy Calibrations</b>	<b>49</b>
3.1	Introduction . . . . .	49
3.2	Theory . . . . .	50
3.3	Materials and Methods . . . . .	53
3.3.1	The Magnet . . . . .	53
3.3.2	Field Mapping . . . . .	53
3.3.3	Ray Tracing . . . . .	63
3.3.4	The Spectrometer . . . . .	76
3.4	Results and Discussion . . . . .	87
3.4.1	Energy Calibration of the Linac . . . . .	87
3.4.2	Beam Characteristics . . . . .	94
3.4.3	Error Analysis . . . . .	97
3.5	Conclusion . . . . .	97
<b>4</b>	<b>Accurate Measurement of Electron Energy Spectra Using a Large NaI Detector</b>	<b>100</b>
4.1	Introduction . . . . .	100
4.2	Choice of Detector . . . . .	100
4.2.1	High Purity Germanium Detectors . . . . .	101
4.2.2	Large NaI Detector . . . . .	105
4.3	Sensitivity to Measurement Geometry . . . . .	109
4.4	Measurement of Electron Spectra . . . . .	112
4.5	Gain Stabilization . . . . .	115
4.6	Detector Response . . . . .	118
4.6.1	Detector Window . . . . .	124
4.6.2	Detector Non-linearity . . . . .	125
4.7	Pulse Pile-up . . . . .	129
4.7.1	Measurement of Low Energy Contamination . . . . .	133
4.7.2	Modulator Noise . . . . .	137
4.8	Conclusions . . . . .	137
<b>5</b>	<b>Accurate Measurements of the Collision Stopping Powers for 5 to 30 MeV Electrons</b>	<b>139</b>
5.1	Introduction . . . . .	139
5.2	Materials and Methods . . . . .	140
5.2.1	Absorbing Disks . . . . .	140
5.2.2	Measurement of Electron Spectra . . . . .	141
5.2.3	Monte Carlo Simulations . . . . .	142



5.2.4	Detector Response and Stopping Power Extraction . . . . .	143
5.3	Results . . . . .	146
5.3.1	Uncertainty Analysis . . . . .	146
5.3.2	Measured Stopping Powers . . . . .	150
5.3.3	Implications for Dosimetry . . . . .	159
5.4	Conclusions . . . . .	167
<b>6</b>	<b>Summary and Conclusions</b>	<b>169</b>
6.1	Summary of Results . . . . .	169
6.1.1	Chapter 2: A Detailed Study of a Proposal for the Measurement of Electron Collision Stopping Powers . . . . .	169
6.1.2	Chapter 3: A Magnetic Spectrometer for Electron Energy Calibrations	170
6.1.3	Chapter 4: Accurate Measurement of Electron Energy Spectra Using a Large NaI Detector . . . . .	170
6.1.4	Chapter 5: Accurate Measurements of Collision Stopping Powers for 5 to 30 MeV Electrons . . . . .	171
6.2	Future Work and Conclusions . . . . .	172
<b>A</b>	<b>Changing Discrete Interaction Cross Sections in EGS4</b>	<b>173</b>
<b>B</b>	<b>Absorbers for Stopping Power Measurements</b>	<b>178</b>
B.1	Aluminum Disks . . . . .	178
B.2	Other Elemental Absorbers . . . . .	178
B.3	Plastic Absorbers . . . . .	180
B.4	Water Absorber . . . . .	180

# List of Figures

2.1	Illustration of electron interactions . . . . .	13
2.2	The effects of discrete interactions and multiple elastic scattering . . . . .	16
2.3	Relationship between $t_{\text{eff}}$ and $\theta_{\text{max}}$ . . . . .	18
2.4	Relationship between $\kappa$ and $\epsilon$ for Be . . . . .	21
2.5	Relationship between $\kappa$ and $\epsilon$ for Ta . . . . .	22
2.6	Components of the pulse height distribution for Ta . . . . .	24
2.7	Effect of bremsstrahlung on Be . . . . .	26
2.8	Effect of bremsstrahlung on Ta . . . . .	27
2.9	Effect of bremsstrahlung on spectral shape for Ta . . . . .	28
2.10	Example of no photons reaching the detector . . . . .	30
2.11	Effect of photons on NaI detector . . . . .	31
2.12	Effect of AE . . . . .	33
2.13	Effect of step size on stopping power . . . . .	37
2.14	Technique for generating simulated spectra . . . . .	39
2.15	Verification of uncertainty estimates . . . . .	40
2.16	Effect of counting statistics . . . . .	42
2.17	Variation of fit window for simulated spectrum . . . . .	43
2.18	Behaviour of $\chi^2$ distribution near its minimum . . . . .	46
3.1	Illustration of the sharp cutoff. . . . .	52
3.2	Vacuum box for Anac magnet. . . . .	54
3.3	Magnet for effective point of measurement . . . . .	57
3.4	Effective point of measurement for two Rawson probes. . . . .	58
3.5	Effect of field strength on fringing field shape. . . . .	60
3.6	Comparison of entrance and exit fringing fields. . . . .	61
3.7	Field inside pole faces increases toward exit side. . . . .	62
3.8	Schematic of spectrometer as a magnetic circuit. . . . .	64
3.9	Geometry for ESPLINE ray tracing program . . . . .	66
3.10	Example of field symmetry between pole faces . . . . .	68

3.11	The thirteen point grid used to determine off-axis field components. . . . .	70
3.12	Geometry for RAYTRACE . . . . .	71
3.13	Comparison of alignment and SCOFF reference frames . . . . .	73
3.14	The path of an electron through the measured field. . . . .	77
3.15	Sample high current spectrum . . . . .	80
3.16	Schematic of magnetic spectrometer. . . . .	81
3.17	Low current spectra . . . . .	82
3.18	Residual fields of the magnetic spectrometer . . . . .	85
3.19	Effect of residual fields on alignment. . . . .	86
3.20	Schematic of the 90-B beam line . . . . .	90
3.21	Effect of M1 slit. . . . .	92
3.22	Residuals from fitting electron energy to DVM . . . . .	93
3.23	Effective bending radius for 90-B. . . . .	95
3.24	Effect of S1 slit. . . . .	96
4.1	HPGe response at 10 MeV. . . . .	102
4.2	HPGe response at 30 MeV. . . . .	103
4.3	Schematic of germanium detector crystals. . . . .	104
4.4	Calculated absorber spectra for HPGe at 10 MeV. . . . .	106
4.5	Calculated absorber spectra for HPGe at 30 MeV. . . . .	107
4.6	Schematic cross section of the large NaI detector . . . . .	108
4.7	Effect of beam radius on no-absorber spectra . . . . .	110
4.8	Effect of beam radius, $1 \text{ g cm}^{-2}$ copper. . . . .	111
4.9	Effect of slab-detector separation. . . . .	113
4.10	Example of fitting a simulated spectrum over entire energy range . . . . .	114
4.11	Schematic of the electron spectrum measurement geometry. . . . .	116
4.12	Schematic of components used for spectroscopy and gain stabilization. . . . .	117
4.13	Typical performance of the gain stabilization unit. . . . .	119
4.14	Gain stabilization summary at 15 MeV. . . . .	120
4.15	Gain stabilization summary at 25 MeV. . . . .	121
4.16	FWHM versus energy for no-absorber spectra. . . . .	123
4.17	FWHM for several materials with sponge excluded. . . . .	126
4.18	FWHM for several materials with sponge included. . . . .	127
4.19	Schematic of measurement of NaI axial response. . . . .	130
4.20	Scan of detector response with depth. . . . .	131
4.21	Effect of pile-up at low energies. . . . .	132
4.22	Sample event-time distribution. . . . .	134
4.23	Pile-up correction using measured and flat event time distributions. . . . .	135

4.24	Example of a fit to a pile-up corrected spectrum. . . . .	136
5.1	Example of no-absorber fit. . . . .	144
5.2	Example of with absorber fit. . . . .	145
5.3	Measured values of $\kappa$ for elemental absorbers. . . . .	151
5.4	Measured stopping powers for beryllium. . . . .	152
5.5	Measured stopping powers for aluminum. . . . .	153
5.6	Measured stopping powers for copper. . . . .	154
5.7	Measured stopping powers for tantalum. . . . .	155
5.8	Measured values of $\kappa$ for graphite. . . . .	157
5.9	Measured stopping powers for graphite. . . . .	158
5.10	Measured stopping powers for A-150 plastic. . . . .	160
5.11	Measured stopping powers for C-552 plastic. . . . .	161
5.12	Schematic of aluminum vessel used in water stopping power measurements .	162
5.13	Measured stopping powers for water. . . . .	163
5.14	Measured of $\kappa$ for dosimetric materials. . . . .	164

# List of Tables

2.1	Dependence of path length on angle . . . . .	19
2.2	Effect of step size on $t_{\text{eff}}$ . . . . .	35
2.3	Apparent offsets for different fit windows . . . . .	45
3.1	Specifications of spectrometer magnet. . . . .	55
3.2	Comparison of SCOFF and RAYTRACE . . . . .	75
3.3	Corrections for earth's field. . . . .	88
3.4	Breakdown of uncertainties related to energy calibration . . . . .	98
5.1	Estimated uncertainties in stopping powers . . . . .	149
A.1	MSTEST results of bremsstrahlung cross section scaling . . . . .	175
A.2	MSTEST results of Møller cross section scaling . . . . .	177
B.1	Thicknesses of aluminum absorbers . . . . .	179
B.2	Thicknesses of elemental absorbers . . . . .	181
B.3	Thicknesses of plastic absorbers . . . . .	182



# Chapter 1

## Introduction

Cancer is a disease that affects nearly one in four Canadians, and the incidence of new cancers is on the rise [1]. Nearly one half of new cancer patients will receive radiation therapy, either by itself or in conjunction with surgery or chemotherapy.

Radiation controls cancer by causing damage to important cellular structures, such as DNA. The amount of damage, and hence the probability of controlling the tumour, is directly related to the *absorbed dose*, defined as the amount of energy imparted per unit mass of the material [2].

The aim in radiotherapy is to deliver a prescribed radiation dose to the tumour, while minimizing concomitant dose to healthy tissue. Accurate delivery of the treatment dose is crucial. Errors in delivered dose as low as 5% have been shown to affect tumour control or normal tissue response [3], [4], [5].

Different sources of radiation are used in radiotherapy. In *brachytherapy*, radioactive sources are placed in, or close to, the tumour. *Teletherapy* uses external beams of photons or electrons to deliver the treatment. Ultimately, all dose is deposited by charged particles, usually electrons, which cause ionization and excitation in the target materials. Accurate delivery of prescribed radiation doses therefore requires detailed knowledge of the energy deposition by electrons. Of particular interest is the rate at which electrons lose energy in a material, a quantity known as the *stopping power*. Stopping powers play crucial roles in radiation dosimetry; they are central to measurements of absorbed dose (see, e.g. [6], [7]), and radiation transport calculations [8]. Errors in stopping powers translate directly into

errors in dose [9].

At present, all values of electron stopping powers are based on a theoretical model, with calculated stopping powers tabulated in reference sources such as Report 37 of the International Commission on Radiation Units and Measurements (ICRU) [10]. The uncertainties on these theoretical stopping powers are not well established, but have been estimated to be 0.5%-1% ( $1\sigma$ ) for electron energies greater than 100 keV. This thesis presents the first measurements of electron stopping powers capable of testing these theoretical values at this level of uncertainty.

The thesis begins with a review of the stopping power theory, and the current state of experimental data.

## 1.1 Stopping Power

Consider an energetic (several MeV) electron traversing a slab of some material of thickness  $t$ . There are four principal types of interactions which such an electron may undergo.

- Collisions with atoms at large impact parameters, which lead to ionization and excitation of the atomic electrons. Such interactions are termed “soft” collisions, because the energy transfer per collision is small.
- Collisions with individual atomic electrons at small impact parameters (on the order of the atomic radius). The target (atomic) electron is given sufficient energy to cause secondary ionization along a new track. Such “secondary” electrons are termed  $\delta$  rays.
- Deflections in the presence of strong Coulomb fields, usually around the atomic nucleus, which result in the emission of a photon which radiates energy away from the incident electron. Such radiation is called *bremsstrahlung*, from the German for “braking” radiation.
- Elastic collisions with atomic nuclei, which result in a change in the electron’s direction but no appreciable energy loss. These elastic collisions give rise to very tortuous paths for electrons.



Each of the above interactions is inherently stochastic, and it is impossible to predict which interactions an individual electron will undergo at a particular site. This inherent randomness results in different interaction histories for each incident electron, so that the energy distribution for an electron beam which has passed through a layer of material is spread out, or “straggled”. Variations in energy loss processes give rise to *energy loss straggling*, while differences in path length (and therefore energy loss) due to variations in elastic scattering events give rise to *path length straggling*.

However, in the non-stochastic limit of many electrons, it is useful to talk about average quantities. For radiation dosimetry, the most important such quantity is the *stopping power*, defined as the average rate at which electrons lose kinetic energy  $T$  per unit path length  $x$ ,

$$S = \frac{dT}{dx}, \quad (1.1)$$

with appropriate units of  $\text{MeV cm}^{-1}$ . In practice, it is more useful to divide equation 1.1 by the material density  $\rho$  to give the mass stopping power,

$$\frac{S}{\rho} = \frac{1}{\rho} \frac{dT}{dx}, \quad (1.2)$$

in which case the units are  $\text{MeV cm}^2\text{g}^{-1}$ . This removes sample-to-sample variations in stopping power with density.

Sometimes the method of energy loss is important for understanding a particular dosimetric or radiological problem. For this reason, the stopping power is divided into two terms: the *collision* stopping power, which encompasses energy transfers to atomic electrons, and the *radiative* stopping power, which describes energy losses due to radiative effects (bremsstrahlung emission). The total stopping power is therefore given by:

$$\left(\frac{S}{\rho}\right)_{\text{tot}} = \left(\frac{S}{\rho}\right)_{\text{col}} + \left(\frac{S}{\rho}\right)_{\text{rad}}. \quad (1.3)$$

Each of these components will now be discussed separately.

### 1.1.1 Radiative Stopping Power

Radiative losses occur when the electron is deflected in the presence of a strong coulomb field. Usually this occurs in the vicinity of the atomic nucleus, although electron-electron

bremsstrahlung events do occur. The average rate of energy loss ( $\text{MeV cm}^2\text{g}^{-1}$ ) due to radiative processes for an electron of energy  $T$  is given by

$$\left(\frac{S}{\rho}\right)_{\text{rad}} = N \int_0^T k \frac{d\sigma_{\text{brem}}}{dk} dk, \quad (1.4)$$

where  $N$  is the number of atoms per gram of material,  $d\sigma_{\text{brem}}/dk$  is the bremsstrahlung cross section (for both nuclear and electron-electron bremsstrahlung) per atom, differential in photon energy  $k$ .

There is no single theoretical treatment which yields  $\sigma_{\text{brem}}$  for all electron energies. Instead, the cross section is evaluated differently in two energy regimes. For electron energies below 2 MeV, the ICRU stopping powers employ the numerical evaluations of Tseng and Pratt [11], while for energies greater than 50 MeV, the cross section is evaluated analytically using expressions derived in the Born approximation [10]. In the intermediate energy region (2 to 50 MeV), the cross section is determined by interpolating between the two results. The estimated uncertainty in  $\left(\frac{S}{\rho}\right)_{\text{rad}}$  is 3-5% [10]. Measurements by Faddegon *et al.* of forward-directed bremsstrahlung [12] and angular distributions of bremsstrahlung [13] agreed with the theoretical values, although the integrated measured bremsstrahlung yield per electron tended to be higher than the theoretical value by about 10% for low atomic number targets.

The *radiation yield*,  $Y(T_o)$ , given by,

$$Y(T_o) = \frac{1}{T_o} \int_0^{T_o} \left( \frac{S(T)_{\text{rad}}}{S(T)_{\text{tot}}} dT \right), \quad (1.5)$$

is the fraction of an electron's energy that is emitted as bremsstrahlung radiation as the electron comes to rest.

### 1.1.2 Collision Stopping Power

The collision stopping power encompasses all interactions which result in a transfer of energy from the incident electron to the target electron. As discussed above, these transfers fall into two categories: “soft” collisions which transfer small amounts of energy at relatively large distances, and “hard” collisions in which the target electron receives sufficient energy to cause secondary ionization along a new track. The collision stopping power can be written

as

$$\left(\frac{S}{\rho}\right)_{\text{col}} = \left(\frac{S}{\rho}\right)_{\text{soft}} + \left(\frac{S}{\rho}\right)_{\text{hard}}. \quad (1.6)$$

The soft collision term can be thought of as comprising those collisions which result in an energy transfer less than some predefined cutoff energy  $W_c$ , while the hard collision term describes all transfers from  $W_c$  to the maximum,  $T_{\text{max}}$ . For electrons, the maximum energy transfer is taken to be  $T/2$ , since the secondary electron is indistinguishable from the primary electron. That is,

$$\left(\frac{S}{\rho}\right)_{\text{col}} = NZ \int_0^{W_c} W \frac{d\sigma}{dW} dW + NZ \int_{W_c}^{T/2} W \frac{d\sigma}{dW} dW, \quad (1.7)$$

where  $N$  is the number of atoms of atomic number  $Z$  per gram in the target,  $d\sigma/dW$  is the interaction cross section per electron differential in energy transfer  $W$ .

### Soft Collision Term

For energy transfers less than  $W_c$ , Bethe ([14], [15], [16]) derived the following expression:

$$\left(\frac{S}{\rho}\right)_{\text{soft}} = \frac{2\pi NZ r_e^2 m_o c^2}{\beta^2} \left[ \ln \left( \frac{2m_o c^2 \beta^2 W_c}{(1 - \beta^2) I^2} \right) - \beta^2 \right], \quad (1.8)$$

where  $r_e$  is the classical electron radius,  $m_o c^2$  is the electron rest mass,  $\beta = v/c$  (i.e. the particle velocity over the speed of light), and  $I$  is the mean excitation energy of the electrons in the target. (For a discussion of the original derivation, the reader is referred to [17] or [18]).

Evaluation of the soft collision term requires the mean excitation energy (or mean excitation potential),  $I$ , for the material. Purely theoretical evaluations of  $I$ -values are complicated, so current values are determined from three principal sources: oscillator strength measurements for gases, dielectric response functions for liquids and solids, and stopping power measurements for protons and alpha particles (see, e.g. [19], [20]). The last are possible because radiative losses and elastic scattering are almost negligible for ions, so measurements of energy loss through a given material thickness, along with corrections for electron binding, lead directly to  $I$ -values.

### Hard Collision Term

If the energy transferred to an electron is large compared to its binding energy, the interaction resembles a collision between free electrons. This was the approach taken in deriving the

Møller cross section [21]. Relativistic and spin effects were taken into account, as were exchange effects resulting from the close passage of the incident particle to the target particle.

The differential Møller cross section per electron is:

$$\frac{d\sigma_{\text{Møller}}}{dW} = \frac{2\pi r_e^2 m_o c^2}{\beta^2 W^2} \left[ 1 + \frac{W^2}{(T - W)^2} + \frac{\tau^2}{(\tau + 1)^2} \left( \frac{W}{T} \right)^2 - \frac{(2\tau + 1)}{(\tau + 1)^2} \frac{W}{(T - W)} \right], \quad (1.9)$$

where  $\tau = T/m_o c^2$  is the ratio of the incident electron's kinetic energy to the electron rest mass, and other quantities are as described above.

Combining equations 1.7, 1.8, and 1.9 gives the following expression for the collision stopping power:

$$\left( \frac{S}{\rho} \right)_{\text{col}} = \frac{2\pi N Z r_e^2 m_o c^2}{\beta^2} \left[ \ln(T/I)^2 + \ln(1 + \tau/2) + F^-(\tau) - \delta \right], \quad (1.10)$$

where

$$F^-(\tau) = (1 - \beta^2)[1 + \tau^2/8 - (2\tau + 1) \ln 2]. \quad (1.11)$$

and  $\delta$  is the density effect correction, which will be discussed in the next section. Notice that the final expression for the collision stopping power is independent of the cutoff energy transfer,  $W_c$ . This results from dropping higher order terms in the evaluation of equation 1.10, so that the integral of the Møller cross section contains only the logarithm of  $W_c$ . This seems to imply that the Bethe term is applicable to arbitrarily high energy transfers, or that the Møller cross section works for even small energy transfers. Neither of these extensions is valid. However, the following restrictions are placed on  $W_c$ : (a)  $W_c$  must be large compared with the binding energies of the atomic electrons in the stopping medium and (b) impact parameters associated with energy losses smaller than  $W_c$  must be large compared to atomic dimensions. This limits the use of the Bethe term and Møller cross section to regimes where the assumptions inherent in each remain valid.

## The Density Effect

The electric field of an incident electron will polarize the atomic electrons, so that the net field, and hence the stopping power, is reduced. This reduction in stopping power due to polarization is usually called the density effect, because it is most pronounced in dense materials.

The density effect can be calculated based on the dielectric response function of the material. This has been done for aluminum [22] and water [23]. However, the dielectric response function frequently is not known. Sternheimer [24] introduced an approximate method for calculating the density effect. In this model, the medium was assumed to be homogeneous, and a correction factor was introduced so that the sum of electron energy levels for a given atom was consistent with the mean ionization potential used in the calculation of the collision stopping power. This quite complicated expression was used to evaluate several values of  $\delta$  for several materials, and the results were parameterized in a simplified expression by Sternheimer and Peierls [25]. The ICRU stopping powers employed a numerical evaluation of the Sternheimer density effect correction using the best available physical data [26].

The density effect becomes more important at higher energies, where distant collisions are more prevalent due to the Lorentz contraction.

### 1.1.3 Restricted Stopping Power

Sometimes the quantity of interest is how much energy the electron loses locally, such as within the gaseous volume of an ion chamber. In such a case, large energy transfers to secondary electrons are of little interest, since most of the energy will be deposited a significant distance away from the track of the primary electron. The restricted stopping power  $L(T, \Delta)$  is defined as the average energy loss per unit path length resulting from energy transfers less than a certain cutoff energy  $\Delta$ . This entails replacing  $T/2$  with  $\Delta$  in equation 1.7 to give

$$\frac{L(T, \Delta)}{\rho} = \frac{2\pi N Z r_e^2 m_o c^2}{\beta^2} \left[ \ln(T/I)^2 + \ln(1 + \tau/2) + G^-(\tau, \eta) - \delta \right], \quad (1.12)$$

where  $\eta = \Delta/T$ , and

$$G^-(\tau, \eta) = -1 - \beta^2 + \ln[4(1 - \eta)\eta] + (1 - \eta)^{-1} + (1 - \beta^2)[\tau^2 \eta^2 / 2 + (2\tau + 1) \ln(1 - \eta)]. \quad (1.13)$$

Restricted stopping powers are used in Spencer-Attix cavity theory calculations to relate the dose in a dosimeter (such as an ion chamber) to the dose in the surrounding medium. In the context of this thesis, they will arise in the discussion of Monte Carlo simulations, where they are used to describe electron energy losses between hard collisions.

## 1.2 The Need for Accurate Stopping Power Measurements

The uncertainty on the ICRU 37 stopping powers is estimated to be between 0.5% and 1% ( $1\sigma$ ) for electron energies greater than 100 keV [10]. However, this seems to reflect an estimate of the impact of uncertainties on input parameters (such as  $I$ ) rather than an expression of confidence in the underlying theory [27].

### 1.2.1 Theoretical Problems

There is reason to suspect that there may be problems with the collision stopping power. The Bethe soft collision term was derived using the first Born approximation. It should therefore be valid provided that [28],

$$\left(\frac{Z}{137\beta}\right)^2 \ll 1,$$

a condition which is not satisfied for materials with high atomic numbers  $Z$ .

Furthermore, the Sternheimer density effect correction was derived assuming that the absorbing medium is homogeneous, and that the polarizability of the medium is the same in all directions. For many materials, including compounds, mixtures, and crystals, these assumptions are not satisfied.

### 1.2.2 Historical Changes

The theoretical stopping powers have undergone many substantial changes since Berger and Seltzer [29] published their tabulated values in 1964. Usually these changes are a result of new experimental data for  $I$ -values, which have the biggest impact at low energies. Even at 10 MeV, however, the stopping power for water changed by 1.2% and that for gold by 1.6% (nearly a  $2\sigma$  difference) from Berger and Seltzer (1964) to ICRU 37. Since the publication of ICRU 37, new measurements of  $I$ -values for water and graphite [30] have resulted in further changes in the accepted stopping power.

The density effect correction for aluminum has been re-evaluated by Inotouki and Smith [22] using semi-empirical dielectric response data, rather than the Sternheimer approach. Ashley [23] has similarly re-evaluated the density effect correction for water. These evaluations are believed to be more accurate than the Sternheimer values. In the case of water, the resulting stopping power is 0.5% higher at 1 MeV, and 0.5% lower at 10 MeV. The aluminum values agree within 0.2%. Nonetheless, these discrepancies underscore the need for accurate measurements in a regime where the density effect correction is important (several MeV).

These historical changes, and the problems with the theory discussed in the previous section, indicate that there may be problems with the low energy transfer (i.e. “soft collision”) component of the collision stopping power.

### 1.2.3 Lack of Experimental Confirmation

Very few measurements of electron stopping powers have been attempted for electron energies of several MeV, and none have demonstrated sufficient accuracy to test the theoretical values at the 1% level.

One of the earliest measurements was performed by Hereford [31], who measured stopping powers for several materials relative to graphite using a Geiger-Muller counter.

Several investigators have made measurements of electron spectra using magnetic spectrometers. Goldwasser *et al* [32] and Hall *et al* [33] measured changes in the most probable energy for electron beams passed through thin foils, and compared their results to the Landau electron straggling distribution. Paul and Reich measured stopping powers for beryllium, graphite, iron, lead, and water with uncertainties ranging from 5 to 10% [34]. Westmark used a similar experiment and presented stopping powers relative to beryllium and aluminum [35]. Mikado *et al* measured average energy losses for 24.8 MeV electrons at several angles around absorbers [36] in an attempt to establish an experimental expression for energy loss per path length. Their results were later compared with Monte Carlo simulations by Antolak and Williamson [37]. However, the energy resolution was insufficient to test the theoretical stopping powers.

The most accurate measurement to date was performed by Feist and Müller [38], who used a ferrous sulfate dosimeter to measure the total energy transported by 5.3 MeV elec-

trons through slabs of polystyrene. Their result agreed with the theoretical value within their stated uncertainty of 1.2%. However, Rogers and Faddegon [39] pointed out that the uncertainty was in fact nearly 5% due to a 0.2% uncertainty in the energy absorption measurement.

More recently, Burns *et al* [40] reported measurements of stopping power ratios using range measurements modified by Monte Carlo simulations. The quoted uncertainty was 0.5%, but assumed the only errors in the stopping powers were due to small errors in input values. Ross and MacPherson [41] showed that for this reason the method could not measure uniquely the stopping power ratio at a given energy.

In 1992, Faddegon *et al* [42] proposed a technique for measuring electron collision stopping powers using a large sodium iodide (NaI) detector to measure the changes in electron energy spectra when absorbing slabs of known thicknesses were placed in the electron beam. Monte Carlo simulations were performed to account for the many interactions which took place, and the difference in energy between the measured and calculated spectra was related to an error in the collision stopping power. The technique suffered from uncertainties in energy calibration, gain drift, and detector response. Also, the relationship between the measured energy difference and collision stopping powers was not well established, and the role of uncertainties in the Monte Carlo simulations was not investigated in sufficient detail. Consequently, the errors in their measured stopping powers were estimated to be 5-10%.

### 1.3 Guide to the Thesis

The aim of this project has been to make the most accurate measurements of electron collision stopping powers yet recorded by improving the technique of Faddegon *et al* and reducing the associated experimental uncertainties.

This work begins (Chapter 2) by revisiting the technique of Faddegon *et al*, and proposes a new interpretation of the difference in energy loss between measured and calculated spectra. The limitations of the technique are investigated and the uncertainties contributed by the Monte Carlo simulations are quantified. In addition, experimental requirements for accurate measurements of electron stopping powers are discussed.



Chapter 3 addresses one of the major obstacles to an accurate stopping power measurement: the calibration of the incident electron energy. It describes the design, construction, and operation of a magnetic spectrometer capable of establishing electron energy with an uncertainty of 0.3%.

Chapter 4 discusses the measurement of electron energy spectra with sufficient accuracy and precision to make meaningful stopping power measurements. The choice of spectrometer and geometric considerations for the experimental setup are discussed. The precise operation of the sodium iodide detector is discussed in detail, including the characterization of the response of the detector using electron beams, techniques used to control photomultiplier tube gain drift, and the elimination of pulse pile-up.

Chapter 5 describes the measurement of electron collision stopping powers, drawing on the techniques described in the three previous chapters. Corrections for non-linearity are introduced, and the overall uncertainties in the final measurements are discussed. Measured stopping powers are presented in graphical form for several materials.

Appendix A discusses the technique used to modify discrete interaction cross sections in the EGS4 Monte Carlo code.

Appendix B lists mechanical measurements of mass and thickness for the absorbers used in the stopping power measurements.

## Chapter 2

# A Detailed Study of a Proposal for the Measurement of Electron Collision Stopping Powers

### 2.1 Introduction

In 1992, Faddegon *et al* [42] reported a technique for the measurement of collision stopping powers, where a large sodium iodide (NaI) spectrometer was used to measure the shift in electron energy when an absorbing slab was placed in an electron beam. Monte Carlo simulations were used to predict the pulse height distributions in the NaI crystal, accounting for electron beam interactions in the absorber, beam window, detector cladding, and surrounding air (see figure 2.1). Energy differences between the calculated and measured spectra were then related to an error in the theoretical unrestricted collision stopping powers employed in the simulations. The technique, as reported, suffered from several shortcomings. Experimentally, the uncertainty in stopping power was limited by uncertainties due to gain drift, energy calibration, and detector nonlinearity. Theoretically, the relationship between the measured energy differences and collision stopping power was not well established, and the impact of radiative energy losses was not quantified. Moreover, uncertainties in stopping power due to uncertainties in the Monte Carlo simulations were not addressed in sufficient detail. This

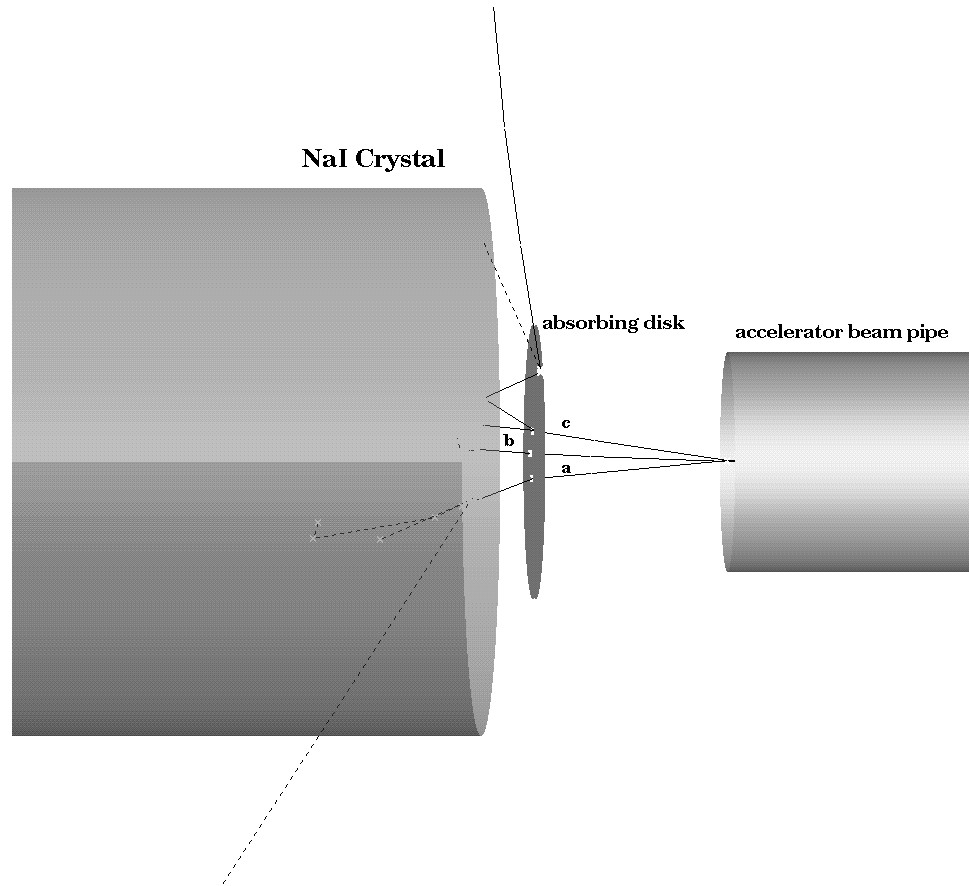


Figure 2.1: An illustration of some of the electron interactions for 10 MeV electrons on  $1 \text{ g cm}^{-2} \text{ Cu}$ . Electron “a” is deflected by the beam window of the accelerator, and travels obliquely through the absorber where it emits a photon (dashed line) which is absorbed in the NaI crystal. A second photon created in the NaI crystal escapes, carrying energy away. Electron “b” travels through the absorber and deposits all of its remaining energy in the detector. Electron “c” emits a  $\delta$ -ray in the absorber, which then “backscatters” from the detector toward the absorber, where it undergoes a radiative interaction.

chapter revisits the approach of Faddegon *et al* and presents a justification for relating the energy differences to errors in collision stopping power. The impacts of uncertainties in the Monte Carlo simulations are discussed, and the sensitivity and limitations of the fitting procedure are investigated. The experimental problems are addressed in Chapters 3 and 4.

## 2.2 Revised Formalism

We begin with a review of the technique of Faddegon *et al*. For a more complete discussion the reader is referred to the original paper [42]. Electron spectra were measured using a large NaI spectrometer with and without an absorbing slab placed in the beam. Monte Carlo simulations of each measurement were performed to predict the pulse height distribution in the spectrometer, taking into account interactions in the beam window, absorbing slab, detector cladding, and surrounding air. These calculated spectra were broadened with a Gaussian function to mimic the intrinsic detector resolution (pulse-to-pulse variations in pulse height) [43]. The energy at the centre of the  $i^{th}$  bin of the measured spectrum was taken to be

$$E_i = \beta_2(i - \beta_3), \quad (2.1)$$

where  $\beta_2$  defines the energy calibration (MeV/bin) and  $\beta_3$  is the bin offset.

For the no-absorber spectra,  $\beta_3$  was fixed at zero, as determined through precision pulser measurements. The parameter  $\beta_2$ , along with an area normalization factor, which resulted in the minimum  $\chi^2$  deviation with respect to the measured spectra, were then determined by least squares minimization using the program FITMC [44].

For the absorber spectra, it was assumed that the same calibration factor,  $\beta_2$ , would apply. The gain parameter was then fixed, allowing the offset to vary in the fit. This gave the bin offset  $\beta_3'$  (where the prime denotes that there is an absorber in the beam, consistent with the notation of Faddegon *et al*). The energy difference (i.e., the difference in energy lost) between the calculated and measured transmitted spectra was therefore:

$$\Delta E_{MC} - \Delta E_{meas} = \beta_2 \beta_3' = \epsilon. \quad (2.2)$$

where  $\Delta E_{MC}$  is the energy lost traversing the slab in the Monte Carlo calculation and  $\Delta E_{meas}$

is the measured energy loss in the slab. The measured stopping power was taken to be

$$\left(\frac{S_{\text{col}}}{\rho}\right)_{\text{meas}} = \frac{\Delta E_{\text{meas}}}{t_{\text{eff}}}, \quad (2.3)$$

where  $t_{\text{eff}}$  is the average path length of all primary electrons through the absorber. Similarly, the ICRU37 stopping power was given by the Monte Carlo change in energy,  $\Delta E_{\text{MC}}$ :

$$\left(\frac{S_{\text{col}}}{\rho}\right)_{\text{ICRU}} = \frac{\Delta E_{\text{MC}}}{t_{\text{eff,MC}}}. \quad (2.4)$$

Which leads to the relationship:

$$\left(\frac{S_{\text{col}}}{\rho}\right)_{\text{ICRU}}^{\text{meas}} = 1 - \frac{\beta_2 \beta_3'}{t_{\text{eff}} \left(\frac{S}{\rho}\right)_{\text{ICRU}}}. \quad (2.5)$$

In the original paper, the absorber thickness  $t$  was used in place of  $t_{\text{eff}}$ , with the assumption that the error would be small.

The fitting of electron spectra is largely insensitive to the low energy portions of the spectra, and the measured offset is dominated by the position of the leading (i.e., high energy) edge. This is discussed in greater detail in section 2.4.4. The underlying assumption in using equation 2.5 is that a change in average energy is reflected in an identical change at the leading edge. However, this is not proven.

The position of the leading edge of a transmitted electron spectrum depends on continuous energy loss as well as low energy discrete interactions. If discrete interactions are completely ignored, the characteristic energy straggling is lost (figure 2.2). Also shown in figure 2.2 is the result of excluding multiple elastic scattering, so that the shape and location of the peak are defined solely by energy loss processes. Again the peak is shifted in energy, and is more sharply defined due to the omission of path length straggling. This dependence on path length straggling is one reason why the Landau energy loss straggling distribution alone is insufficient for describing spectral shapes at these energies (5 to 30 MeV) and thicknesses (0.5 to 3 g cm<sup>-2</sup>). The impact of multiple scattering on stopping power measurements will be further discussed in section 2.3.3.

We concentrate for now on the collision component of the electron stopping power; radiative effects will be discussed in section 2.3.1. As discussed in Chapter 1, the collision stopping power is found by combining the Bethe soft collision equation for continuous energy loss with the Møller cross section for high energy transfers and a correction for the

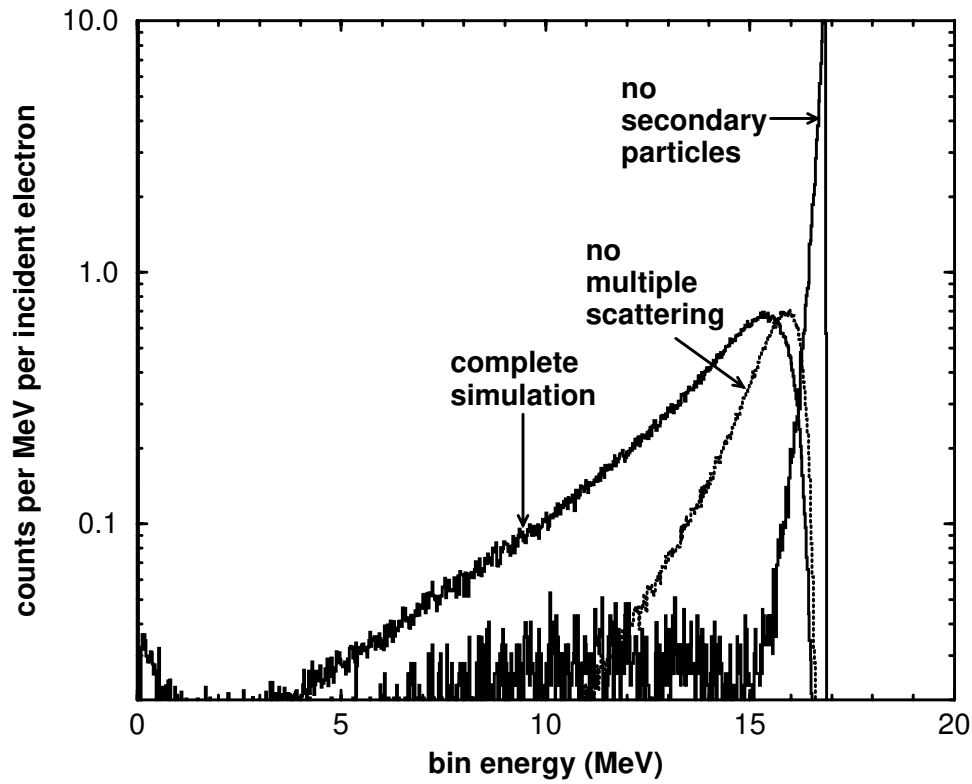


Figure 2.2: The effects of discrete interactions and multiple elastic scattering on a 20 MeV electron spectrum through a  $3 \text{ g cm}^{-2}$  copper absorber. Exclusion of knock-on electrons not only reduces straggling, but results in a dramatic shift in the leading edge of the spectrum. Exclusion of multiple scattering has a similar effect, albeit less pronounced.

polarization of atomic electrons in dense media. In the Monte Carlo simulations, the Bethe term and density correction are combined with low energy Møller events below a certain energy cutoff,  $\Delta$ , in a restricted stopping power,  $L(T, \Delta)/\rho$ , so that the collision stopping power is given by:

$$\left(\frac{S(T)}{\rho}\right)_{\text{col,ICRU}} = \frac{L(T, \Delta)}{\rho} + NZ \int_{\Delta}^{T/2} W \frac{d\sigma_{\text{Møller}}}{dW} dW, \quad (2.6)$$

where  $T$  is the incident electron energy,  $N$  is the number of atoms of atomic number  $Z$  per gram of material,  $W$  is the energy transferred to target electrons and  $\sigma_{\text{Møller}}$  is the Møller cross section. We now introduce the quantity  $\kappa$ , which is an additive term in the stopping power equation which represents the error contained in either the low energy transfer component of the stopping power, the density effect correction, or some combination of the two. So the real stopping power is,

$$\left(\frac{S(T)}{\rho}\right)_{\text{col,real}} = \left(\frac{S(T)}{\rho}\right)_{\text{col,ICRU}} + \kappa = \frac{L(T, \Delta)}{\rho} + \kappa + NZ \int_{\Delta}^{T/2} W \frac{d\sigma_{\text{Møller}}}{dW} dW. \quad (2.7)$$

Although less straightforward,  $\kappa$  could also be interpreted as being due to some error in the Møller cross section. In order to determine the impact of  $\kappa$  on measured spectra, various values of  $\kappa$  were added to the restricted stopping power of the absorber in Monte Carlo simulations of 7 and 30 MeV electrons incident on targets of beryllium, copper, and tantalum of various thicknesses. In each case, the calculated pulse height distribution was broadened to account for detector response, and the offset from the broadened default spectrum was determined by least squares fitting, using the program FITMC [44].

Earlier work [39] determined the effective path length,  $t_{\text{eff}}$ , using the EGS4 user code MSTEST to average the path lengths of all primary electrons which pass through the absorber. For this work, such a calculation constitutes an overestimate of the path length, since electrons with very tortuous paths contribute significantly to  $t_{\text{eff}}$  but lose too much energy to impact on  $\epsilon$ . This is illustrated in figure 2.3, which depicts the average path length for 7 MeV electrons through a  $0.5 \text{ g cm}^{-2}$  tantalum absorber. For each point, electrons which exit the absorber with an angle greater than  $\theta_{\text{max}}$  have been excluded from the calculation of  $t_{\text{eff}}$ . The path length correction is constant at around 7% for  $\theta_{\text{max}}$  less than  $20^\circ$ , then increases steadily as electrons with more tortuous paths are included in the calculation.

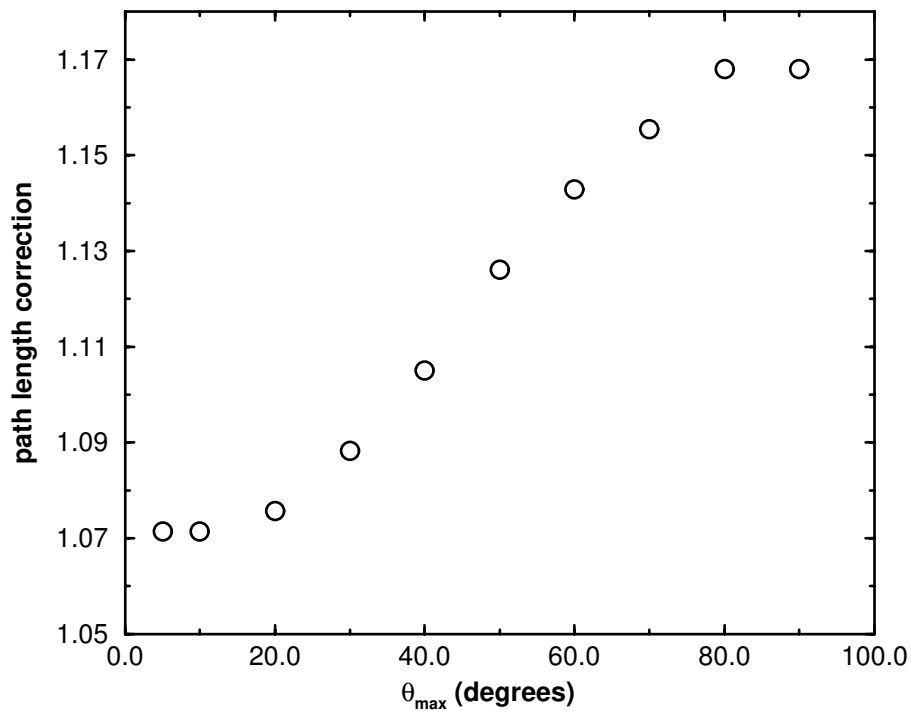


Figure 2.3: The variation of path length with exit angle for 7 MeV electrons through a  $0.5 \text{ g cm}^{-2}$  tantalum absorber. The path length correction increases dramatically when electrons which exit the absorber at high angles are included in the calculation of  $t_{\text{eff}}$ .



Aluminum ( $t=0.819 \text{ g cm}^{-2}$ )				
$\theta_{\max}$	$t_{\text{eff}} \text{ (g cm}^{-2}\text{)}$	$\frac{t_{\text{eff}}}{t}$	$E_{\text{avg}}$	
5°	0.833	1.018	5.570	
10°	0.835	1.019	5.551	
25°	0.842	1.029	5.476	
90°	0.872	1.065	5.218	
Copper ( $t=0.925 \text{ g cm}^{-2}$ )				
$\theta_{\max}$	$t_{\text{eff}} \text{ (g cm}^{-2}\text{)}$	$\frac{t_{\text{eff}}}{t}$	$E_{\text{avg}}$	
5°	0.974	1.053	5.360	
10°	0.982	1.062	5.330	
25°	1.004	1.085	5.251	
90°	1.096	1.185	4.969	
Tantalum ( $t=0.797 \text{ g cm}^{-2}$ )				
$\theta_{\max}$	$t_{\text{eff}} \text{ (g cm}^{-2}\text{)}$	$\frac{t_{\text{eff}}}{t}$	$E_{\text{avg}}$	
5°	0.922	1.15	5.570	
10°	0.939	1.17	5.551	
25°	0.962	1.21	5.476	
90°	1.154	1.45	5.218	

Table 2.1: The variation of  $t_{\text{eff}}$  as the maximum exit angle is increased for Al, Cu, and Ta absorbers at 7 MeV. Including all primary electrons in the calculation of  $t_{\text{eff}}$  overestimates the path lengths of those electrons which contribute to the high energy component of the electron spectrum.

Table 2.1 summarizes the calculations of such “restricted path lengths” for 7 MeV electrons on absorbers of aluminum, copper, and tantalum as  $\theta_{\max}$  was decreased from  $90^\circ$  to  $5^\circ$ . The largest impact both on path length and average transmitted energy occurs for large angle events ( $\theta_{\max} > 25^\circ$ ). For the beryllium and tantalum absorbers, the slope of a graph of  $\epsilon$  versus  $\kappa$  is equal to the path length calculated for  $\theta_{\max} = 20^\circ$  within 1%, regardless of absorber thickness or incident energy (figures 2.4 and 2.5). Therefore,

$$\kappa = -\frac{\epsilon}{t_{\text{eff}}^r}, \quad (2.8)$$

where  $t_{\text{eff}}^r$  is evaluated for  $\theta_{\max} = 20^\circ$ .  $t_{\text{eff}}^r$  is greater than  $t$  by at most 15% (1 g cm<sup>-2</sup> Ta at 7 MeV); usually, the difference is less than 5%. The choice of  $\theta_{\max}$  is somewhat arbitrary, and merely provides a convenient parameter for relating  $\kappa$  to  $\epsilon$ . A positive value for  $\epsilon$  indicates that the Monte Carlo energy loss is greater than the measured energy loss.

The measurement of  $\epsilon$  leads to a correction to the soft collision part of the electron stopping power. We can relate the measured correction to the unrestricted collision stopping power if we assume that there are no errors in the theoretical model for the hard collision component of the stopping power. Combining equation 2.7 with equation 2.8, the measured stopping power will be

$$\left(\frac{S}{\rho}\right)_{\text{meas}} = \left(\frac{S}{\rho}\right)_{\text{ICRU}} - \frac{\epsilon}{t_{\text{eff}}^r},$$

making the ratio of measured to ICRU stopping powers

$$\left(\frac{S}{\rho}\right)_{\text{ICRU}}^{\text{meas}} = 1 - \frac{\epsilon}{t_{\text{eff}}^r \left(\frac{S}{\rho}\right)_{\text{ICRU}}}. \quad (2.9)$$

Equation 2.9 is similar to the equivalent equation presented by Faddegon *et al*, except that  $t_{\text{eff}}$  has been replaced by  $t_{\text{eff}}^r$ . This difference arises from a recognition that only electrons which pass through the slab with little multiple scattering contribute to the high energy edge of the electron spectrum. The current result was derived from assuming an error in the soft collision component of the collision stopping power and relating that error to measured offsets between calculated and measured spectra. Equation 2.9 follows only if there are no errors in the hard collision component of the stopping power. On the other hand, the original equation was derived from the definition of the unrestricted collision stopping power, assuming changes in average energy would be mirrored exactly at the leading edge.

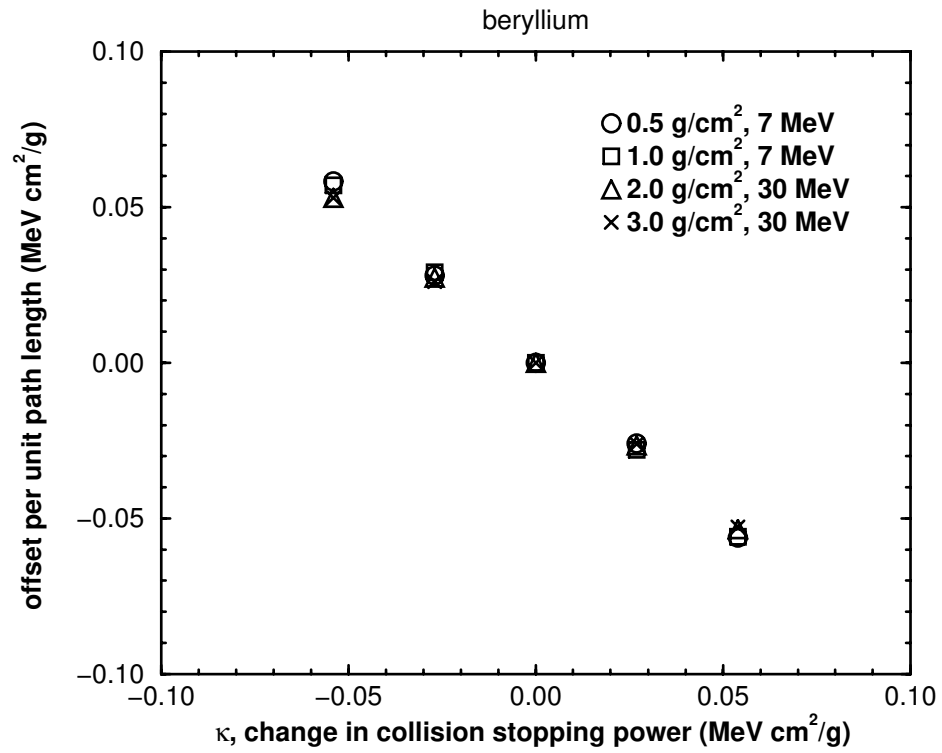


Figure 2.4: The measured offset per unit path length in beryllium is found to be equal to the additive correction to the collision stopping power,  $\kappa$ , within 1% for a wide range of thicknesses and energies.

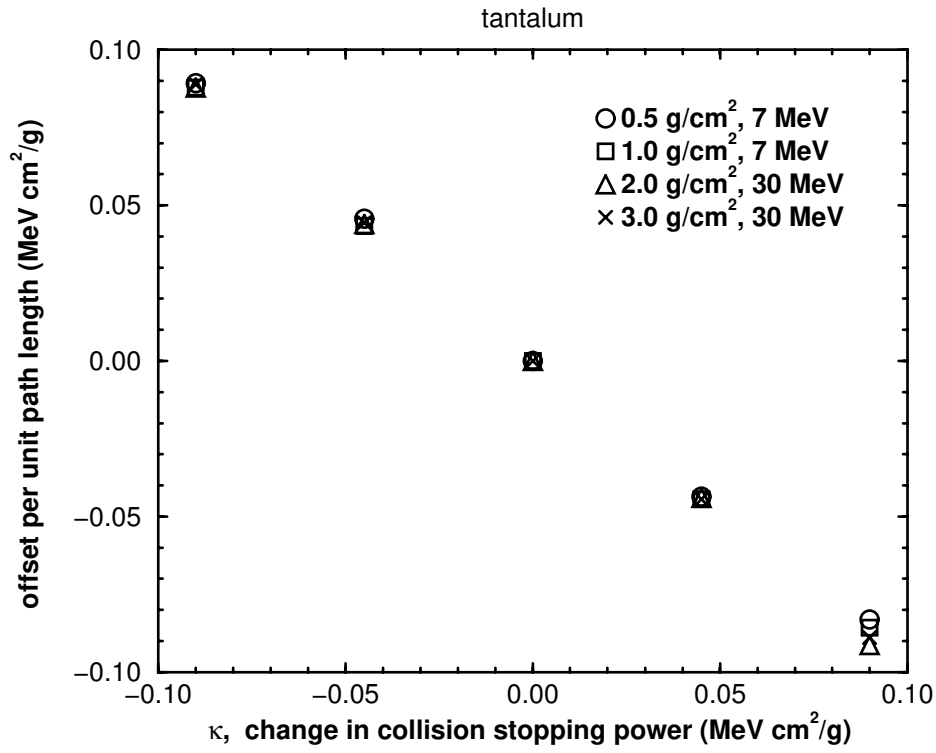


Figure 2.5: The measured offset per unit path length in tantalum is found to be equal to the additive correction to the collision stopping power,  $\kappa$ , within 1% for a wide range of thicknesses and energies.

## 2.3 Sensitivity to Monte Carlo Uncertainties

So far we have shown that errors in the low energy transfer component of the collision stopping power can be determined from measurable offsets between calculated and measured spectra. This relationship is only valid if the technique is insensitive to other components of the measurement and corresponding simulation. Consider figure 2.6 which shows the calculated pulse height distribution for a 10 MeV electron beam impinging on a nominally  $1 \text{ g cm}^{-2}$  tantalum absorber, as calculated using the EGS4 user code DOSRZ, with the ICRU 37 stopping powers employed [45], [46]. Also shown is the fluence spectrum of particles entering the detector, determined using the BEAM code [47]. The vertical axis has arbitrary units. Note that the peak of the pulse height distribution coincides closely in energy with the peak of the primary electrons. The bremsstrahlung photons which are shown entering the detector are not directly evident in the pulse height spectrum because they are mostly absorbed coincident with their parent electrons. Incomplete reabsorption of bremsstrahlung photons coupled with radiative losses from the detector crystal lead to a wider electron peak than is due to primary electrons only, so the sensitivity to bremsstrahlung production in the detector must be investigated. Low energy knock-on collisions give rise to the energy straggling of the peak as seen in figure 2.6. Higher energy delta rays do not affect the peak, but contribute significantly to the stopping power due to the large amount of energy each electron may carry away from the primary beam. We consider now the effects of these discrete interactions on the offset,  $\epsilon$ . The technique for changing the discrete interaction cross sections is described in detail in Appendix A.

### 2.3.1 Dependence on $S_{\text{rad}}$

The large NaI detector re-absorbs most photons generated in the absorbing slab. To a first approximation, then, the technique is insensitive to radiative losses and is a measure of only the collisional energy loss in the slab. This approximation is refined by the fact that Monte Carlo simulations are used to track the emitted photons and account for those which do not reach the detector. However, the possibility remains that radiative losses are incompletely or incorrectly modeled, and contribute to  $\epsilon$ .

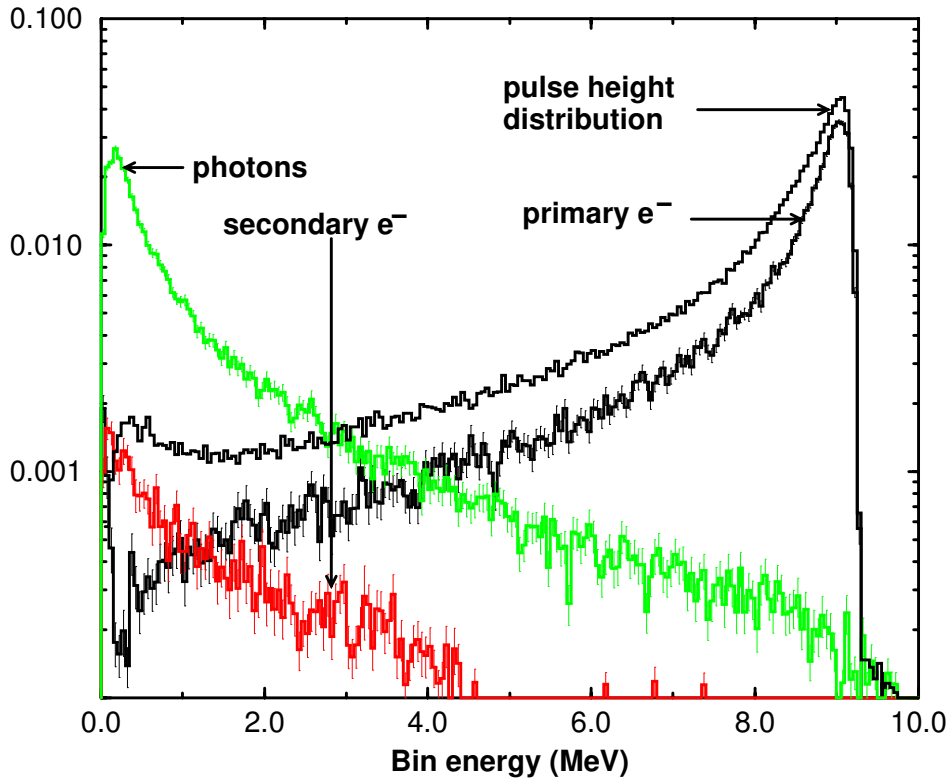


Figure 2.6: Calculated pulse height distributions and energy fluence spectra for 10 MeV electrons through  $1 \text{ g cm}^{-2}$  tantalum. The peak of the pulse height distribution corresponds to that of the primary electron spectrum, but is broader due to incomplete photon absorption. The threshold for secondary particle creation has been set to 10 keV.

The EGS4 user code DOSRZ was used to simulate the passage of 10 and 20 MeV electrons through absorbers of beryllium and tantalum. The pulse height spectrum inside the spectrometer was predicted for different values of the bremsstrahlung cross section. Each Monte Carlo spectrum was then fit to the broadened default Monte Carlo pulse height distribution.

Figure 2.7 shows the impact of a 40% change in the bremsstrahlung cross section for a  $2.0 \text{ g cm}^{-2}$  slab of beryllium. There is no discernible effect for 10 MeV or 20 MeV electrons for  $\pm 20\%$  changes in the photon emission. Figure 2.8 shows a similar plot for a  $1.0 \text{ g cm}^{-2}$  tantalum absorber. Here the apparent collision stopping power changes linearly by about 1% for a  $\pm 20\%$  change in the bremsstrahlung cross section. The reasons for this can be seen in figure 2.9, which shows the calculated pulse height distributions for 30 MeV electrons incident on  $2.0 \text{ g cm}^{-2}$  tantalum for different values of the tantalum bremsstrahlung cross section. The calculated spectra have been broadened to account for detector response. The production of bremsstrahlung has an impact on the energy straggling distribution, and hence on the leading edge of the spectrum. The integral cross section for bremsstrahlung events is assumed to be accurate to within 3-5% [10]. Faddegon [48], and Faddegon *et al* [13] have made measurements of bremsstrahlung spectra from thick targets and found that measured and calculated photon fluence per incident electron agreed within 10%. For the worst case of thick tantalum absorbers, this level of error would lead to a 0.25% change in the measured collision stopping power. We assume the  $1\sigma$  uncertainty for the tantalum stopping power is 0.1%. For the other absorbers, the effect is much less.

Another way to view the issue of photon emission is to assume that there is some error in the emission cross section differential in angle, so that the predicted number of photons striking the detector is wrong. The importance of this effect can be tested by considering the worst case, in which no photons generated in the slab reach the detector. This is accomplished in the Monte Carlo simulation by setting the photon transport cutoff in the slab, PCUT, equal to the incident electron energy. This results in photons being created in the absorber and then depositing their energy on the spot, so that no radiative energy from the slab is absorbed by the detector. For 30 MeV electrons incident on  $3 \text{ g cm}^{-2}$  tantalum, this results in an apparent 2% change in collision stopping power (consistent with extrapolating figure 2.8 to zero radiative cross section). This is a small effect, considering that the radiative stopping

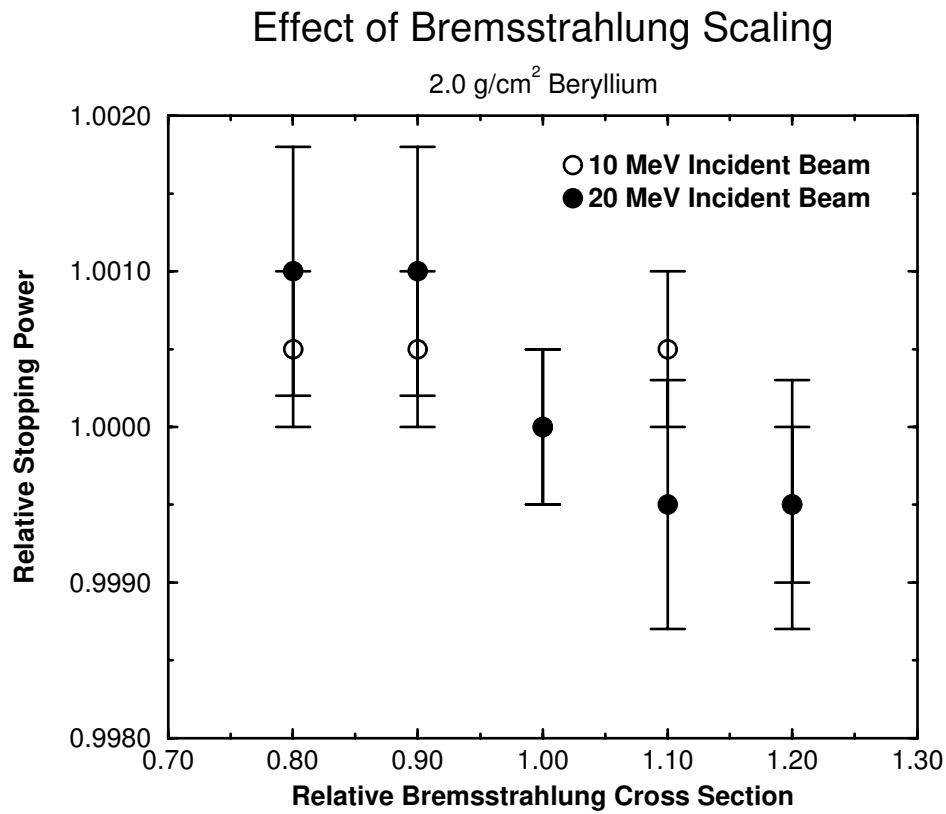


Figure 2.7: Effect of bremsstrahlung cross section on stopping power measurement for a  $2.0 \text{ g cm}^{-2}$  beryllium absorber. The extracted stopping power is insensitive to large uncertainties in the radiative cross section of the absorber.



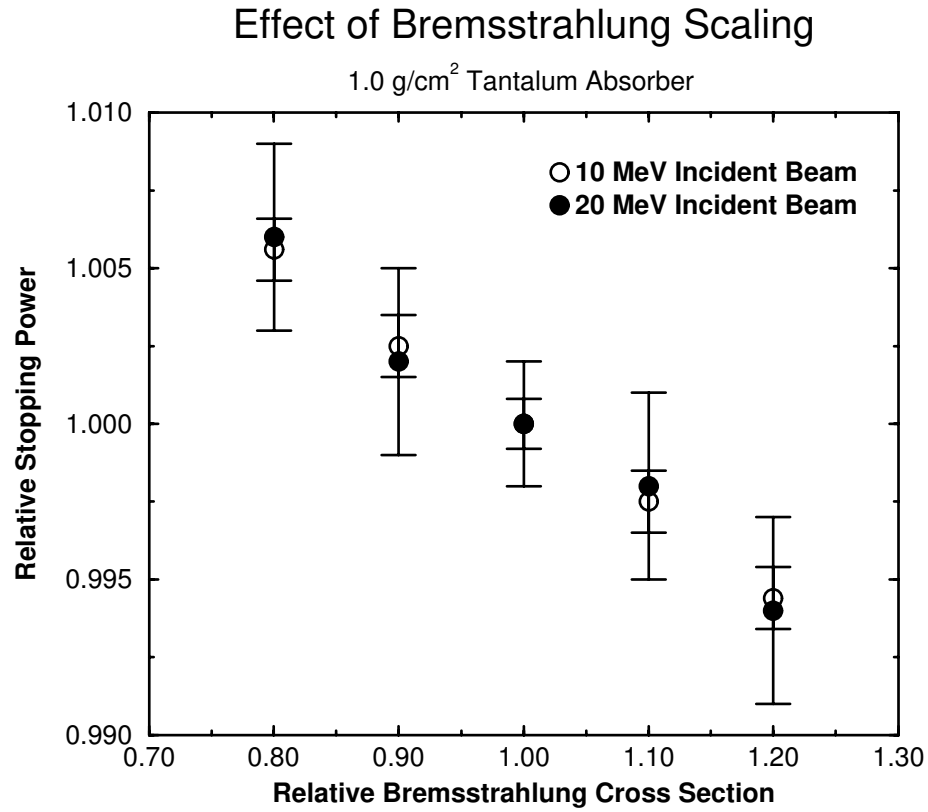


Figure 2.8: Effect of bremsstrahlung cross section on stopping power measurement for a 1.0 g cm<sup>-2</sup> tantalum absorber. The extracted collision stopping power shows a slight sensitivity to the radiative cross section due to electron energy straggling effects in the slab.

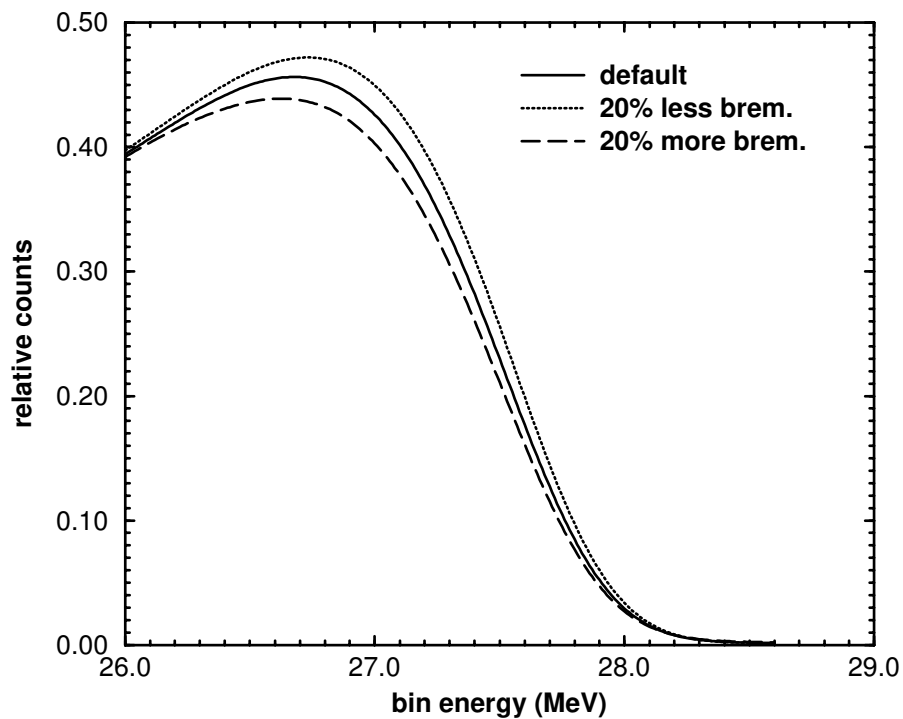


Figure 2.9: Effect of bremsstrahlung cross section on the calculated pulse height distributions for 30 MeV electrons incident on a  $2.0 \text{ g cm}^{-2}$  tantalum absorber. Reduced photon emission results in a more sharply peaked spectrum; increased emission tends to smear the spectrum.

power for tantalum is nearly twice the collision stopping power at 30 MeV. The reason for the insensitivity can be seen in figure 2.10, which depicts a simulated pulse height spectrum for the case where all photons with energy greater than 10 keV are simulated compared with the case where all photons are created and deposited on the spot. The average energy changes greatly, as electrons are moved out of the full energy peak when they lack their coincident photons. However, the leading edge of the spectrum is only mildly affected, because some electrons lose no or very little energy to radiative events. This places an absolute upper limit on the sensitivity to the radiative stopping power of the absorber. In reality, the effect is much less because at high energies most photons are emitted in the forward direction and the detector presents nearly  $2\pi$  geometry.

So far, only the effects of radiative losses in the absorbing slab have been considered. Clearly, if the bremsstrahlung cross sections in the NaI detector are in error, then the predicted pulse height distribution used to extract the stopping power would be suspect. To test the sensitivity of the response of the NaI detector to the discrete interaction cross sections, simulations were run for a 20 MeV electron beam incident on the NaI crystal. Three different cases were considered: using the default cross sections, a 20% increase in the bremsstrahlung cross section, and a 20% decrease in the bremsstrahlung cross section. Figure 2.11 shows the results of the three calculations. Decreasing the radiative cross section results in a more pronounced peak, since radiative losses from the detector are reduced. The magnitude of the change in peak height can be estimated by considering the probability of photon absorption in the detector. On average, a 20 MeV electron emits 11 photons as it comes to a rest in the NaI crystal. Each of these photons has, on average, a 5% chance of escaping the detector. If a photon escapes, the electron is lost from the peak, so the probability of an electron depositing all its energy is

$$P \approx (0.95)^{11} = 0.57.$$

If the bremsstrahlung cross section is increased by 20%, then the probability becomes

$$P \approx (0.95)^{13} = 0.51.$$

The predicted change in peak height is 12%, which is consistent with figure 2.11. Similarly, increasing the probability of a bremsstrahlung event results in decreased peak efficiency. Fit-

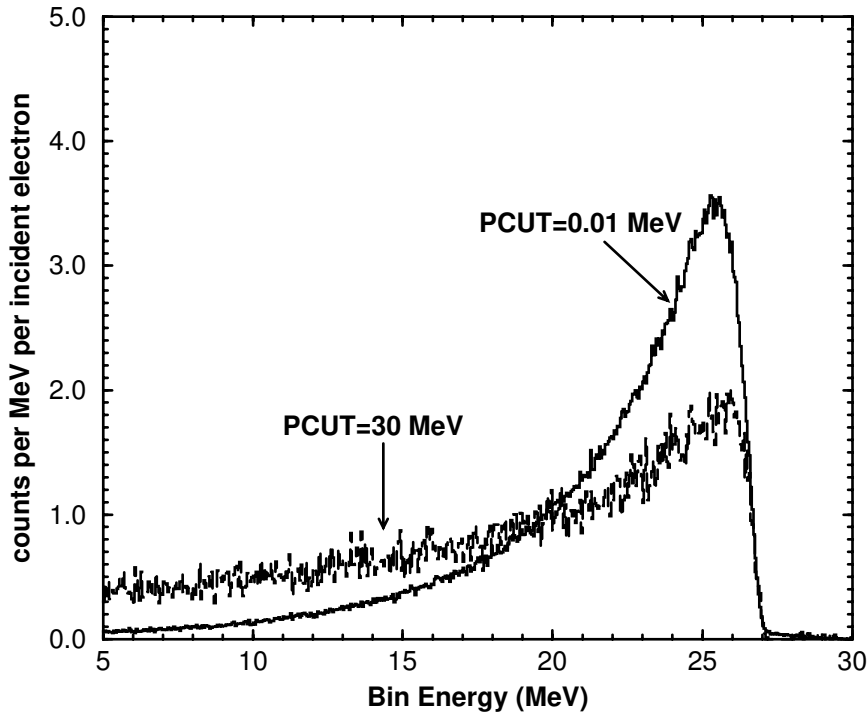


Figure 2.10: The role of photon production in the measurement of electron collision stopping powers is demonstrated by forcing any created photons to deposit their energy locally (high PCUT in EGS4). The result is a flattening of the electron spectrum as the radiative energy fails to reach the detector. Even so, the effect on the leading edge of the spectrum is minor.

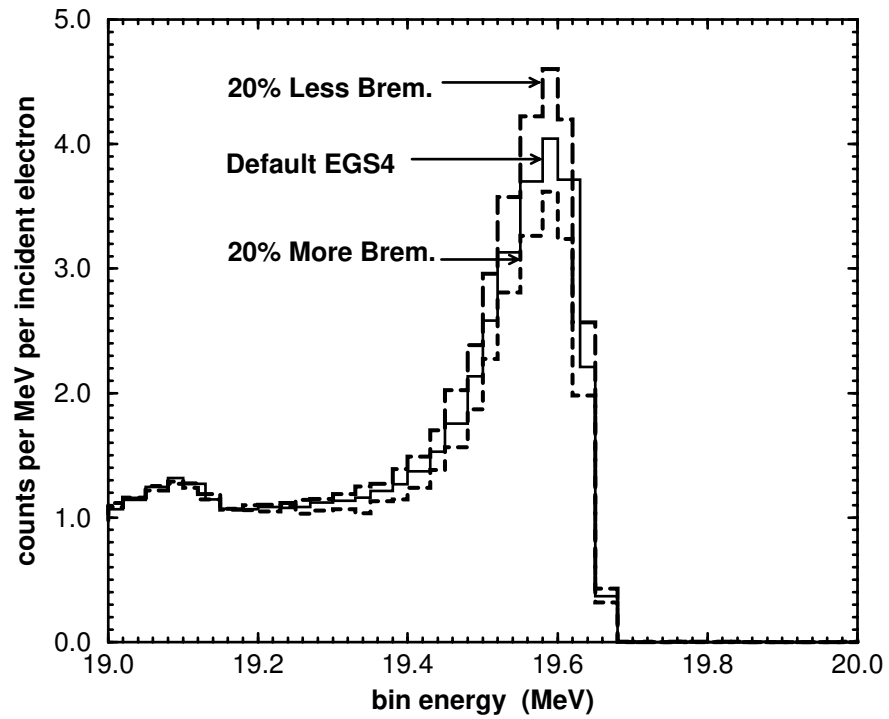


Figure 2.11: Calculated pulse height spectrum inside the NaI detector for different values of bremsstrahlung interaction cross section. The incident electron energy is 20 MeV; the energy loss and straggling are due to the window materials for the detector.

ting the three spectra to a simulated spectrum yielded the same value for the gain parameter (equation 2.1), within the uncertainty of 0.03%.

### 2.3.2 Role of the Møller Cross Section

The hard collision component of the electron stopping power is described by the integral of the Møller cross section which describes collisions between free electrons. Errors in the Møller cross section are carried directly into errors in the unrestricted stopping power. However, electrons which undergo large energy transfers play little role in the position of the leading edge of the transmitted spectrum.

In the context of this work, the Møller cross section plays a secondary role, in that it is used to describe electron transport through all materials, including the absorbing slab. Specifically, accurate simulation of discrete energy transfers is required to accurately predict the characteristic energy loss straggling distribution. If the cutoff for the creation of secondary electrons (the EGS4 parameter AE) is set too high, then low-energy discrete transfers are treated as continuous energy losses, and the straggling distribution becomes narrower. Figure 2.12 shows the effect of changing AE in the simulation of 20 MeV electrons through a nominally  $1 \text{ g cm}^{-2}$  tantalum absorber. There is no difference between the spectra calculated using AE=512 keV and AE=521 keV (AE is expressed as the sum of kinetic and rest mass energy). For AE=700 keV, the spectrum becomes strongly peaked, and can not be made to fit a measured spectrum without unrealistically varying the broadening function. The spectrum for AE=2 MeV is strongly peaked and shifted in energy due to the increase in restricted stopping power. For the simulations used in stopping power measurements, an AE value of 521 keV was chosen.

### 2.3.3 Dependence on Path Length

The path length traveled by an electron through an absorber is invariably greater than the thickness of the absorber due to the cumulative effect of elastic scattering off of atomic nuclei. This process must be modeled faithfully if the correct stopping power is to be extracted. However, it is impractical to simulate every elastic collision, so many collisions are grouped

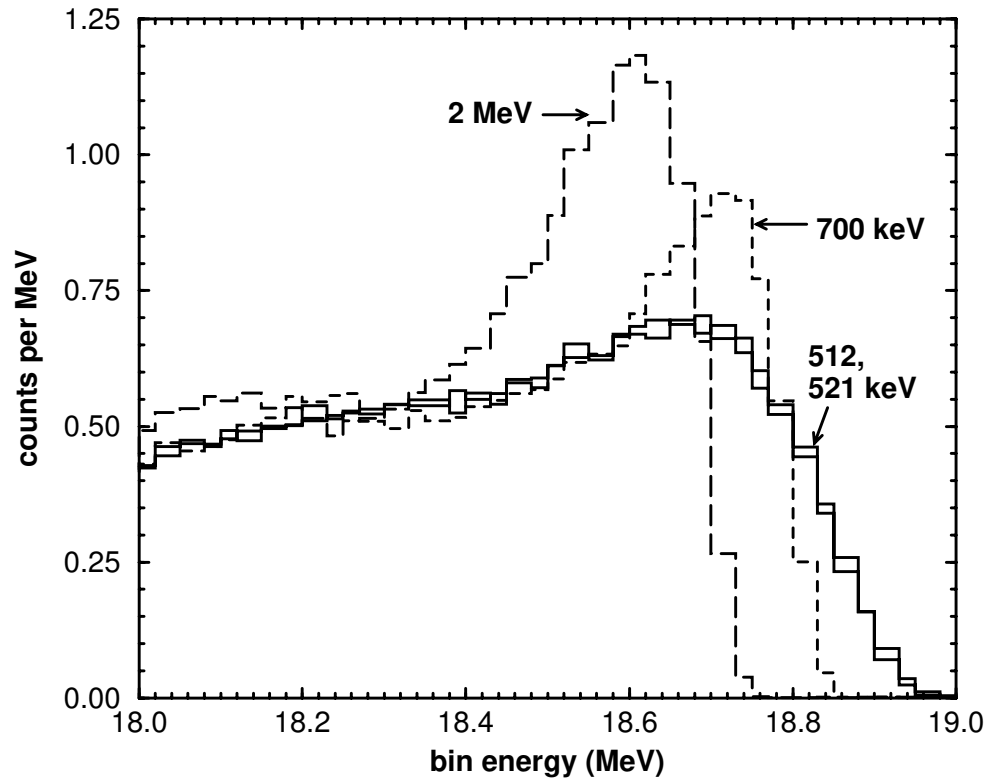


Figure 2.12: The role of the cutoff for the creation of secondary electrons (the EGS4 parameter AE) in the simulation of transmitted spectra (in this example 20 MeV electrons through a  $1 \text{ g cm}^{-2}$  tantalum absorber). If AE is 512 keV (kinetic plus rest mass energy) or less, the proper straggling distribution is predicted. When AE=700 keV, the spectrum is much narrower. As AE is increased further, the peak is shifted due to the increase in the restricted stopping power, and the straggling of the peak is reduced.

together in a multiple scattering step, at the end of which the scattering angle is sampled from a multiple scattering distribution, a technique proposed by Berger [49]. For small step sizes, the simulated path will closely resemble the actual path. For large step sizes, a path length correction may be required to account for the difference between the actual curved path and the straight multiple scattering step.

In terms of stopping power measurements, two issues arise. First, is there a dependence of path length on the size of a multiple scattering step? If so, there could be errors in the simulation if care is not taken in the selection of step size. Second, what absolute uncertainty may be attributed to the path length due to uncertainties in the multiple scattering distributions? Ultimately, such uncertainties limit the accuracy of the proposed stopping power measurement.

Electron transport in the EGS4 code system is accomplished with PRESTA (the Parameter Reduced Electron Step Transport Algorithm) [50] which optimally selects multiple scattering step sizes, using a path length correction to correct for the difference between straight steps and the actual curved paths of electrons. The sizes of the steps are governed by the applicability of the Molière multiple scattering theory, but can be restricted by placing an upper bound, ESTEPE, on the fractional energy lost in a multiple scattering step. The smaller ESTEPE, the more closely the simulation follows the true path of the electron, and the smaller the path length correction [51]. Table 2.2 displays the difference between the thickness of an absorber and the calculated curved path for all primary electrons incident on a 1 cm beryllium absorber and a 1 mm tantalum absorber, calculated for different values of ESTEPE. The incident energy is 10 MeV. The curved path length is independent of step size, even for the case of ESTEPE=0.10, where the size of a multiple scattering step is limited only by the distance to discrete interactions. As we have seen, averaging over all path lengths constitutes an overestimate of the path length for the stopping power measurement, although it does provide a rigorous test of the electron transport calculation. A more meaningful test for the stopping power work is to study the effect of the multiple scattering step size on the apparent stopping power (or  $\epsilon$ ). Figure 2.13 shows that the measured stopping power for a  $3 \text{ g cm}^{-2}$  copper slab is largely insensitive to the value of ESTEPE used in the simulation. More importantly, the default PRESTA simulation is entirely consistent with



	Curved path (cm)	
ESTEPE	Be t=1 cm	Ta t=1 mm
0.001	$1.037 \pm 0.002$	$0.163 \pm 0.002$
0.005	$1.038 \pm 0.002$	$0.159 \pm 0.002$
0.010	$1.036 \pm 0.002$	$0.158 \pm 0.002$
0.100	$1.038 \pm 0.002$	$0.157 \pm 0.002$

Table 2.2: Dependence of path length on multiple scattering step size for 10 MeV electrons on 1 cm beryllium and 1 mm tantalum absorbers. The average path length for all primary electrons is independent of multiple scattering step size.

those using very small step sizes, suggesting the PRESTA step-size selection algorithm is adequate for these calculations. It is worth noting that for very large step sizes there is a small but measurable change in the result, suggesting the path length is no longer being accurately modeled. Such large values of ESTEPE are outside the applicable energy loss regime for the PRESTA algorithm. Nonetheless, the magnitude of this effect is small, even for precise stopping power measurements, and such large step sizes would be avoided in any event.

The simulations required for stopping power measurements have been shown to be independent of step size. However, the absolute uncertainty on the curved path must also be known. In EGS4, the multiple scattering angles are sampled based on the theory of Molière, which is based on a small angle approximation [52]. Comparisons with measured scattering distributions of Hanson [53] and Roos [54] have showed good agreement in terms of the mass scattering power for thin slabs. Li and Rogers [55] have estimated that the mass scattering power (mean square scattering angle per path unit length) calculated by Monte Carlo simulation has a  $1\sigma$  uncertainty of  $\pm 2\%$  when the effects of secondary particle creation are considered. We therefore take the error in the square of the multiple scattering angle on any given scattering step to be less than 2%. This represents a 2% uncertainty in the difference between the path taken through the slab and the slab thickness (since the path length correction is proportional to  $1/\cos\theta$ ) [51]. For the materials and energies studied in this work, the curved path length is usually between 1 and 5% greater than the absorber thickness. This means that the path length uncertainty is usually below 0.1%, but can be as high as 0.3% for the thickest tantalum absorber at 7 MeV.

## 2.4 Preliminary Experimental Considerations

### 2.4.1 Simulated NaI Spectra

Measuring several electron spectra from the National Research Council (NRC) linear accelerator to empirically determine such things as appropriate counting statistics for stopping power measurements was impractical, due to the cost of operation and the time required to

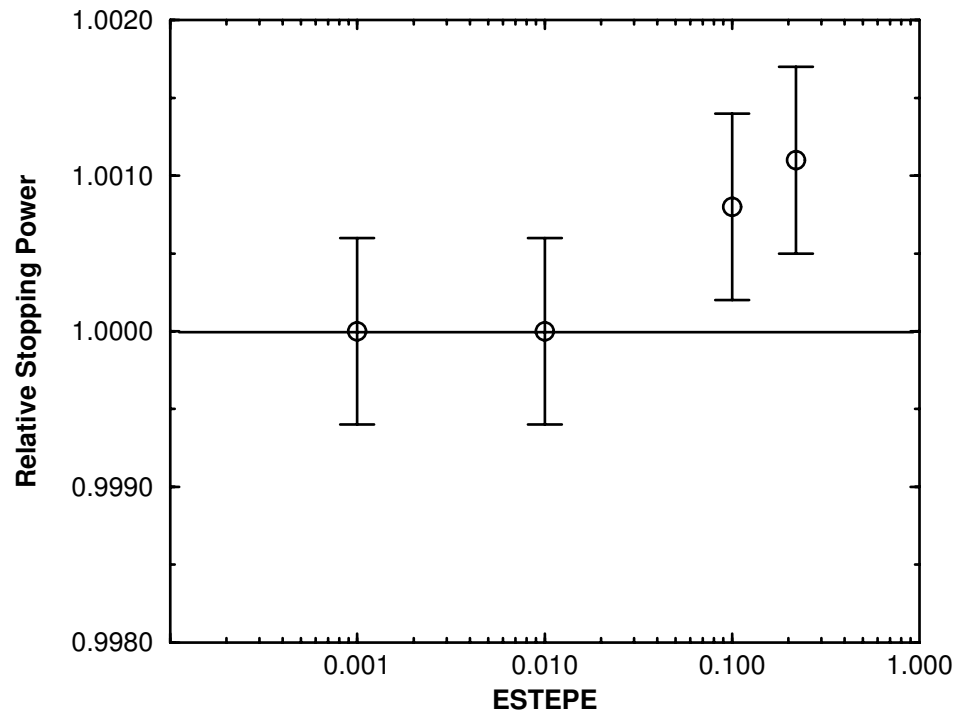


Figure 2.13: Relative change in stopping power for 20 MeV electrons incident on  $3 \text{ g cm}^{-2}$  copper, evaluated at different values of ESTEPE, normalized to the result using the default PRESTA electron transport algorithm. There is a modest but measurable change when the length of a multiple scattering step approaches the thickness of the slab (20% energy loss). However, the size of the effect is not significant for stopping power measurements.

acquire a large number of counts. The following approach was used to generate simulated spectra that mimicked the response of the NaI detector in terms of spectral shape (including intrinsic resolution), but which had zero uncertainties due to gain drift or energy calibration.

Monte Carlo simulations of the experimental geometry were performed to predict the pulse height distribution inside the detector. A large number of histories was simulated to reduce the statistical uncertainty in the calculated pulse height distributions to effectively zero. The Monte Carlo spectra were broadened with a Gaussian response function to account for the intrinsic resolution of the NaI detector. The broadened Monte Carlo spectrum was then used as a probability density function ( $\text{pdf}(i)$ , where  $i$  is the bin number) which was integrated and normalized to yield the cumulative probability function ( $\text{cpf}(i)$ ) for the simulated spectrum. Random sampling of the  $\text{cpf}(i)$   $N$  times gives  $N$  values of energy that are distributed according to  $\text{pdf}(i)$  (figure 2.14) [56]. This simulated spectrum has similar resolution and response characteristics to the actual detector, but has zero systematic uncertainty due to energy calibration or gain drift. Furthermore, the statistical uncertainty in the simulated spectrum can be readily varied by adjusting the number of counts in the spectrum. This provided an opportunity to test the uncertainty estimates provided by the fitting routine, and from there determine the counting statistics required for stopping power measurements.

### 2.4.2 Uncertainty Verification

The fitting routine is capable of providing uncertainty estimates on the fitted parameters based on the shape of the  $\chi^2$  distribution around its minimum [57]. To test whether these uncertainty estimates are reasonable, ten simulated spectra were generated for 30 MeV electrons on a  $2 \text{ g cm}^{-2}$  beryllium target. Each spectrum consisted of 50000 simulated counts, and each was given a different random number seed to mimic spectra acquired at different times. The simulated spectra were then fit to a calculated pulse height distribution. Figure 2.15 shows the variation of the resulting offset about its mean value. The error bar on each point represents the estimated uncertainty from the fit. The dashed lines show the standard deviation of the set, which is the same as the estimated uncertainty (0.5 bins).

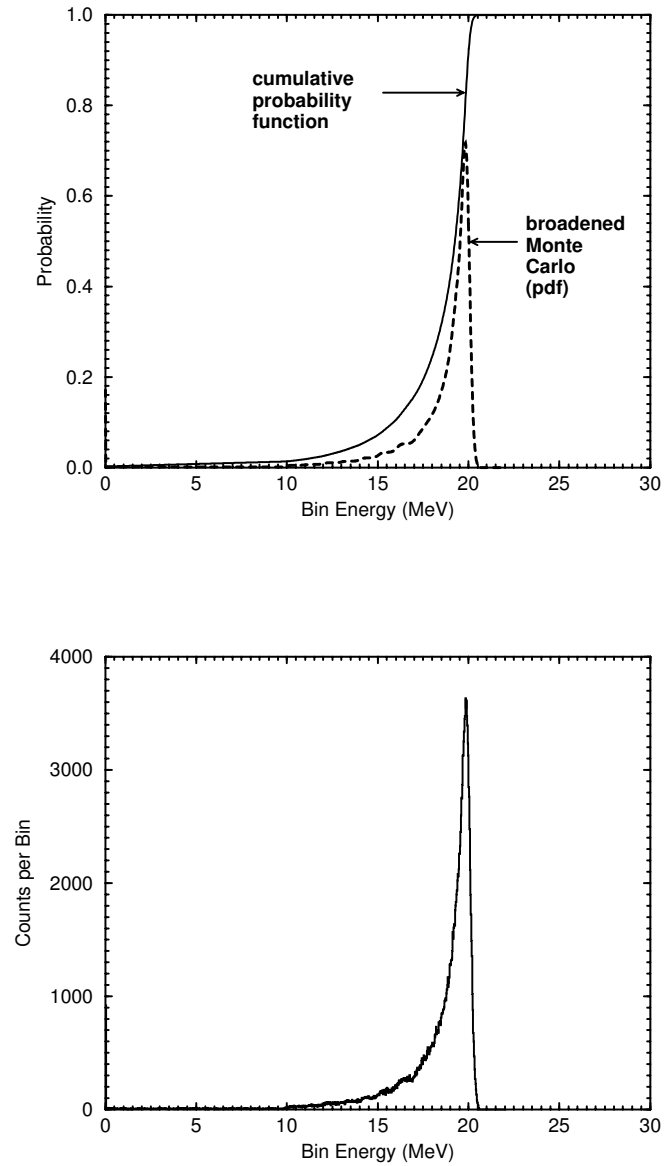


Figure 2.14: The broadened Monte Carlo spectrum is integrated to give a cumulative probability distribution (top), which is inverted and sampled to provide simulated measured spectra whose counting statistics can be readily varied (bottom).

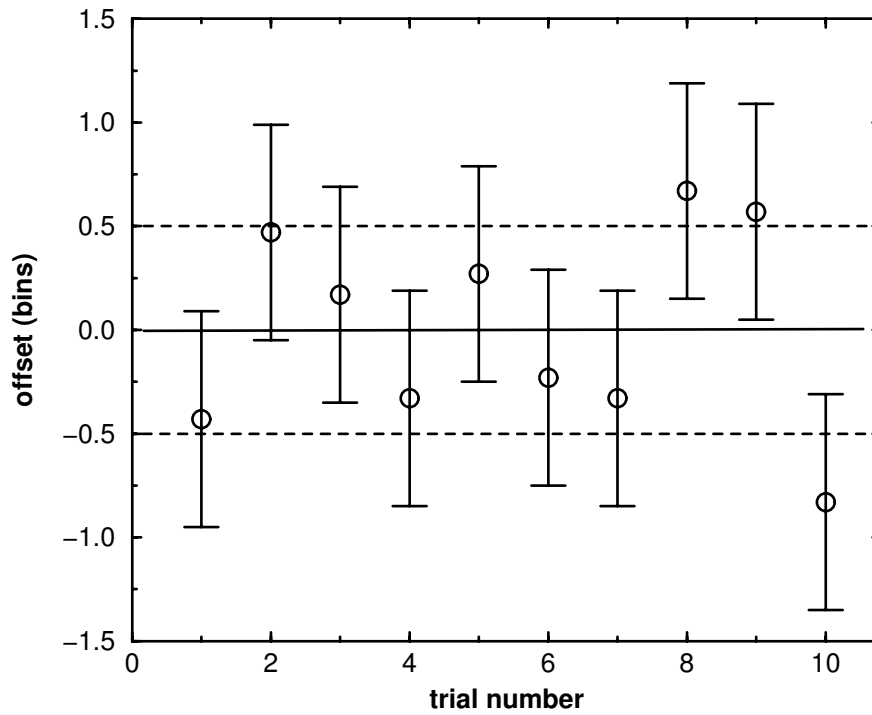


Figure 2.15: Measured offsets for ten simulated spectra for 30 MeV electrons on  $2 \text{ g cm}^{-2}$  Be. The measured values are distributed about the mean value with a standard deviation of 0.5 bins (indicated by dashed lines), which is exactly the estimated uncertainty on each point.

### 2.4.3 Counting Statistics

The aim of this work is to measure stopping powers with as low uncertainties as possible. The overall uncertainty will depend partially on the statistical uncertainties arising from the fit of the Monte Carlo spectra to the measured spectra. Since the statistical uncertainties in the Monte Carlo spectra can in principle be made very small by simulating a large number of histories, the limiting factor is the counting statistics on the measured spectra. The effect is largest for thinnest slabs, where a small uncertainty in bin offset reflects a relatively large uncertainty in energy lost.

Simulated spectra were generated for 20 MeV electrons incident on  $0.82 \text{ g cm}^{-2}$  of aluminum. The total number of counts in each spectrum ranged from 1000 to 1 million. Figure 2.16 shows the convergence of the measured stopping power normalized to that measured for the 1 million count spectrum. The statistical uncertainty drops to 0.2% for 50,000 counts, and to 0.1% for 200,000 counts. The former represents about 20 minutes beam time on the NRC accelerator, the latter requires nearly an hour and a half. The large increase in beam time for a modest decrease in uncertainty was deemed unnecessary, since other experimental uncertainties (e.g., energy calibration) were expected to dominate. The impact of counting statistics is lessened for thicker absorbers, as the uncertainty in the offset (a fraction of a bin) represents a smaller fraction of the energy lost (several hundred bins).

### 2.4.4 Range of Fit

The sensitivity to range of fit was investigated using a simulated spectrum for 20 MeV electrons on  $3 \text{ g cm}^{-2}$  copper. The upper limit of the fit window was fixed near the upper limit of the spectrum, and the apparent  $\epsilon$  determined for several widths of the fit window (figure 2.17). The results are summarized in table 2.3. The extracted offset is found to be insensitive to the range of fit, provided that the leading edge and part of the peak are included. The uncertainty decreases as more bins are included in the fit, but this is at the cost of increased computing time (from a few seconds to several minutes). Nearly optimal uncertainty is obtained for the 200 bin window, which just encompasses the rollover in the peak (example “c” in figure 2.17). In all subsequent fits, care was taken to include this

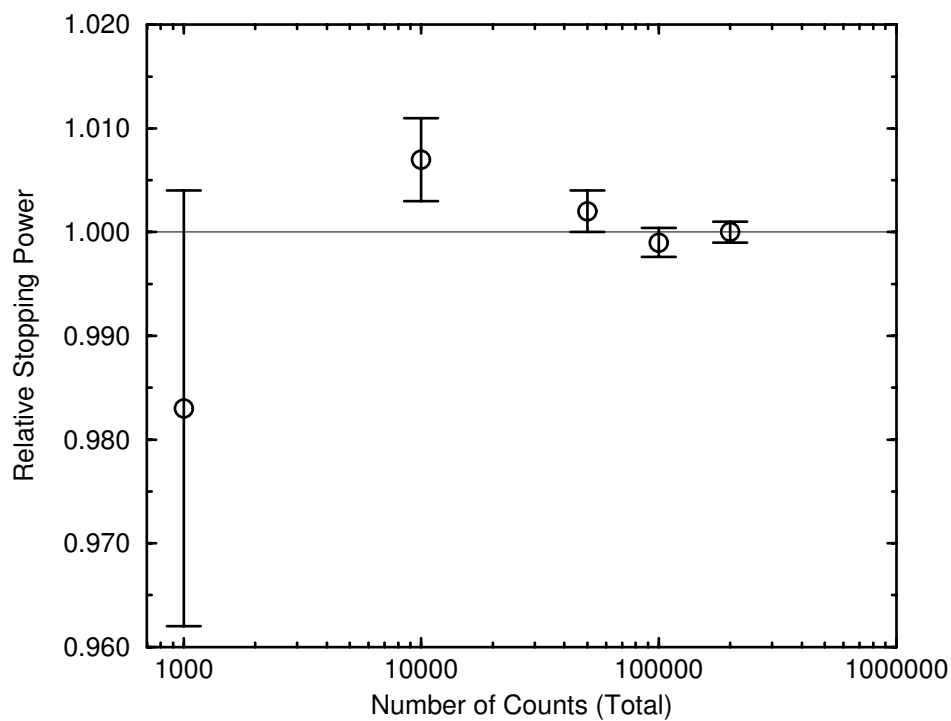


Figure 2.16: Relative change of extracted stopping power for 20 MeV electrons on  $0.82 \text{ g cm}^{-2}$  Al as the number of counts in the spectrum is increased. The error bars represent the  $1\sigma$  uncertainty as determined during the fit from the shape of the  $\chi^2$  distribution.



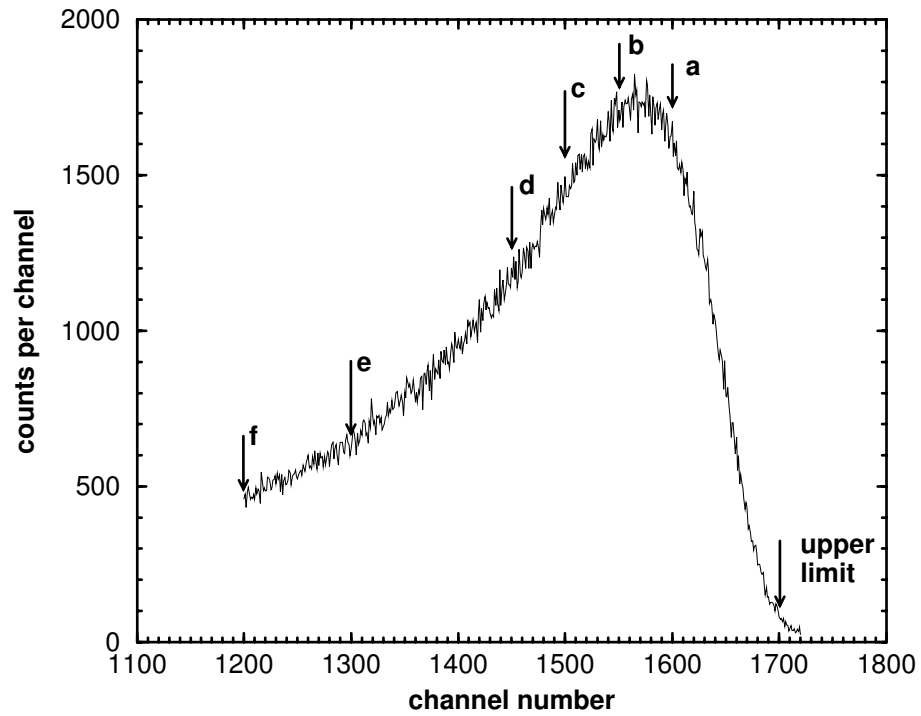


Figure 2.17: The simulated spectrum for 20 MeV electrons on  $3 \text{ g cm}^{-2}$  copper used to study the effects of the range of fit. The upper bin of the fit window was fixed at bin 1700, and offsets were determined for widths of <sup>a</sup>100, <sup>b</sup>150, <sup>c</sup>200, <sup>d</sup>250, <sup>e</sup>400, and <sup>f</sup>500 bins.

rollover, but in general the range of fit is not a critical parameter.

### 2.4.5 Binning Requirements

The measured spectra consisted of 10 keV bins. Faddegon *et al* estimated that the precision of the fitting procedure would be limited to  $\pm 1$  bin, providing a 10 keV uncertainty on the energy loss measurements. In fact, this is an overestimate. As the offset is varied, the  $\chi^2$  between the measured and calculated spectra varies smoothly for changes in offset much less than a single bin (figure 2.18). The shape of the variation closely approximates a quadratic, as would be expected [57]. The  $1\sigma$  uncertainty is defined by the interval  $\chi^2 < \chi^2_{min} + 1$ , and in this example is about 0.2 bins. If the bin size is increased, the result of the fit is not greatly changed, although the  $\chi^2$  per degree of freedom degenerates quickly. For the case of a 20 MeV no-absorber beam, changing from 10 keV bins (150 bins over peak) to 80 keV bins (19 bins over peak), changes  $\chi^2/\nu$  from 0.88 ( $P=0.15$ ) to 1.71 ( $P=0.97$ ) which is not considered acceptable<sup>1</sup>.

### 2.4.6 Sensitivity of the Method

In the absence of experimental gain drifts, the sensitivity of the technique is limited by counting statistics in the detector. This effect is most pronounced for thin absorbers, where statistical uncertainties in the offset represent a larger fraction of the energy loss. However, for thick absorbers, with 5 MeV energy loss, the statistical uncertainty of 0.5 bins (5 keV) suggests 0.1% effects should be observable. This level of uncertainty is never achieved, due to the other theoretical uncertainties described above coupled with experimental uncertainties in absorber thickness, energy calibration, gain drift and detector response.

---

<sup>1</sup>Here the value  $P$  is the probability that  $\chi^2$  for a correct model should be less than the observed value [58]. A large value of  $P$  indicates a poor model, while a very small value of  $P$  may reflect an overestimate of the underlying uncertainties.

Width (bins)	$\epsilon$ (keV)	$\sigma_\epsilon$ (keV)	$\chi^2/\nu$
100	38	8	1.30
150	36	3	1.08
200	35	2.3	1.03
250	33	1.9	1.03
400	34	1.7	1.04
500	34	1.7	1.04

Table 2.3: The importance of the range of fit was investigated by increasing the number of bins included in the fit window (figure 2.17). The extracted offset  $\epsilon$  is largely insensitive to the range of fit, although the uncertainty decreases as more bins are included.

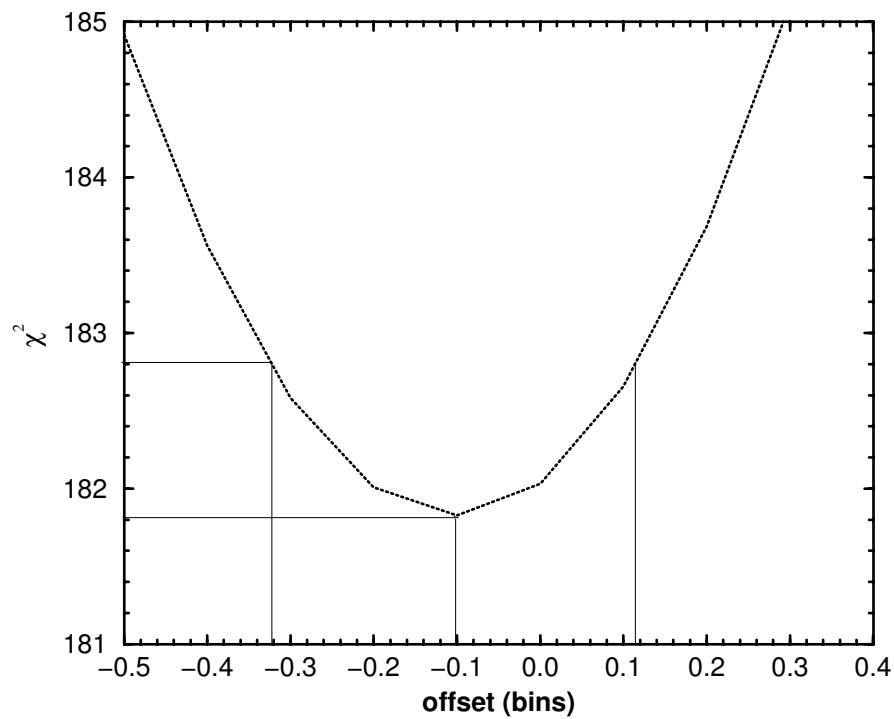


Figure 2.18:  $\chi^2$  exhibits a smooth variation about its minimum, suggesting binning artifacts are not a problem. The estimated uncertainty in the offset is described by the interval enclosed in  $\chi^2 < \chi^2_{min} + 1$ .

## 2.5 Conclusions

The technique of Faddegon *et al* for measuring collision stopping powers has been revised. Differences in energy loss,  $\epsilon$ , between measured and Monte Carlo calculated spectra are still determined by least squares fitting of the measured spectra to Gaussian-broadened Monte Carlo spectra with and without an absorbing slab in the beam. The quantity  $\kappa$ , defined as an additive correction to the low energy component of the collision stopping power, has been introduced.  $\kappa$  has been shown to be equal to  $\epsilon$  divided by the path length of electrons with scattering angles less than  $20^\circ$ , within one per cent, for all materials and energies from 7 to 30 MeV.

The technique is largely insensitive to radiative energy losses in the absorber, except for a small effect for high atomic number materials, where the added uncertainty is estimated to be 0.1%. Similarly, errors in the bremsstrahlung cross section for the NaI detector affect the peak efficiency of the calculated response function, but have no effect on the energy scale or  $\epsilon$ . Other uncertainties due to the Monte Carlo simulations arise principally from errors in the effective path length caused by inaccurate modeling of elastic multiple scattering. Taking conservative estimates of the uncertainty in the Monte Carlo path length estimations, the effective path length through the slab can be considered accurate to within 0.1% for most absorbers, with a larger uncertainty applying to high atomic number materials, such as tantalum, at low energies. There is no systematic relationship between  $\epsilon$  and the size of a multiple scattering step.

Preliminary considerations for stopping power measurements have been investigated using simulated spectra generated using broadened Monte Carlo pulse height distributions as probability density functions. Statistical uncertainties in energy loss on the order of 0.2% should be achievable for  $5 \times 10^4$  counts in each electron spectrum, representing about 20 minutes of beam time on the NRC linear accelerator. The measured offset is only mildly sensitive to the range of fit, provided that the leading edge of the spectrum is included along with the top of the electron peak. The technique has been shown to be capable of detecting energy offsets within a fraction of a 10 keV bin, which means that the sensitivity could be as high as 0.1% for large energy losses (5 MeV or greater). However, this level of sensitivity

will generally be masked by experimental uncertainties due to energy calibration, detector response and gain drift. The control of these effects will be described in the next chapters, which will also present measured stopping powers for a variety of materials.

# Chapter 3

## A Magnetic Spectrometer for Electron Energy Calibrations

### 3.1 Introduction

The measurement of electron stopping powers described in this thesis uses a large, nearly totally-absorbing sodium iodide (NaI) spectrometer to measure the change in electron energy spectrum when an absorbing slab is placed in the beam. If the desired uncertainty of less than 1% in the measured stopping powers is to be achieved, then the energy calibration of the NaI spectrometer must be established to better than 1%. Unfortunately, there are no convenient radioisotopes available for calibration at the energy range of interest here (5 - 30 MeV). Consequently, the electron beam from the linear accelerator must be used to provide the energy calibration.

Earlier work has established the energy calibration of the NRC linear accelerator using electron range measurements, a photonuclear resonance in the  $^{16}\text{O}$   $\gamma$ -n reaction, and measurements of magnetic flux in the beam bending magnet. The uncertainty in the calibration resulting from these measurements was not well established, but was estimated to be about 1% [59]. This level of uncertainty was deemed insufficient for this work, so a new method of energy calibration was needed.

Several calibration options were considered. Electron range measurements were not considered appropriate because of their inherent dependence on electron stopping pow-

ers [60], [61]. The energy resolution associated with photonuclear resonance measurements has been shown to be about  $\pm 1\%$  [59], which is not adequate for this work. Other techniques were considered which depended on interaction kinetics to establish incident energy. These included mass scattering power measurements [62], Cerenkov threshold measurements [63], and calibrations based on measurement of the Compton distribution resulting from the interactions of bremsstrahlung photons generated by the electrons [64], [65]. However, the accuracy of these methods was not expected to be greater than the range method. Magnetic spectrometry, on the other hand, has been shown to be capable of accuracies of much better than 1% [66], [67]. For this reason, it was decided that a magnetic spectrometer should be constructed and used to provide an energy calibration for the NRC linac. This chapter describes the design and operation of that spectrometer.

## 3.2 Theory

It is well known that a particle of charge  $q$  traveling with a velocity  $\vec{v}$  in a magnetic field  $\vec{B}$  will experience a Lorentz force  $\vec{F}$  given by:

$$\vec{F} = q\vec{v} \times \vec{B}. \quad (3.1)$$

If the motion of the particle is perpendicular to the direction of the magnetic field, then for a constant field the motion is circular with centripetal force:

$$\frac{mv^2}{r} = qvB, \quad (3.2)$$

where  $m$  is the mass of the particle and  $r$  is the radius of curvature. Since  $E = mc^2$  equation 3.2 can be written as

$$Br = \frac{Ev}{c^2q} = \frac{E\beta}{cq},$$

where

$$\beta = \frac{v}{c} = \sqrt{\frac{E^2 - (m_0c^2)^2}{E^2}},$$

and  $m_0c^2$  is the rest mass of an electron. Therefore we have,

$$Br = \frac{1}{cq} \sqrt{E^2 - (m_0c^2)^2}. \quad (3.3)$$



For an electron of kinetic energy  $T$  in MeV, with  $r$  expressed in cm and  $B$  in kG,

$$r = \frac{1}{0.2999B}(T^2 + 2Tm_0c^2)^{\frac{1}{2}}. \quad (3.4)$$

Equation 3.4 can be arranged to provide the kinetic energy:

$$T = \sqrt{0.08994B^2r^2 + (m_0c^2)^2} - m_0c^2. \quad (3.5)$$

So the bending radius of an electron moving in a magnetic field of strength  $B$  is dependent only on its kinetic energy. For a constant magnetic field, the angle of deflection,  $\Phi$ , would be given by

$$\Phi = \frac{s}{r},$$

where  $s$  is the path length through the magnet.

In a real magnet system, the field is not constant, but falls off gradually as one moves away from the pole faces. One can approximate particle transport through the magnet as if the field were constant out to a certain point, where it falls immediately to zero (figure 3.1). Such a point is referred to as the effective field boundary (efb) or Sharp Cut Off Fringing Field (SCOFF). Since the integral of magnetic field over the path taken is the same in each case, a particle passing through the real magnet system will undergo the same angular deflection as a particle traveling through the imaginary constant field extended to the SCOFF.

A magnet acts to focus an electron beam, in much the same way as a lens focuses light, and a full theory of magnetic optics has been developed [68], [69]. The SCOFF approach forms the basis for the first-order theory of magnet optics, and provides a very good estimate of charged particle paths through a magnet system. It remains, however, an approximation, and if very low uncertainties are desired, as was the case with this study, then higher-order effects must be taken into account. For this work, the focusing properties of the magnet were of little consequence, as a detailed energy analysis could be performed based solely on the dispersive properties of the magnet in the horizontal plane (equation 3.4). Consequently, optical properties of the magnet, such as magnification and focal length, are not discussed.

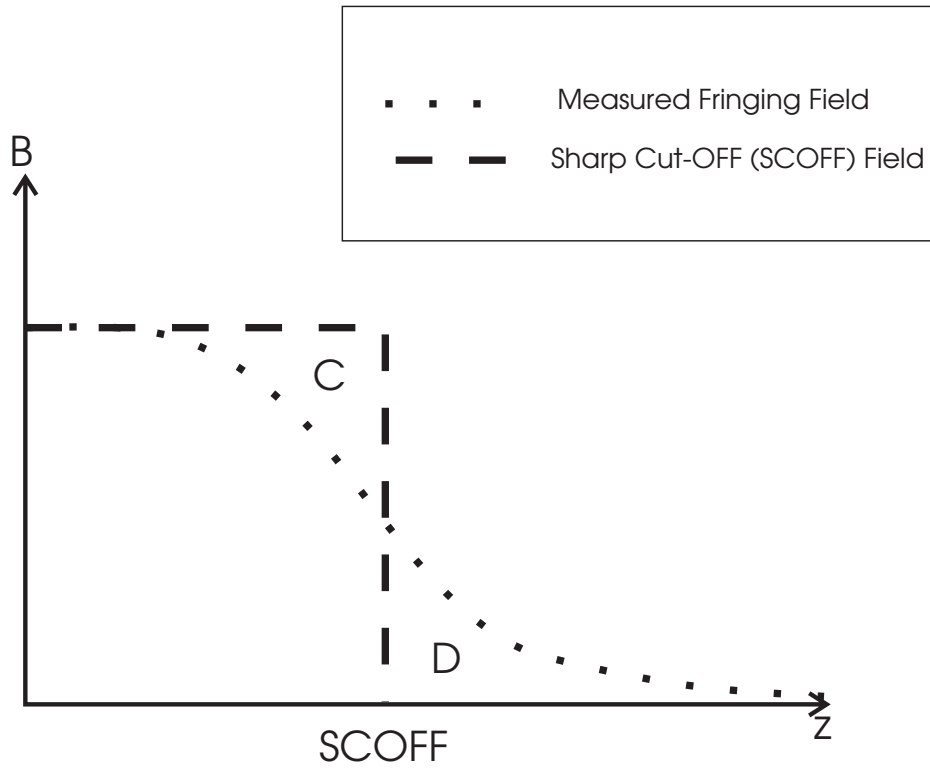


Figure 3.1: In the sharp cutoff approximation the areas C and D are equal, so the integral of the uniform field is the same as the integral of the real fringing field.

## 3.3 Materials and Methods

### 3.3.1 The Magnet

The magnet used for this work was a large beam-switching magnet (Anac Model 3456) which was formerly used to control the paths of ion beams emerging from the NRC Van der Graaff accelerator. The magnet comprises two low-carbon steel poles housed in a steel frame. The pole edges are tapered to reduce saturation. Surrounding the poles are two water-cooled coils wound using 5 cm (2 inch) copper tape, separated by mylar insulation between windings. The magnet is supplied with a stainless steel vacuum chamber, which provides an entrance portal and exit portals for deflections of  $0^\circ$ ,  $15^\circ$ ,  $30^\circ$ , and  $45^\circ$  (figure 3.2). In order to achieve maximum resolution, it was decided that the beam should be deflected through one of the  $45^\circ$  ports. This would provide the maximum path length in the magnet, and thus the greatest spatial separation of energies. Table 3.1 lists some important specifications of the magnet.

### 3.3.2 Field Mapping

One of the first objectives was to map out the relative field of the magnet over the region traversed by the electron beam. For this work, a rotating coil magnetometer was chosen over a Hall probe magnetometer, largely because of the latter's extreme sensitivity to field orientation. The magnetometer (Rawson-Lush model 924, No. 17116), consists of a 0.48 cm (3/16 inch) diameter coil rotating at the end of a long probe and sheathed in a protective aluminum cover. The coil rotates at 30 Hz producing a sinusoidal emf which is compared, via a bridge-balance, with the emf produced by a reference generator at the other end of the shaft. The relative phase between the coil and reference generator is minimized by rotating the stationary parts of the generator. The device measures only the component of the field which is perpendicular to the axis of rotation. This was advantageous in that axial components of the fringing fields, which cause no deflection, would not be measured.

The Rawson probe was mounted on an adjustable positioning stand, so that its longitudinal position could be varied by over 25 cm, with a precision of  $\pm 0.01$  cm. Lateral position

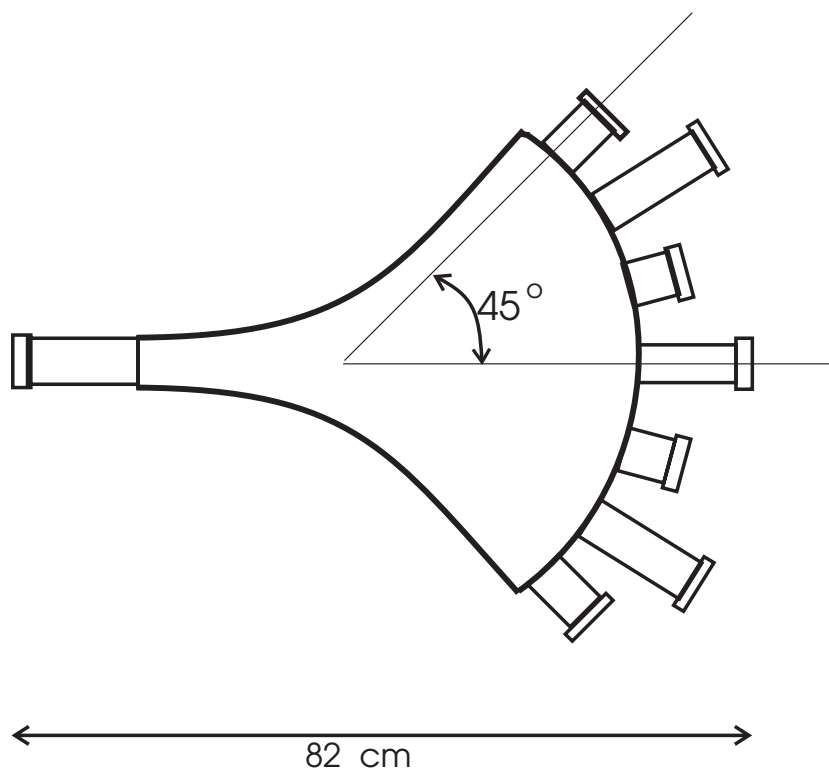


Figure 3.2: Schematic of the vacuum box for the Anac magnet (top view), showing beam portals for various deflections.

Field	0 - 1.65 Tesla (16.5 kgauss) <sup>a</sup>
Pole Gap	3.025 cm <sup>b</sup>
Angular Deflection	44.943° <sup>b</sup>
Exit Shim Angle	26.28° <sup>a</sup>
Entrance Shim Angle	0° <sup>a</sup>
Bending Radius (45°)	45.36 cm <sup>b</sup>

Table 3.1: Specifications of spectrometer magnet. <sup>a</sup> denotes manufacturer's specifications; <sup>b</sup> indicates the quantity is based on in-house measurements.

could be varied by  $\pm 2$  cm, again with a precision of  $\pm 0.01$  cm.

Prior to mapping the field, it was necessary to know the effective point of measurement of the probe (i.e. the position of greatest sensitivity). The protective cover had etchings which were supposed to indicate the centre of the coil, but it was not known how well the etchings correlated with the actual coil position. Furthermore, the large size of the coil called into question its spatial resolution.

Conical pole faces were machined for a permanent magnet, as shown in figure 3.3. The magnetic flux between these pole faces was expected to be very high between the vertices of the cones, and then fall off rapidly. The probe was moved between the pole faces, and the magnetic field as a function of position was recorded. A 3 mm offset was noticed between the etchings on the probe and the apparent centre of the magnet. The procedure was repeated with a Rawson probe with a much smaller coil ( $\frac{1}{8}$  inch diameter), and no offset was observed, indicating that the coil of the large probe was in fact offset from the etchings by 3 mm. Closer examination of the rotating shaft indicated that this was indeed the case, and the problem was corrected. Figure 3.4 shows the results of these measurements after correcting the offset in the large coil. The close agreement between the small coil probe and the large coil probe indicated that the larger coil width did not significantly broaden the shape of the flux density curve, so spatial resolution was not considered a significant problem.

The magnet was provided with an aluminum alignment plate, which could be attached to the bottom pole face (field mapping was performed without the vacuum box in place). Grooves were machined in the plate which corresponded to the rays of the final paths the particles would travel if deflected by the field. In order to facilitate alignment, an aluminum tube was fitted with cross hairs at each end. The tube sat in the alignment grooves, providing a means of visually aligning the probe with the magnet. With the alignment tool in place, the Rawson probe was sighted along the paths the electrons were expected to take, i.e. with the normal entrance position, and along the  $45^\circ$  exit position. In order to determine the position of the probe, a pin was placed at the vertex of the alignment plate (the intersection of the  $0^\circ$  and  $45^\circ$  grooves), and an aluminum rod of known length was placed in the alignment groove so as to be just touching the end of the probe and the vertex pin. In this way, measurement position was determined to better than  $\pm 0.5$  mm.

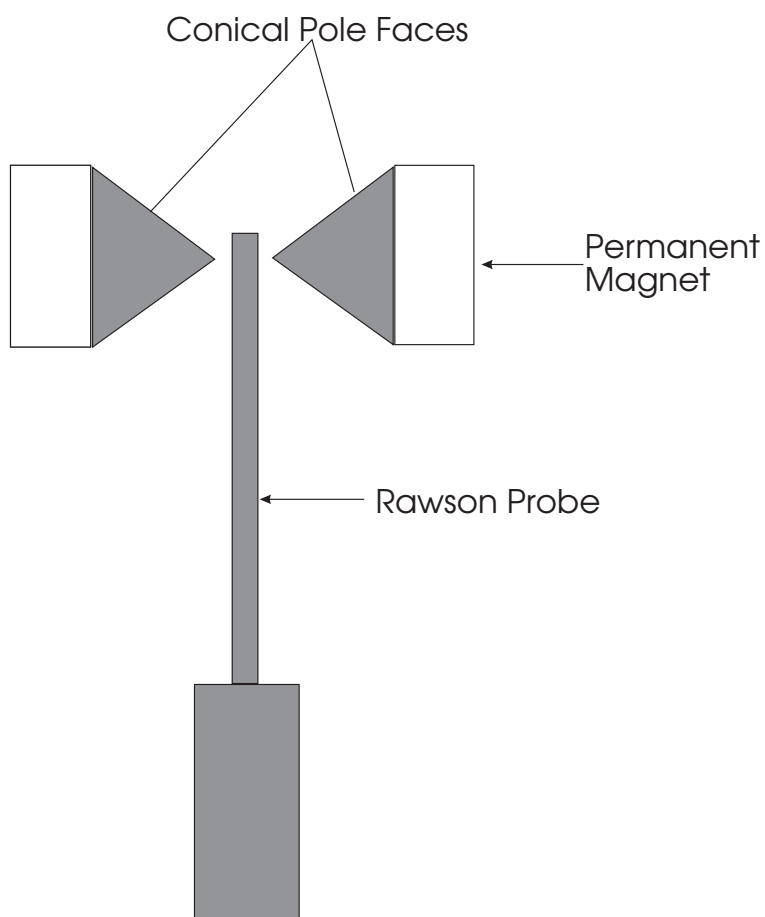


Figure 3.3: Schematic of permanent magnet arrangement used to determine the effective point of measurement for the Rawson probes (top view).

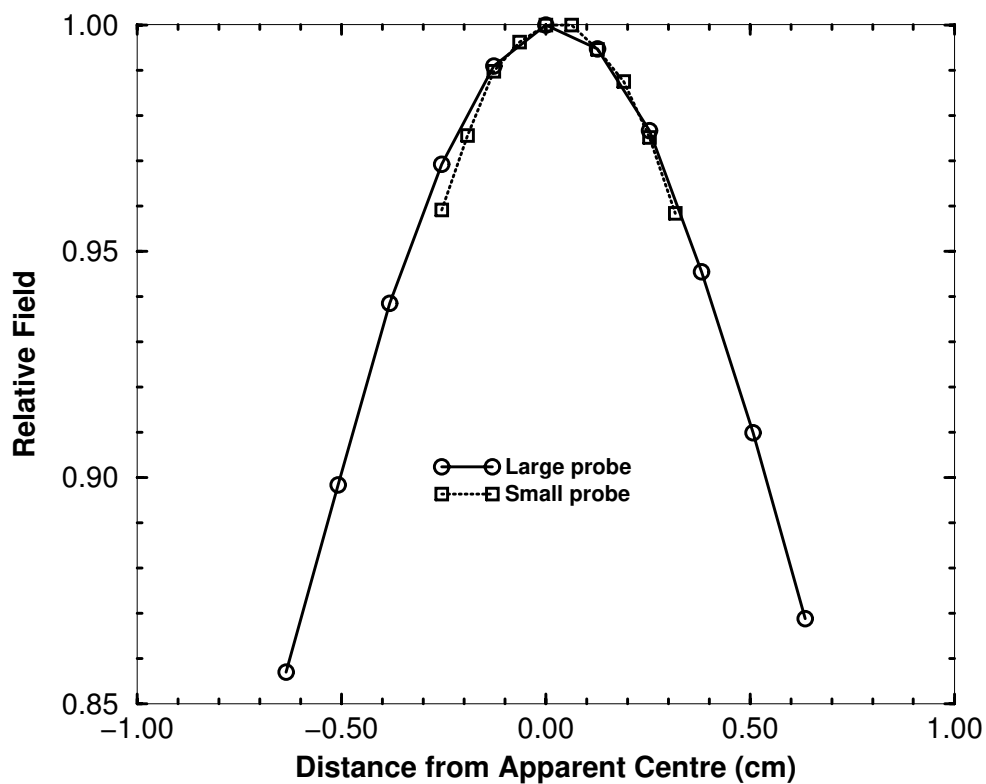


Figure 3.4: The effective point of measurement for each Rawson magnetometer was determined by passing it between a permanent magnet with conical pole faces. No significant broadening was introduced by the larger probe.



Field measurements were performed in the fringing field regions as well as inside the pole faces, where the field was expected to be constant. Readings were taken at intervals of 2.5 mm. In addition to measurements along the central axes, measurements were taken at horizontal and vertical offsets of  $\pm 1$  cm to ensure that the relative fields did not change unexpectedly in any region the electron beam could conceivably cross. Field mapping was performed at two different field settings ( $\approx 0.2$  and  $0.4$  T) to ensure that the shape of the relative field was independent of field strength for the magnetic fields considered here. The relative fields were equal within 0.1 mm (figure 3.5), yielding identical sharp cut-offs. Since the fields of interest in this study are significantly lower (0.07 to 0.3 T), one can assume that saturation effects are not important in the fringing field region.

The measured fringing fields are shown in figure 3.6. No difference greater than 0.1% was found between fields measured along the central axis, and those measured at displacements of  $\pm 1$  cm on the horizontal and vertical axes. Integrating the entrance fringing fields yielded a SCOFF of  $19.11 \pm 0.05$  cm from the vertex of the alignment plate, in rather poor agreement with the manufacturer's value of 18.88 cm. Similarly, the exit SCOFF was measured to be  $18.44 \pm 0.05$  cm from the vertex, rather than 18.63 cm as suggested by the manufacturer. Detailed mechanical measurements revealed that the position of the vertex of the alignment plate did not correspond to the position quoted by the manufacturer in the manual. The size of the offset (approximately 1 mm in the backward direction) is consistent with the discrepancies noted in the fringing field measurements. However, if the sharp cut-off is quoted with respect to the edge of the pole faces, the measured results of  $4.8 \pm 0.5$  mm on the entrance side and  $5.5 \pm 0.5$  mm on the exit side agree reasonably well with the manufacturer's values of 5.9 mm and 5.6 mm, respectively. Moreover, if the measured field is integrated to determine the actual bending radius, the measured result of 45.36 cm is in good agreement with the design value of 45.29 cm, leading to a difference in transmitted energy of only 0.15%.

Inside the pole faces, where the field was expected to be constant, the field was noticed to increase steadily as the probe was moved from the entrance to the exit side of the pole faces (figure 3.7). This is probably due to the sector shape of the magnet, which results in more magnetic material at the exit side. While the magnitude of the change was small, it

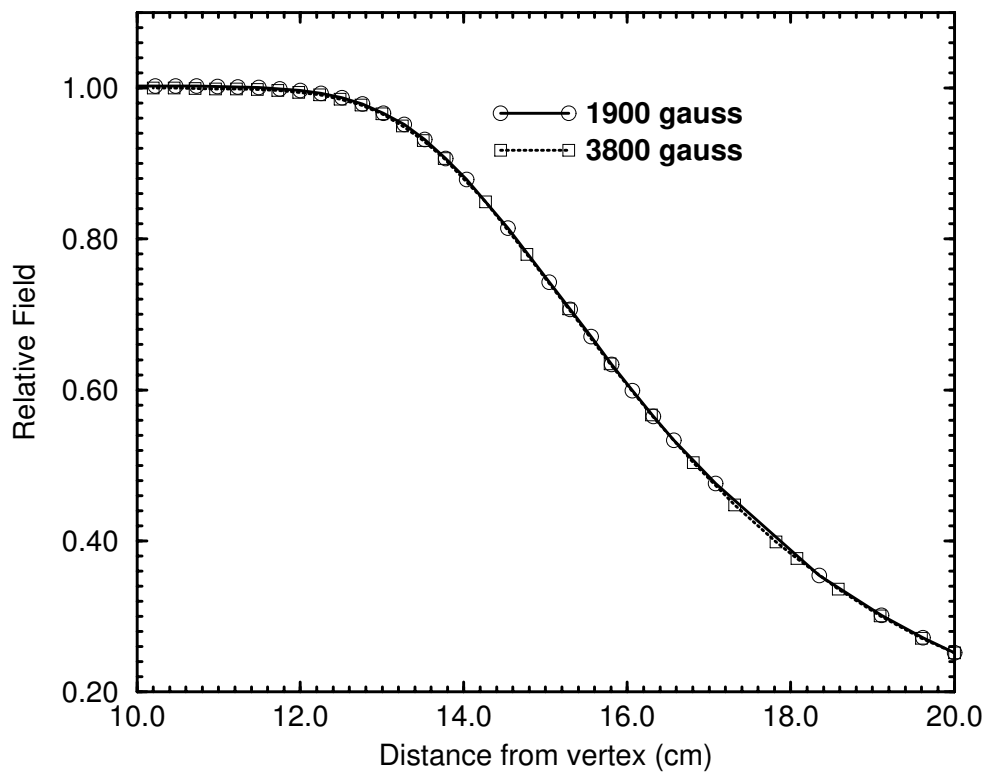


Figure 3.5: Measured exit fringing fields at two different field values. The relative fields are in excellent agreement, demonstrating that saturation effects are not important at the field levels considered in this study.

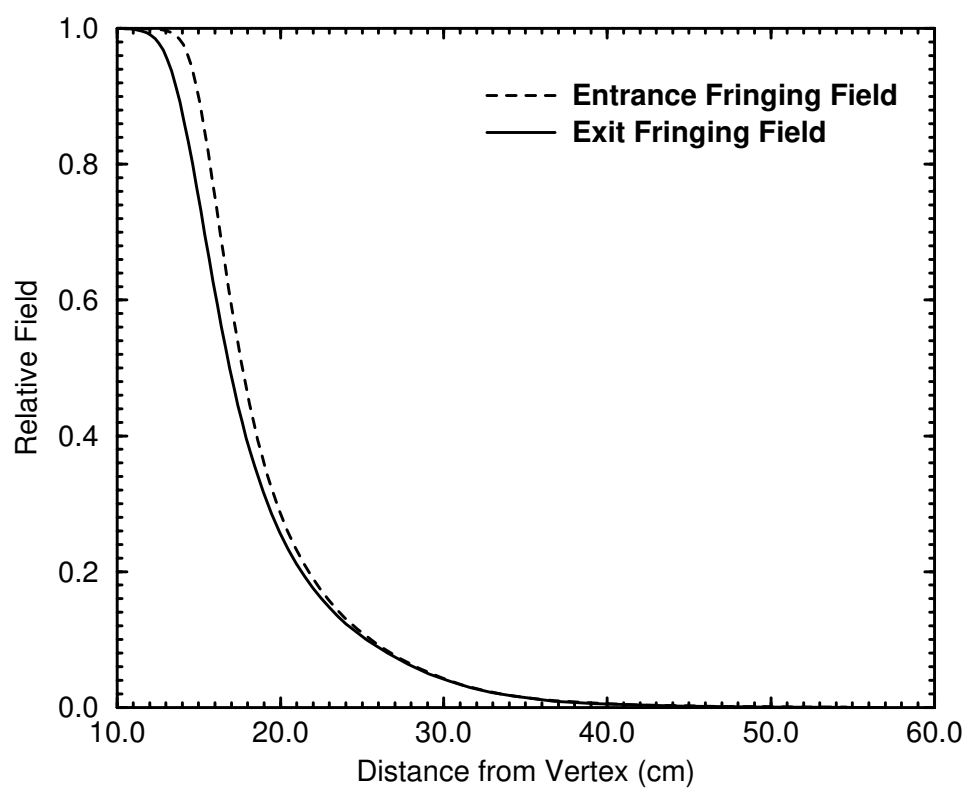


Figure 3.6: Comparison of entrance and exit fringing fields.

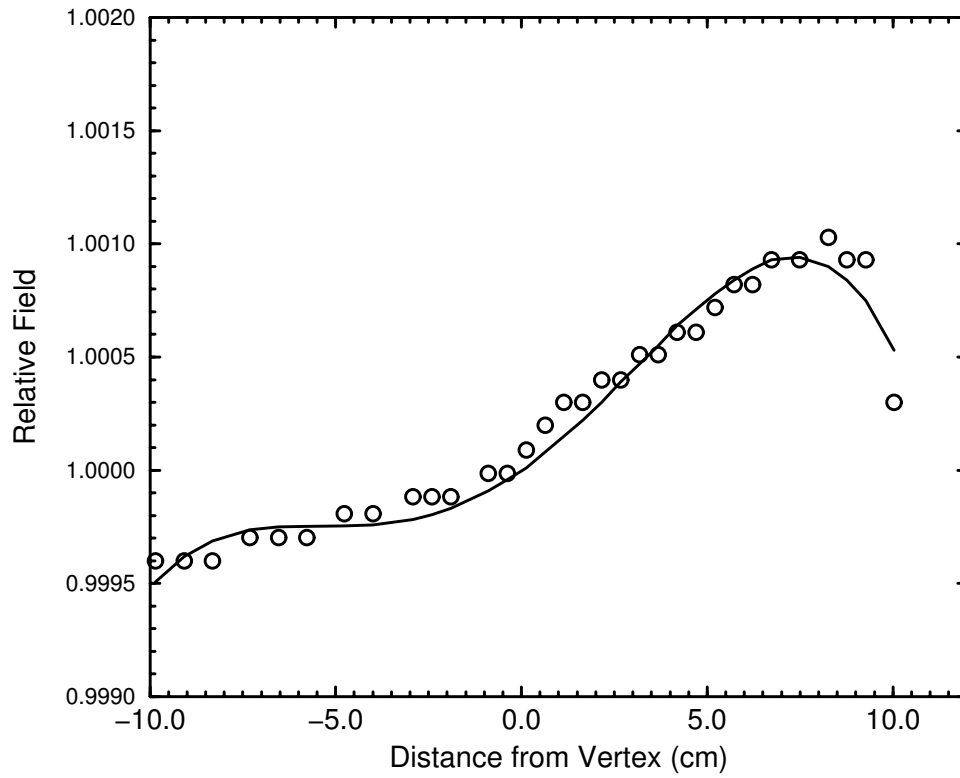


Figure 3.7: Field inside pole faces increases toward exit side. The measured field has been fit with a polynomial for use in analysis.

was considered significant enough to be included in later analysis.

The stainless steel vacuum box was not expected to perturb greatly the magnetic field inside the pole faces. To test this, several mock-ups of the vacuum assembly were made using stainless steel tubes and boxes of the approximate thickness of the vacuum box. Magnetic field measurements with and without the stainless steel were consistent within  $\pm 0.05\%$ . The perturbation caused by the vacuum box also can be estimated based on the relative permeability of stainless steel.

The magnet poles, vacuum box, and air gap comprise a magnetic circuit (figure 3.8). The magnetic flux of the circuit is equal to the magnetomotive force  $NI$  divided by the reluctance  $\mathcal{R}$ . With the vacuum box in place, the flux is [70]:

$$\Phi_1 = \frac{NI}{\frac{L_p}{\mu_p A} + \frac{L_{\text{box}}}{\mu_{\text{box}} A} + \frac{L_{\text{air}}}{\mu_{\text{air}} A}}, \quad (3.6)$$

where the subscript p refers to the poles,  $A$  is the area through which the flux density will be measured (i.e. the pole faces).  $L_p$  can be measured around the supporting frame.

If the box is removed, then the flux becomes:

$$\Phi_2 = \frac{NI}{\frac{L_p}{\mu_p A} + \frac{L_{\text{air}}}{\mu_{\text{air}} A}}. \quad (3.7)$$

So the ratio of fluxes is:

$$\frac{\Phi_1}{\Phi_2} = \frac{\frac{L_p}{\mu_p} + \frac{L_{\text{box}}}{\mu_{\text{box}}} + \frac{L_{\text{air}}}{\mu_{\text{air}}}}{\frac{L_p}{\mu_p} + \frac{L_{\text{air}}}{\mu_{\text{air}}}}. \quad (3.8)$$

Considering that  $\mu_{\text{box}} \approx 1.00005$  and that  $\mu_p \approx 10^5$ , we find that  $\frac{\Phi_1}{\Phi_2} = 1.00003$ . Therefore it is safe to assume that the presence of the vacuum box does not perturb the measured field.

### 3.3.3 Ray Tracing

If the magnetic field produced by the magnet were constant inside the pole faces and zero everywhere else, then the problem of extracting the electron energy would be trivial (equation 3.5). This is essentially the SCOFF approach. However, since the field falls off gradually in the fringing field regions, the bending radius changes continuously there, and the true path of an electron of kinetic energy  $T$  is no longer circular. This problem can be overcome by

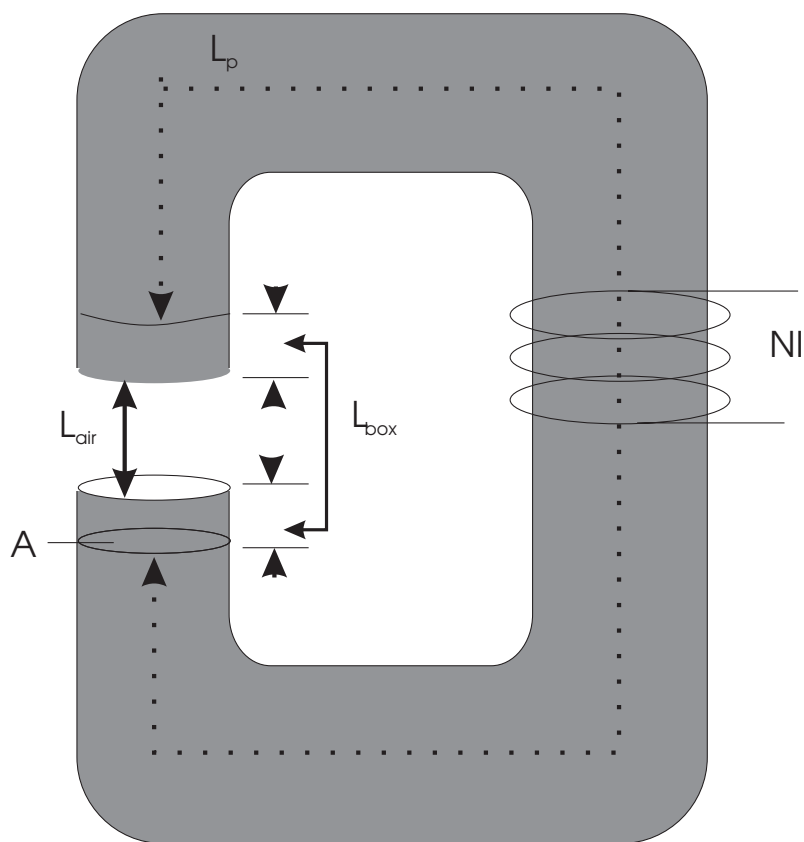


Figure 3.8: Schematic of spectrometer as a magnetic circuit.

realizing that over a small element of path length the field is constant, and the path can be considered circular within that element. Summing over several such elements constitutes, in effect, integration of the equations of motion. Such a technique is known as *ray tracing*. Two approaches to the ray tracing problem were taken for this work. Initially, a FORTRAN program, called ESPLINE, was written to simulate the passage of electrons through the magnet based on measured fringing field data. For more detailed analysis, the program RAYTRACE was used [71].

### Program ESPLINE

The algorithm for ESPLINE is as follows. Fringing field data are read in as coordinate pairs of distance from the magnet vertex (i.e. intersection of entrance and exit rays) and magnetic field relative to the magnetic field at the magnet vertex.

The electron is initialized in terms of its energy  $T$ , position  $(x, y)$ , and direction cosine with respect to the central axis (figure 3.9). The user is then prompted to enter a step size,  $\delta$ , and magnetic field in kG. The electron then moves a distance  $\delta$  in its original direction. That is:

$$x' = x + \delta \cos \Phi,$$

$$y' = y + \delta \sin \Phi.$$

If the particle is in the fringing field regions, the magnetic field at the centre of the step is determined by cubic spline interpolation of the measured fringing field data, otherwise, the maximum field is assumed. The bending radius is then determined by equation 3.4. Since the bending radius  $r$  is orthogonal to the motion everywhere, the new angle will be

$$\Phi = \Phi + \Delta\Phi,$$

where

$$\Delta\Phi = \tan^{-1} \left( \frac{\delta}{r} \right).$$

The position  $(x, y)$  and angle  $\Phi$  are written out at each step. The process continues until the electron leaves the fringing field region and the program terminates. ESPLINE was useful in determining the basic behaviour of electrons passing through the magnet. For

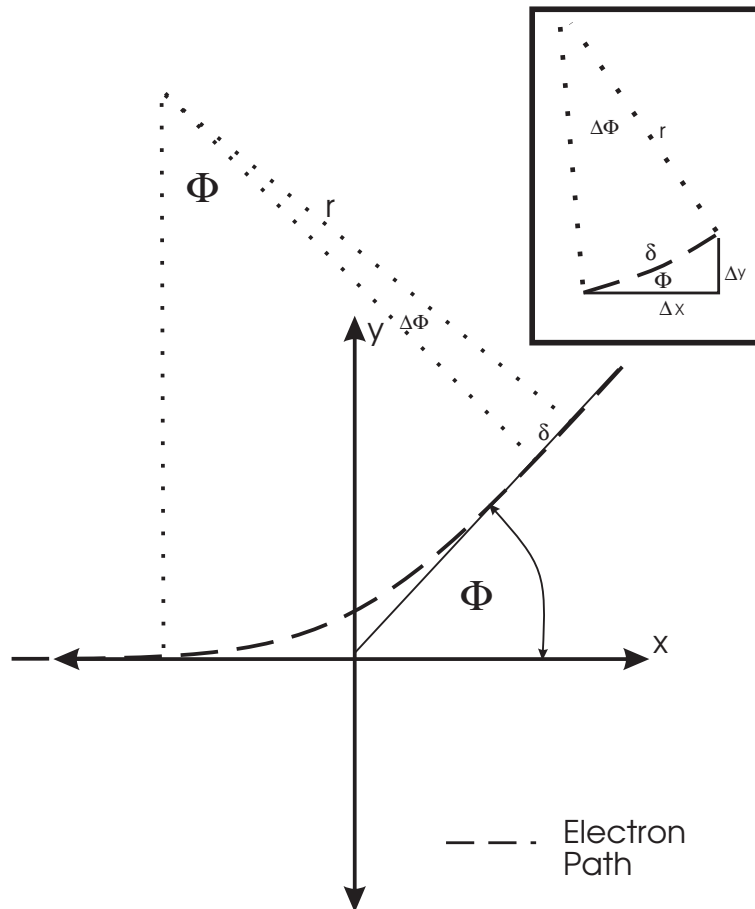


Figure 3.9: Geometry for ESPLINE ray tracing program. If  $\delta$  is small enough the path is nearly straight.



instance, it was able to determine the approximate slit size necessary to achieve adequate resolution (2 mm for 0.2%). However, the algorithm was too simplistic to provide the level of accuracy desired for this work. For example, the shape of the pole faces was not taken into account; the magnet was essentially treated as being circular with 0° shim angles everywhere. Moreover, no provision was made for the simulation of radial magnetic field components. A more physically rigorous approach to the ray tracing problem was needed.

### Program RAYTRACE

RAYTRACE [71] was developed at the Massachusetts Institute of Technology (MIT) for the design of beam transport systems. It is a general use code which allows the simulation of ion transport through various ion-optical components, including dipole magnets. Complex pole shapes and magnetic fields can be entered parameterically. RAYTRACE simulates ion transport by performing a fourth order Runge-Kutta integration of the equations of motion resulting from equation 3.1.

Median plane transverse magnetic field data are entered as input, and components of the magnetic field off the median plane are calculated for all three directions and included in the simulation. In order to calculate components of magnetic field off the median plane, RAYTRACE takes advantage of the symmetry of the dipole magnet (figure 3.10). The magnetic field components can each be expressed as a Taylor series expansion in the transverse direction,  $y$  (figure 3.10). By symmetry, we know that the transverse ( $y$ ) component will have only even terms, while the longitudinal ( $x$  and  $z$ ) components will have only odd terms. To fourth order, then, the expressions are given by [71]:

$$B_x(y) = y \frac{\partial B_x}{\partial y} + \left( \frac{y^3}{3!} \right) \frac{\partial^3 B_x}{\partial y^3}, \quad (3.9)$$

$$B_y(y) = B_y + \left( \frac{y^2}{2!} \right) \frac{\partial^2 B_y}{\partial y^2} + \left( \frac{y^4}{4!} \right) \frac{\partial^4 B_y}{\partial y^4}, \quad (3.10)$$

and

$$B_z(y) = y \frac{\partial B_z}{\partial y} + \left( \frac{y^3}{3!} \right) \frac{\partial^3 B_z}{\partial y^3}, \quad (3.11)$$

where the terms are evaluated on the median plane ( $y=0$ ). From Maxwell's equations, we know that

$$\nabla \cdot \vec{B} = 0, \quad (3.12)$$

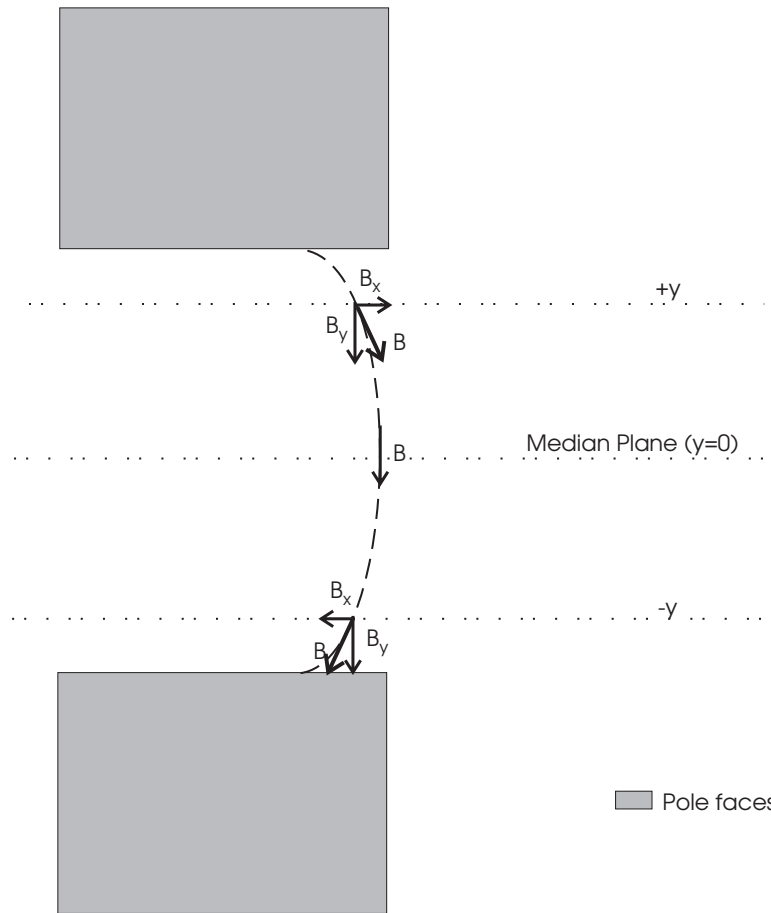


Figure 3.10: Sample magnetic field line between pole faces. By symmetry, the  $y$  component of the magnetic field is an even function of  $y$  about the median plane. The  $x$  and  $z$  components are odd functions.

and also that

$$\nabla \times \vec{B} = 0 \quad (3.13)$$

for a steady state field with no residual magnetization or electric field. We can rewrite equation 3.12 as

$$\frac{\partial B_y}{\partial y} = - \left( \frac{\partial B_x}{\partial y} + \frac{\partial B_z}{\partial y} \right). \quad (3.14)$$

From equation 3.13 we know that

$$\frac{\partial B_x}{\partial y} = \frac{\partial B_y}{\partial x},$$

and

$$\frac{\partial B_z}{\partial y} = \frac{\partial B_y}{\partial z}.$$

This means that partial derivatives of  $B_x$  and  $B_z$  can be calculated only from changes of the transverse field,  $B_y$  in the median ( $x$ - $z$ ) plane. This is fortunate, since the only input data are parameterizations of  $B_y$  as a function of  $z$  in the entrance and exit coordinate systems. Parallel paths in the entrance and exit coordinate system are assumed to have the same parameterization of field (this is consistent with the measurements reported in section 3.3.2). Changes in  $B_y$  in the median plane are calculated using a 13 point grid (figure 3.11) which is aligned along the direction of the electron's motion. Grid point separations of 1 cm inside the poles and 0.3 cm in the fringing field region are used. Derivatives in  $x$  and  $z$  are determined numerically from this grid, and used to evaluate equations 3.9, 3.10 and 3.11. When the electron is moving parallel to the entrance or exit  $z$  axis, many of the the partial derivatives are zero. This is also true when the electron is in the uniform field region. However, when an electron is in the fringing field region these derivatives are non zero. The deflections calculated using these off-axis fields are very small (typically less than 2 mm for reasonable entrance offsets).

The geometry of RAYTRACE is quite complex, and merits some discussion here. For a more detailed discussion of the geometry, the reader is referred to the RAYTRACE manual [71]. The magnetic element is considered to consist of three distinct regions: an entrance fringing field region (AB), a uniform field region (BC), and an exit fringing field region (CD)(figure 3.12). Each region has its own coordinate system, in addition to the entrance and exit coordinate systems. All calculations are made with respect to a region's coordinate

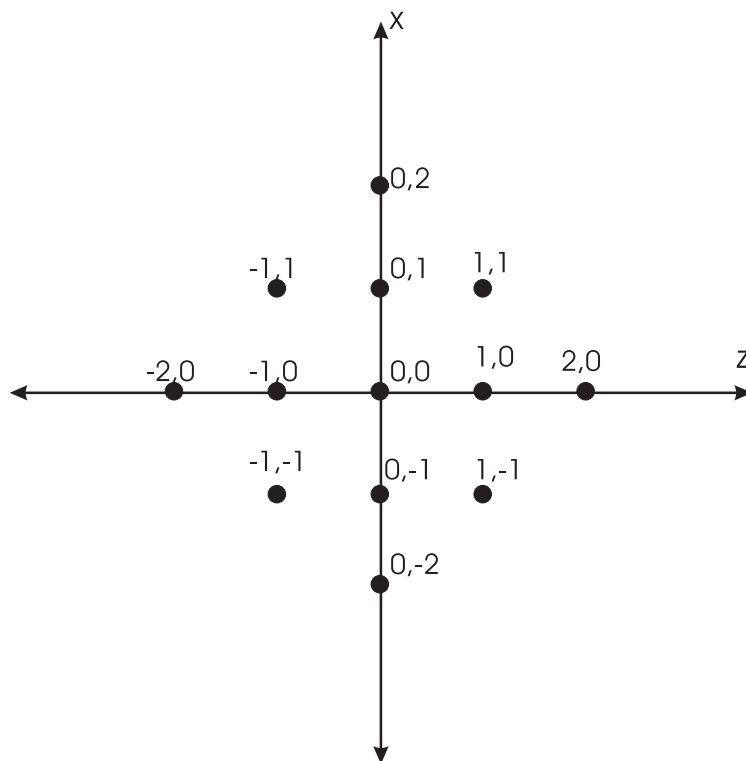


Figure 3.11: The thirteen point grid used to determine off-axis field components. The coordinates refer to array indices; the true spacing is determined by the user. The grid is aligned with the electron's direction of motion ( $z$ -axis).

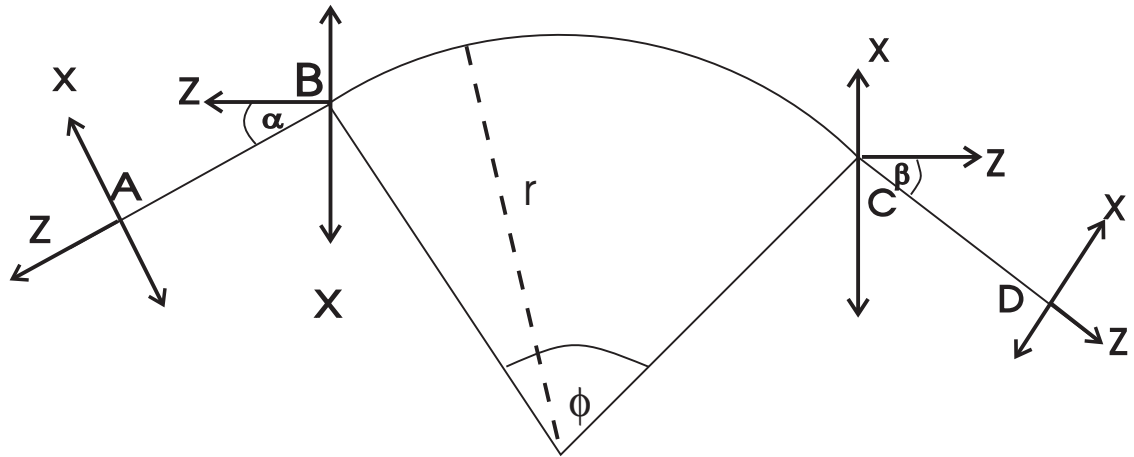


Figure 3.12: Geometry for RAYTRACE. The effect of the field is evaluated in the entrance fringing field (AB), the uniform field (BC), and the exit fringing field (CD).

system. Transformations to new systems are performed at predefined crossover points. The sharp cut-offs of the magnet are used to establish the BC coordinate system. The design radius,  $r$ , is taken as the bending radius for a particle moving through the SCOFF field of strength  $B_o$ . The shim angles  $\alpha$  and  $\beta$  represent the angle made between the ion beam and the SCOFF field, which follows the shape of the pole faces. The curvature of the pole faces can either be parameterized by a polynomial, or by the radius of curvature for a sector magnet such as the one used in this study.

Measured fringing fields are entered as six coefficients, C00 . . . C05 for the entrance fields and C10 . . . C15 for the exit fields. The coefficients are obtained by least-squares fitting the measured field data to

$$B_y = \frac{B_o - B_R}{1 + e^S} + B_R, \quad (3.15)$$

where  $B_o$  is the uniform field,  $B_R$  is a constant background field, and

$$S = C00 + C01s + C02s^2 + C03s^3 + C04s^4 + C05s^5.$$

Here

$$s = \frac{z}{D},$$

where  $z$  is the distance from the SCOFF and  $D$  is the pole gap. The user must also specify the extent of the fringing field in each direction (both into and out of the magnet) beyond the sharp cutoff points B and C. The extremes of the fringing fields define the crossover points, where RAYTRACE performs coordinate system transformations. The field nonuniformity depicted in figure 3.7 was parameterized by a 3<sup>rd</sup> order polynomial from which field values inside the pole faces were calculated. In this case,  $B_o$  refers to the field at the vertex.

RAYTRACE reports the final position in terms of the coordinate system D, which is defined by the ray resulting from deflection of a particle with energy  $T$  given by equation 3.5 through the SCOFF field. This makes interpretation of the results slightly more complicated because, as has already been stated, the SCOFF rays do not correspond to the alignment plate.

Figure 3.13 depicts the effect of using the SCOFF field to determine the final path of the electron. The SCOFF rays are shown as bold lines. The dashed lines represent the rays projected by the alignment plate. This essentially results in two frames of reference:

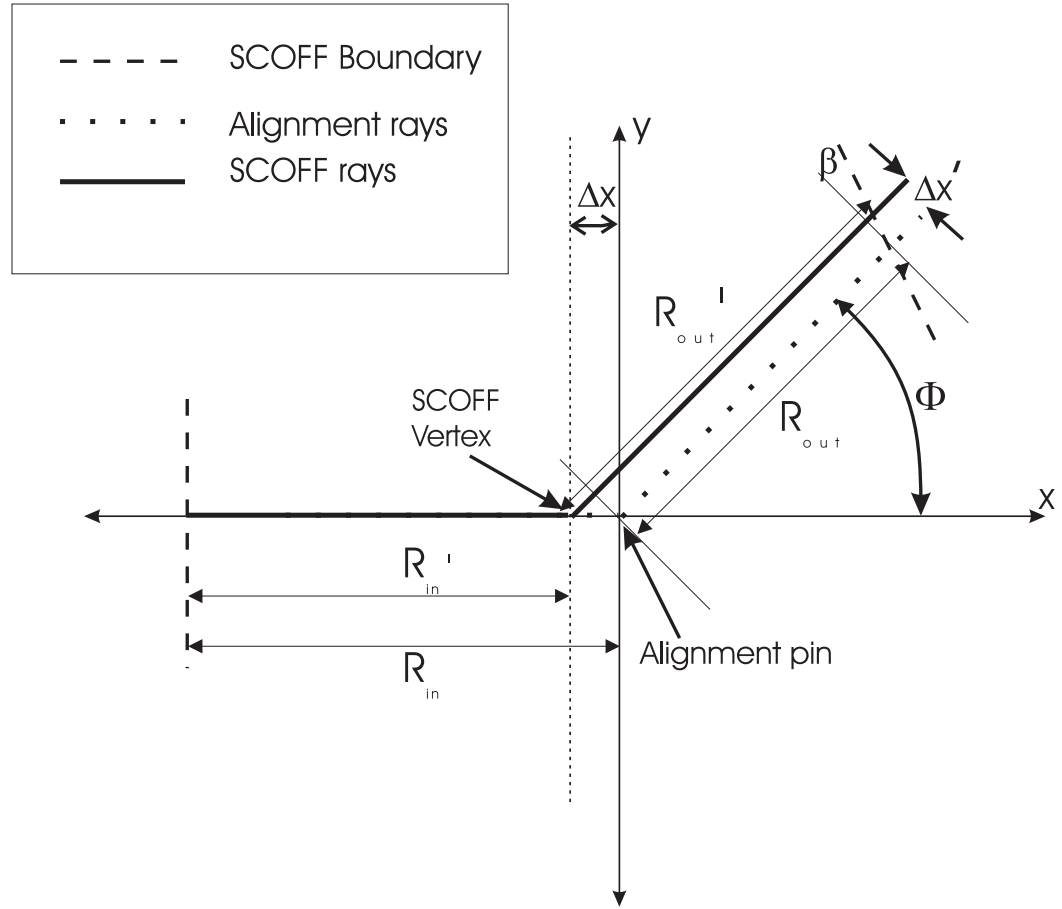


Figure 3.13: Measurements made in the alignment frame of reference (dotted lines) are used to determine the SCOFF frame of reference required for RAYTRACE calculations (solid lines). The two coordinate systems are offset by an amount  $\Delta x$ .

a SCOFF frame and an alignment plate frame. For each coordinate system, the angle of deflection is the same. However, the exit path of the electron in the alignment plate frame is offset from the SCOFF path by an amount  $\Delta x'$ . The problem is exacerbated if the electron does not exit the magnet at right angles, but rather at some shim angle  $\beta$ .

If the distance from the vertex to the exit effective field boundary in the alignment frame of reference is  $R_{\text{out}}$ , then the distance  $R'_{\text{out}}$  from the SCOFF vertex to the effective field boundary is

$$R'_{\text{out}} = R_{\text{out}} + \Delta x \cos \Phi + \Delta x \sin \Phi \tan \beta.$$

For the entrance ray we have

$$R'_{\text{in}} = R_{\text{in}} - \Delta x.$$

By symmetry, we expect  $R'_{\text{out}} = R'_{\text{in}}$  (*i.e.* the SCOFF rays are equal) so substituting  $\Phi = 45^\circ$ ,  $\beta = 26.28^\circ$ , and measured values for  $R_{\text{in}}$  and  $R_{\text{out}}$  gives  $\Delta x = 0.33$  cm so  $\Delta x' = 0.22$  cm. The SCOFF rays are each 18.79 cm (from vertex to SCOFF boundary). This also yields the first-order bending radius,  $r$ , (used in equation 3.5) which is 45.36 cm.

This means that an electron with bending radius  $r$  in the SCOFF field will actually emerge 2.2 mm to the right of the ray established by the alignment plate. Put another way, the paths of interest from RAYTRACE simulations are those which exit the magnet system with an  $x$  offset of 2.2 mm from the D coordinate system. For the energies considered here, a 2.2 mm offset can represent a 0.2% change in energy.

In the final analysis, RAYTRACE simulations were used to convert measured magnetic field spectra to electron energy spectra. Table 3.2 compares the magnetic field required to deflect an electron through the rays defined by the alignment plate (as calculated by RAYTRACE ) with the field required to deflect an electron through  $45^\circ$  in the SCOFF approximation. Note that the fields are equal within 0.1%. While the RAYTRACE electron exits the magnet at the correct *position*, its direction differs from the SCOFF electron by several milliradians. This has no impact on the energy analysis, however, since transmission of the electron is all that is required for spectrometry. A corollary of this result is that the user may employ first order analysis (equation 3.5) without compromising accuracy. The reason for this can be seen by comparing the actual path of an electron through the true field with the circular path it would take in the SCOFF approach, as shown schematically in



Electron Energy (MeV)	RAYTRACE Field (kG)	SCOFF Field (kG)
5.00	0.405	0.405
10.03	0.775	0.774
20.05	1.512	1.512
30.01	2.245	2.244
40.00	2.980	2.979

Table 3.2: Comparison of calculated field required to give transmission with SCOFF field needed to give 45° deflection.

figure 3.14. In the real field, the electron is deflected long before the SCOFF by the entrance fringing fields. The radius of curvature changes constantly outside the uniform field region, leading to offsets inside the magnet. Outside the magnet, the exit fringing field continues to deflect the electron with a constantly changing radius of curvature, so that the true ray crosses the SCOFF ray about 6 mm past the effective field boundary with a relative angle of  $-2^\circ$ . By the time the electron leaves the fringing field, it is offset from the SCOFF ray by approximately 2 mm with a relative angle of  $0.1^\circ$ .

### 3.3.4 The Spectrometer

The position and direction of the electron beam at the exit portal of the 90-B beam line of the linac are determined by a rotating wire profile monitor, which is designed to rotate so that it crosses the beam in both the horizontal and vertical directions. For initial alignment, a laser was set up at a distance of 5 m from the exit window. A shutter was placed between the laser and the profile monitor, and was triggered to open whenever the monitor passed through the horizontal or vertical centre, exposing the monitor wire to the laser light. The laser was adjusted until the centre of the beam illuminated the profile monitor as it made its sweeps in both the horizontal and vertical planes. Once the laser had been aligned with the profile monitor, two sets of cross-hairs were placed between it and the linac and centred on the laser beam, optically defining the  $0^\circ$  or “straight-through” axis for the spectrometer. The aluminum alignment plate was then placed on the bottom pole face, and the optical alignment tool was set in the  $0^\circ$  groove. The laser was replaced with a telescope which was aligned with the two cross-hairs. The position of the magnet was adjusted until both sights in the alignment tool were aligned with the crosshairs.

After the alignment of the magnet was completed, the alignment tool was moved to the  $45^\circ$  groove, and the telescope was placed opposite, about 4 m from the magnet. Again, two sets of crosshairs were placed between the magnet and the telescope, and aligned with the sights of the alignment tool. This optically defined the  $45^\circ$  axis.

For the magnet to be used as a spectrometer, the path of the beam through the magnet had to be well defined. To this end, analyzing slits were placed at both the entrance and exit sides of the magnet. Each slit comprised two 2 cm thick copper rods. The position of

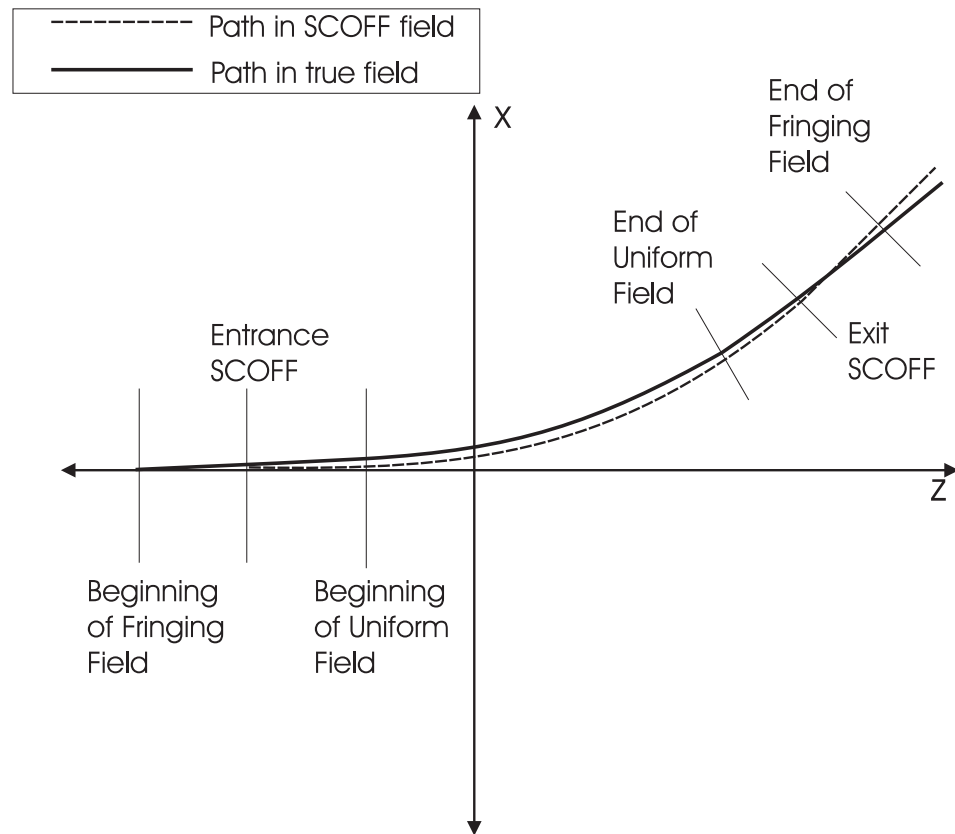


Figure 3.14: The path of an electron through the measured field compared with the circular path it would take in a uniform SCOFF field. The radius of curvature changes constantly in the fringing field regions, leading to offsets at the effective field boundaries.

each rod was controlled by an electric motor connected to a remote controller. By changing the rod positions, both the gap size and its offset from the central axis could be changed and read out remotely. Gap size was calibrated by closing the slits on stainless steel slabs of known thickness.

Before the vacuum box was put in place and the magnet reassembled, the entrance slit had to be aligned with the  $0^\circ$  axis. The slit was closed to provide a small gap, and the offset was changed until the gap was aligned with both crosshairs, as viewed through the telescope. With the entrance slit in place, the vacuum box was adapted to the linac, and the magnet reassembled. The exit slit was then fixed to the vacuum box, and aligned with the  $45^\circ$  axis in the same manner as the entrance slit was aligned with the  $0^\circ$  axis. The vacuum box was then sealed, and the beam line pumped down to create a vacuum. Mechanical measurements of the slit jaw positions outside the beam pipe were made and used to verify slit positions after pump-down.

The magnetic field was controlled by a second Rawson probe (Rawson Lush model 920) placed as closely as possible to the centre of the magnet. This probe was connected to an F8 microcontroller. If the reading from the controlling Rawson probe decreased, the magnet current was increased to compensate, and *vice-versa*. In this way, the magnetic field could be controlled to better than 0.01%.

While the Rawson probe provided excellent precision in controlling the magnetic field, the absolute calibration of magnetic field was based on an NMR probe (Sentec Type 1000) which was known to be accurate to better than one part per million (ppm). From NMR measurements, a calibration factor of  $(1.7192 \pm 0.0001) \times 10^{-2}$  gauss per Rawson unit was determined. For the larger probe used in the fringing field measurements, the calibration factor was found to be 1.999 gauss per Rawson unit.

The next step was to confirm proper operation of the spectrometer. To align the electron beam along the  $0^\circ$  axis, a scintillating phosphor was placed over the  $0^\circ$  exit window. A hole in the centre of the phosphor was aligned with the crosshairs. With the entrance slit fully open, the beam was centred on the profile monitor and the hole in the scintillating screen. It was then aligned on the  $0^\circ$  axis within  $\pm 0.002$  radians. The entrance slit was then closed down to a gap of 2 mm, which was small enough to provide good entrance geometry without

scraping the beam.

Current into the spectrometer was measured using a toroidal current monitor (TCM). The exit slit was also closed to a gap width of 2 mm, in order to sharply define the beam path. An aluminum block was used to measure current transmitted through the spectrometer at high beam currents. To acquire an energy spectrum, the magnetic field was set and the currents from the exit monitor and the TCM were integrated for thirty seconds. The ratio of exit current to entrance current was recorded for several magnetic field values. In this way, a plot of intensity *vs.* magnetic field and hence intensity *vs.* energy could be generated. Equation 3.5, along with the bending radius of 45.36 cm were used to convert this to an energy spectrum. An example of a measured spectrum is given in figure 3.15. For low beam currents, such as those required for stopping power measurements, a plastic scintillator was used to measure exit current; the entrance current was too weak to monitor accurately. Changes in accelerator beam current might have been expected to skew the energy peak. However, the centroid of the measured spectrum was found to be constant to within 0.1% over the course of several runs. Zero degree alignment was confirmed by placing a small lead collimator at the “straight-through” position, and a second plastic scintillator was used to measure the beam current transmitted through this collimator. The magnetic field was varied by a few gauss in each polarity to sweep the beam over the collimator slit. The field which provided maximum transmission was used to determine the horizontal offset of the beam at the collimator. From there, any corrections to the measured energy due to steering could be determined (see equation 3.17). The correction was always less than 0.2%. A schematic of the spectrometer is shown in figure 3.16. Examples of spectra measured at low currents at 10 and 20 MeV are given in figure 3.17.

### Summary of Ray Tracing Results

ESPLINE was compared with RAYTRACE for the specific test case of a magnet with circular pole faces. The fringing fields were assumed to be sharply cut off. Successive calculations were run to determine the magnetic field necessary to deflect a 20 MeV electron beam through 45°. The two programs gave results which agreed with each other and also with the expected value from equation 3.3. Further tests were conducted using the measured fringing

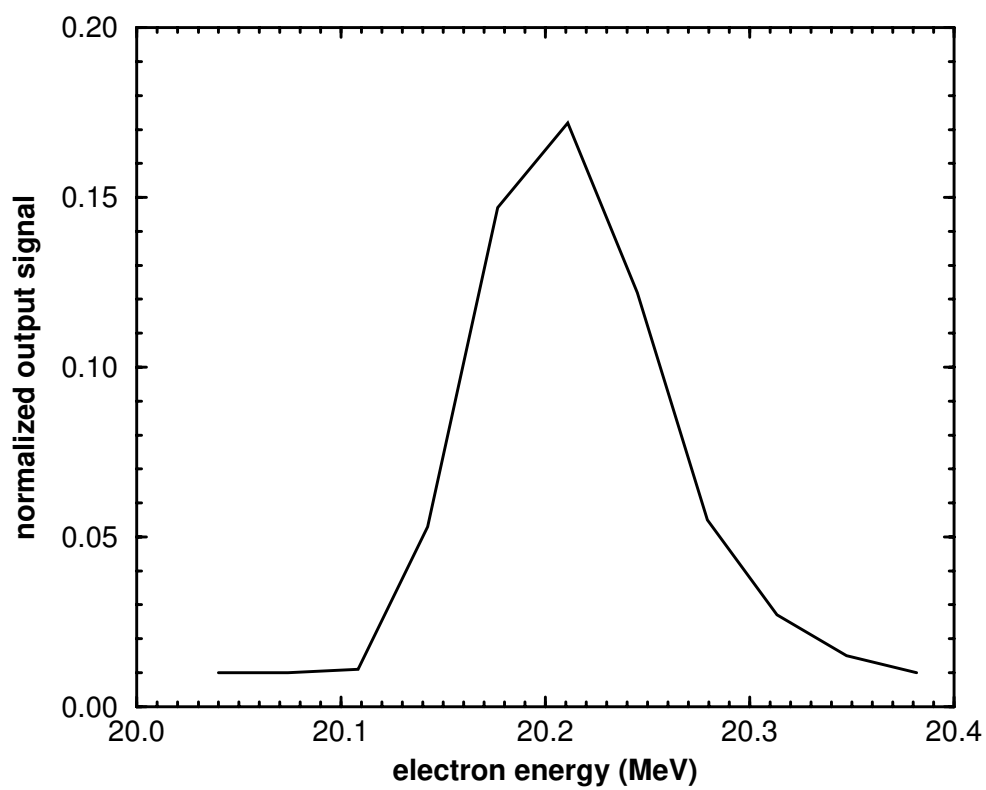


Figure 3.15: Sample of typical electron energy spectrum at 20 MeV, measured at high beam current.

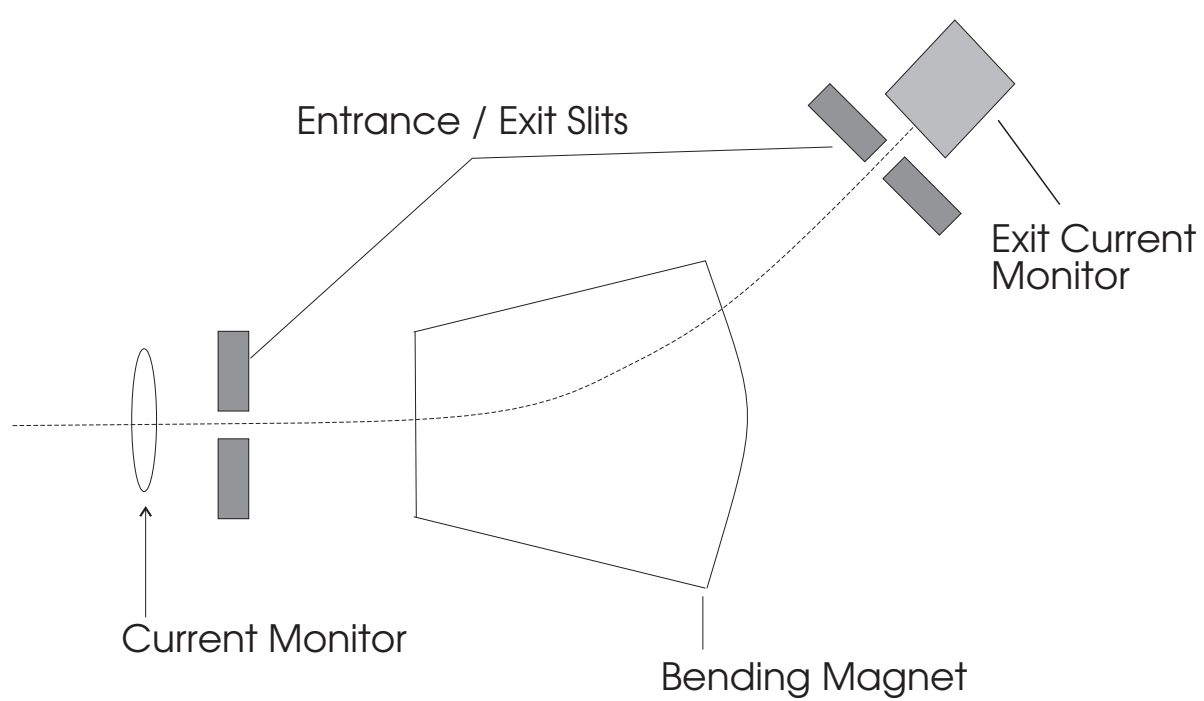


Figure 3.16: Schematic of magnetic spectrometer.

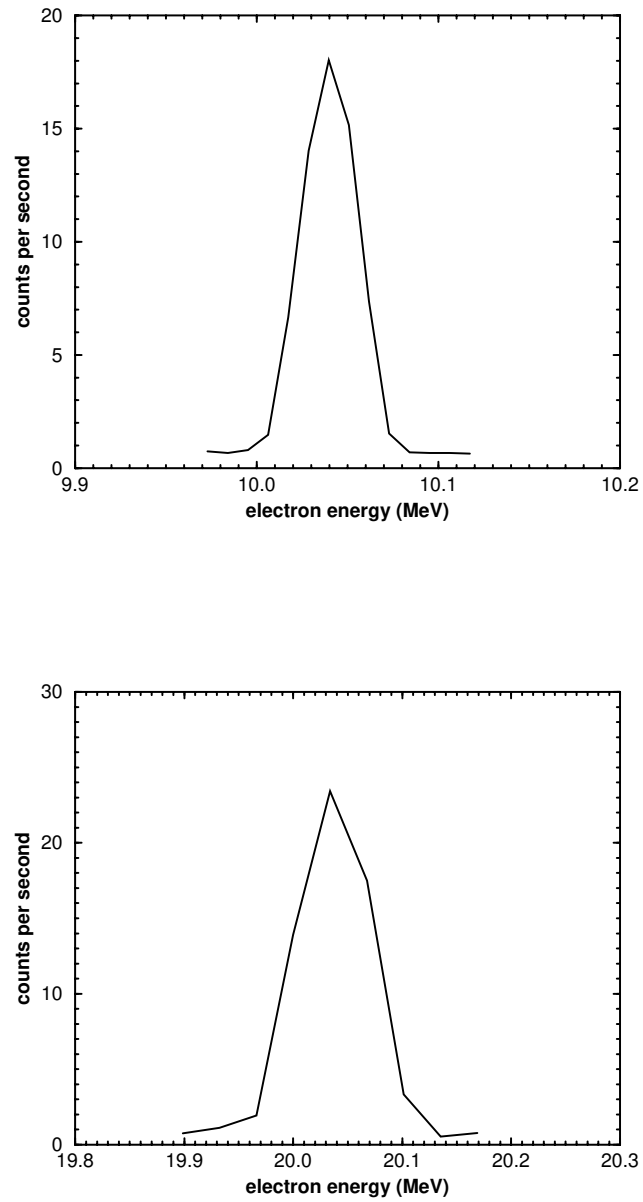


Figure 3.17: Electron spectra at 10 (top) and 20 MeV (bottom) measured at low beam current (tens of electrons per second). The M1 and S1 slits were each set at 0.2 cm.



field data and assuming a circular magnet. Again, the two programs agreed in predicting the field strength required to deflect a 20 MeV electron through 45°.

RAYTRACE was chosen for most calculations because of its more complete treatment of magnetic field calculations and more flexible geometric modeling. In addition to providing a conversion from magnetic field to electron energy, RAYTRACE was also used to estimate the energy resolution of the spectrometer and uncertainties in energy calibration arising from uncertainties in beam geometry.

Several parameters could affect the final energy measured by the spectrometer, including slit size, beam spot size, entrance offsets in the horizontal plane, angular deflections and divergence, and the intrinsic energy distribution of the beam. The effect of slit size could be determined directly from RAYTRACE simulations. The change in measured energy with respect to offsets in the horizontal plane was found to be

$$\frac{1}{E} \frac{\partial E}{\partial x} \approx 0.01 \text{ cm}^{-1}, \quad (3.16)$$

at both the entrance and exit slits. From this we conclude that each 2 mm slit corresponds to  $\pm 0.1\%$  in energy. The change in energy with respect to entrance angle was

$$\frac{1}{E} \frac{\partial E}{\partial \theta} \approx 0.001 \text{ mrad}^{-1}. \quad (3.17)$$

The overall uncertainty due to geometric effects was estimated as follows. First, the intrinsic resolution of the spectrometer is due to the finite width of the exit slit. A monoenergetic beam incident on the straight through axis would appear to be 0.2% wide due to the 2 mm exit slit gap. This is an absolute limit on the precision of the instrument. Extra uncertainty arises due to uncertainties in beam entrance geometry and beam width at the exit slit. The entrance geometry is constrained to 2 mm by the entrance slit, which corresponds to  $\pm 0.1\%$ . However, this represents a worst case; the standard ( $1\sigma$ ) uncertainty is assumed to be 0.05%. In order to measure beam size and estimate the divergence, Gaf-chromic film was mounted to the 0° exit window of the spectrometer, and irradiated at an electron current of 80 nA for 10 seconds. The measured spot was less than 3 mm in diameter. Assuming the same beam size at the exit slit (for a given energy), makes the distribution 0.3% wide (full width at tenth maximum). Again, this is a worst case, and the standard uncertainty

is estimated at 0.1%. Considering that the spot was measured nearly 2 m upstream of the entrance slits, the maximum divergence of the beam must be less than 1 milliradian (i.e. less than 0.1% in terms of energy). The uncertainty due to beam divergence is taken as 0.05% ( $1\sigma$ ). These geometric effects were added in quadrature with one half of the magnet's resolution (i.e. 0.1%) to give a geometric uncertainty of 0.16%. A more conservative estimate places this uncertainty at 0.2%.

### Residual Magnetic Fields

The final energy measured for the electron beam depends on its entrance angle relative to the magnetic spectrometer. The beam was aligned with the scintillating screen by adjusting the steering in the 90-B beam line with the magnet set to zero field. At low energies, this could lead to alignment problems, as the beam is deflected by the earth's magnetic field and residual fields outside the magnet due to hysteresis and magnetization of materials in the beam line. In such a case, the beam would be steered into the magnet at some non-zero angle to compensate for the deflection. Figure 3.18 shows measured residual fields after applied magnetic fields of 400 and 1500 gauss for the entrance and  $0^\circ$  exit portals, respectively. The average field over the entire range is approximately 1.5 gauss on each side and is not greatly reduced by a simple degaussing of the magnet. The maxima correspond to the positions of flanges where the beam pipes are joined to the vacuum box, suggesting that the bolts which fasten the flanges have been magnetized.

As discussed above, these residual fields result in an alignment error for the beam, whose impact on the energy calibration can be determined as follows. Consider the case where the electron beam enters the magnet precisely on the “straight-through” axis. Due to deflections caused by the residual magnetization, the beam will appear offset a distance  $\Delta x_{\text{resid}}$ . The beam entrance angle must then be adjusted by  $\theta_{\text{corr}} = \Delta x_{\text{resid}}/D_{\text{mag}}$  where  $D_{\text{mag}}$  is the distance over which the particle is under the influence of the residual field (figure 3.19).  $\Delta x_{\text{resid}}$  can be estimated as follows. For small angles

$$R_{\text{resid}} = (R_{\text{resid}} + \Delta x_{\text{resid}}) \cos \theta_{\text{resid}},$$

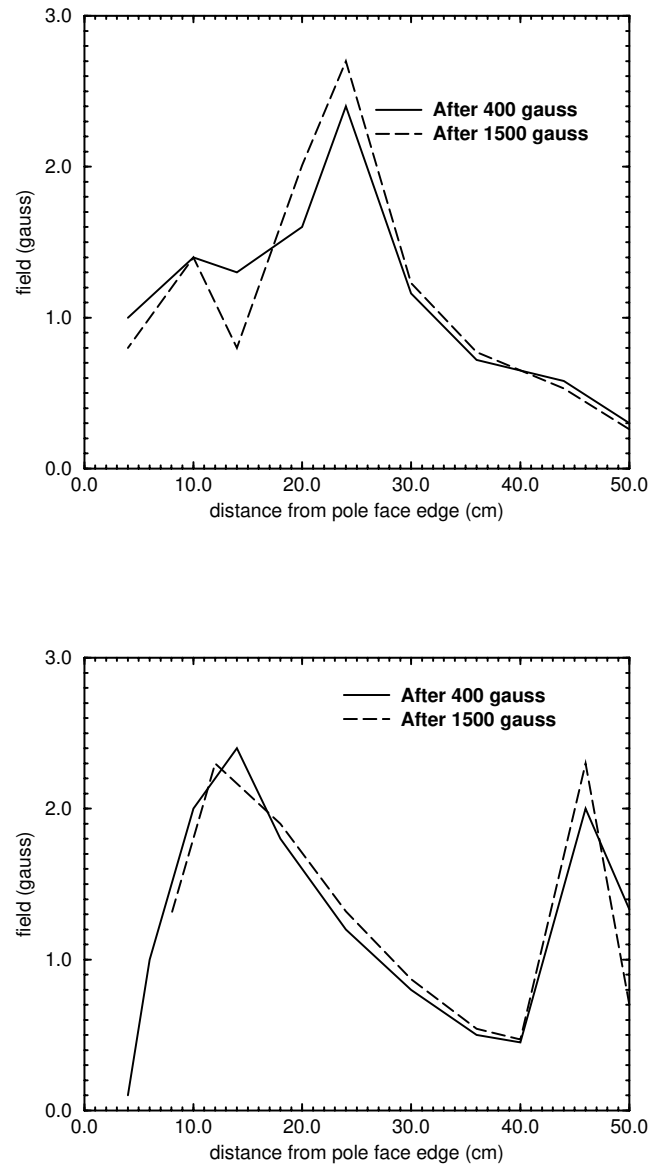


Figure 3.18: Residual fields on the entrance (top figure) and exit (bottom figure) side of the magnetic spectrometer, as measured after applied fields of 400 and 1500 gauss. The peaks correspond to the location of the beam pipe flanges.

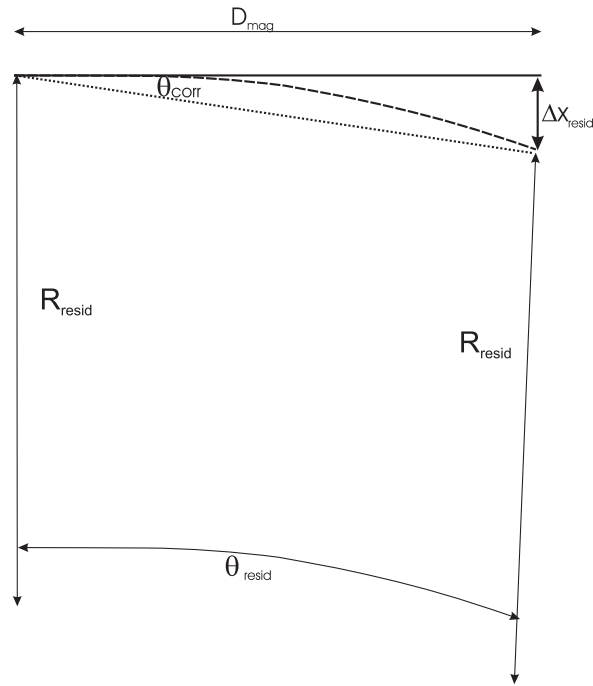


Figure 3.19: Residual fields lead to an offset ( $\Delta x_{\text{resid}}$ ) with respect to the “straight through” path through the spectrometer (solid line). This results in a correction in steering  $\theta_{\text{corr}}$ .  $D_{\text{mag}}$  is the distance from the profile monitor to the exit phosphor.

where  $R_{\text{resid}}$  is the bending radius of the residual field. One can write

$$R_{\text{resid}} \approx (R_{\text{resid}} + \Delta x_{\text{resid}}) \left(1 - \frac{\theta_{\text{resid}}^2}{2}\right),$$

from which

$$\Delta x_{\text{resid}} \approx R_{\text{resid}} \frac{\theta_{\text{resid}}^2}{2}. \quad (3.18)$$

The effect of the residual fields was estimated by treating the residual fields as a constant 1.5 gauss over 40 cm, followed by a 30 cm zero field region (i.e. inside the pole faces), then another 1.5 gauss, 40 cm field. At 5 MeV, in the entrance region, the change in position is 0.06 cm and the change in angle is 3 milliradians. Inside the pole faces, this change in angle leads to a further 0.1 cm offset, followed by another 0.06 cm change in the exit field. The net offset is just over 2 mm, for a steering correction of 2 milliradians, or 0.2% (equation 3.17). The effect is lessened at higher energies.

### Earth's Magnetic Field

The value for the earth's magnetic field is approximately 0.55 gauss, opposite to the direction of the applied field of the spectrometer. This causes a decrease in required magnetic field due to steering effects as discussed in the previous section (figure 3.19). This effect is somewhat reduced by a similar shift in beam position at the exit slit. The net impact of the earth's field on energy calibrations can be estimated as the sum of these entrance (steering) and exit (offset) effects. The steering effect was estimated assuming the earth's field acted over a distance of 2 m. The exit offset was estimated assuming the earth's field acted over a distance of 1 m (from the pole face to the exit slit). Table 3.3 summarizes the geomagnetic field corrections for each energy.

## 3.4 Results and Discussion

### 3.4.1 Energy Calibration of the Linac

This project was initiated with the expectation of performing a one-time calibration of the 90-B beam line of the NRC linear accelerator. Before proceeding, a brief description of this

Energy (MeV)	$R_{\text{earth}}$ (cm)	Entrance Effect (Steering)	Exit Effect (Offset)	Net correction
5	33000	+0.15%	-0.3%	-0.15%
7	45000	+0.1%	-0.2%	-0.1%
10	64000	+0.08%	-0.15%	-0.08%

Table 3.3: Corrections required for the effect of the earth's magnetic field. At 5 MeV the true field is 0.15% lower than the field calculated with no earth's field correction. At energies greater than 10 MeV the corrections are negligible.

portion of the accelerator is in order. The 90-B beam line normally is used for dosimetry of high energy electrons and x-rays. It consists of two dipole magnets, each of which deflects the electron beam through  $45^\circ$  (figure 3.20). Between the dipole magnets is a slit system which restricts the energy range transmitted through the magnet system, along with a quadrupole magnet which counteracts divergence of the beam. The two dipoles are connected in series, and current to the dipoles is monitored externally with a digital voltmeter (DVM). Changing the magnetic fields of the dipoles also changes the electron energy which can be transmitted through the beam line. It was hoped that the current delivered to the dipoles could be related to electron energy with sufficient accuracy for the stopping power work (i.e., better than 0.5%). Early measurements of electron energy showed rather large residuals when compared with the measured magnetic fields inside the 90-B bending magnets. Furthermore, the reproducibility of beam energy for a given 90-B magnet setting was poor, and changes in energy of up to 1% were observed. To understand these effects, it is necessary to look more closely at the geometry of the bending optics of the 90-B beam line.

The linear accelerator consists of four waveguide sections in which the electrons are accelerated. Electron energy is controlled by adjusting the RF power to each section, as well as the relative phase between each section. The direction of the electron beam is controlled by steering magnets located upstream of the dipole assembly. When the dipole current is set, both the steering and waveguide phase are adjusted to allow transmission through the slit system S1 and onto the profile monitor at the end of the beam line. However, the entrance to the bending magnet system is not well defined either in terms of angle or position. As a result, the beam could have lateral shifts of up to 2 cm from the centre of the beam line, and angular displacements of up to 9 mrad. RAYTRACE was used to simulate the path of the electron beam through the 90-B beam line. First-order approximations were used with respect to the dipole magnets. Measurements of the dimensions of the quadrupole were used to describe the quadrupole effect. The magnetic field inside the quadrupole was estimated by varying the quadrupole field in the simulations until the beam was focused at the M2 magnet. The quadrupole had no impact on the mean transmitted energy.

Simulations of the bending system indicate that offsets such as those previously discussed could translate into energy differences of  $\pm 0.7\%$ . It is likely that the observed 1% energy

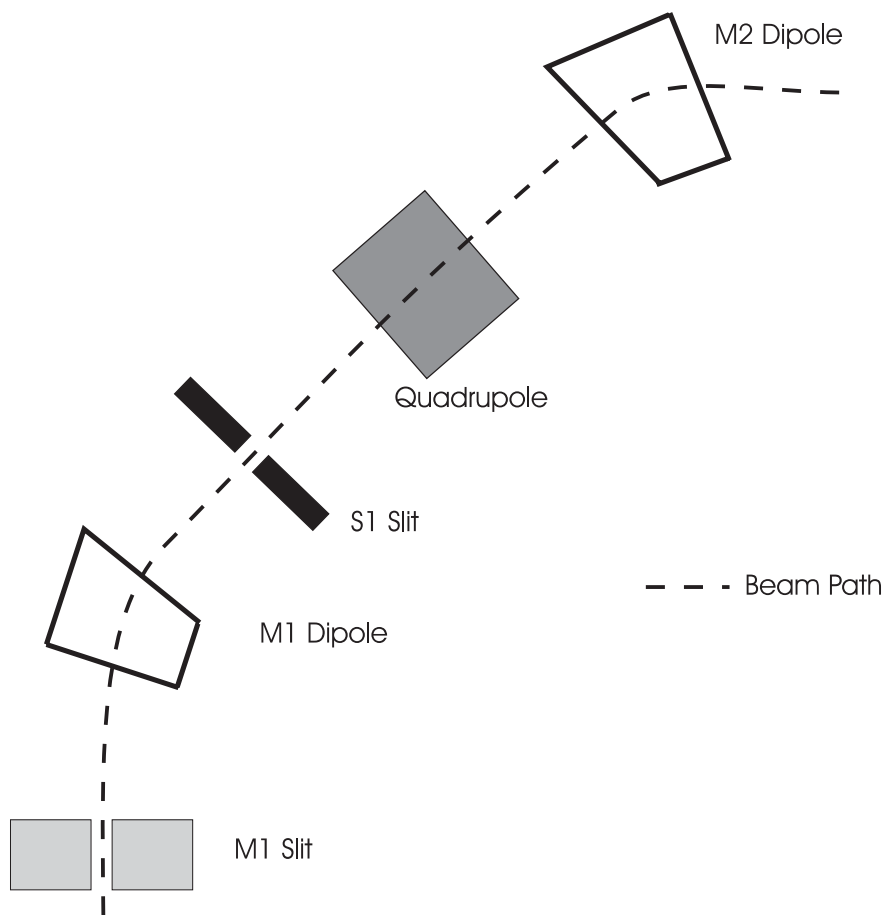


Figure 3.20: Schematic of 90-B beam line. The dipoles each deflect the beam through  $45^\circ$ , while the quadrupole corrects for dispersion of the beam introduced by the dipole M1. Energy spread is controlled by the slit, S1.



shift was caused by a change in geometry being compensated by a change in energy (phase adjustments). This problem has been partially resolved by introducing an entrance slit system upstream of the M1 magnet, so that lateral drifts are minimized. The M1 slit consists of movable thick aluminum jaws, and provides a range of entrance widths from 0.2 cm to several cm in both the horizontal and vertical directions. The effect of the M1 slit on the transmitted energy spectrum is modest (figure 3.21). With the slit closed down to 0.2 cm, variations in observed beam energy are on the order of  $\pm 0.2\%$ . This is at the cost of a large reduction in transmitted beam current, which may not be desirable for applications where high dose rates are required.

With the M1 slit, transmitted energy  $T$  was found to vary roughly linearly with the reading of the DVM,  $V_M$ . The equation

$$T = 22.77V_M - 0.00088, \quad (3.19)$$

will predict energy to within 0.4% from 5 to 30 MeV (figure 3.22). The corresponding relationship given in [59] was

$$T_{\text{old}} = 22.36V_M + 0.0850. \quad (3.20)$$

The difference between the old and new calibrations can be written as

$$\frac{T - T_{\text{old}}}{T} = 0.0180 - \frac{0.0859}{T}. \quad (3.21)$$

For a given setting of  $V_M$ , the new, more accurate calibration gives electron energies that are 0.1%, 0.9%, and 1.4% higher than the old calibration at 5, 10, and 20 MeV, respectively. Although this result suggests that previous assignments of electron energies should be increased, it is important to note that the new calibration was done with the M1 slits in place. Without the M1 slits, variations in energy of up to 1% were noted, and this uncertainty would have to be considered in any retrospective evaluation of energy.

Figure 3.22 shows the residuals resulting from the fit of equation 3.19. The largest error seems to reside in the 5 MeV point. This might be expected, as the non-linearity of equation 3.5 is greatest at low energies. A more robust calibration would relate the actual field inside the M1 magnet to transmitted energy. At each energy, a measurement of the

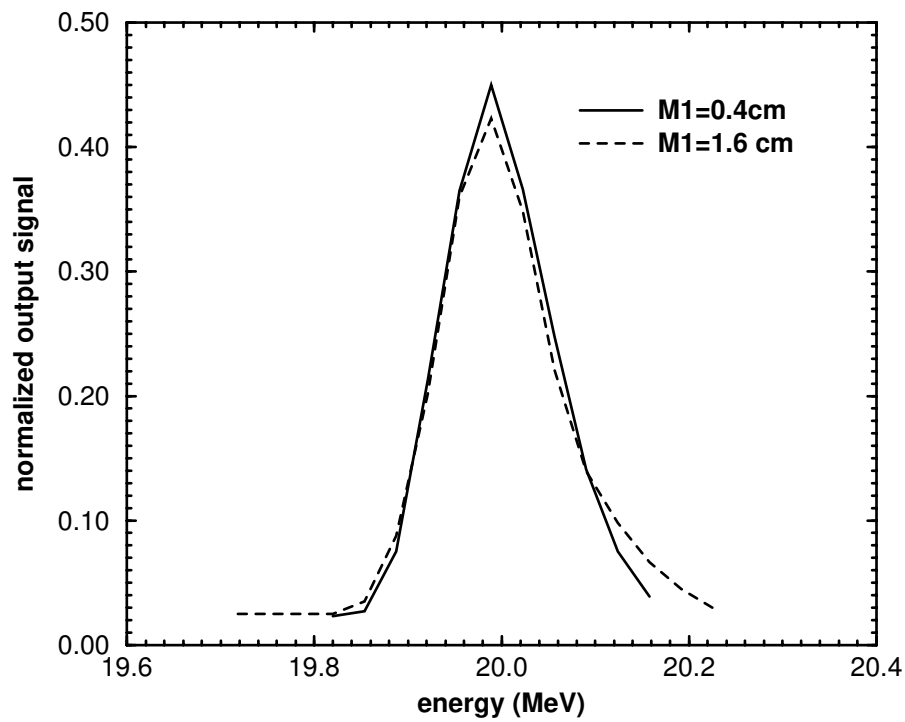


Figure 3.21: Variation in transmitted spectrum with width of M1 slit. The S1 slit has been set to 0.4 cm. Closing the M1 slit from 1.6 cm to 0.4 cm has no appreciable impact on the measured spectrum.

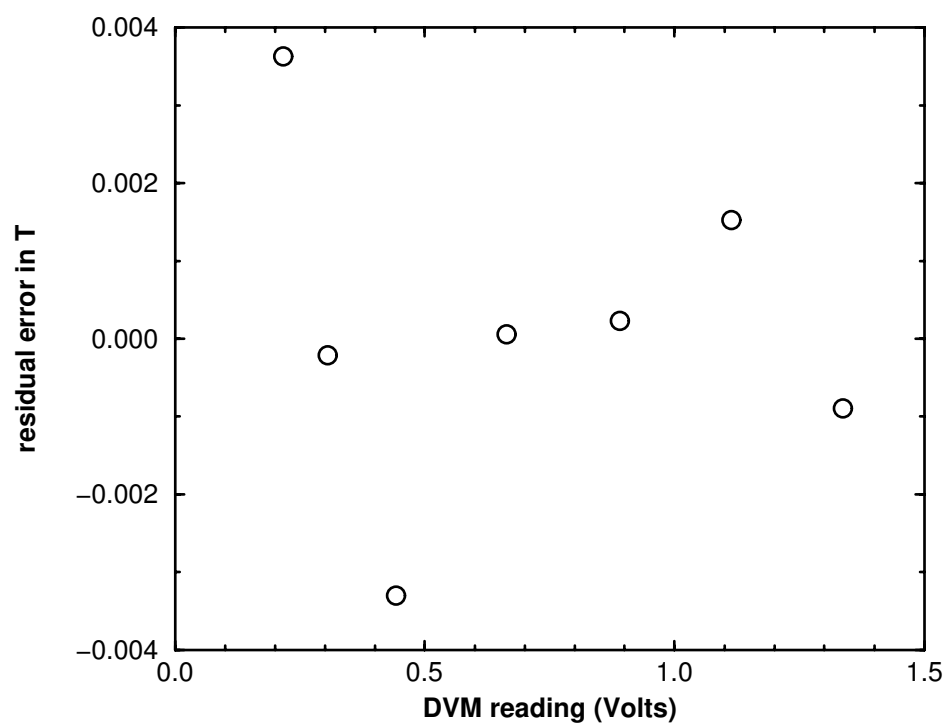


Figure 3.22: Residuals from a linear fit of electron energy to M1 magnet current as measured using the DVM.

field inside the M1 magnet was made using a Rawson rotating coil magnetometer. The M1 field was found to vary linearly with  $V_M$ :

$$B_M = 2.270V_M + 0.0467, \quad (3.22)$$

where  $B_M$  is in kG. The 90-B optics were approximated as a single dipole, and the effective bending radius was determined at each energy using equation 3.4 (figure 3.23). The effective radius at 5 MeV is 0.5% higher than the average of the other points. This may reflect effects of the earth's magnetic field or hysteresis effects at the 90-B dipoles which have not been taken into account. A global fit of  $B_M$  and  $T$  from 7 to 30 MeV according to equation 3.5 gives an effective bending radius of 33.51 cm. Therefore, the equation

$$T = \sqrt{101B_M^2 + 0.2611} - 0.511 \quad (3.23)$$

will predict electron energy from 7 to 30 MeV within 0.25%. Combining this with equation 3.22 gives the somewhat complicated

$$T = \sqrt{520.4V_M^2 + 21.41V_M + 0.4811} - 0.511, \quad (3.24)$$

which offers improved accuracy over equation 3.19. However, the uncertainty in the latter is still a factor of at least 2 less than an earlier attempt at this calibration [59].

### 3.4.2 Beam Characteristics

The magnetic spectrometer presented an opportunity to study in detail the properties of the accelerator beam. Energy spreads in the beam are controlled by the slit system S1 depicted in figure 3.20. The approximate spread in the beam was known, but no means of testing was previously available. Electron spectra were acquired at 10 MeV for various slit openings, with the M1 entrance slit set to 0.2 cm. The transmitted current was observed to decrease as the slit was closed, and the energy spread decreased from about 3% FWHM for a 1.6 cm slit opening to about 0.4% FWHM for a slit opening of 0.2 cm (figure 3.24). Some of this residual width is attributed to the intrinsic resolution of the spectrometer (0.2%) and the effect of the finite width of the beam (estimated at 0.2%). By combining these effects in quadrature, the energy spread of the incident beam is estimated to be 0.3% at FWHM.

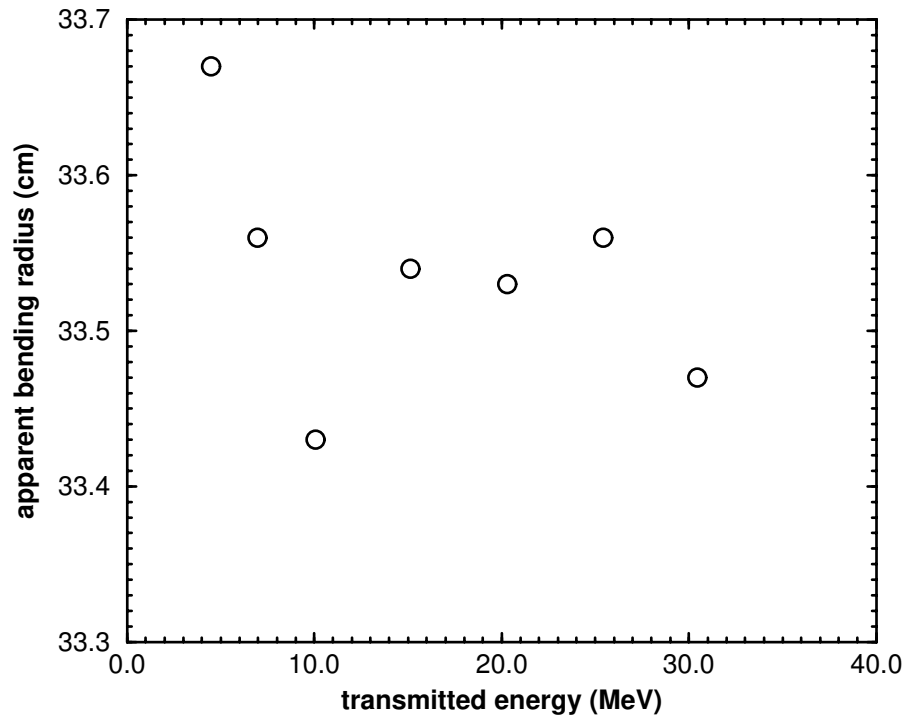


Figure 3.23: By treating the 90-B dipole assembly as a single dipole, an effective bending radius was calculated at each energy. The 5 MeV point does not agree well with those calculated at other energies.

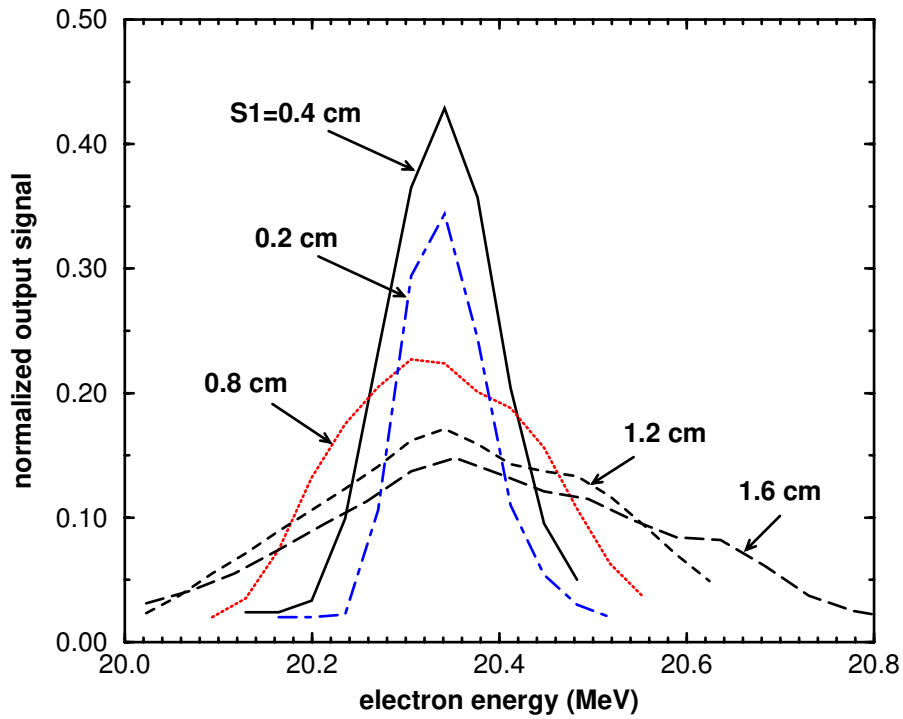


Figure 3.24: Variation in transmitted spectrum with width of S1 slit. The M1 slit has been set to 0.4 cm. Closing the S1 slit from 1.6 cm to 0.2 cm reduces the FWHM of the transmitted spectrum from 2.5% to 0.4%.

### 3.4.3 Error Analysis

The measured fringing fields are expected to be accurate in terms of position to within 0.5 mm on each side. This corresponds to a  $\pm 0.2\%$  uncertainty in energy. The intrinsic resolution and uncertainties due to beam geometry have been combined to estimate the “geometric” uncertainty in the measured energy at 0.2%. Uncertainties in bending angle (which impacts on the calculated design radius and, ultimately, on energy), magnetic field, and the effect of vacuum box contribute less to the overall energy uncertainty, which is about 0.3%. Table 3.4 summarizes the uncertainties associated with the energy measurement.

## 3.5 Conclusion

A magnetic spectrometer has been constructed and adapted to the 90-B beam line of the NRC electron linear accelerator. The spectrometer consists of a dipole magnet which deflects the electron beam through  $45^\circ$ . The intrinsic resolution of the spectrometer is 0.2%, and the uncertainty in measured energy, (which includes uncertainties due entrance geometry, beam size, and fringing fields) is estimated to be  $\pm 0.3\%$ . This level of uncertainty represents a factor of 3 improvement over the previous electron energy calibration, and is sufficiently small to allow precise measurements of electron stopping powers.

The spectrometer has revealed reproducibility problems in transmitted energy at the 90-B beam line, which have been attributed to variations in beam position at the entrance to the 90-B optics. A beam-defining slit has been added before the 90-B magnets, which improves reproducibility in energy to better than 0.2%, albeit at the cost of transmitted current.

The full width at half maximum (FWHM) of the electron beam at the exit window of the accelerator depends on the amount of geometrical restriction imposed at the S1 slit of the 90-B bending magnets. The full width at half maximum of the energy spread of the electron beam varies from nearly 3% with a 1.6 cm slit opening to 0.3% with the slit closed to 0.2 cm.

Electron energy at the 90-B beam line has been calibrated in terms of current supplied to the  $45^\circ$  dipoles. The energy predicted from the new calibration is up to 1.5% higher

Intrinsic resolution and beam geometry	0.2%
Magnetic field	0.01%
Entrance/exit fringing fields	0.2% ( $\pm 0.5$ mm each side)
Stainless steel vacuum box	0.05%
Quadratic sum	$\approx 0.3\%$

Table 3.4: Breakdown of uncertainties related to energy calibration. All uncertainties are estimated as  $1\sigma$ .



than that estimated using an earlier calibration. However, without the new beam defining slit, energy changes of 1% are possible. This should be considered in any re-evaluation of previous energy calculations.

## Chapter 4

# Accurate Measurement of Electron Energy Spectra Using a Large NaI Detector

### 4.1 Introduction

The measurement of electron stopping powers described in this thesis entails accurate extraction of the difference in energy loss between simulated and measured electron spectra. Since these energy loss differences are expected to be small, precise knowledge of the response of the radiation detector is required.

This chapter discusses the choice of a spectrometer for the measurement of electron stopping powers, and the calibration and operation of that spectrometer in a regime where precise stopping power measurements are possible.

### 4.2 Choice of Detector

The original stopping power measurements were performed with a large sodium iodide (NaI) detector [42]. This spectrometer was advantageous for stopping power measurements, as it is nearly totally absorbing. However, there are several drawbacks associated with using a NaI detector. First of all, its inherent resolution is poor, about 2% at 20 MeV, which could mask

small differences in energy loss. Also, the photomultiplier tube (PMT) gain has been known to drift by as much as 3%; such gain drifts would be unacceptable for precision stopping power measurements. Furthermore, NaI detectors and photomultiplier tubes are known to exhibit non-linear energy responses, especially for large light pulses.

### 4.2.1 High Purity Germanium Detectors

Semiconductor detectors, such as High Purity Germanium (HPGe) spectrometers, offer much better intrinsic resolution than NaI detectors, with excellent linearity. In theory, then, they should be sensitive to much smaller changes in stopping power. Also, the absence of a photomultiplier tube removes the gain drifts associated with NaI detectors. As a prelude to stopping power measurements, the feasibility of using HPGe detectors was investigated.

One drawback of HPGe spectrometers is that the detector crystals are typically much smaller than the large NaI crystal used in the first measurement phase. The first step was to determine the minimum size of Ge crystal necessary to stop the 5 to 30 MeV electrons expected to be used in the study. The EGS4 user code DOSRZ was used to predict the pulse height distributions 10 and 30 MeV electrons would generate inside cylindrical Ge crystals of various sizes. The steel exit window of the linear accelerator was also included in the simulations. At each energy, the shape of the pulse height distribution inside the Ge crystal was studied as both the depth and radius of the crystal were varied. At 10 MeV (figure 4.1) the full energy peak is visible for all detector sizes. At 30 MeV, the full energy peak is no longer visible for detector radii less than 2 cm or thicknesses less than 3 cm (figure 4.2). Also seen in figure 4.2 is a small valley just below the full energy peak, due to the fact that secondary electrons with kinetic energies less than 10 keV were not simulated [72]. The valley is masked by straggling for the 10 MeV simulations. Ge detectors with crystals larger than this are readily available, although they are usually manufactured in a “coaxial” geometry, with a hole in the centre. This is done to achieve uniform electric field throughout the crystal, and works well for photon counting. However, it is nearly useless for measurements in electron beams, as most particles would be incident on the centre of the detector. Instead, a “planar” geometry is desired, where the active volume of the Ge crystal forms a cylinder (see figure 4.3). The largest commercially available planar detectors have dimensions near the

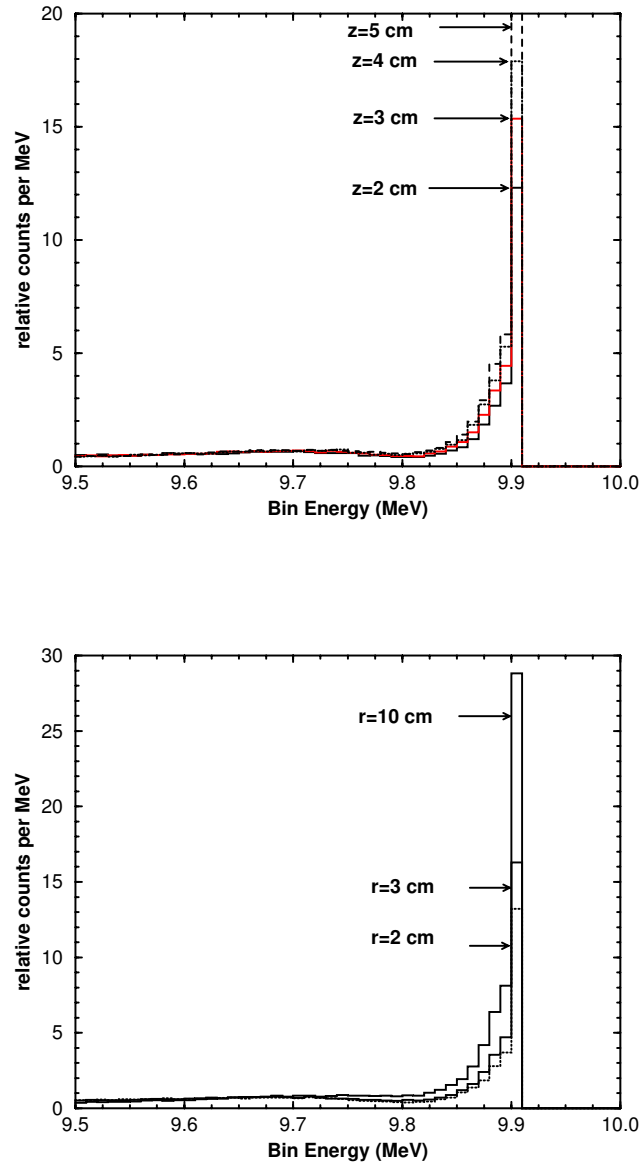


Figure 4.1: Predicted pulse height distributions for HPGe crystals of various thicknesses (top,  $r=10$  cm) and radii (bottom,  $z=10$  cm) for 10 MeV electrons. While the efficiency drops for smaller crystals, a distinct electron peak is evident for all crystals.

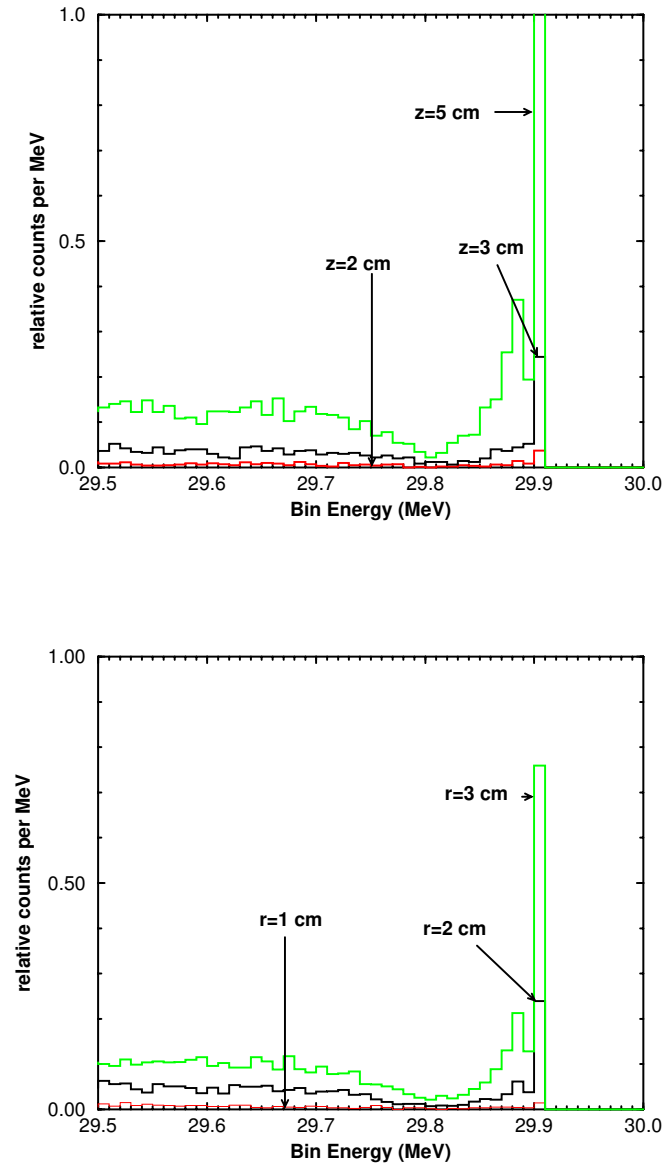


Figure 4.2: Predicted pulse height distributions for HPGe crystals of various thicknesses (top,  $r=10$  cm) and radii (bottom,  $z=10$  cm) for 30 MeV electrons. The full energy peak is lost for thicknesses of 2 cm or less or radii of 1 cm or less.

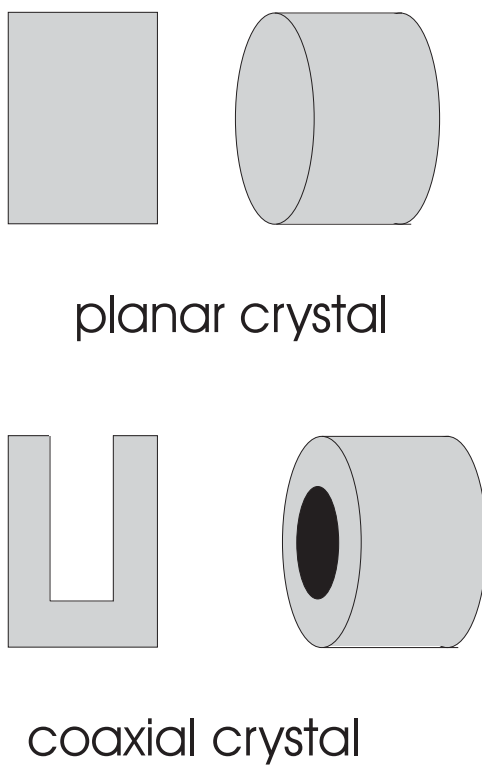


Figure 4.3: Cross section and oblique views of the typical crystal geometries available for high purity germanium detectors. The coaxial type offers larger detector volumes but is unsuitable for electron beam measurements.

minimum necessary for high energy measurements (2 cm radius, 3 cm thick). The behaviour of such a crystal in the presence of thin ( $0.5 \text{ g cm}^{-2}$ ) absorbers of beryllium and tantalum was studied. Figure 4.4 compares the pulse height distributions at 10 MeV for a 2 cm radius by 3 cm thick detector with what would be seen by a hypothetical fully absorbing 10 cm by 10 cm HPGe detector. For both beryllium and tantalum absorbers, the full energy peak is easily visible. For 30 MeV, however, the peaks are not visible (figure 4.5). This is due to the increased bremsstrahlung cross section at higher energies. The hypothetical totally absorbing detector clearly shows the full energy peak, but photon losses from the comparatively small planar HPGe crystal are too great for energy loss measurements at this energy.

The small size of planar HPGe detectors makes them very sensitive to radiative losses by the electron beam. They could be used for stopping power measurements only in a regime where photon losses are small (low incident energy, thin absorbers, and low atomic numbers). For this reason, as well as their relatively high cost, HPGe detectors were not used for this work.

### 4.2.2 Large NaI Detector

The major drawback for HPGe detectors is their sensitivity to radiative energy losses by the electron beam in both the absorbing slab and the detector crystal itself. Accurate measurements of the collision component require a spectrometer with a much higher photon detection efficiency.

The detector chosen for stopping power measurements was the large NaI detector used by Faddegon *et al* in stopping power [42] and bremsstrahlung measurements [12], [13]. The NaI crystal is 20 cm in diameter and 25 cm thick. The crystal is enclosed in 0.32 cm aluminum cladding. A thin window of 0.025 cm aluminum was provided by the manufacturer, so as to minimally affect the electron spectrum as it enters the NaI detector. This window will be discussed further in section 4.6.1. The detector crystal and photomultiplier tube were shielded in a lead housing to reduce noise from background radiation. The front face of the lead housing was machined to hold an aluminum mount for the absorbers used in the stopping power measurements. A schematic cross section of the NaI detector is shown in figure 4.6.

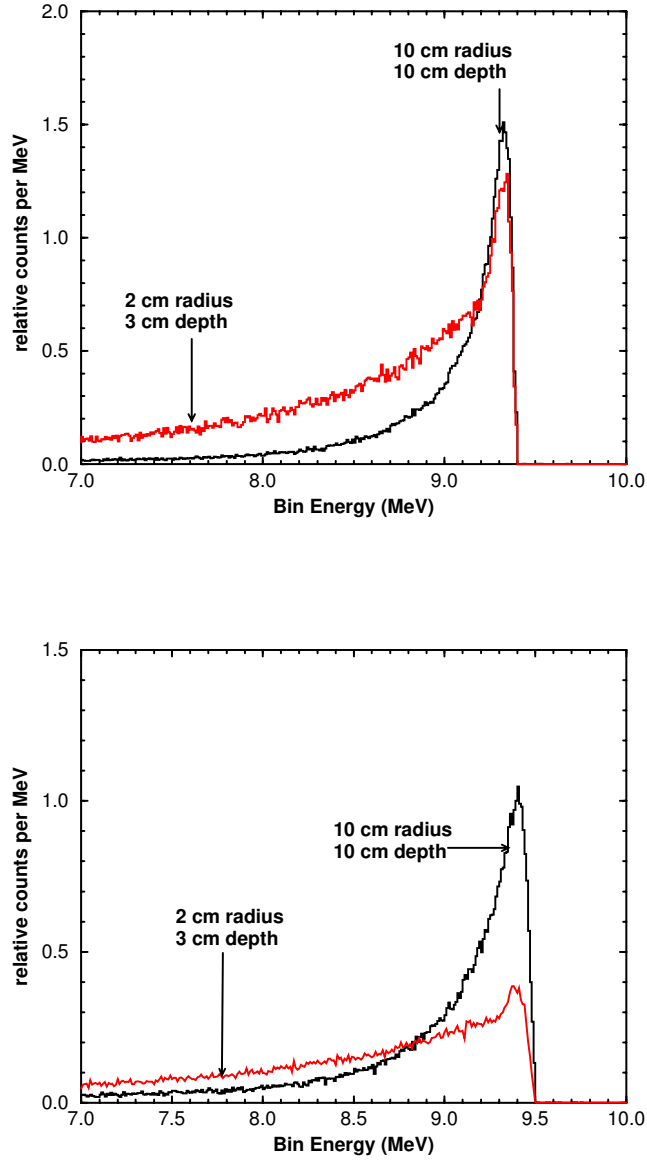


Figure 4.4: Predicted pulse height distributions in a 2 cm radius, 3 cm thick Ge crystal for 10 MeV electrons incident on  $0.5 \text{ g cm}^{-2}$  absorbers of beryllium and tantalum. Also shown is the pulse height distribution in an unrealistically large, totally absorbing HPGe detector. For each material the full energy electron peak is visible.



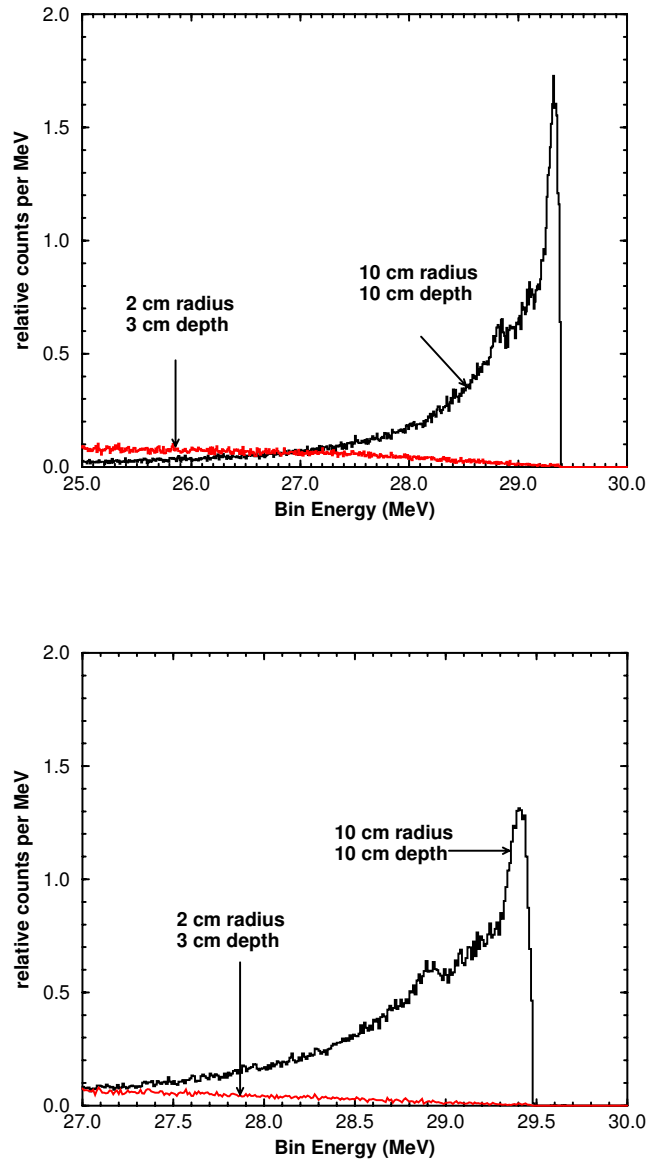


Figure 4.5: Predicted pulse height distributions in a 2 cm radius, 3 cm thick Ge crystal for 30 MeV electrons incident on  $0.5 \text{ g cm}^{-2}$  absorbers of beryllium and tantalum. Due to lost photons generated in the absorber and detector, the peak can not be distinguished. Shown for comparison is the expected peak for a very large detector.

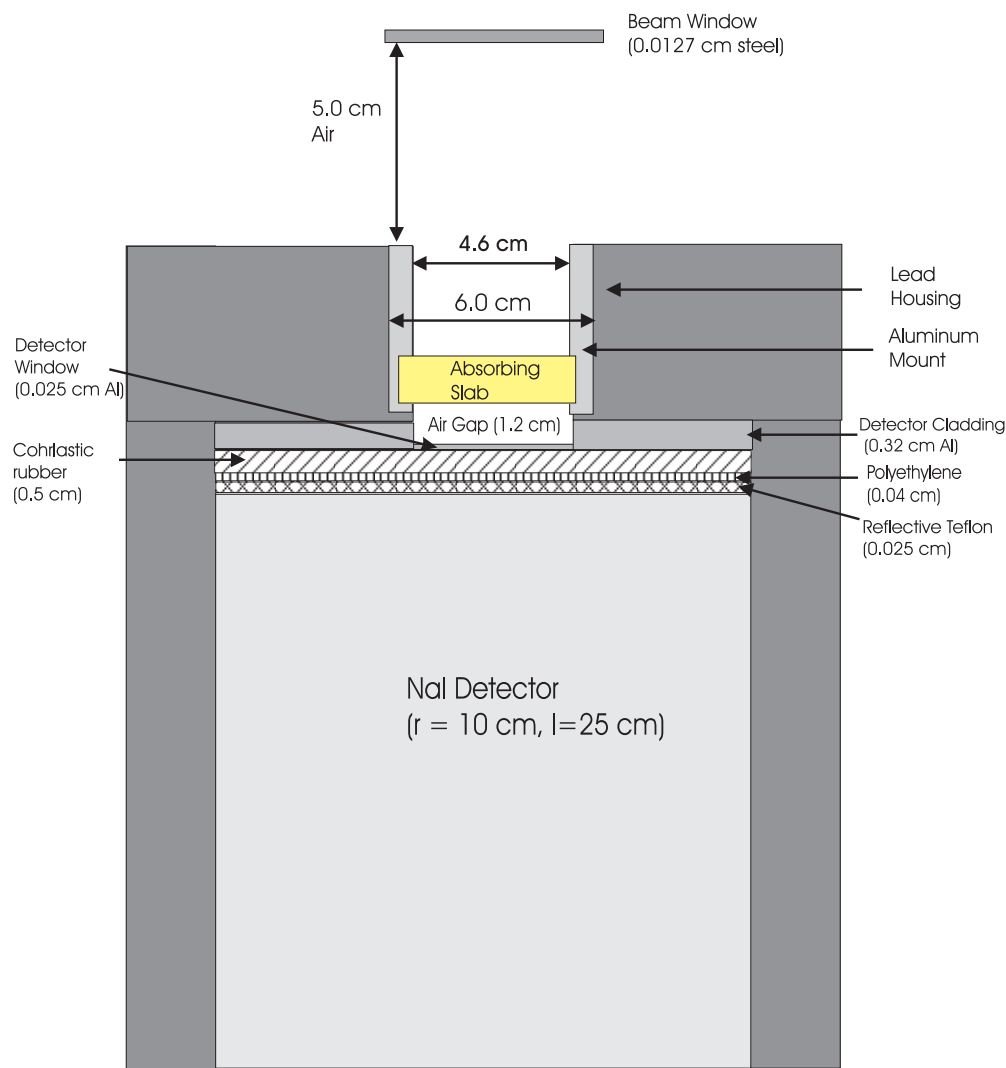


Figure 4.6: Schematic cross section of the large NaI detector used in the electron measurements. The back portion of the crystal and housing have been omitted.

### 4.3 Sensitivity to Measurement Geometry

Accurate measurement of the energy offset relies on Monte Carlo simulations to predict the energy lost in an absorbing disk. If a significant fraction of the electron energy is lost elsewhere, say in the absorber holder or detector cladding, an erroneous measurement may result. This raises the issue of sensitivity to experimental geometry. Specifically, three components of the geometry are of concern: the beam radius, the separation between the beam exit window and the absorbing slab, and the separation between the absorber and the NaI detector.

Beam radius is important in the sense that a large beam could have a significant fraction of its electrons miss the target due to scattering in the accelerator exit window, or miss the detector window due to scattering in the target. This could lead to particles entering the detector from the lead housing, aluminum holder, or detector cladding, distorting the electron spectrum. DOSRZ simulations were run for 10 and 20 MeV electrons incident on targets of graphite, aluminum, copper, and tantalum. For each case, the beam size was varied from 1 mm radius to 3 cm radius (i.e. bigger than the absorbing slab or beam window). The resulting measured offset proved to be insensitive to the beam size. The reason for this can be seen in figures 4.7 and 4.8, which show the effects of beam size for 10 MeV electrons without an absorber, and with  $2.0 \text{ g cm}^{-2}$  tantalum in the beam. Increasing the beam radius impacts primarily on the lower energy part of the spectrum (i.e. more bremsstrahlung photons due to interactions in the absorber mount and lead housing). Since the energy offset measurements depend on the peak and leading edge of the spectrum, the results are unchanged, even for unrealistically large beam sizes. As the detector housing is moved away from the beam window, the fraction of primary electrons which strike the absorber decreases. Therefore, the importance of contributions from the detector housing and absorber mount increases. DOSRZ simulations at 10 and 20 MeV, however, reveal that the measured stopping power is independent of linac - detector separation from 0.1 cm to 10 cm. This is not surprising, since both the detector mount and lead shielding are sufficiently thick to totally stop any electron striking them. Photons generated in these regions will be of lower energy than the main electron peak, and therefore have no effect on the measured peak offset.

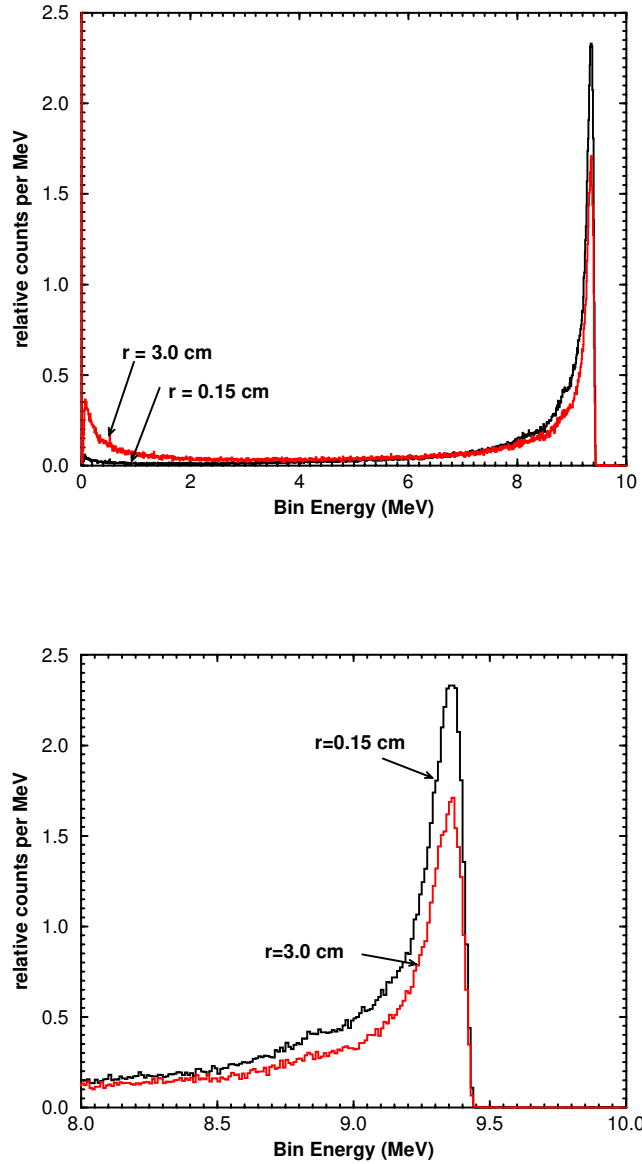


Figure 4.7: Effect of beam radius on no-absorber spectra for 10 MeV electrons. A larger beam radius results in a more pronounced low energy component (top), but the peak is largely insensitive to the beam size used in the simulation (bottom).

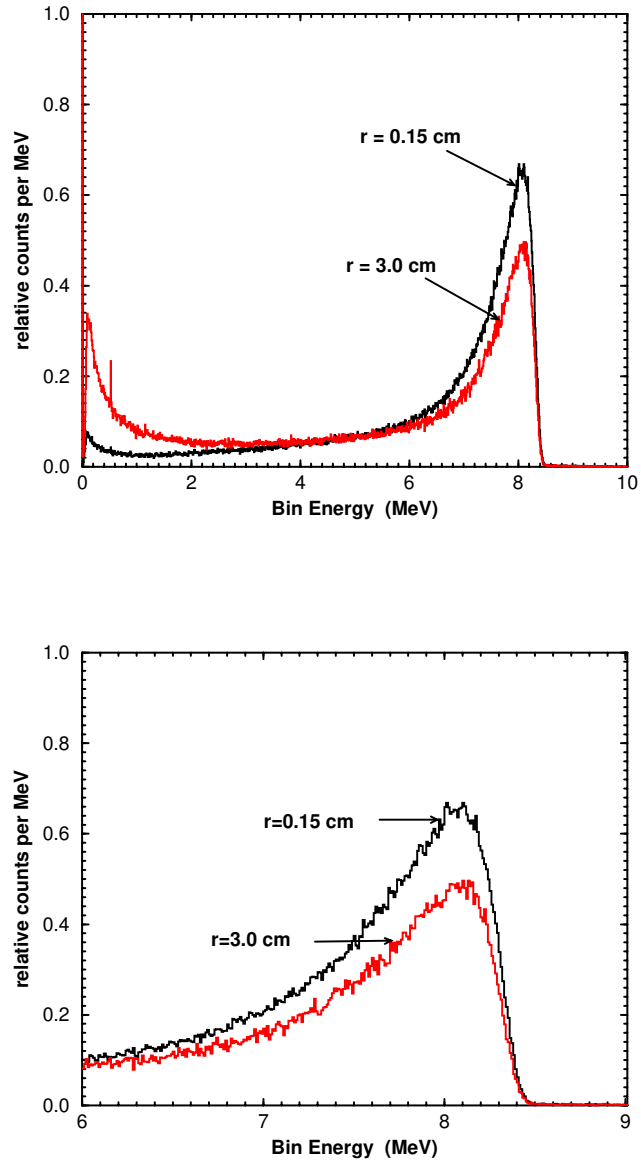


Figure 4.8: Effect of beam radius on the simulation of 10 MeV electrons traversing  $1 \text{ g cm}^{-2}$  copper. There is an increase in low energy photons due to interactions in the holder and lead housing (top), and the peak is less sharply defined, but unchanged in terms of energy (bottom). The positron annihilation peak (511 keV) seen on the 3 cm spectrum originates in the lead housing, and so is absent from the narrow beam spectrum.

The most important geometrical consideration is the separation between the absorbing slab and the window of the NaI detector. Simulations were performed for holder-detector separations ranging from 0.1 cm to 3 cm (corresponding to slab-detector separations of 0.6 to 3.5 cm). For a 10 MeV beam the measured offset did not change, provided that only the peak and leading edge of the spectrum were included in the fit. If lower energy regions were included for large separations, the quality of the fit was poor. This is because a large fraction of the emergent electrons strike the detector cladding rather than the detector window. This extra 3 mm of aluminum resulted in an additional 1 MeV energy loss, causing an extraneous peak to appear below the main absorber peak (figure 4.9). During measurements, the detector-holder separation is normally 1.2 cm, which should have no effect on the energy loss measurements.

Ultimately, the energy shift measurements are relatively insensitive to geometrical considerations provided the peak and leading edge of the spectrum are used in the fit. However, the Monte Carlo simulations should be able to adequately predict the whole spectrum, provided that proper values of beam radius, detector position and so on are provided. Figure 4.10 shows the spectrum resulting when  $1.0 \text{ g cm}^{-2}$  copper is placed in a 10 MeV electron beam. Superimposed is the fit Monte Carlo spectrum which was calculated using the measured beam size (0.3 cm), beam-detector, and slab-detector separations. The agreement is excellent ( $\chi^2/\nu=1.017$ ).

## 4.4 Measurement of Electron Spectra

The National Research Council (NRC) electron linear accelerator was operated at a nominal pulse repetition rate of 240 Hz and an approximate pulse width of  $2 \mu\text{s}$ . The average beam current was one electron every fourth beam pulse. The NaI crystal was positioned so that its lead housing was within 5 cm of the steel exit window of the linear accelerator's magnetic spectrometer (beam-detector distance of 10 cm). The pulses from the detector were amplified by a linear amplifier (EG&G Ortec 572) and stored in a PC/MCA (Canberra S100) through an analog to digital converter (Canberra 8701).

Events due to background radiation were further reduced by gating the readout of the

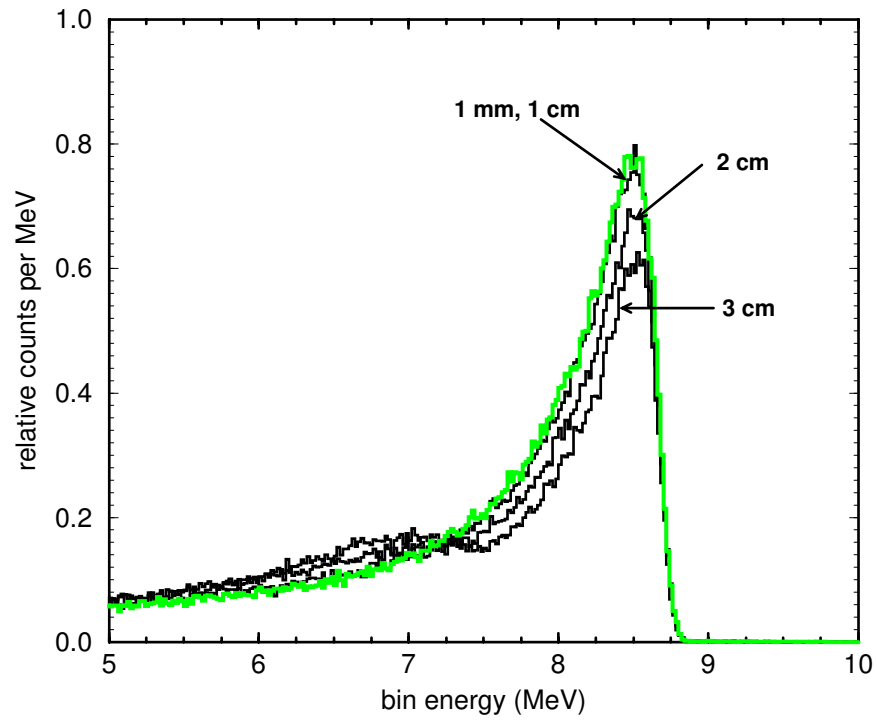


Figure 4.9: Effect of slab-detector separation on the simulation of 10 MeV electrons traversing  $1 \text{ g cm}^{-2}$  Cu. An additional peak, due to energy loss in the detector cladding, is evident for larger separations.

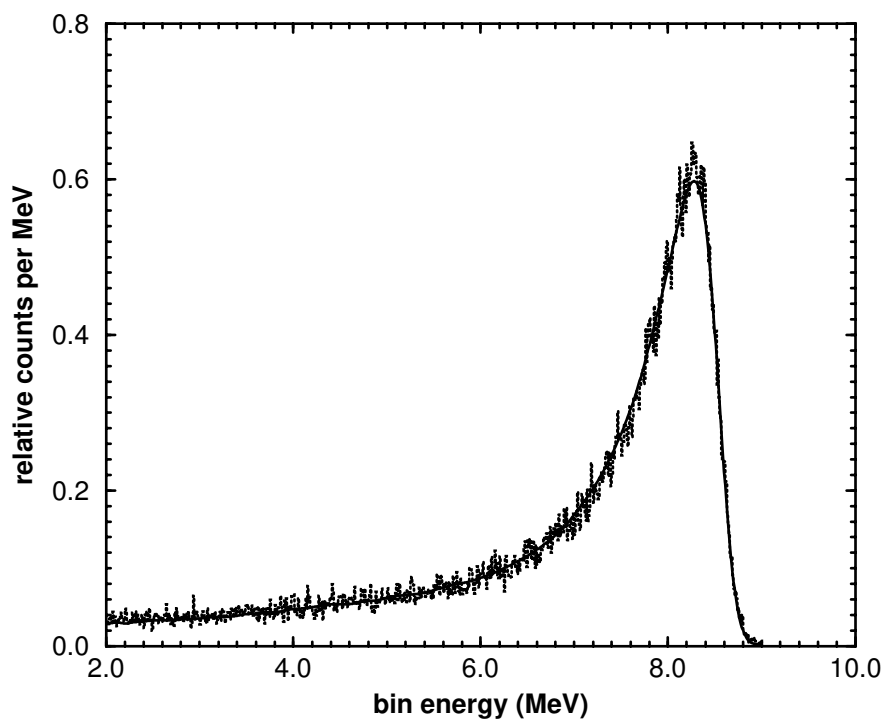


Figure 4.10: Example of fitting a simulated spectrum (smooth line) to the measured spectrum (histogram) over the entire energy range for 10 MeV electrons incident on  $1.0 \text{ g cm}^{-2} \text{ Cu}$ . The chi-square per degree of freedom is 1.017 ( $P = 0.63$ ).



ADC on the linac beam triggers. Random summing of nearly-coincident pulses, known as pulse pile-up, was reduced using the following technique. The anode signal from each pulse was input to a discriminator which began a fast timer. If another anode pulse was detected within  $10\ \mu\text{s}$  of the first pulse, that beam pulse was labeled as a pile-up event. A pulse was accepted by the ADC only if the following conditions were satisfied: a beam trigger was supplied, an event was detected in the NaI detector (anode discriminator triggered), and no pile-up events were detected.

The mean energy of the electron beam was determined to within 0.3% using a magnetic spectrometer which was specifically built for the National Research Council (NRC) linear accelerator (Chapter 3 or [73]). Once the electron energy was established, the magnet was set to zero field and the beam directed into the NaI detector for spectroscopy measurements (figure 4.11).

## 4.5 Gain Stabilization

Photomultiplier tube gain drift is a well documented phenomenon (see e.g. [74], [75]). Furthermore, there is a mild temperature dependence for the light output from NaI detectors [76]. Accurate measurements of peak shift required that the photomultiplier tube drift, which was measured to be as large as 3%, along with the NaI response, be controlled to better than 0.1%. The gain of the spectrometer system was held constant by placing a  $^{60}\text{Co}$  source approximately 40 cm upstream of the detector window. This kept the count rate sufficiently low that pile-up with the electrons could be adequately controlled by the pile-up rejection circuitry (since the ADC readout was gated on triggers from the linear accelerator, only one  $^{60}\text{Co}$  photon was detected for every 20 electrons). The  $^{60}\text{Co}$  signal was amplified on a separate channel and monitored using a separate MCA (Canberra Series 90) and ADC (Canberra 8076). The output from the ADC also was directed to a Gain Stabilization Unit (Canberra 8200) which automatically adjusted the high voltage (HV) supplied to the photomultiplier tube to compensate for apparent drifts in the 1.33 MeV photopeak. A schematic of the gain stabilization and spectroscopy components is shown in figure 4.12. Adjustments of  $\pm 0.3\%$  were observed over a time scale of several minutes, but the mean gain was controlled

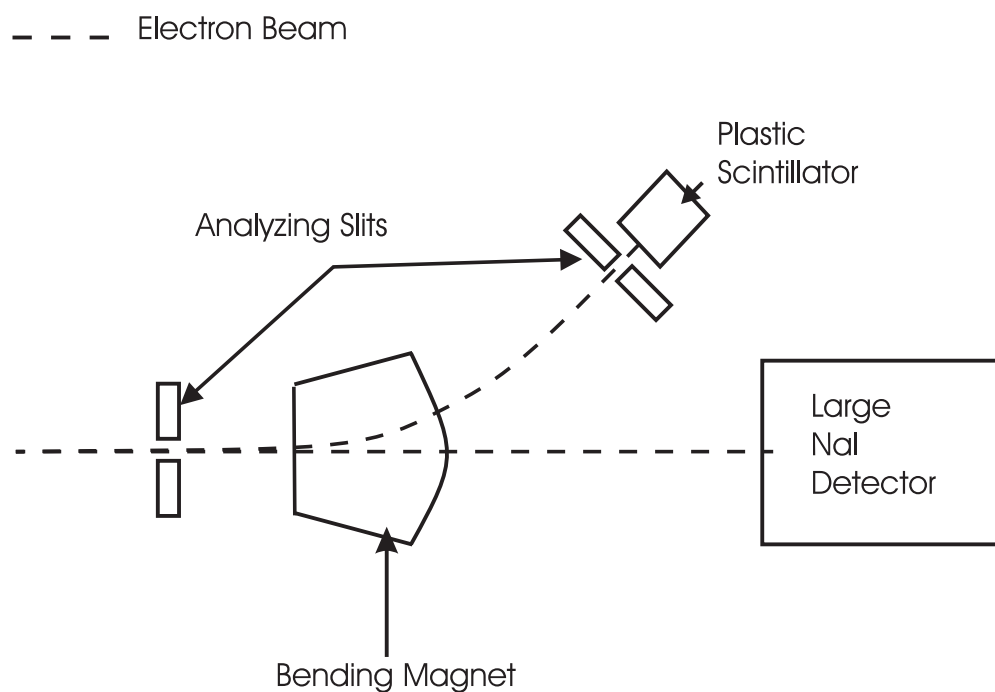


Figure 4.11: Schematic of the electron spectrum measurement geometry. A  $45^\circ$  magnetic spectrometer is used to determine the electron beam energy to within 0.3%. The magnet is then set to zero field and the beam passed into the large NaI detector. For simplicity, the beam pipes and magnet vacuum box are omitted.

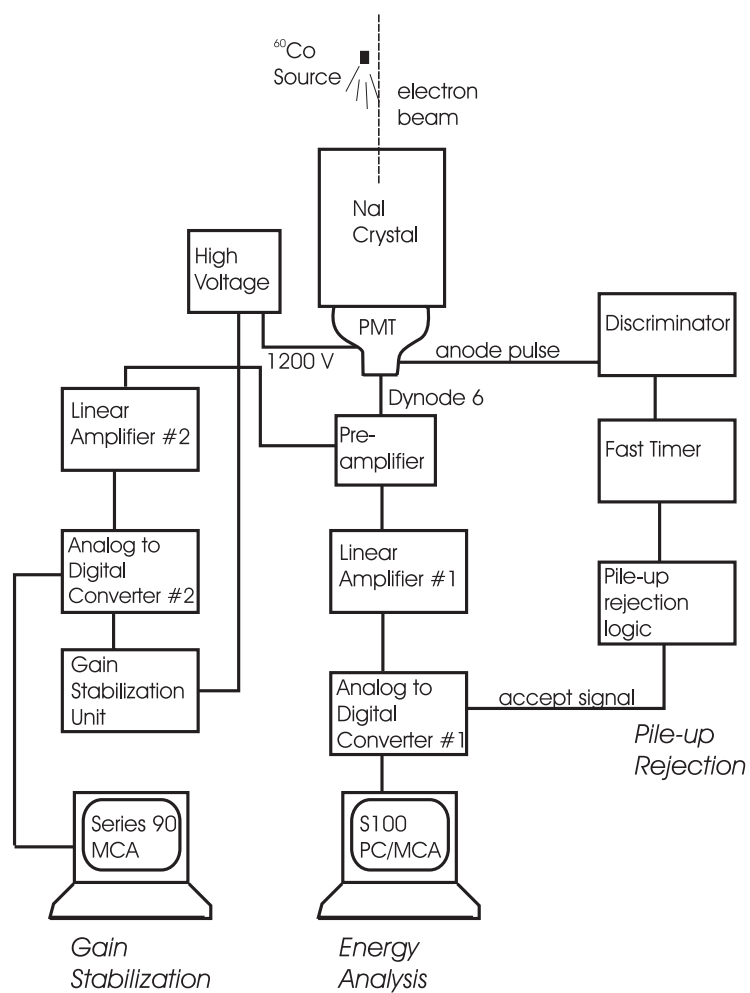


Figure 4.12: Schematic of components used for spectroscopy and gain stabilization.

to within 0.03% over any measurement day (see figure 4.13).

The electronic gain of the stabilization components was monitored using a precision pulser input to the pre-amplifier, with a reference voltage kept constant to one part in 30000, and was found to be constant within 0.03% over the course of a given measurement day.

The changes in electronic offset (so called “zero drifts”) and electronic gain of the energy analysis components were monitored by supplying precision electronic pulses from a BNC pulser to the detector preamplifier. The amplitudes of the electronic pulses were determined by the output of an Aston digital to analog converter (DAC). Linear regression of pulse voltage versus channel number revealed that the offset was constant within a fraction of a channel over several days, while the electronic gain did not change more than  $\pm 0.01\%$ .

The overall performance of the gain stabilization technique is illustrated in figures 4.14 and 4.15. In each figure, the electronic gain of the stabilization components, as determined *via* precision electronic pulser, is plotted for several measured spectra. Also shown is the incident electron energy (determined by magnetic spectrometry) and the response of the NaI detector to each electron spectrum. All points are normalized to the value at the first measurement. For the 15 MeV data, the incident electron energy and electronic gain are constant to within 0.05%, while the response of the detector is generally constant to within 0.1%, except for occasional 0.15% excursions from the mean value. This can be explained by re-examining figure 4.13, which shows occasionally large corrections over a time scale of several minutes. Since the spectra are acquired for 20 minutes, the gain drift correction may be incomplete. To work around this problem, any absorber measurements were “bracketed” with no-absorber measurements, and the average response determined to better than 0.05%. The 25 MeV results show similar behavior, except that there is an apparent 0.2% change in incident electron energy. Fortunately, this change is mirrored in the response of the NaI detector. In general, we conclude that the gain is stable to within 0.1%.

## 4.6 Detector Response

The initial energy calibration of the electron spectra was determined using the 4.439 MeV  $\gamma$ -line of an americium-beryllium neutron capture source. The final energy calibration and

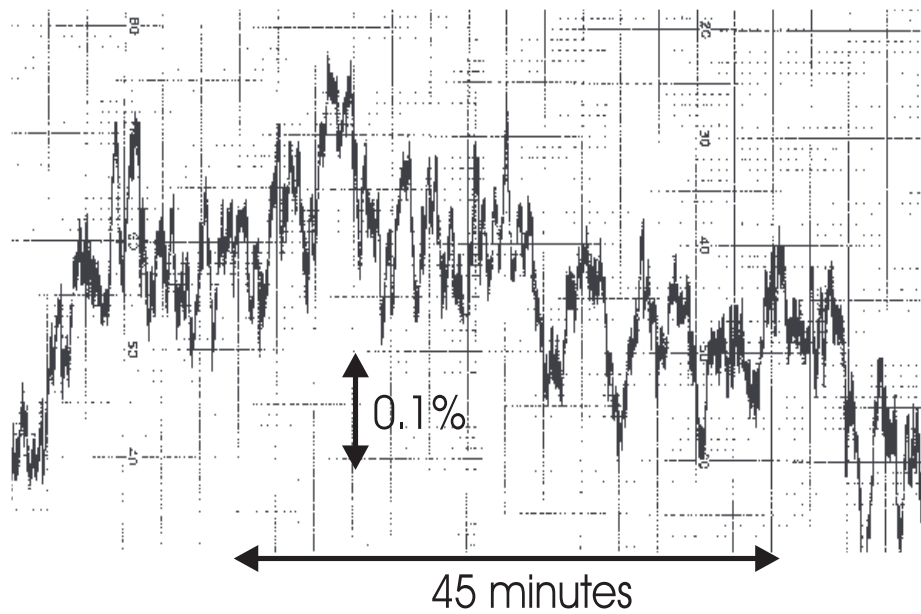


Figure 4.13: Typical performance of the gain stabilization unit. The response is characterized by rapid 0.1% fluctuations about the mean value, which varies more slowly. In this example, a correction to the gain of nearly 0.3% has been applied over the course of an hour.

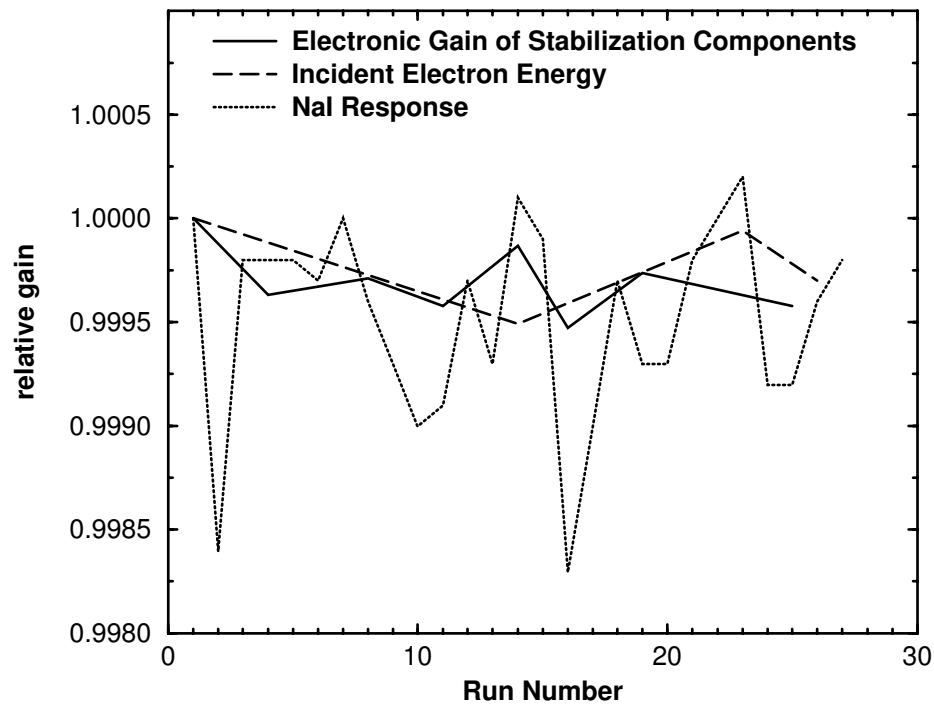


Figure 4.14: Gain stabilization summary at 15 MeV. The incident energy and electronic gain are constant to within 0.05%, and the response of the NaI detector is constant to within 0.1% except for occasional 0.15% excursions attributed to partial gain correction over the acquisition time (20 minutes).

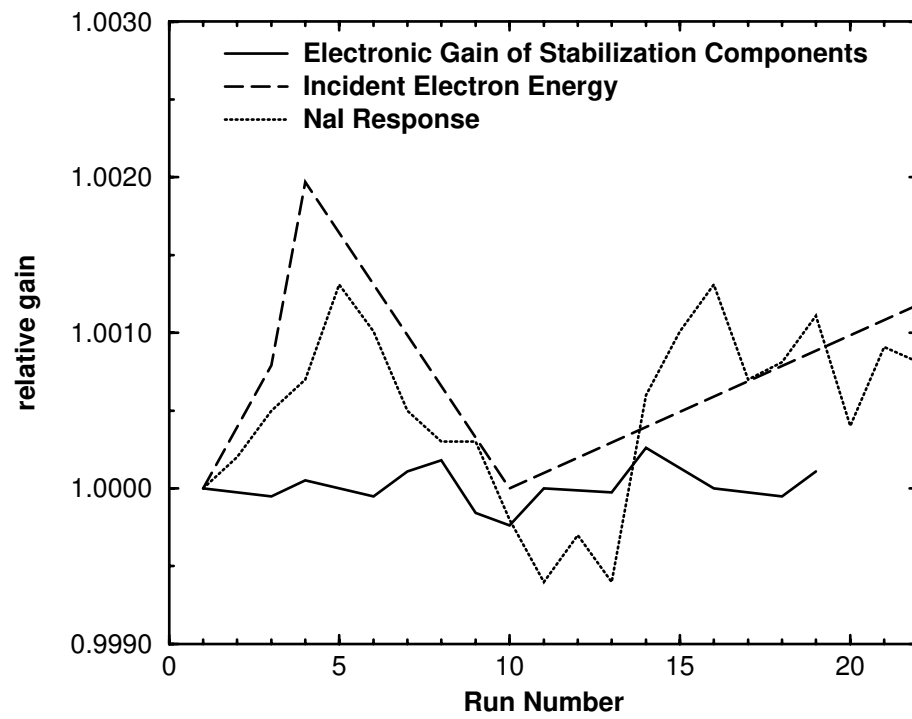


Figure 4.15: Gain stabilization summary at 25 MeV. The response of the NaI detector tracks the 0.2% change in incident electron energy to within 0.1%.

extraction of measured stopping powers relied on fitting the Monte Carlo calculated spectra to the measured electron spectra. The technique was demonstrated by Faddegon *et al* [42]. The details are reiterated here.

The EGS4 user code DOSRZ was used to predict the pulse height spectrum in the NaI detector. The true electron energy, as determined by magnetic spectrometry, was used as the initial energy in the simulation. The experimental geometry was modeled faithfully, including accelerator window, detector window, aluminum cladding, lead shielding, and surrounding air. For the no-absorber spectra, the Monte Carlo calculated pulse height distributions were broadened to account for detector response. The energy axis was scaled and the spectrum normalized to obtain the smallest  $\chi^2$  deviation with respect to the measured data. The full width at half maximum of the broadening function appears to vary linearly in energy (figure 4.16), although from the literature [43] the following functional form for the FWHM of the response function is expected:

$$\Gamma_G = \beta_1 \left( \frac{E}{E_{\text{ref}}} \right)^n, \quad (4.1)$$

where  $\beta_1$  is a broadening parameter with units of energy and is determined from fits of the no-absorber spectra.  $E_{\text{ref}}$  is a reference energy, and  $n$  is a dimensionless constant. For this set of measurements,

$$\Gamma_G = 0.064(E)^{0.64}, \quad (4.2)$$

was determined by fitting equation 4.1 to the FWHM determined for no-absorber electron spectra at 5, 7, 10, 15, 20, 25, and 30 MeV ( $E_{\text{ref}} = 1.0$  MeV) (figure 4.16). This is consistent with earlier results [44].

Each measured spectrum was rebinned into 10 keV bins for ease of analysis. The rebinning was based on the position of the Am-Be  $\gamma$  line and the measured electronic offset. The measured spectrum was then fit to the broadened Monte Carlo spectrum, and the gain was allowed to vary to get the minimum  $\chi^2$  compared to the calculated spectrum so that the calibrated no-absorber energy scale is given by:

$$E = \beta_2 C, \quad (4.3)$$

where  $C$  is the bin number. This assumes complete linearity and no energy offsets in the detector response, conditions which may not be satisfied. However, when the *local* energy



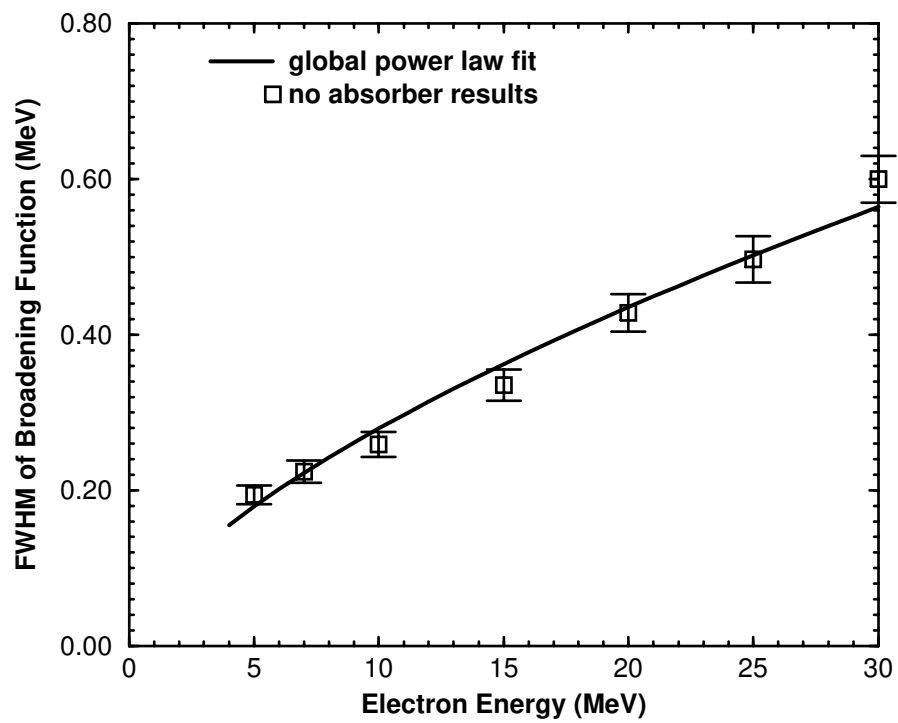


Figure 4.16: The global broadening function for the measured electron spectra is determined by a power law fit to the FWHM of measured no-absorber spectra.

response is determined at each incident energy, then the *global* response curve can be determined by fitting the apparent bin number,  $E/\beta_2(E)$ , as a function of incident energy  $E$ , to give

$$C = a + bE + cE^2. \quad (4.4)$$

where  $a = -38 \pm 5$ ,  $b = 103.3 \pm 0.4 \text{ MeV}^{-1}$ , and  $c = -0.051 \pm 0.01 \text{ MeV}^{-2}$ . Two important features of the NaI response stand out: 1) the presence of a 38 bin (360 keV) energy offset and 2) a mild energy non-linearity. Of these, the offset is most important and will be discussed first.

### 4.6.1 Detector Window

The NaI detector was designed to have a thin window of 0.025 cm aluminum for the electron work, so as to minimally perturb the incoming spectrum. As such, the packing sponge shown in figure 4.6 was to have been cut out. However, the energy offset shown by equation 4.4 is entirely consistent with the energy loss expected in this sponge layer. The presence of the packing sponge was verified by the following photon attenuation measurements.

Calibrated sources of  $^{109}\text{Cd}$  and  $^{241}\text{Am}$  were obtained, whose  $4\pi$  emission rates were known to within 2%<sup>1</sup>. Each source was sandwiched between thin mylar sheets, and the source diameters were less than 3 mm. The packing sponge was made of cohrlastic foam, which is a type of silicone rubber. Photon cross sections were generated using the PEGS4 program [77]. The  $^{109}\text{Cd}$  emits several x-rays in the 22 to 25 keV energy range, but due to the relatively poor resolution of the NaI detector, these appear as a single 22 keV peak. This 22 keV photopeak would be much more strongly attenuated than the 59.4 keV photopeak of the  $^{241}\text{Am}$  source. At a given measurement distance, the count rate from the  $^{109}\text{Cd}$  source,  $I_{\text{Cd}}$  would be:

$$I_{\text{Cd}} = I_{\text{o,Cd}} \Omega' e^{-\mu(22)t_{\text{win}}} e^{-\mu(22)t_{\text{sponge}}}, \quad (4.5)$$

where  $I_{\text{o,Cd}}$  is the  $4\pi$  emission rate of the  $^{109}\text{Cd}$  source,  $\Omega'$  is the fractional solid angle subtended by the detector window,  $e^{-\mu(22)t_{\text{win}}}$  is the attenuation in the aluminum window and reflective teflon backing at 22 keV, and  $e^{-\mu(22)t_{\text{sponge}}}$  is the attenuation in the packing

---

<sup>1</sup>The author is grateful to Dr. Dallas Santry of the National Research Council for his assistance in providing calibrated photon sources.

sponge (if present). Similarly, for the  $^{241}\text{Am}$  source,

$$I_{\text{Am}} = I_{\text{O,Am}} \Omega' e^{-\mu(59)t_{\text{win}}} e^{-\mu(59)t_{\text{sponge}}}. \quad (4.6)$$

If the sources are placed in the same location, then the ratio of these equations is:

$$\frac{I_{\text{Cd}}}{I_{\text{Am}}} = \frac{I_{\text{O,Cd}} e^{-\mu(22)t_{\text{win}}} e^{-\mu(22)t_{\text{sponge}}}}{I_{\text{O,Am}} e^{-\mu(59)t_{\text{win}}} e^{-\mu(59)t_{\text{sponge}}}}. \quad (4.7)$$

In the absence of the sponge, this ratio is calculated to be 1.10; with the sponge it is 0.90. Measurements were performed at source-detector distances of 20 and 30 cm. At 20 cm, the ratio of count rates was  $0.92 \pm 0.02$ , and at 30 cm, the ratio was  $0.91 \pm 0.02$ , confirming the presence of the packing sponge.

Excluding the sponge in the Monte Carlo simulations leads to poor fits for spectra where absorbing disks are present in the beam, as the extra path length and energy straggling are not accounted for. The quality of the fits can be improved by allowing the broadening to vary in each case. However, when this is done the broadening appears to depend on absorber thickness, especially for high Z materials (figure 4.17). Moreover, there is a mild coupling between the offset and the broadening, so that artificial offsets appear if the change in broadening with respect to the no-absorber case is large. Including the sponge in the simulation gives the correct straggling, and equation 4.2 gives acceptable fits (figure 4.18).

The presence of the packing sponge is supported by the global electron energy calibration, the consistency in broadening for all absorbers, and by an independent photon attenuation measurement. Furthermore, the manufacturer was unable to confirm that the sponge had been removed. For these reasons it was included in all simulations.

### 4.6.2 Detector Non-linearity

When the sponge is included in the no-absorber simulations, the energy response of the detector is given by

$$C = a + bE + cE^2, \quad (4.8)$$

where  $a = 3.5 \pm 3$ ,  $b = 103.1 \pm 0.4 \text{ MeV}^{-1}$ ,  $c = -0.0485 \pm 0.01 \text{ MeV}^{-2}$ , and all energies are expressed in MeV. The small offset may indicate a residual error in the energy lost in the window materials, but is essentially zero within its 3 bin uncertainty. This offset plays no

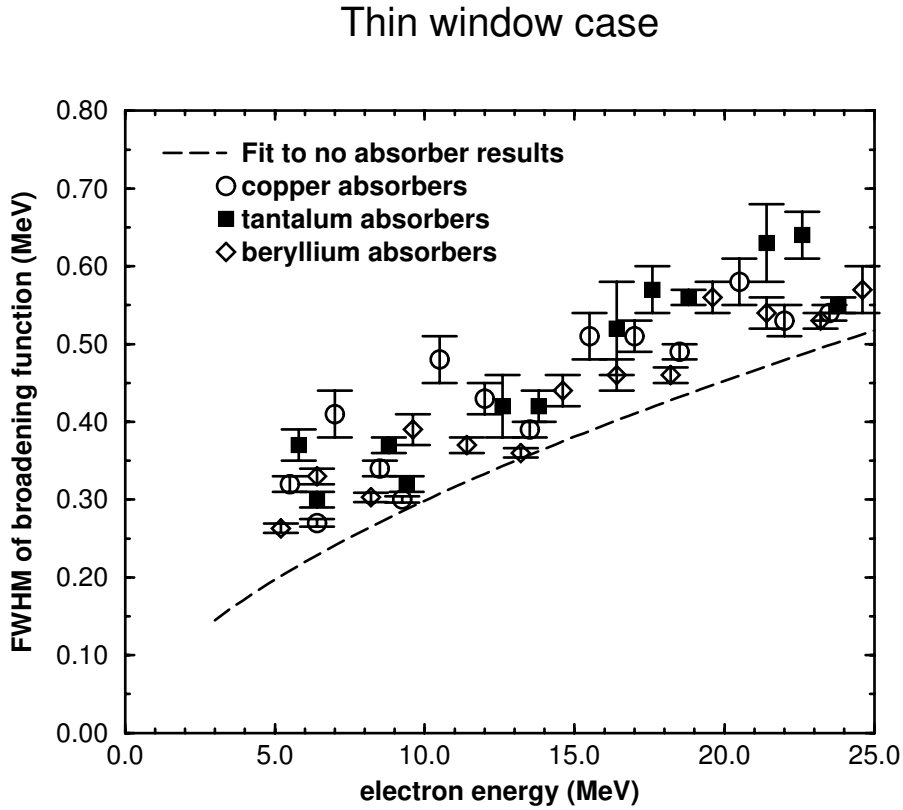


Figure 4.17: Ignoring the sponge in the simulations results in FWHM which appear to depend on atomic number and absorber thickness. Here the fit to no-absorber results refers to simulations without the sponge, and is not the same as in figure 4.18 or equation 4.2.

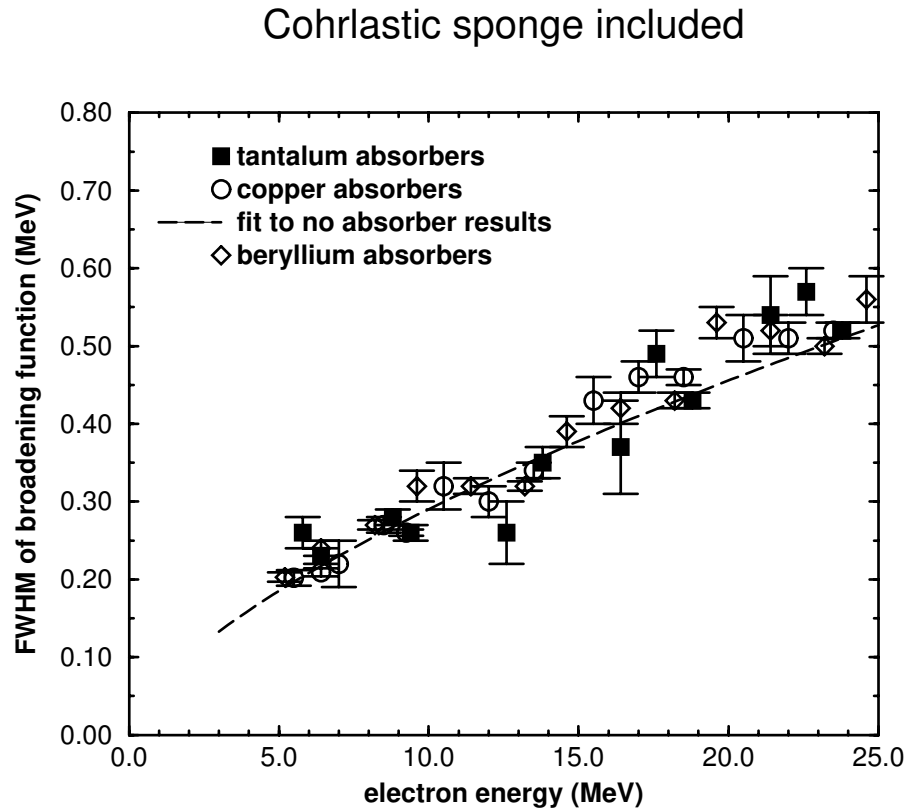


Figure 4.18: Including the packing sponge in the simulations means that the broadening is independent of absorber or thickness. Here the no-absorber fit is the same as in figure 4.18 and equation 4.2.

role in the local calibration (the derivative of equation 4.8). Note that the nonlinearity in  $E$  remains, and is consistent with that seen in equation 4.4. The source of this non-linearity will now be investigated.

Photomultiplier tubes are known to respond non-linearly under certain conditions of large pulse amplitudes or high count rates [78]. Linearity of the photomultiplier tube has been established using a precision light pulser (BNC Model 6000) mounted at the base of the NaI crystal. The output of the Aston DAC was used as the reference voltage for the light pulser. Both the pulser and ADC readout were gated in order to reduce signals due to background radiation events in the detector. Pulse intensities simulating 2-50 MeV events were used, at count rates of 100 and 1000 counts per second. Plotting light pulser reference voltage versus channel centroid reveals that the photomultiplier tube responds linearly within 0.1% over the entire simulated energy range, so the photomultiplier tube must be ruled out as the source of the non-linearity.

Another explanation is that the relative response of the detector varies with depth. We assume that the observed pulse height for a given energy deposited in the detector depends on the location of the interaction, and this dependence can be described by a function  $r(z)$ . We make the approximation that electrons deposit their energy continuously, so the increment in pulse height  $P$  as an electron moves from  $z$  to  $z + dz$  in the detector would be

$$\delta P = S_{\text{NaI}} r(z) dz, \quad (4.9)$$

where  $S_{\text{NaI}}$  is the stopping power in NaI. For an electron of energy  $E_o$ , the total pulse height would be

$$P = S_{\text{NaI}} \int_0^{z_{\text{max}}} r(z) dz, \quad (4.10)$$

where  $z_{\text{max}} = E_o/S_{\text{NaI}}$  is the maximum depth of penetration in the detector (here multiple scattering and secondary particles are ignored). If the response were constant, i.e.  $r(z) = a$ , then

$$P = S_{\text{NaI}} a z_{\text{max}} = a E_o, \quad (4.11)$$

i.e., the pulse height is linearly proportional to energy deposited. Now consider the case where the response varies linearly with depth in the detector, i.e.  $r(z) = a + bz$ . In this

case

$$P = S_{\text{NaI}} \left[ az + \frac{bz^2}{2} \right]_0^{z_{\text{max}}} = aE_o + b'E_o^2, \quad (4.12)$$

where  $b' = b/2S_{\text{NaI}}$ . So a linear dependence of pulse height with depth would result in a quadratic response for electron beams as seen in equation 4.8.

The relative response along the axis of the detector was measured using a  $^{60}\text{Co}$  source. The detector was enclosed in a lead castle to provide shielding from background radiation, and the  $^{60}\text{Co}$  source was sandwiched between lead bricks so that a 5 mm “slice” of the detector response was taken at each depth (figure 4.19). The centroids of the 1.17 and 1.33 MeV photopeaks were determined at each position, and found to decrease with depth (figure 4.20). If the response is normalized to the response at 1 cm, the relative response  $r'(z)$  is given by

$$r'(z) = 1.004 - 0.0038z. \quad (4.13)$$

If we assume that the  $S_{\text{NaI}} \approx 7 \text{ MeV/cm}$ , then we can estimate  $b'$  to be 0.0003, which is comparable to the value of 0.0005 estimated from equation 4.8. It seems plausible, then, to attribute the observed non-linearity to a variation in detector response with depth.

## 4.7 Pulse Pile-up

If the separation time between consecutive pulses is less than the width of the anode pulse at the discriminator ( $\approx 200 \text{ ns}$ ), then the pulses will not be rejected by the pile-up rejection circuitry described in section 4.4. Usually this would not be a problem for electron spectra, since most of the electrons are located in the peak, and the pile-up events would have (to a first approximation) twice the energy of the single event peak. However, for lower energy electrons on thick, high atomic number targets, there are many more low energy photons compared to the full energy electron peak (since electrons which radiate photons have a lower chance of reaching the detector). This leads to a much “flatter” spectrum, with a large number of low energy counts due to photons. When these low energy counts pile up with the full energy peak, a significant distortion can result, and the quality of the fit is poor (figure 4.21). The problem was resolved using the pile-up correction routines for pulsed beam spectroscopy developed by Faddegon and implemented at NRC [79]. These routines

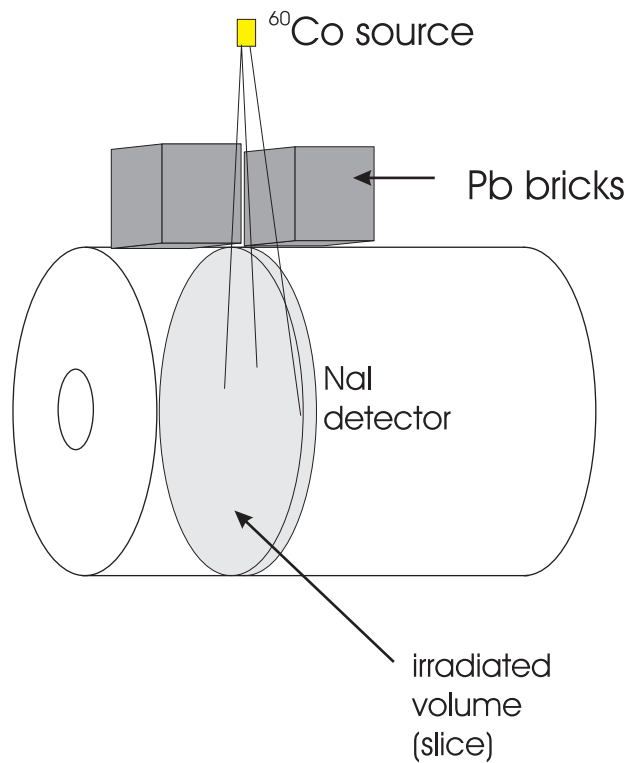


Figure 4.19: Schematic of geometry used to measure the axial response,  $r(z)$ , of the NaI detector. The lead shielding has been omitted.



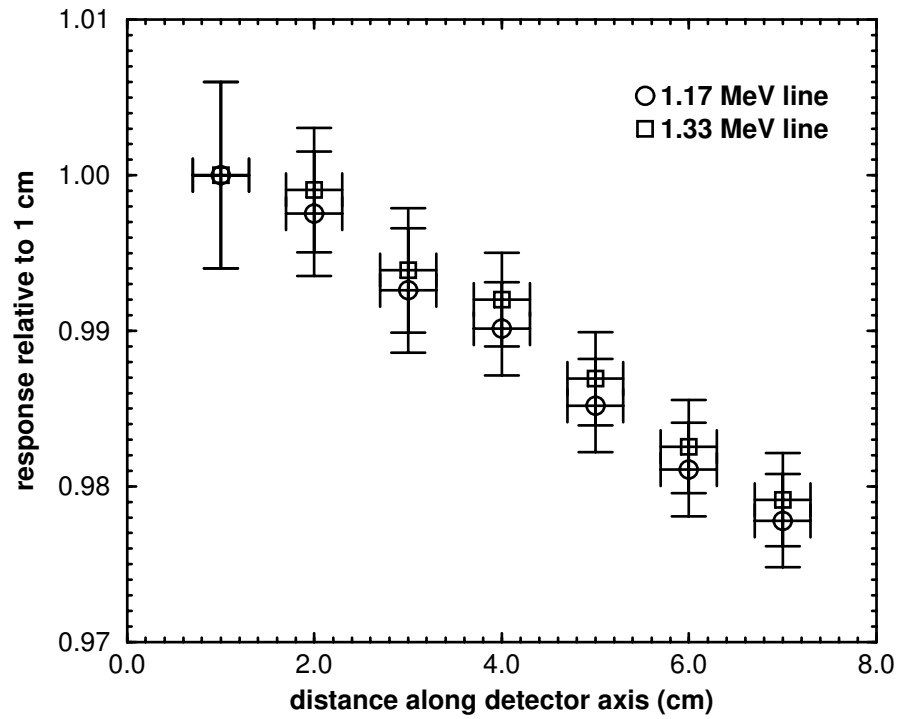


Figure 4.20: Relative response of NaI detector with depth as determined using a  $^{60}\text{Co}$  source. The response changes by 0.38% per cm, which may explain the non-linearity of energy response for electrons.

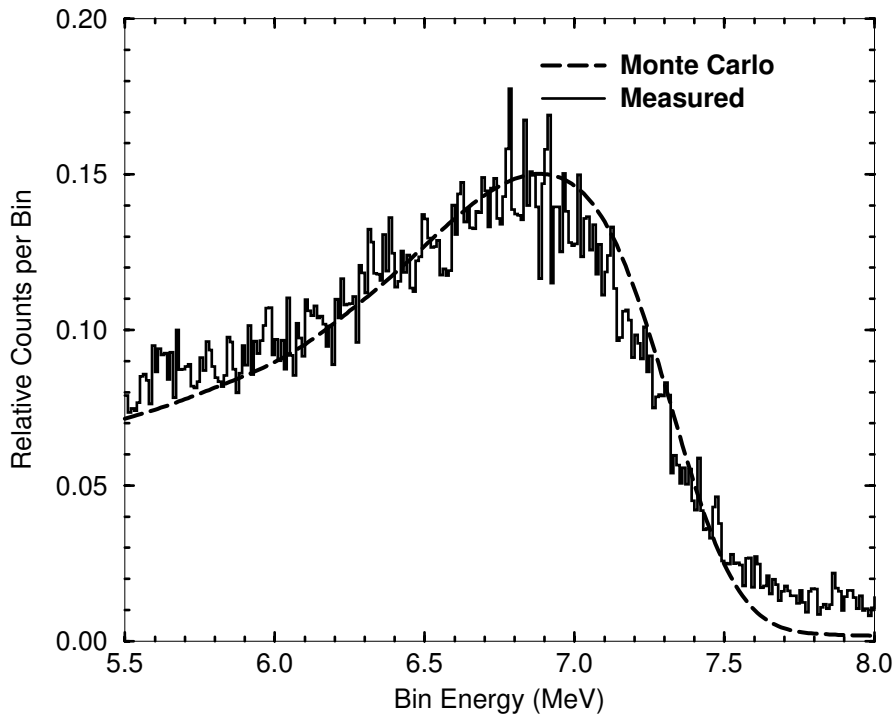


Figure 4.21: For low energy electrons incident on thick, high Z targets, there are many low energy photons which pile up with the full energy peak. The quality of the fit is poor ( $\chi^2$  per degree of freedom  $\approx 2.6$ ,  $P = 1.0$ ).

estimate the pile-up spectrum from the measured spectrum based on the pulse width, the event resolution time, and the mean event rate per pulse. The beam current per pulse is assumed to have structure, described by an “event-time distribution” (etd),  $\eta(t)$ , which is the probability of a count occurring between times  $t$  and  $t+dt$  in a pulse of width  $T$ . The etd is used to estimate the probability of detecting  $m$  events given  $n$  events within a given beam pulse,  $p_{m|n}$ . These conditional probabilities are used to estimate a pile-up spectrum from the measured spectrum using an iterative routine. The pile-up spectrum is then subtracted from the measured spectrum.

Figure 4.22 shows an etd measured at 10 MeV with a time-to-amplitude converter which measured the time between the start of the beam trigger and the detection of a pulse. The run time was 600 seconds. Note that the etd has a definite structure, with several spikes. These spikes have no discernible impact on the pile-up correction. Figure 4.23 shows estimated pile-up spectra for a 10 MeV beam incident on a  $0.5 \text{ g cm}^{-2}$  copper slab. The pile-up spectrum has been estimated using the measured etd (figure 4.22) and a flat etd (equal probability of detecting an event anywhere within a beam pulse). The iteration was performed four times. The pile-up spectra are very similar, and are indistinguishable in terms of stopping power measurements. For this reason, a flat etd was assumed for all pile-up corrections.

Figure 4.24 shows the results of a fit to a pile-up corrected spectrum for 10 MeV electrons on  $2.0 \text{ g cm}^{-2}$  copper. The quality of the fit is significantly improved compared with figure 4.21 ( $\chi^2_\nu \approx 0.93$ ,  $P = 0.22$ ).

### 4.7.1 Measurement of Low Energy Contamination

The stopping power measurement relies on a no-absorber spectrum to establish the energy scale, and an absorber spectrum to determine stopping power. If low energy photons generated elsewhere in the linear accelerator, say at the bending magnets, arrived coincident with electrons, they would pile-up and affect the energy calibration. The addition of an absorber could shield these photons, so that the energy scale for the energy loss measurements would not correspond to the no-absorber measurements, which could lead to errors in measured stopping power.

The low energy component of the spectrum was measured in the following manner. With

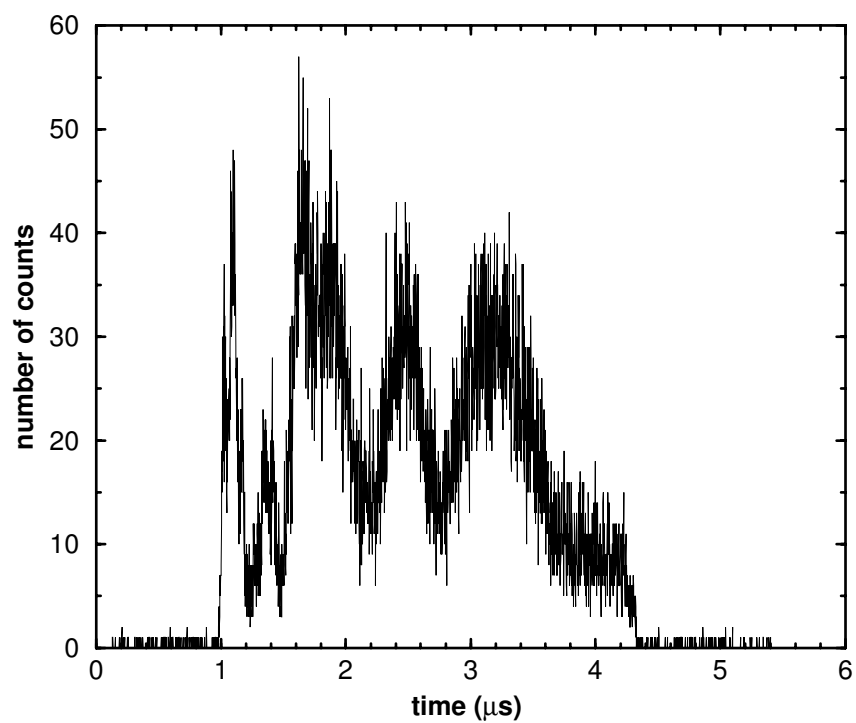


Figure 4.22: Measured event-time distribution at 10 MeV. There is significant structure within the beam pulse which has no effect on the pile-up corrections.

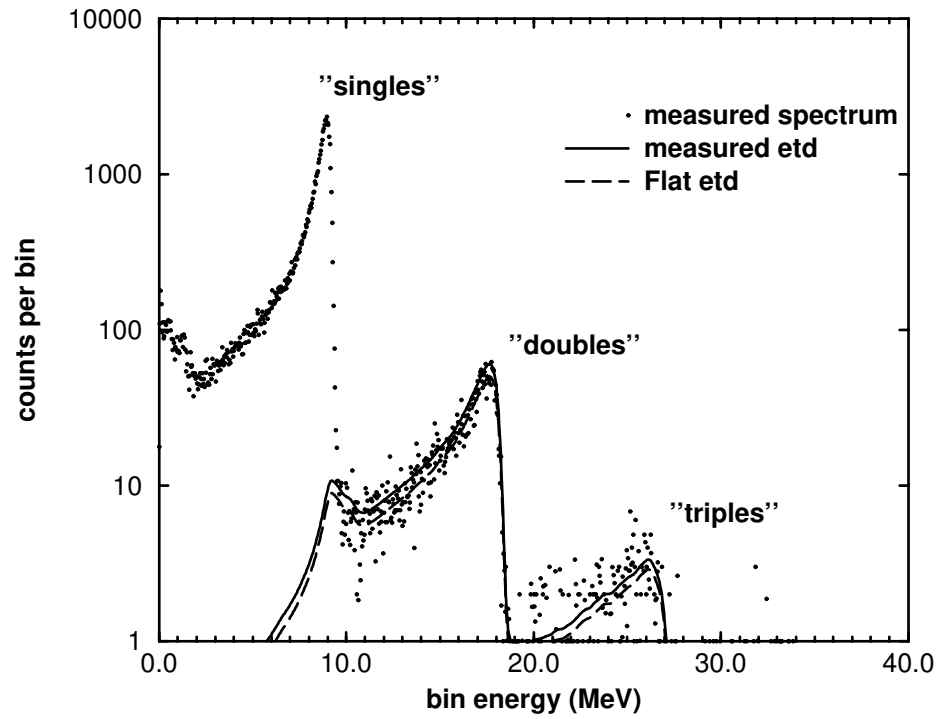


Figure 4.23: An example of pulse height estimation for 10 MeV electrons incident on 0.5 g cm<sup>-2</sup> copper. The pile-up spectrum for a flat etd (dashed line) closely resembles that estimated using the measured etd (solid line).

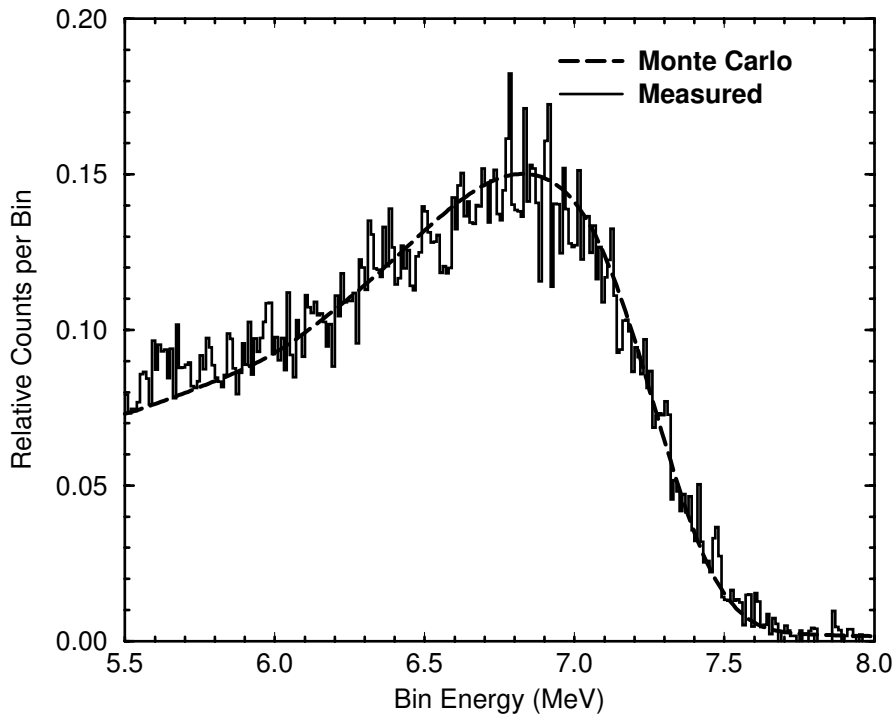


Figure 4.24: The pile-up corrected spectrum for 10 MeV on  $2 \text{ g cm}^{-2}$  copper gives a much better fit with the calculated spectrum compared to the uncorrected case (figure 4.21). The  $\chi^2$  per degree of freedom improves from 2.6 ( $P = 1.0$ ) to 0.93 ( $P = 0.22$ ).

the electron beam off, but ADC readout gated on beam triggers, the count rate from 0 to 1 MeV was monitored on the Series 90 MCA. The electron beam was then deflected away from the detector using the magnetic spectrometer (figure 4.11), and the low energy count rate measured again. No difference in low energy count rate was observed.

### 4.7.2 Modulator Noise

Electronic noise from the modulator tank of the linear accelerator appears as a 22 mV offset at the input to the ADC used for energy analysis. The electron pulses arrived at the ADC coincident with the modulator noise. This introduced a four channel electronic offset to the measured spectra which was subtracted before analysis.

## 4.8 Conclusions

The accurate measurement of electron energy spectra using a large NaI detector has been described. The NaI detector was chosen over high purity germanium (HPGe) detectors largely because its larger size lessens its sensitivity to radiative processes and extends the energy range over which useful measurements can be made. An HPGe detector may still be useful for energy loss measurements where photon losses are unimportant, i.e. low electron energy on thin, low atomic number absorbers.

The energy loss measurements have been shown to be insensitive to geometrical considerations such as incident beam radius, linac-absorber separation, and absorber-detector separation.

Gain drifts have been reduced from nearly 3% to less than 0.1% by gain stabilization on the 1.33 MeV photopeak of a  $^{60}\text{Co}$  source.

The energy calibration of the NaI spectrometer was established using a magnetic spectrometer to determine the incident electron energy to within 0.3%. This energy was used in a Monte Carlo simulation of the detector and its surrounding materials to predict the pulse height distribution inside the NaI crystal. A gain parameter was determined at each energy by fitting a measured spectrum to the broadened Monte Carlo spectrum. The global energy response was determined from a fit to the response at all energies. This revealed a mild

energy non-linearity which has been attributed to a measured change in response along the axis of the spectrometer.

The presence of extra window material, attributed to rubber packing, was revealed by an offset term in the global energy response and confirmed by photon attenuation measurements at 22 and 59.4 keV using calibrated sources of  $^{109}\text{Cd}$  and  $^{241}\text{Am}$ . Inclusion of this extra material in the Monte Carlo simulations is required to predict the proper straggling distributions in the transmitted electron spectra.

Pulse pile-up corrections are required for thick, high atomic number absorbers at low energies where low energy photons can distort the shape of the spectrum. Pile-up was removed from the measured spectra using the pile-up corrections for pulsed-beam spectroscopy developed by Faddegon.



# Chapter 5

## Accurate Measurements of the Collision Stopping Powers for 5 to 30 MeV Electrons

### 5.1 Introduction

In Chapter 2, it was proposed that the electron mass collision stopping power,  $(S/\rho)_{\text{col}}$ , could be expressed as

$$\left(\frac{S}{\rho}\right)_{\text{col}} = \left(\frac{S}{\rho}\right)_{\text{ICRU}} + \kappa, \quad (5.1)$$

where  $(S/\rho)_{\text{ICRU}}$  is the theoretical mass collision stopping power, as tabulated in ICRU 37, and  $\kappa$  is an additive correction which accounts for errors in the theoretical stopping powers.  $\kappa$  can be determined as follows.

The change in electron energy when an absorbing slab of known thickness is placed in an electron beam is measured using a large sodium iodide (NaI) spectrometer. Monte Carlo simulations of the measurement are performed, taking into account the detector crystal, window, and surrounding materials. This results in a predicted pulse height spectrum inside the detector. The Monte Carlo spectrum is broadened to account for detector response. Errors in the ICRU 37 collision stopping powers used by the Monte Carlo simulation are revealed as an energy offset,  $\epsilon$ , between the measured and calculated spectra. In the earlier

chapter it was demonstrated that

$$\kappa = -\frac{\epsilon}{t_{\text{eff}}^r}, \quad (5.2)$$

where  $t_{\text{eff}}^r$  is the pathlength of the electrons through the absorber, excluding those electrons with scattering angles greater than  $20^\circ$ . The offset has been shown to be insensitive to radiative interactions in the absorber or detector, while the possible error introduced by the multiple scattering algorithm used in the Monte Carlo simulation is always less than 0.3%, even for low electron energies and high atomic number absorbers.

Chapters 3 and 4 were concerned with reducing experimental uncertainties so that accurate measurements of  $\epsilon$  and hence  $\kappa$  could be made. This chapter presents measured collision stopping powers for 5 to 30 MeV electrons in the context of the revised approach, drawing on the experimental procedures described in the earlier chapters. The general measurement technique of Faddegon *et al* has been maintained, but improvements have been made which reduce the uncertainty in the measured stopping power from more than 5% to around 0.5%.

## 5.2 Materials and Methods

### 5.2.1 Absorbing Disks

The absorbers used for the stopping power measurements were disks of nominally 5 cm diameter. Four different elemental materials were studied: beryllium, aluminum, copper, and tantalum. This provided a wide range of atomic numbers and densities. In addition, energy losses in C-552 air equivalent plastic, A-150 tissue equivalent plastic, standard graphite, pyrolytic graphite, and water have been measured.

The precise diameter of each disk was measured using Mitutoya Series 500 digital calipers, with an uncertainty of 0.001 cm (0.02%). Mass was determined using a Mettler PM460 digital balance, with an uncertainty of  $\pm 0.001$  g (less than 0.02% for the lightest absorber). Together, the mass and area measurements were sufficient to provide the surface density (mass per unit area) assuming right cylindrical geometry. Uniformity of each disk was verified using a Mitutoyo micrometer (No. 100-260) to measure the thickness at several points on each disk within  $\pm 0.00025$  cm. Complete descriptions of the mechanical properties of all

absorbers are given in Appendix B.

### 5.2.2 Measurement of Electron Spectra

The mean energy of the electron beam was determined to within 0.3% using the magnetic spectrometer described in Chapter 3. The National Research Council (NRC) electron linear accelerator was operated at a nominal pulse repetition rate of 240 Hz and an approximate pulse width of 2  $\mu$ s. The average beam current was one electron every fourth beam pulse. A large (20 cm diameter by 25 cm length) sodium iodide detector (Bicron) was chosen as the radiation detector. The NaI crystal was optically coupled to a photomultiplier tube (SRC B125B01). The detector crystal and photomultiplier tube were shielded in a lead housing to reduce noise from background radiation. The front face of the lead housing was machined to hold an aluminum mount for the 5 cm diameter absorbers used in the stopping power measurements (see figure 4.6). The pulses from the detector were amplified by a linear amplifier (Ortec 572) and stored in a PC/MCA (Canberra S100) through an analog to digital converter (Canberra 8701). The detector housing was placed within 5 cm of the steel exit window of the linac's magnetic spectrometer (beam-detector distance of 10 cm). Events due to background radiation were further reduced by gating the readout of the ADC on the linac beam triggers. Random summing of nearly-coincident pulses, known as pulse pile-up, was reduced using the following technique. The anode signal from each pulse was input to a discriminator which began a fast timer. If another anode pulse was detected within 10  $\mu$ s of the first pulse, that beam pulse was labeled as a pile-up event. A pulse was accepted by the ADC only if the following conditions were satisfied: a beam trigger was supplied, an event was detected in the NaI detector (anode discriminator triggered), and no pile-up events were detected. Pile-up correction routines [79] were used to correct for pile-up events not resolved by the pile-up rejection circuitry.

The gain of the spectrometer system was held constant by placing a  $^{60}\text{Co}$  source approximately 40 cm upstream of the detector window. This kept the count rate sufficiently low that pile-up with the electrons could be adequately controlled by the pile-up rejection circuitry (since the acquisition of electron spectra was gated on beam pulses, only one  $^{60}\text{Co}$  photon for every 20 electrons). The  $^{60}\text{Co}$  signal was amplified on a separate channel and monitored

using a separate MCA (Canberra Series 90) and ADC (Canberra 8076). The output from the ADC also was directed to a gain stabilization unit (Canberra 8200) which automatically adjusted the high voltage (HV) supplied to the photomultiplier tube to compensate for apparent drifts in the 1.33 MeV photopeak. Adjustments of  $\pm 0.3\%$  were observed over a time scale of several minutes, but the mean gain was controlled to within  $0.03\%$  over any measurement day. The electronic gain of the stabilization components was monitored using a precision pulser input to the pre-amplifier, with a reference voltage kept constant to one part in 30000, and was found to be constant within  $0.1\%$  over the course of a given measurement day. Changes in electronic offset (so called “zero drifts”) and electronic gain of the energy analysis components were monitored by supplying precision electronic pulses from a BNC (Berkley Nuclear Corporation) pulser to the detector preamplifier. The amplitudes of the electronic pulses were set by the output of an Aston digital to analog converter (DAC). Linear regression of pulse voltage versus channel number revealed that the offset was constant within a fraction of a channel over several days, while the electronic gain did not change more than  $\pm 0.01\%$ .

### 5.2.3 Monte Carlo Simulations

The EGS4 [80] user code DOSRZ was used along with the PRESTA algorithm [50] to simulate fully electron transport through the entire experimental geometry, including beam window, detector cladding, lead housing, and aluminum absorber mount. The stopping powers from ICRU 37 were used [45], [46]. The most probable energy of the linac beam, as determined *via* the magnetic spectrometer, was used to provide the initial electron energy. The electron beam was assumed to be monoenergetic; sampling the measured electron energy distribution from the magnetic spectrometer made no difference in the simulations. The threshold for secondary electron creation, AE, and the electron energy cutoff, ECUT were each set to 521 keV (kinetic + rest mass energy). The threshold for photon creation, AP, and photon transport cutoff were each set at 10 keV. The pulse height spectrum in the NaI crystal was scored for 400,000 histories.

### 5.2.4 Detector Response and Stopping Power Extraction

The energy calibration relied on fitting the Monte Carlo calculated spectra to electron spectra acquired with no absorber in the beam. The Monte Carlo calculated pulse height distributions were broadened to account for detector response. The broadening function was taken as a Gaussian with full width at half maximum (FWHM) given by:

$$\Gamma_G = 0.064(E)^{0.64}. \quad (5.3)$$

Equation 5.3 was determined by fitting calculated to measured no-absorber electron spectra at a variety of incident electron energies. Each Monte Carlo simulation used the true electron energy, as determined via magnetic spectrometry (Chapter 3), as the initial electron energy before the accelerator window. The energy of the  $i^{\text{th}}$  bin of the measured spectrum was taken as,

$$E_i = \beta_2 C_i, \quad (5.4)$$

where  $\beta_2$  is a gain parameter relating energy to bin number,  $C_i$ .  $\beta_2$  was determined at each energy by least squares fitting of the measured spectrum to the Monte Carlo no-absorber spectrum, which used the true electron energy,  $E_o$ , as measured by magnetic spectrometry. For each energy, the energy scale and area normalization were allowed to vary. The global energy response of the detector was determined by fitting  $C_o = E_o/\beta_2$  vs  $E_o$ , and was found to be

$$C = a + bE + cE^2, \quad (5.5)$$

where  $a = 3.5 \pm 3$ ,  $b = 103.1 \pm 0.4 \text{ MeV}^{-1}$ ,  $c = -0.049 \pm 0.01 \text{ MeV}^{-2}$ , and all energies are expressed in MeV. The offset is essentially zero within its uncertainty, and plays no role in the energy loss measurements. The non-linearity has been linked to a measured change in response of the detector along its axis (see Chapter 4). All measured spectra were rebinned to correct for the non-linearity of equation 5.5.

Figure 5.1 illustrates the fitting procedure for nominally 15 MeV electrons, with no absorber in the beam. The 511 keV escape peak is evident. If the fit is repeated for the case where there is an absorber in the beam, then errors in the theoretical collision stopping powers employed by the Monte Carlo simulation result in an offset between the measured and calculated spectra (figure 5.2).

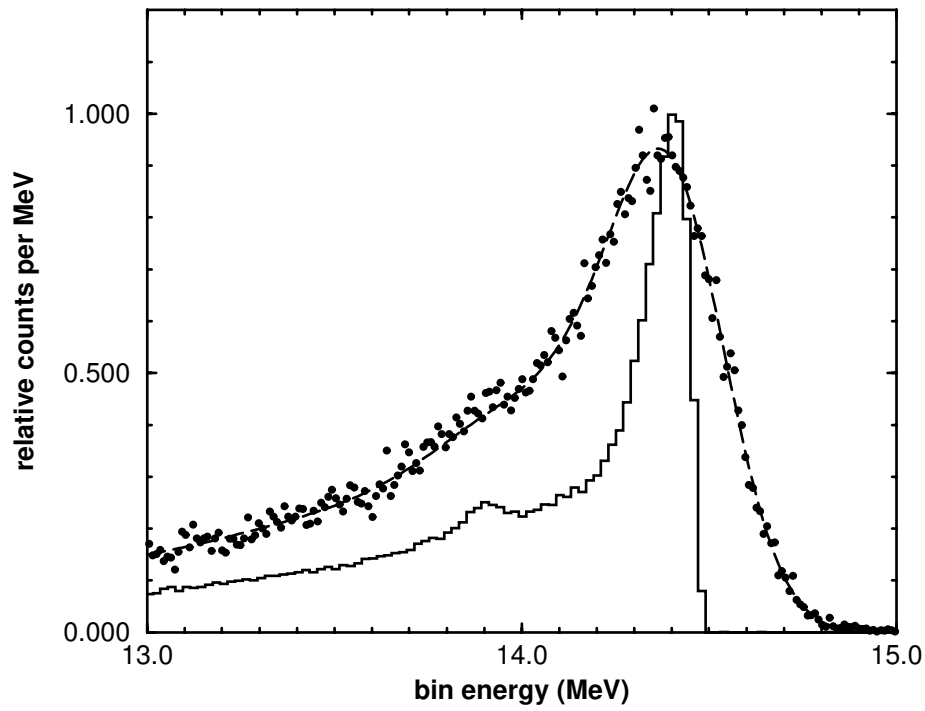


Figure 5.1: Illustration of the fitting procedure used in stopping power measurements for 15 MeV electrons. In this example there is no absorber in the beam. The 511 keV escape peak is evident in the unbroadened peak, which has been scaled to fit on the plot. The broadening and energy scale are varied to get the best  $\chi^2$  fit with respect to the measured spectrum (dots).

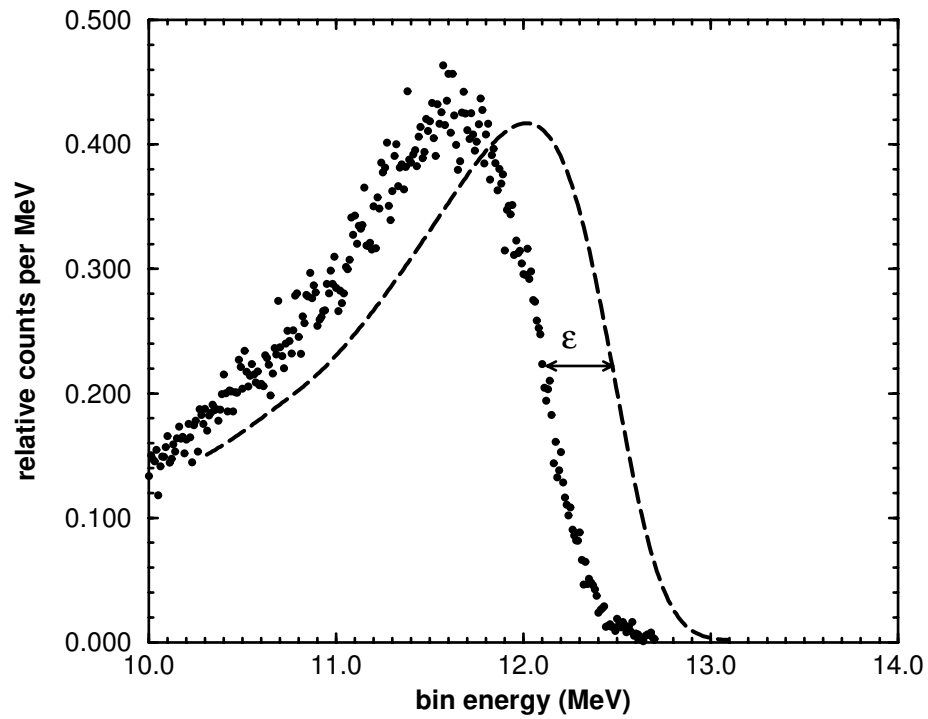


Figure 5.2: Continuation of the example of the fitting procedure. The electron energy is 15 MeV. In this example, there is an aluminum absorber in the beam. With the energy scale established (figure 5.1), errors in the most probable energy may be revealed as energy offsets between the broadened Monte Carlo spectrum (dashed line) and the measured spectrum (dots). The offset has been exaggerated here to illustrate the technique.

We call the gain parameter resulting from fitting the linearized no-absorber spectrum  $\beta'_2$ .  $\beta'_2$  was used to establish the energy scale for the spectrum measured with an absorber in the beam. The broadening was fixed, and the bin offset,  $\beta'_3$  which resulted in the minimum  $\chi^2$  deviation with respect to the broadened Monte Carlo absorber spectrum was determined by least squares fitting. The energy offset,  $\epsilon$ , between the Monte Carlo and measured spectra is

$$\epsilon = \beta'_2 \beta'_3. \quad (5.6)$$

The stopping power correction,  $\kappa$ , is therefore (equation 5.2)

$$\kappa = -\frac{\beta'_2 \beta'_3}{t_{\text{eff}}^r}, \quad (5.7)$$

where  $t_{\text{eff}}^r$  was determined from Monte Carlo simulations. In most instances,  $t_{\text{eff}}^r$  was greater than the absorber thickness,  $t$ , by only a few per cent.

## 5.3 Results

### 5.3.1 Uncertainty Analysis

The measurements of  $\kappa$  are subject to two types of uncertainties [81]. Type A uncertainties are those which can be determined by statistical methods, and include the effects of gain drift, counting statistics, and the uncertainties in the fitting parameters. Type B uncertainties are those which can not be determined statistically, but must be known *a priori*. These include errors in energy calibration, absorber thickness, and systematic problems in the Monte Carlo simulations.

The fitting parameters were each determined by minimizing the  $\chi^2$  deviation between the broadened calculated spectrum and the measured spectrum. This technique leads directly to estimates of the statistical uncertainties associated with each parameter [57]. The measured offsets had uncertainties ranging from 0.2 of a bin to several bins, which represented uncertainties in the final energy loss of 0.1% to 0.3%. The energy calibration factor,  $\beta'_2$  typically had an uncertainty of  $\pm 0.01\%$ . The statistical uncertainty on the broadening parameter was quite small, around 0.2%, which itself had little effect on the measured stopping power (0.04%).



Gain drifts were held to less than 0.1%, which could lead to as much as a 1% change in stopping power for the thinnest slabs. This uncertainty was reduced by bracketing each absorber spectrum with a no-absorber calibration. The average calibration of the two no-absorber spectra was used in the fit, reducing the effect of gain drifts by a factor of two. The effect is less than 0.5% for the thinnest absorbers, and is considerably smaller for all other absorbers.

Type B uncertainties arise in the energy calibration of the magnetic spectrometer, uncertainties in the thicknesses of the absorbing slabs, and uncertainties in the Monte Carlo simulations. Since the electron beam is used to establish the energy calibration, the uncertainty in the energy loss is essentially the uncertainty in electron energy, which has been shown to be  $\pm 0.3\%$  using magnetic spectrometry [73]. The energy loss will also have a 0.3% uncertainty.

The absorbers were disks of 5 cm diameter. The mass thickness of each slab was determined from mass and area measurements, and compared with direct thickness measurements. The standard errors on the mass thicknesses were less than 0.2%. Also, repeat measurements were performed for each absorber thickness, with no provision for alignment of the disks, and no large variations in stopping power were observed. This, coupled with the fact that measurements at different thicknesses showed excellent consistency, suggests that the thicknesses were indeed uniform with no density inhomogeneities.

However, the technique requires accurate simulation of the effective path length through the absorber in the Monte Carlo simulation. The difference between the measured thickness and the true path length is at most 15% for 7 MeV electrons on a thick Ta target; for higher energies and thinner or lower atomic number absorbers the difference is much less ( $< 5\%$ ). To a first approximation, the extra path length through an absorber is proportional to the square of the multiple scattering angle. Li and Rogers [55] have estimated the error in the Monte Carlo scattering power at 2%. Taking the uncertainty in the extra path length to be 2% gives the uncertainty due to path length simulation at 0.3% for the low energy tantalum case, and less than 0.1% for the other absorbers. The uncertainty due to uncertainties in the bremsstrahlung cross section is less than 0.1%.

The final uncertainty on any individual measurement of stopping power results from

combining each of the above measurements in quadrature. That is,

$$\sigma_S = \left( \sigma_{\text{gain drift}}^2 + \sigma_{\text{broadening}}^2 + \sigma_{\beta_2}^2 + \sigma_{\beta_3'}^2 + \sigma_{\text{energy}}^2 + \sigma_{\text{path length}}^2 + \sigma_{\text{brem}}^2 \right)^{1/2}, \quad (5.8)$$

where each  $\sigma$  is the fractional uncertainty in a given quantity. For example, for the 1 g cm<sup>-2</sup> tantalum absorber at 7 MeV, the uncertainty on a given measurement is

$$\sigma_S = \left[ (0.1)^2 + (0.04)^2 + (0.01)^2 + (0.3)^2 + (0.3)^2 + (0.3)^2 + (0.1)^2 \right]^{1/2} = 0.63\% \approx 0.7\%.$$

Here the uncertainty is dominated by uncertainties in the offset ( $\sigma_{\beta_3'}$ ) and path length ( $\sigma_{\text{path length}}$ ). At higher energies, the variations in gain drift become important, so for the 1 g cm<sup>-2</sup> beryllium absorber at 25 MeV, the uncertainty is

$$\sigma_S = \left[ (0.5)^2 + (0.04)^2 + (0.01)^2 + (0.1)^2 + (0.3)^2 + (0.05)^2 + (0.01)^2 \right]^{1/2} = 0.6\%.$$

The uncertainty due to gain drift is largest for thin absorbers.

Table 5.1 summarizes the uncertainties discussed in this section. The final uncertainties, which ranged from 0.4% to 0.7% ( $1\sigma$ ), were determined by taking the quadrature sum.

<b>Class A Uncertainties</b>	
Gain Drift	< 0.5 %
Broadening Parameter $\beta_1$	0.04 %
Energy Calibration Factor $\beta'_2$	0.01%
Offset $\beta'_3$	0.1% to 0.3%
<b>Class B Uncertainties</b>	
Detector Calibration	0.3%
Effective Path Length <sup>a</sup>	0.1% to 0.3%
Discrete Cross Sections	0.2%
<b>Quadrature Sum</b>	0.4% to 0.7%

Table 5.1: Estimated uncertainties in stopping powers. <sup>a</sup>Includes uncertainties in measured thickness and Monte Carlo simulations.

### 5.3.2 Measured Stopping Powers

#### Stopping Powers for Elements

Stopping powers were measured for four elemental materials: beryllium, aluminum, copper, and tantalum. This provided a wide range of atomic numbers ( $Z=4$  to 73) and densities ( $\rho \approx 2$  to  $16 \text{ g/cm}^3$ ) over which to test the theoretical stopping powers.

Figure 5.3 shows measured values of the stopping power correction,  $\kappa$ , for each of the elemental absorbers. Here all values of  $\kappa$  at a given incident energy have been averaged together.  $\kappa$  is essentially zero for all materials and energies, with the exception of aluminum at higher energies, where  $\kappa$  is consistently greater than zero, with an average value of  $0.012 \pm 0.003 \text{ MeV cm}^2 \text{ g}^{-1}$ .

Figures 5.4 to 5.7 show the measured results compared to the values tabulated in ICRU 37. Each circle represents a measurement of the stopping power at a particular thickness and energy. Stopping powers are reported at the electron energy of the midpoint of the absorber. There is no apparent trend with absorber thickness, even for high atomic number absorbers at low energies, suggesting multiple scattering in the absorbers is correctly modeled.

The excellent agreement for the cases of copper ( $Z=27$ ) and tantalum ( $Z=73$ ) is encouraging. The relatively high ionization potentials for these materials mean that the atomic electrons can no longer be considered free, at least for low energy transfers, so the use of the Møller cross section at low energies may have been considered suspect. Also the large amount of multiple scattering which lower energy electrons undergo in these materials presents a serious test of the Monte Carlo simulations. However, no systematic deviations from the theory are evident.

#### Results for Materials of Dosimetric Interest

Measured stopping powers are presented for several materials of dosimetric interest: graphite (both standard and pyrolytic), A-150 tissue equivalent plastic, C-552 air equivalent plastic, and water (figures 5.8 to 5.11, and 5.13). Each open circle represents a stopping power measurement at a particular absorber thickness and energy. Stopping powers are presented for the energy at the midpoint of the absorber.

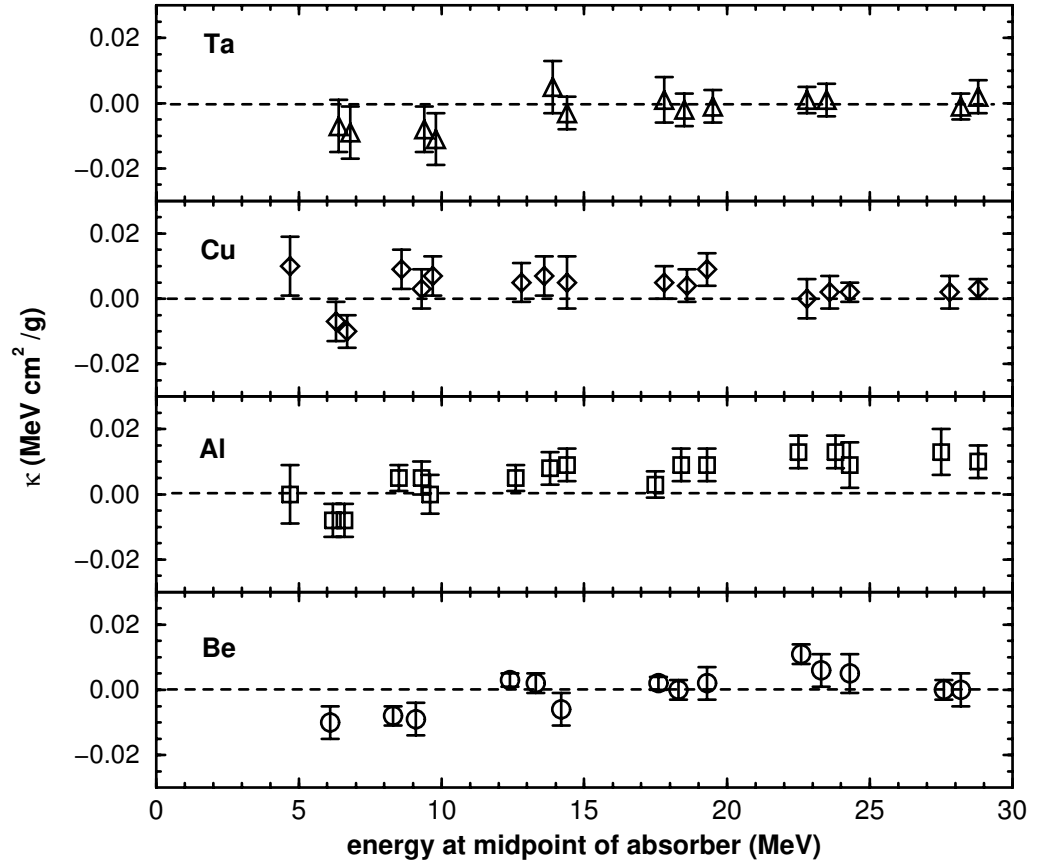


Figure 5.3: Measured values of the stopping power correction,  $\kappa$ , for the elemental absorbers. Each point represents the average value of  $\kappa$  from all measurements at a particular incident energy and absorber thickness, and is reported at the energy at the midpoint of the absorber.  $\kappa$  is nearly zero for all materials and energies, except for aluminum, where it is systematically greater than zero from 20 to 30 MeV.

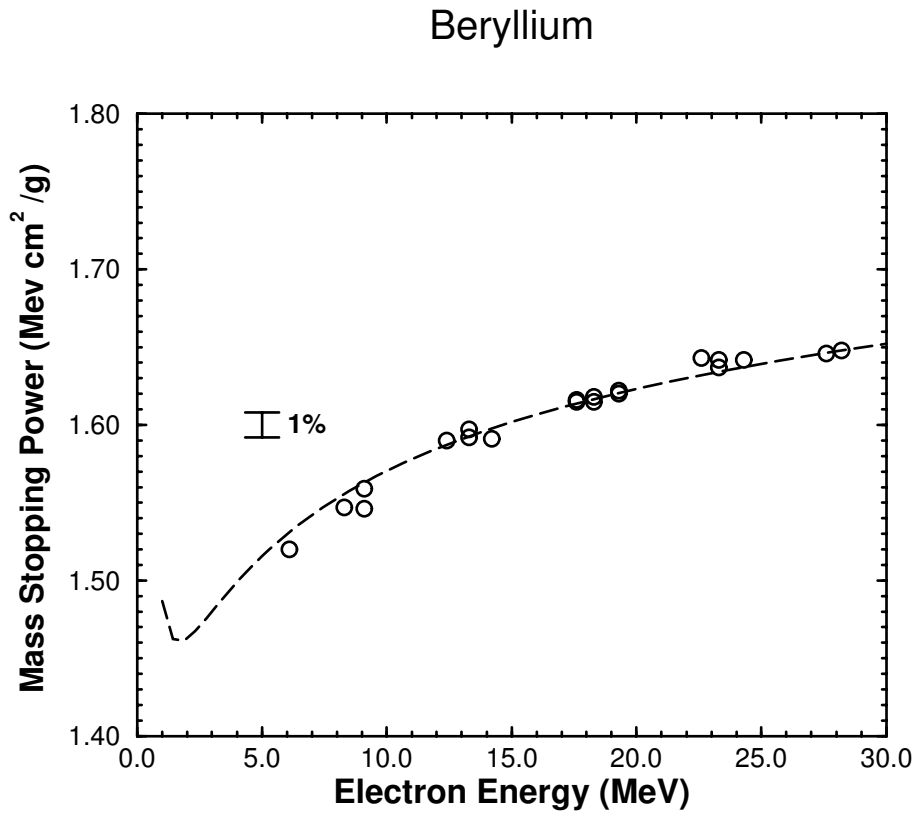


Figure 5.4: Measured stopping powers for beryllium compared with ICRU 37 values. For each measured point, the stopping power is evaluated at the energy at the midpoint of the absorber.

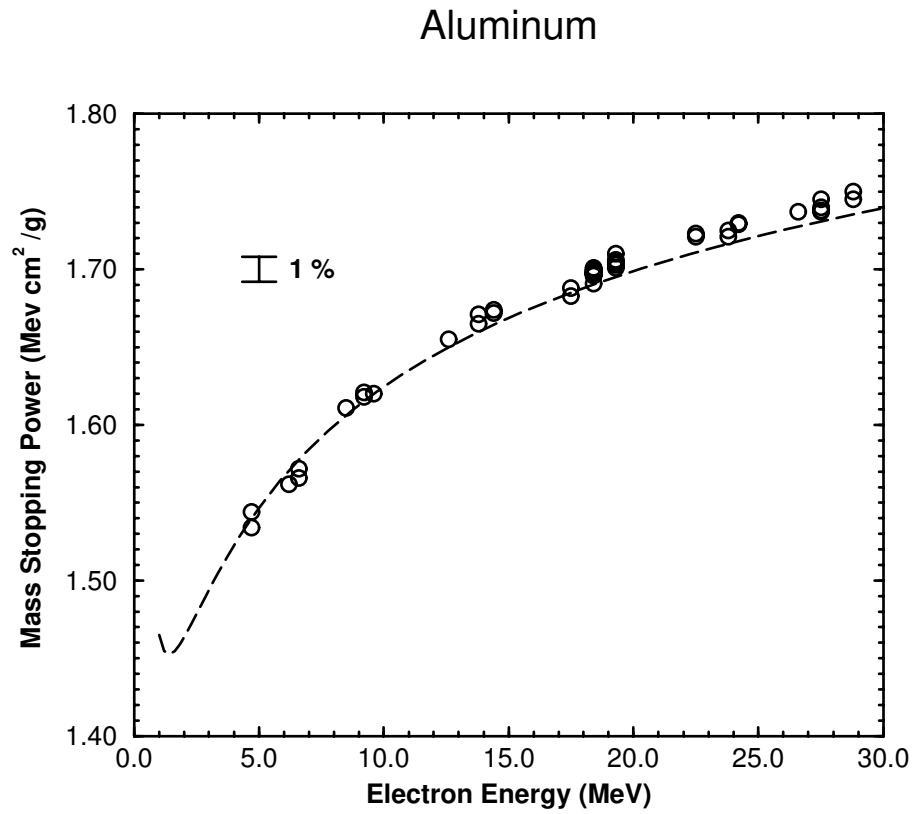


Figure 5.5: Measured stopping powers for aluminum compared with ICRU 37 values. For each measured point, the stopping power is evaluated at the energy at the midpoint of the absorber.

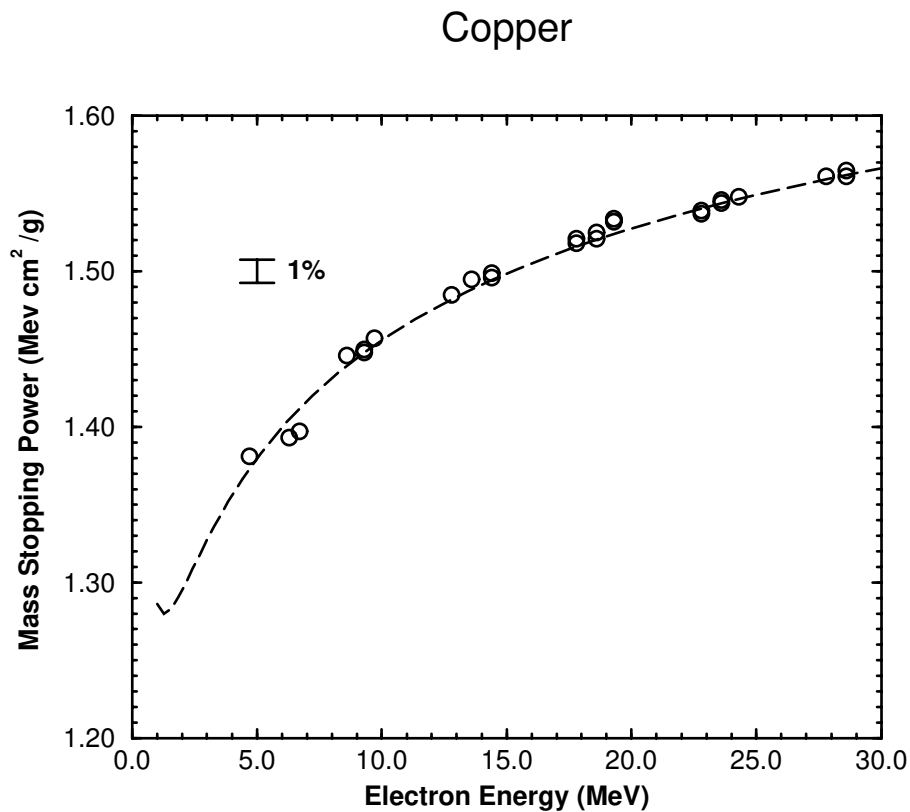


Figure 5.6: Measured stopping powers for copper compared with ICRU 37 values. For each measured point, the stopping power is evaluated at the energy at the midpoint of the absorber.



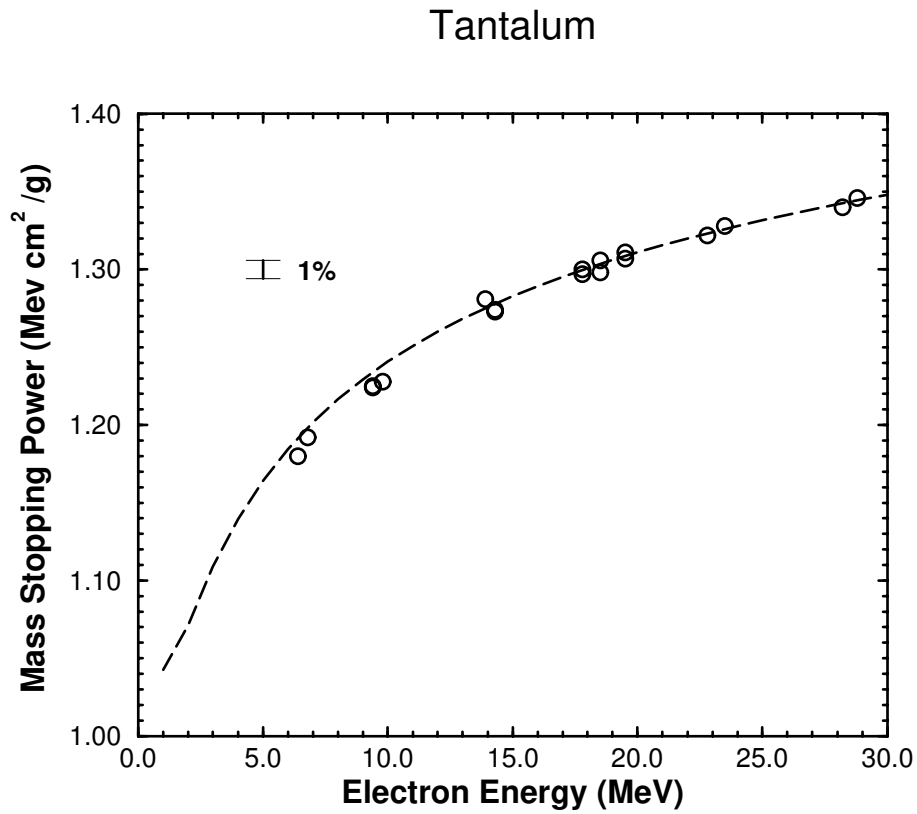


Figure 5.7: Measured stopping powers for tantalum compared with ICRU 37 values. For each measured point, the stopping power is evaluated at the energy at the midpoint of the absorber.

Graphite was chosen for two reasons. First, it is widely used in standards dosimetry in graphite-walled ion chambers and graphite calorimeters. In this sense the graphite stopping power impacts directly on the way dose is measured world-wide. Second, graphite is physically interesting in that it is not homogeneous, but consists of grains of crystalline graphite packed together with voids between them, so that the bulk density of graphite is less than the density of the individual grains. Depending on which density is used to evaluate the density effect correction, the stopping power can change by as much as 1%. Figure 5.8 shows measured values of  $\kappa$  for both the bulk and grain stopping powers. For the grain stopping powers,  $\kappa$  is essentially zero, while for the bulk density values,  $\kappa$  is consistently low by about  $0.018 \text{ MeV cm}^2 \text{ g}^{-1}$ . Figure 5.9 displays the measured stopping powers for graphite from 7 to 30 MeV. Also shown are the theoretical values evaluated using the bulk density ( $\rho = 1.700 \text{ g cm}^{-3}$ , solid line) and grain density ( $\rho = 2.265 \text{ g cm}^{-3}$ , broken line). The measured stopping power is consistent with the grain density stopping power for all absorber thicknesses and energies. This suggests that the range of the density effect correction is less than the diameter of the individual graphite microcrystals, even at 30 MeV. This establishes that the grain density stopping power should be used in all graphite-related dosimetry and calculations, contrary to the recommendations of ICRU 37. Also plotted on figure 5.9 are the measured stopping powers for pyrolytic graphite, which has been pressed at high temperatures to eliminate the voids so that the bulk and grain densities are essentially the same. Not surprisingly, the measured stopping powers for pyrolytic graphite are entirely consistent with those for grain graphite, with the exception of one point at 25 MeV which is considered a statistical outlier.

A-150 tissue equivalent plastic and C-552 air equivalent plastic are used in ion chamber construction. Each plastic is an inhomogeneous mixture, so the Sternheimer density effect correction may not be correct. Moreover, the ICRU evaluations for these materials treat each component as non-conducting, when in fact the carbon black used in their construction is conducting. The authors of ICRU 37 were aware of this problem, and attributed a 0.2% uncertainty to it. Also, as non-elemental samples, these plastics provide a test of Bragg additivity used for the determination of  $I$ -values, although the sensitivity to errors in  $I$  in this energy regime is modest. Figures 5.10 and 5.11 show measured stopping powers for A-

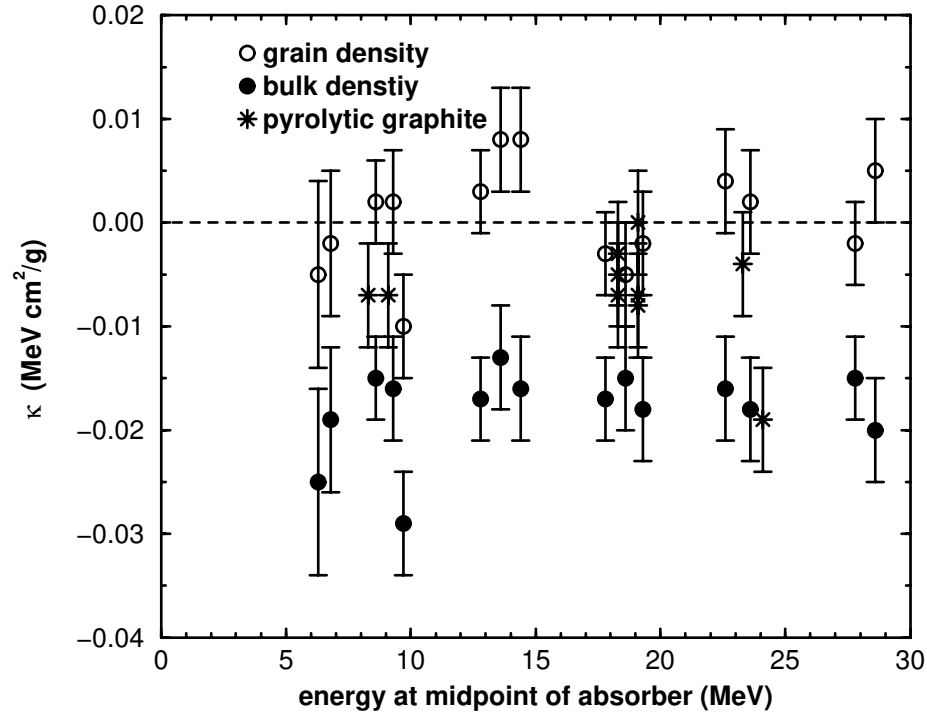


Figure 5.8: Measured values of the stopping power correction,  $\kappa$ , for graphite. Each point represents the average of all measurements at a given incident energy and absorber thickness, and is reported at the energy at the midpoint of the absorber. The correction for the grain density stopping power is essentially zero, while for the bulk density stopping power a correction of  $-0.02 \text{ MeV cm}^2 \text{ g}^{-1}$  is necessary at all energies. Also shown are measured  $\kappa$  values for pyrolytic graphite, which agree with the grain density values at all energies with the exception of one point at 25 MeV, which is considered a statistical outlier. This confirms that the grain density stopping power is appropriate for graphite.

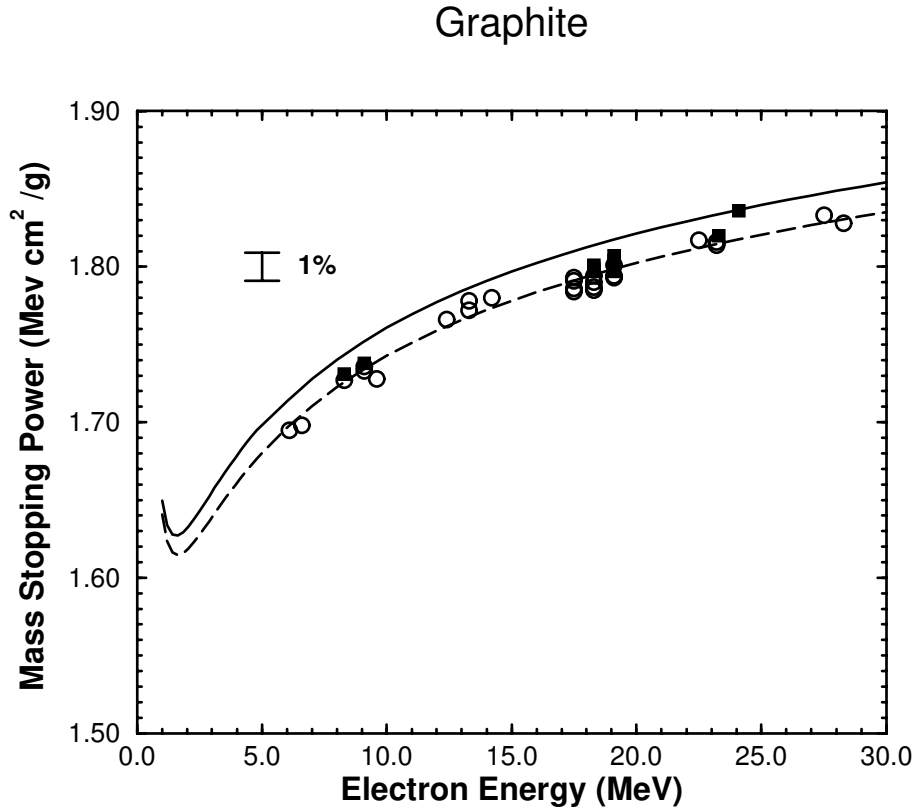


Figure 5.9: Measured stopping powers for graphite compared with ICRU 37 values. For each measured point, the stopping power is evaluated at the energy at the midpoint of the absorber. The broken line is the ICRU37 mass collision stopping power evaluated using the grain density of graphite ( $\rho = 2.265 \text{ g cm}^{-3}$ ). The solid line shows the ICRU37 stopping power evaluated using the bulk density ( $\rho = 1.700 \text{ g cm}^{-3}$ ). The squares represent measurements on pyrolytic graphite, and are also consistent with the grain density stopping power.

150 and C-552 plastics, respectively. Measurements were made for incident electron energies of 25, 20, and 10 MeV, and agree very well with the predicted values of ICRU 37.

Water was chosen for study because of its radiological importance. A vessel was designed to hold approximately  $2 \text{ g cm}^{-2}$  water in rigid geometry while adding little uncertainty to the energy loss measurements (figure 5.12). The walls of the vessel are made of aluminum, 0.5 mm thick. A 2% uncertainty in the energy lost in the walls equates to  $\pm 10 \text{ keV}$  in the overall energy loss, or about 0.2%. The stopping power of water was measured for incident energies of 10, 20, and 25 MeV, and is in agreement with the theoretical values employed by the Monte Carlo simulations, which used the Sternheimer density effect corrections. Also shown is the collision stopping power for water calculated using the density effect correction of Ashley [23]. In this case, the agreement is less good, but still within experimental uncertainty (figure 5.13). Values of the stopping power correction,  $\kappa$ , for water, A-150 plastic and C-552 plastic are shown in figure 5.14.

### 5.3.3 Implications for Dosimetry

#### Water Stopping Power

The measured stopping powers for water show better agreement with the theoretical stopping powers evaluated using the density effect correction of Sternheimer than those which use the Ashley correction. However, the difference between the two approaches is less than 0.5%, close to the  $1\sigma$  uncertainty in the experimental values. The change in ionization potential for water from 75 eV in ICRU 37 to 80 eV based on recent proton stopping measurements by Bischel and Hiraoka [30] would cause only a 0.1% change in this energy range. Also, the 1.5% discrepancy between measured and calculated values of  $R_{50}$  for 20 MeV electrons from the NRC accelerator reported by Ding and Rogers [82] can not be attributed to an error in the water stopping power. It is more likely that the observed difference was due to an error in the initial energy calibration, which has been shown to be low by at least 0.7% [73].

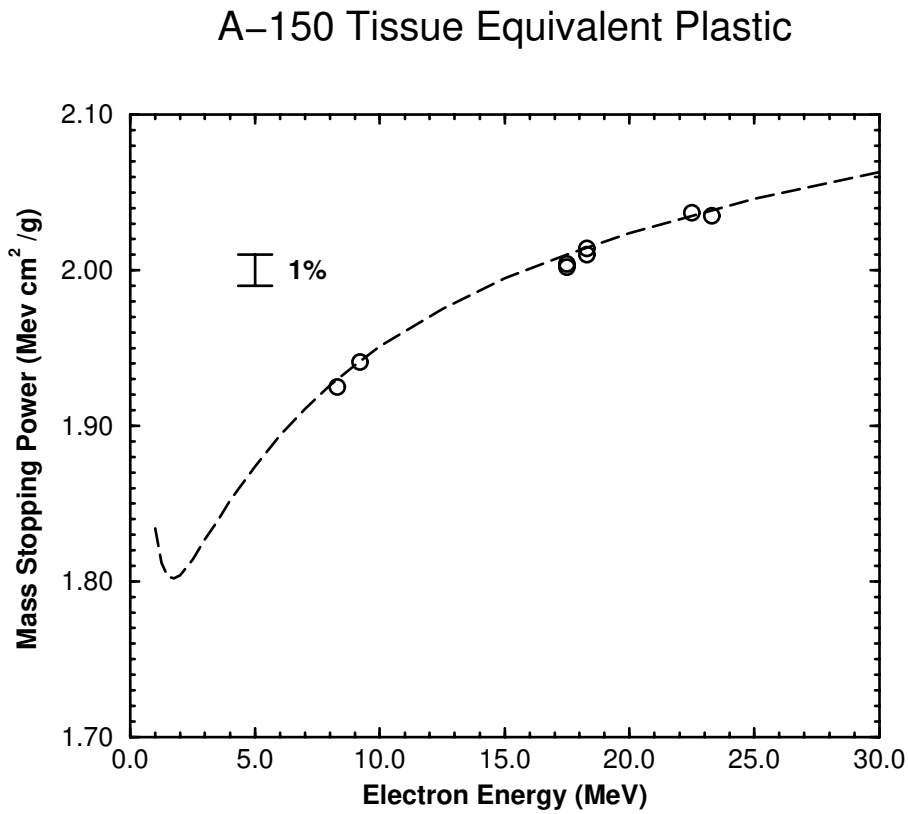


Figure 5.10: Measured stopping powers for A-150 tissue equivalent plastic compared with ICRU 37 values. For each measured point, the stopping power is evaluated at the energy at the midpoint of the absorber.

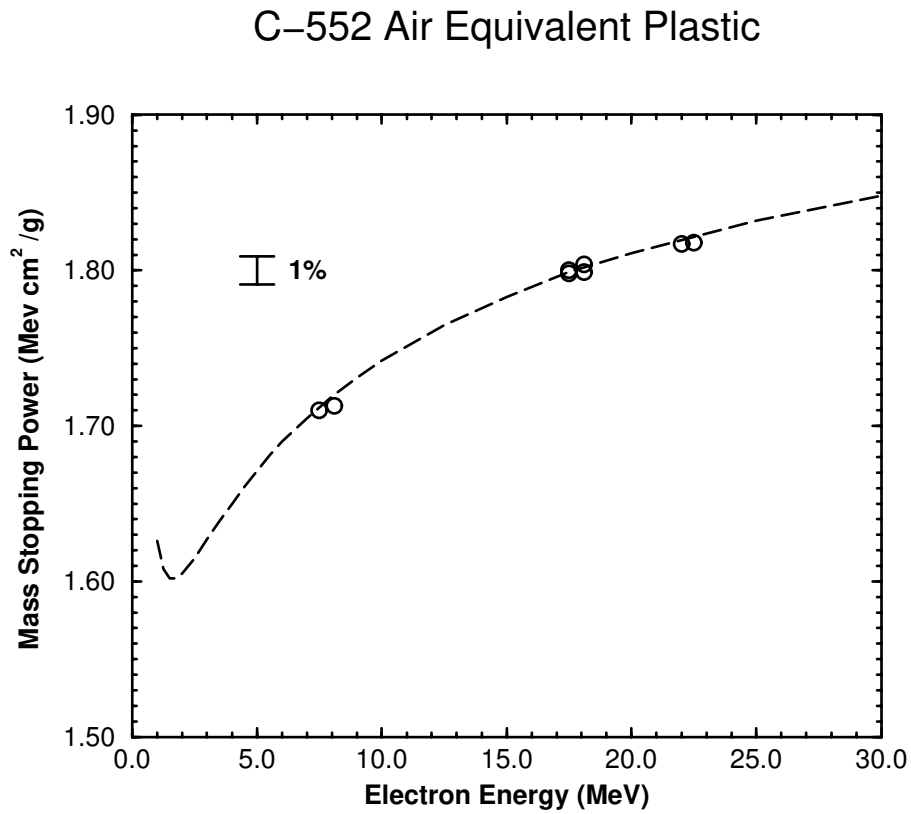


Figure 5.11: Measured stopping powers for C-552 air equivalent plastic compared with ICRU 37 values. For each measured point, the stopping power is evaluated at the energy at the midpoint of the absorber.

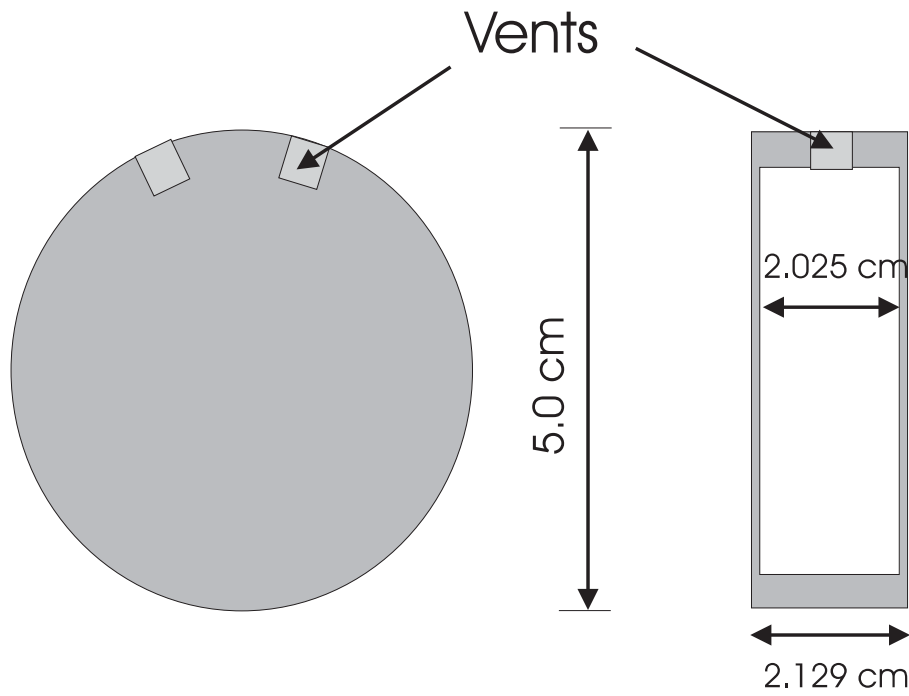


Figure 5.12: Schematic of aluminum vessel used in water stopping power measurements. The walls are 0.5 mm aluminum, which represents at most an extra 0.2% uncertainty in the water stopping power measurements. The vents are used to facilitate emptying and also to equilibrate pressure so that the walls of the vessel are not distorted.



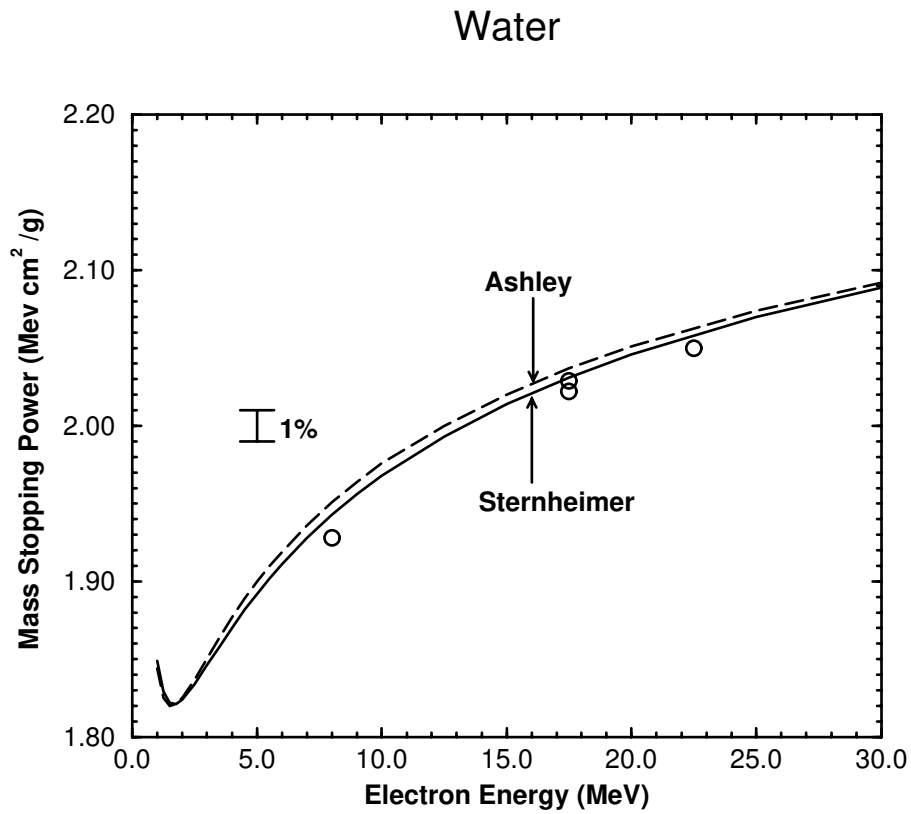


Figure 5.13: Measured stopping powers for water compared with ICRU 37 values calculated using the Ashley and Sternheimer density effect corrections. For each measured point, the stopping power is evaluated at the energy at the midpoint of the absorber.

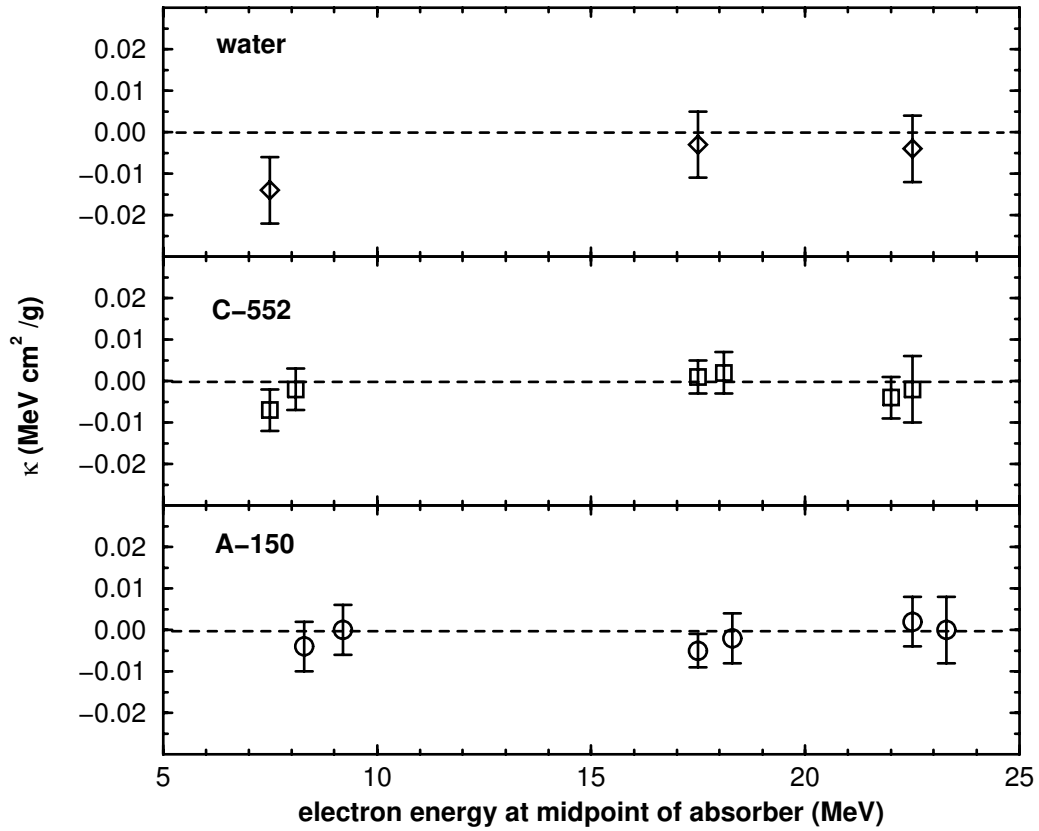


Figure 5.14: Measured values of the stopping power correction,  $\kappa$ , for materials of dosimetric interest. Each point represents the average of all measurements at a given incident energy and absorber thickness, and is presented at the electron energy at the midpoint of the absorber.

### Air Kerma Calibrations

Ion chamber dosimetry has as its basis a measurement of air kerma in a  $^{60}\text{Co}$  beam, using a graphite walled ion chamber. The conversion from measured ionization inside the chamber to dose relies on the ratio of restricted stopping powers of graphite and air  $\left(\frac{L}{\rho}\right)_{\text{air}}^{\text{gr}}$ . In the past, it has never been clear whether to use the bulk or grain densities for the graphite stopping power, leading to an extra 0.2% uncertainty in all ion chamber dose measurements. The measured stopping powers presented in this report clearly demonstrate that the grain density is appropriate, so this uncertainty is removed.

A much larger uncertainty in  $\left(\frac{L}{\rho}\right)_{\text{air}}^{\text{gr}}$  at  $^{60}\text{Co}$  energies is due to a 10% change (from 78 to 87 eV) in the ionization potential for graphite due to new measured proton stopping data [30]. The change in stopping power is nearly 1.2% at 300 keV [83]. However, the change is less than 0.4% in the energy range considered here. As this is less than the experimental uncertainty, no comment can be made on the I-value for graphite.

### $\epsilon G$ for Ferrous Sulfate

The use of ferrous sulfate solution as a dosimeter requires the radiation chemical yield,  $G$ , defined as the mean amount of ferric ions produced per energy imparted  $\epsilon$  (not to be confused with our  $\epsilon$ , which describes an energy offset in electron spectra). It is more common to report the product  $\epsilon G$ , as accurate measurements of  $\epsilon$  are difficult. Svensson and Brahme [84] reported values of  $\epsilon G$  measured by several investigators using calorimeters to establish dose in electron beams, and then placing ferrous sulfate dosimeters at reference points in the beams. The values determined using graphite calorimeters were found to agree better with those determined using non-graphite calorimeters if the bulk density was used to determine dose in the graphite calorimeter. The present study indicates that this is not the correct approach. Using the grain density stopping power changes the value of  $\epsilon G$  for electron beams determined with graphite calorimeters by 0.9% from  $351.6$  to  $348.4 \times 10^{-6} \text{ m}^2\text{kg}^{-1}\text{Gy}^{-1}$ . The  $\epsilon G$  value for electron beams should be re-evaluated.

**$(W/e)_{\text{air}}$  for Air**

Another value which is required to relate charge produced in an ion chamber to absorbed dose or air kerma is the mean energy expended to produce an ion pair in air,  $(W/e)_{\text{air}}$ . Measurements of  $(W/e)_{\text{air}}$  can be made using a graphite calorimeter to establish dose in graphite, and a graphite walled ion chamber to measure ionization at a point.  $(W/e)_{\text{air}}$  will be given by

$$\frac{W}{e} = m_{\text{air}} \frac{D_{\text{gr}}}{Q_{\text{air}}} \left( \frac{L}{\rho} \right)_{\text{gr}}^{\text{air}}, \quad (5.9)$$

where  $m_{\text{air}}$  is the mass of air inside the ion chamber,  $\left( \frac{L}{\rho} \right)_{\text{gr}}^{\text{air}}$  is the restricted stopping power ratio of air to graphite,  $D_{\text{gr}}$  is the dose to graphite and  $Q_{\text{air}}$  is the charge collected in the ion chamber. Svensson and Brahme [84] calculated  $(W/e)_{\text{air}}$  for several different electron energies, using the theoretical stopping powers of ICRU 37 and measured values of  $Q_{\text{air}}$  and  $D_{\text{gr}}$  from other investigators. Not surprisingly, the measured  $(W/e)_{\text{air}}$  value depended on which density was chosen to evaluate the graphite stopping power. The effect is about 1%, and is resolved by this study. However, the value of  $(W/e)_{\text{air}}$  in electron beams was found to change by about 1.5% from 1 to 10 MeV, which is not what would be expected. The authors suggested that the change might be due to an error in  $\left( \frac{L}{\rho} \right)_{\text{gr}}^{\text{air}}$ . No such errors in the graphite stopping power have been found, which leaves three possibilities. First, it is possible that there is an error in the air stopping power. Future measurements should endeavor to establish stopping powers in gases. Second, there could be systematic problems with the experimental data. Finally, it is possible that  $(W/e)_{\text{air}}$  actually changes by 1.5% from 1 to 10 MeV. This underscores the need for new measurements of  $(W/e)_{\text{air}}$ .

## 5.4 Conclusions

The experimental limitations associated with the stopping power technique proposed by Faddegon *et al* have been addressed, and the uncertainties in the measurements have been reduced. Energy calibration of the detector has been established to within 0.3% using a magnetic spectrometer to calibrate the incident electron beam. Drift has been controlled to better than 0.03% using a gain stabilization technique to tie photomultiplier tube gain to the pulse height of the 1.33 MeV  $\gamma$ -line from a  $^{60}\text{Co}$  source. With stability and energy calibration established, the energy response of the NaI detector has been mapped from 5 to 30 MeV, revealing a slight energy non-linearity.

Electron stopping powers have been measured for four different elemental absorbers: beryllium, aluminum, copper, and tantalum. The uncertainties on absorber thicknesses are less than 0.2%, and the overall uncertainty in each stopping power measurement is between 0.4% and 0.7% ( $1\sigma$ ). Measured stopping powers agree with theoretical values within experimental uncertainties for all energies and absorber thicknesses, with the exception of a 0.7% discrepancy in the aluminum stopping power from 25 to 30 MeV. There is no discernible trend with absorber thickness, even for high atomic number absorbers at low energies.

The disagreement of the aluminum stopping power with theoretical values seems to appear at higher energies, suggesting an error in the density effect correction. ICRU 37 compares the density effect correction calculated for aluminum by Inokuti and Smith [22] using semi-empirical dielectric response function, with that determined using the Sternheimer approach and the best available values of the ionization potential for aluminum. The difference in collision stopping power for the two approaches was less than 0.2%, so the density effect correction for aluminum was thought to be well understood, and the disagreement noted here is somewhat unexpected. The stopping power correction,  $\kappa$ , has an average value of  $0.012 \pm 0.003 \text{ MeV cm}^2\text{g}^{-1}$ , corresponding to a 4% error in the Sternheimer density effect correction employed by the Monte Carlo simulations. A more pessimistic view is to assert that the theoretical aluminum stopping powers *are* correct, and the difference is due to some systematic experimental error, so that all the other measured stopping powers should be reduced by 0.7% from 25 to 30 MeV.

The stopping powers of several materials of dosimetric interest have been measured. In the cases of A-150 tissue equivalent plastic, C-552 air equivalent plastic, and water, the measured values agree within the experimental uncertainties with the theoretical values.

Measurements of the stopping power of graphite using both standard and pyrolytic graphite samples have shown that the grain density stopping power is correct for graphite, contrary to the recommendations of ICRU 37. These are the first measurements capable of definitively establishing the appropriate form of the graphite stopping power. With this result a 0.2% uncertainty in ion chamber dosimetry is removed. The value of  $\epsilon G$  for ferrous sulfate solution in electron beams may need to be re-analyzed, as the results determined using graphite calorimeters will now be too high by 0.9%. No errors were found which could explain the 1.5% change in  $(W/e)_{\text{air}}$  for electron energies from 1 to 10 MeV electrons. New measurements of  $(W/e)_{\text{air}}$  may help to resolve this issue.

The theory for stopping power of electrons, as presented in ICRU 37, appears to be valid for elemental absorbers in the energy range from 5 to 30 MeV, independent of atomic number and density.

These represent the most accurate measurements of stopping power to date, and a ten-fold reduction in uncertainty from the previous best measurement [38]. For the first time, experimental data have been obtained with sufficient accuracy to test theoretical stopping powers.

# Chapter 6

## Summary and Conclusions

### 6.1 Summary of Results

This chapter will summarize the findings of the thesis on a chapter by chapter basis, and present suggestions for future work.

#### 6.1.1 Chapter 2: A Detailed Study of a Proposal for the Measurement of Electron Collision Stopping Powers

In this chapter, the technique for stopping power measurement proposed by Faddegon *et al* was revised by relating the difference in energy loss between Monte Carlo-calculated and measured spectra to an error in the low energy component of the collision stopping power. This error, termed  $\kappa$ , was shown to be equal to the measured energy offset,  $\epsilon$ , divided by the average path length of all electrons which leave the absorber at angles less than  $20^\circ$ . For the materials and energies considered in this study, using the physical thickness of the absorber is an acceptable approximation.

The technique was shown to be insensitive to radiative energy loss processes, although uncertainties in the bremsstrahlung cross section contribute an extra 0.1% uncertainty to the energy loss measurements for high atomic number absorbers. The uncertainty in simulated path length was estimated to be less than 0.1% for all materials except for high atomic number absorbers at low energies, where the uncertainty was somewhat greater (0.3%).

The statistical uncertainties associated with the measurement were investigated using simulated spectra generated by an inverse sampling technique. It was shown that errors in stopping power as small as 0.1% should be observable for thick absorbers, although such small effects were expected to be masked by other experimental uncertainties.

### **6.1.2 Chapter 3: A Magnetic Spectrometer for Electron Energy Calibrations**

This chapter described the construction of a magnetic spectrometer for determining the energy of electron beams emerging from the NRC linear accelerator. The spectrometer is capable of establishing electron energy with an uncertainty of  $\pm 0.3\%$ , which constitutes a factor of three improvement over the best previous calibration. This level of uncertainty was sufficiently low to allow accurate stopping power measurements.

The spectrometer provided an opportunity to test the properties of the accelerator beam, and revealed energy reproducibility problems attributed to poorly defined beam geometry at the 90-B beam line. These problems have been resolved by the addition of a beam defining slit. The FWHM of the energy distribution of the electron beam is estimated to be 0.3% when the energy analyzing slit is set to its minimum.

### **6.1.3 Chapter 4: Accurate Measurement of Electron Energy Spectra Using a Large NaI Detector**

Chapter 4 began by describing the selection of spectrometer for the stopping power measurements. Monte Carlo simulations were used to show that high purity germanium (HPGe) spectrometers were not suitable because their small size made them too sensitive to radiative energy losses. For this reason, a large sodium iodide detector was chosen as the radiation detector. Monte Carlo simulations were also used to show how different geometric effects, such as detector placement and beam size would have very little impact on the measured spectra.

Gain drifts, which represented one of the major impediments to accurate stopping power measurements, were reduced from 3% to less than 0.1% by gain stabilization on the 1.33 MeV



photopeak of a  $^{60}\text{Co}$  source. Electronic and “zero” drifts were found to be negligible, although a small correction was required to account for the effect of radiofrequency noise from the linac’s modulator tank.

The energy response of the detector was determined using electron beams calibrated by the magnetic spectrometer discussed in Chapter 3. This revealed the presence of extra window material which was confirmed by photon attenuation measurements. The detector was found to respond non-linearly with energy, probably because of a change in response with depth along the detector axis.

The work described in this chapter made possible the measurement of electron spectra with sufficient precision and accuracy for accurate stopping power measurement to proceed.

#### **6.1.4 Chapter 5: Accurate Measurements of Collision Stopping Powers for 5 to 30 MeV Electrons**

This chapter summarized the measurement of electron collision stopping powers for incident electron energies from 5 to 30 MeV. The  $1\sigma$  uncertainties on the measured stopping powers ranged from 0.4% to 0.7%. Four elemental materials were studied for absorber thicknesses ranging from  $0.5 \text{ g cm}^{-2}$  to  $3 \text{ g cm}^{-2}$ . The measured stopping powers agreed with the theoretical values within experimental uncertainty with the exception of aluminum, which showed a 0.7% discrepancy from 25 to 30 MeV. Since this difference shows up at higher energies, it may be due to an error in the density effect correction.

The stopping power for graphite was found to agree with the theoretical value evaluated using the grain density, rather than the bulk density recommended by ICRU 37. This removes a 0.2% uncertainty on all air kerma based calibrations. It also forces a re-evaluation of the values of  $\epsilon G$  determined by graphite calorimetry for Fricke dosimetry. The 1.5% change in  $(W/e)_{\text{air}}$  for electron energies from 5 to 20 MeV observed by Svensson and Brahme can not be attributed to an error in the graphite stopping power.

Other dosimetric materials studied were A-150 tissue equivalent plastic, C-552 air equivalent plastic, and liquid water. The measured stopping powers for the plastics agreed with the theoretical values even though their heterogeneous structure called into question the calculation of the density effect correction and ionization potentials. The measured stopping

power for water also agreed with the theoretical values, and showed better agreement with the stopping powers calculated using the Sternheimer density effect correction rather than the Ashley density effect correction.

## 6.2 Future Work and Conclusions

The confirmation of the theoretical collision stopping powers in the energy regime from 5 to 30 MeV represents a significant improvement in the knowledge of radiation dosimetry. However, some questions remain unanswered with respect to electron stopping powers.

Experimental confirmation of the stopping powers for low energy electrons is still lacking. This is troubling, as the theory may break down as electron binding effects are certain to become more important at lower energies. Future studies should endeavor to make accurate measurements of stopping powers at lower incident energies of interest in radiotherapy (from 0.1 MeV to 5 MeV).

This study presents stopping powers only for condensed materials. Since stopping power ratios relative to air are crucial for dosimetry, measurements of the air stopping power are necessary, and may help to explain the energy dependence of  $(W/e)_{\text{air}}$ . Failing that, new measurements of  $(W/e)_{\text{air}}$  may be required.

All of the absorbers studied here were electrically conducting. In non-conductors, the onset of the density effect correction is delayed until the energy of the incident electron exceeds the a threshold energy, which is defined by the plasma frequency for the material. Below this threshold energy, the density effect correction is zero. Measurements of stopping powers for non-conductors should be made.

The measured stopping powers presented in this thesis constitute the most accurate measurements to date, and the first measurements capable of confirming the theoretical values tabulated in ICRU 37 within 1%. This confirmation means that radiation dosimetry and dosimetric calculations may proceed with more confidence.

# Appendix A

## Changing Discrete Interaction Cross Sections in EGS4

Modifications have been made to the EGS4 Monte Carlo code which allow testing of the effects of bremsstrahlung and Møller cross sections (i.e. discrete interaction cross sections) in Monte Carlo simulations.

A brief description of the role of discrete interaction cross sections in electron transport in the EGS4 Monte Carlo code system is in order. More complete discussions are given elsewhere [80]. Briefly, the mean free path,  $\lambda$ , between discrete interactions is determined by the total interaction cross section,  $\sigma_{\text{total}}$ . That is,

$$\lambda = \frac{M}{N_a \rho \sigma_{\text{total}}}.$$

where  $M$  is the mass number,  $N_a$  is the Avagadro number, and  $\rho$  is the mass density. The distance  $t$  an electron will travel before a discrete interaction is given by

$$t = \lambda \ln(1 - \eta),$$

where  $\eta$  is a random number on the interval  $[0,1)$ . This ensures that the distances will be exponentially distributed about the mean free path.

The total cross section comprises both the bremsstrahlung and the Møller cross sections:

$$\sigma_{\text{total}} = \sigma_{\text{brem}} + \sigma_{\text{Møller}}.$$

The relative probabilities of each type of event is given by its *branching ratio*. For a bremsstrahlung event, the branching ratio is simply

$$B = \frac{\sigma_{\text{brem}}}{\sigma_{\text{total}}}.$$

At the end of each step, therefore, a random number  $\eta$  is chosen. If  $\eta < B$  then the interaction is assumed to be a bremsstrahlung interaction; otherwise, a Møller interaction is assumed. Energy losses along the path between discrete events are assumed to be continuous, and are governed by the restricted stopping power.

Since only the total discrete interaction cross section and branching ratio are available to EGS4, care must be taken so that  $\sigma_{\text{brem}}$  and  $\sigma_{\text{Møller}}$  can be changed and studied independently. Two new variables,  $I_{\text{sig}}$  and  $f_{\text{sig}}$  have been introduced to the EGS4 code to allow independent scaling of the discrete interaction cross sections. If the particle is in the region denoted by the integer  $I_{\text{sig}}$ , then  $\sigma_{\text{brem}}$  can be changed to  $\sigma'_{\text{brem}} = f_{\text{sig}}\sigma_{\text{brem}}$  by setting

$$\sigma'_{\text{total}} = \sigma_{\text{total}}[B(f_{\text{sig}} - 1) + 1]. \quad (\text{A.1})$$

The new branching ratio is then

$$B' = B f_{\text{sig}} \frac{\sigma_{\text{total}}}{\sigma'_{\text{total}}}. \quad (\text{A.2})$$

Similarly, the Møller cross section can be modified by setting

$$\sigma'_{\text{total}} = \sigma_{\text{total}}[B(1 - f_{\text{sig}}) + f_{\text{sig}}]. \quad (\text{A.3})$$

In which case, the new branching ratio will be

$$B' = B \frac{\sigma_{\text{total}}}{\sigma'_{\text{total}}}. \quad (\text{A.4})$$

The EGS4 user code MSTEST was used to evaluate these changes. For a parallel beam of 20 MeV electrons incident on a 3 mm slab of aluminum, the following quantities were scored: average number of bremsstrahlung events per history, average number of Møller interactions per history, and average transmitted energy for electrons which did not undergo discrete events. The electron transport cutoff, ECUT and threshold for Møller interactions, AE, were set to 521 keV (10 keV kinetic energy). The photon transport cutoff PCUT and the

$f_{\text{sig}}$	Brem. events	Møller events	Average energy (no discrete) (MeV)
0.80	$0.349 \pm 0.01$	$7.07 \pm 0.04$	$19.04 \pm 0.01$
0.90	$0.405 \pm 0.01$	$7.08 \pm 0.04$	$19.04 \pm 0.01$
1.00	$0.450 \pm 0.01$	$7.08 \pm 0.04$	$19.04 \pm 0.01$
1.10	$0.498 \pm 0.01$	$7.10 \pm 0.04$	$19.04 \pm 0.01$
1.20	$0.538 \pm 0.01$	$7.08 \pm 0.04$	$19.04 \pm 0.01$

Table A.1: MSTEST results of bremsstrahlung cross section scaling for 20 MeV electrons on nominally  $1 \text{ g cm}^{-2}$  aluminum. The number of bremsstrahlung events per history scales with the variable  $f_{\text{sig}}$  while the number of Møller events and continuous energy loss per electron are unchanged.

threshold for photon generation, AP, were set to 10 keV. Table A.1 summarizes the results for different values of  $f_{\text{sig}}$ . As can be seen, the number of bremsstrahlung events per history are scaled appropriately, while the number of hard collisions and the average transmitted energy for no discrete interactions remain unchanged. Similar tests were run for changes to the Møller cross section, and are summarized in table A.2.

These modifications allow straightforward scaling of discrete interaction cross sections. This facilitates testing the impact of these cross sections on stopping power measurements (or any simulation) without affecting other aspects of the calculation.

$f_{\text{sig}}$	Brem. events	Møller events	Average energy (no discrete) (MeV)
0.80	$0.453 \pm 0.01$	$5.71 \pm 0.04$	$19.04 \pm 0.01$
0.90	$0.452 \pm 0.01$	$6.38 \pm 0.04$	$19.04 \pm 0.01$
1.00	$0.450 \pm 0.01$	$7.08 \pm 0.04$	$19.04 \pm 0.01$
1.10	$0.452 \pm 0.01$	$7.82 \pm 0.04$	$19.04 \pm 0.01$
1.20	$0.449 \pm 0.01$	$8.50 \pm 0.04$	$19.04 \pm 0.01$

Table A.2: MSTEST results of Møller cross section scaling for 20 MeV electrons on nominally  $1 \text{ g cm}^{-2}$  aluminum. The number of Møller events per history scales with the variable  $f_{\text{sig}}$  while the number of bremsstrahlung events and continuous energy loss per electron are unchanged.

# Appendix B

## Absorbers for Stopping Power Measurements

### B.1 Aluminum Disks

The aluminum disks used in the measurement of electron stopping powers were originally made for x-ray absorption work. They were punched from 1199 aluminum alloy, with less than 0.01% non-aluminum impurities [85]. Table B.1 summarizes the measured thicknesses for the aluminum absorbers. The column labeled “identifier” reflects the numerical label given the absorber in the x-ray laboratory. The density of 1199 aluminum is given as  $2.699 \pm 0.001 \text{ g cm}^{-3}$  [86]. Using the mechanical measurements of disks 1 and 2b, the density is found to be  $2.689 \pm 0.003 \text{ g cm}^{-3}$ , or 0.4% low. This is consistent with earlier ionometric measurements<sup>1</sup> of the thickness, which showed 0.6% less attenuation than would be expected for the measured thickness of aluminum and standard density of  $2.699 \text{ g cm}^{-3}$ .

### B.2 Other Elemental Absorbers

Aside from aluminum, six other elemental absorbers were employed in the stopping power study: beryllium, copper, granular graphite, pyrolytic graphite, lead, and tantalum. Table B.2 summarizes the thickness measurements for these disks. Mechanical thickness mea-

---

<sup>1</sup>Dr. Len Van der Zwan, private communication.



Identifier	Thickness (cm)	Diameter (cm)	Mass (g)	Mass Thickness (g cm <sup>-2</sup> )
2	0.1013	5.054	5.472	0.2728
3	0.1018	5.057	5.512	0.2744
5	0.1011	5.050	5.448	0.2720
1	0.5182	5.059	27.998	1.393
2b	0.5172	5.062	27.987	1.391

Table B.1: Thicknesses of aluminum absorbers used in stopping power measurements. The mass thickness was found by dividing the mass of each disk by its area.

measurements were used only to test uniformity, and are not included in this table. All absorbers were found to be uniform within the uncertainty of the micrometer.

### B.3 Plastic Absorbers

Two different plastic materials are used in the stopping power measurements: A-150 tissue-equivalent plastic, and C-552 air equivalent plastic. Three disks of each material were machined, with nominal mass thicknesses of 0.5, 1, and 2 g cm<sup>-2</sup>. The thinnest disks for each plastic showed large nonuniformities in thickness, being up to 6% thicker at the edges than in the centre. The thickest disks were found to be acceptably uniform (within 0.1%) in thickness. For each plastic, the density was taken from mass and volume measurements of the thickest disks. The mass thickness was determined by multiplying this measured density by the thickness at the centre of the each disk. Table B.3 lists the the measured thicknesses for each plastic absorber.

### B.4 Water Absorber

An aluminum vessel was constructed for use in the water stopping power measurements. The vessel is a cylinder with circular walls 0.25 cm thick and planar walls 0.052 cm thick. The inner thickness of the vessel is 2.025 cm, presenting 2.025 g cm<sup>-2</sup> water for the stopping power measurements. A schematic of the vessel is presented in figure 5.12. Measurements of thickness with and without water in the vessel were consistent, indicating that buckling of the vessel walls is not an appreciable problem.

Element	Identifier	Diameter (cm)	Mass (g)	Mass Thickness (g cm <sup>-2</sup> )
Beryllium	1	5.000	18.190	0.926
Beryllium	2	5.000	43.723	2.226
Graphite	3	5.052	9.849	0.4913
Graphite	6	5.052	19.972	0.9963
Graphite	9	5.053	29.990	1.496
Pyrolytic Graphite	1	5.004	21.513	1.094
Pyrolytic Graphite	2	4.992	10.813	0.5534
Pyrolytic Graphite	3	4.991	10.672	0.5455
Copper	13	5.050	18.418	0.9195
Copper	14	5.052	18.419	0.9189
Copper	15	5.052	18.409	0.9184
Tantalum	1	5.098	9.026	0.4422
Tantalum	2	5.100	8.973	0.4392
Tantalum	4	5.102	16.444	0.8049
Tantalum	5	5.102	16.291	0.7974
Tantalum	6	5.102	16.333	0.7989

Table B.2: Thicknesses of elemental absorbers used in stopping power measurements.

Material	Identifier	Mass Thickness (g cm <sup>-2</sup> )
A-150	1	0.487
A-150	2	1.026
A-150	3	2.052
C-552	1	0.531
C-552	2	1.061
C-552	3	2.139

Table B.3: Mass thickness data for plastic absorbers used in stopping power measurements.

# Bibliography

- [1] *Cancer in Ontario: 1994-1995*, Ontario Cancer Treatment and Research Foundation, Toronto, 1995.
- [2] ICRU, Radiation Quantities and Units, ICRU Report 33, ICRU, Washington D.C., 1980.
- [3] A. Brahme, Dosimetric precision requirements in radiation therapy, *Acta Radiol. Oncol.* **23**, 379–391 (1984).
- [4] ICRU, Determination of Absorbed Dose in a Patient Irradiated by Beams of X or Gamma Rays in Radiotherapy Procedures, ICRU Report 24, ICRU, Washington D.C., 1976.
- [5] A. W. B. J. Mijnheer, J. J. Batterman, What degree of accuracy is required and can be achieved in photon and neutron therapy?, *Radiother. Oncol.* **8**, 237 – 252 (1987).
- [6] AAPM TG–21, A protocol for the determination of absorbed dose from high-energy photon and electron beams, *Med. Phys.* **10**, 741 – 771 (1983).
- [7] IAEA, *Absorbed Dose Determination in Photon and Electron Beams; An International Code of Practice*, volume 277 of *Technical Report Series*, IAEA, Vienna, 1987.
- [8] M. J. Berger, Electron stopping powers for transport calculations, in *Monte Carlo Transport of Electrons and Photons*, edited by T. Jenkins, W. Nelson, A. Rindi, A. Nahum, and D. Rogers, pages 57 – 80, Plenum Press, New York, 1989.
- [9] P. Andreo, Consistency in stopping-power ratios for dosimetry, in “Dosimetry in Radiotherapy”, (IAEA, Vienna) Vol 1 , 3 – 11 (1988).

- [10] ICRU, Stopping powers for electrons and positrons, ICRU Report 37, ICRU, Washington D.C., 1984.
- [11] H. K. Tseng and R. H. Pratt, Exact screened calculations of atomic-field bremsstrahlung, *Phys. Rev.* **A3**, 100 – 115 (1971).
- [12] B. A. Faddegon, C. K. Ross, and D. W. O. Rogers, Forward-directed bremsstrahlung of 10 to 30 MeV electrons incident on thick targets of Al and Pb, *Med. Phys.* **17**, 773 – 785 (1990).
- [13] B. A. Faddegon, C. K. Ross, and D. W. O. Rogers, Angular distribution of bremsstrahlung from 15 MeV electrons incident on thick targets of Be, Al and Pb, *Med. Phys.* **18**, 727 – 739 (1991).
- [14] H. A. Bethe, Zur theorie des durchgangs schneller korpuscularstrahlen durch materie, *Ann. Physik* **5**, 325 – 400 (1930).
- [15] H. A. Bethe, Bremsformel fur elektronen relativistischer geschwindigkeit, *Z. für Physik* **76**, 293 – 299 (1932).
- [16] H. Bethe and W. Heitler, On the stopping of fast particles and the creation of positive electrons, *Proc. of Roy. Soc. (London)* **146**, 83 – (1934).
- [17] J. D. Jackson, *Classical Electrodynamics*, John Wiley & Sons, Toronto, 1975.
- [18] P. Sigmund, Energy loss of charged particles in solids, in *Radiation Damage Processes in Materials*, edited by C. H. S. Dupuy, pages 3 – 117, Nato Advanced Study Institutes Series, 1975.
- [19] J. F. Zeigler, Helium: stopping powers and ranges in all elements, in *The Stopping and Ranges of Ions in Matter, vol. 4*, Pergamon Press, New York, 1977.
- [20] H. H. Anderson and J. F. Zeigler, Hydrogen: stopping powers and ranges in all elements, in *The Stopping and Ranges of Ions in Matter, vol. 3*, Pergamon Press, New York, 1977.
- [21] C. Møller, Zur theorie des durchgangs schneller elektronen durch materie, *Ann. Phys.* **14**, 568 – 585 (1932).

- [22] M. Inokuti and D. Y. Smith, Fermi density effect on the stopping power of metallic aluminum, *Phys. Rev.* **B25**, 61 – 66 (1982).
- [23] J. C. Ashley, Density effect in liquid water, *Radiat. Res.* **89**, 32 – 37 (1982).
- [24] R. M. Sternheimer, Density effect for the ionization loss in various materials, *Phys. Rev.* **103**, 511–515 (1956).
- [25] R. M. Sternheimer and R. F. Peierls, General expression for the density effect for the ionization loss of charged particles, *Phys. Rev.* **B3**, 3681 – 3692 (1971).
- [26] R. M. Sternheimer, S. M. Seltzer, and M. J. Berger, Density effect for the ionization loss of charged particles in various substances, *Phys. Rev.* **B26**, 6067 – 6076 (1982).
- [27] IAEA, Atomic and Molecular Data for Radiation Research, IAEA Report IAEA-TECDOC-799, International Atomic Energy Agency, Vienna, Austria, 1995.
- [28] R. D. Evans, *The Atomic Nucleus*, McGraw-Hill, New York, 1955.
- [29] M. J. Berger and S. M. Seltzer, Tables of energy losses and ranges of electrons and positrons, NASA Report SP-3012 (Washington DC) (1964).
- [30] H. Bischel and T. Hiraoka, Energy loss of 70 MeV protons in elements, *Nucl. Inst. Meth.* **B66**, 345 – 351 (1992).
- [31] F. L. Hereford, The specific primary ionization and energy loss of fast electrons in matter, *Phys. Rev.* **74**, 574 – 579 (1948).
- [32] E. L. Goldwasser, F. E. Mills, and A. O. Hanson, Ionization loss and straggling of fast electrons, *Phys. Rev.* **88**, 1137–1141 (1952).
- [33] H. E. Hall, A. O. Hanson, and D. Jamnik, Most probable energy loss of fast electrons, *Phys. Rev.* **115**, 633–635 (1959).
- [34] W. Paul and H. Reich, Energieverlust schneller elektronen in Be, C, H<sub>2</sub>O, Fe und Pb, *Z. Physik* **127**, 429 – 442 (1950).

- [35] T. Westmark, Some measurements on energy loss of 2.8 MeV electrons in light elements and compounds, *Ark. Kemi.* **17**, 101 – 138 (1961).
- [36] T. Mikado and T. Tomimasu, Energy loss of 24.8-MeV electrons by interacting with thick materials, *J. Appl. Phys.* **54**, 3677 – 3687 (1983).
- [37] A. Antolak and W. Williamson, Monte Carlo scattering calculations of 24.8-MeV electrons through C, Al, Cu, and Pb foils, *J. Appl. Phys.* **60**, 2944 – 2948 (1986).
- [38] H. Feist and U. Müller, Measurement of the total stopping power of 5.3 MeV electrons in polystyrene by means of electron beam absorption in ferrous sulfate solution, *Phys. Med. Biol.* **34**, 1863–1869 (1989).
- [39] D. W. O. Rogers and B. A. Faddegon, Re-evaluation of the total stopping power of polystyrene for 5.3 MeV electrons, *Phys. Med. Biol.* **37**, 969–983 (1992).
- [40] D. T. Burns, S. Duane, and M. R. McEwen, A new method to determine ratios of electron stopping powers to an improved accuracy, *Phys. Med. Biol.* **40**, 733–739 (1995).
- [41] C. K. Ross and M. S. MacPherson, Comments on ‘A new method to determine ratios of electron stopping powers to an improved accuracy’, *Phys. Med. Biol.* **41**, 785–788 (1996).
- [42] B. A. Faddegon, C. K. Ross, and D. W. O. Rogers, Measurement of collision stopping powers of graphite, aluminum and copper for 10 and 20 MeV electrons, *Phys. Med. Biol.* **37**, 1561 – 1571 (1992).
- [43] M. J. Berger and S. M. Seltzer, Response functions for sodium iodide scintillation detectors, *Nucl. Inst. Meth.* **104**, 317–332 (1972).
- [44] B. A. Faddegon, L. Van der Zwan, D. W. O. Rogers, and C. K. Ross, Precision response estimation, energy calibration, and unfolding of spectra measured with a large NaI detector, *Nucl. Inst. Meth.* **A 301**, 138 – 149 (1990).
- [45] S. Duane, A. F. Bielajew, and D. W. O. Rogers, Use of ICRU-37/NBS collision stopping powers in the EGS4 system, NRC Report PIRS-0173, Ottawa (1989).



- [46] D. W. O. Rogers, S. Duane, A. F. Bielajew, and W. R. Nelson, Use of ICRU-37/NBS radiative stopping powers in the EGS4 system, National Research Council of Canada report PIRS-0177 (1989).
- [47] D. W. O. Rogers, B. A. Faddegon, G. X. Ding, C. M. Ma, J. Wei, and T. R. Mackie, BEAM: A Monte Carlo code to simulate radiotherapy treatment units, *Med. Phys.* **22**, 503 – 524 (1995).
- [48] B. A. Faddegon, *Bremsstrahlung of 10 to 30 MeV electrons incident on thick targets*, PhD thesis, Carleton University, Ottawa, Canada, 1991.
- [49] M. J. Berger, Monte Carlo calculation of the penetration and diffusion of fast charged particles, *Methods in Comput. Phys.* **1**, 135 – 215 (1963).
- [50] A. F. Bielajew and D. W. O. Rogers, PRESTA: The parameter reduced electron-step transport algorithm for electron Monte Carlo transport, *Nucl. Inst. and Meth.* **B18**, 165 – 181 (1987).
- [51] A. F. Bielajew and D. W. O. Rogers, Electron step-size artefacts and PRESTA, in *Monte Carlo Transport of Electrons and Photons*, edited by T. Jenkins, W. Nelson, A. Rindi, A. Nahum, and D. Rogers, pages 115 – 137, Plenum Press, New York, 1989.
- [52] P. Andreo, J. Medin, and A. F. Bielajew, Constraints on the multiple scattering theory of Molière in Monte Carlo simulations of the transport of charged particles, *Med. Phys.* **20**, 1315 – 1325 (1993).
- [53] A. O. Hanson, L. H. Lanzl, E. M. Lyman, and M. B. Scott, Measurement of multiple scattering of 15.7-MeV electrons, *Phys. Rev.* **84**, 634 – 637 (1951).
- [54] H. Roos, P. Drepper, and D. Harder, The transition from multiple scattering to complete diffusion of high energy electrons, in *Proceedings, 4<sup>th</sup> Symposium on Microdosimetry, Commis. of Eur. Comm. (EUR 5122)*, pages 779–798, 1973.
- [55] X. A. Li and D. W. O. Rogers, Electron mass scattering powers: Monte Carlo and analytical calculations, *Med. Phys.* **22**, 531 – 541 (1995).

- [56] H. Kahn, Use of different Monte Carlo sampling techniques, in Symposium on Monte Carlo Methods, (H.A. Meyer ed.) (John Wiley and Sons, New York) , 146 – 190 (1956).
- [57] D. W. O. Rogers, Analytic and graphical methods for assigning errors to parameters in non-linear least squares fitting, Nucl. Inst. and Meth. **127**, 253 – 260 (1975).
- [58] W. H. Press, B. P. Flannery, S. A. Teukolsky, and W. T. Vetterling, *Numerical Recipes—The Art of Scientific Computing*, Cambridge University Press, Cambridge, 1986.
- [59] C. K. Ross and K. R. Shortt, Energy calibration of the 90-B beam line of the IRS linac, NRC Report PIRS-0021, National Research Council of Canada, Ottawa, Canada, 1985.
- [60] B. B. Sorcini and A. Brahme, An accurate energy-range relationship for high-energy electron beams in arbitrary materials, Phys. Med. Biol. **39**, 795 – 811 (1994).
- [61] B. B. Sorcini, P. Andreo, A. F. Bielajew, S. Hyödynmaa, and A. Brahme, An improved energy-range relationship for high-energy electron beams based on multiple accurate experimental and Monte Carlo data sets, Phys. Med. Biol. **40**, 1135 – 1159 (1995).
- [62] N. Blais and E. Podgorsak, The mass angular scattering power method for determining the kinetic energies of clinical electron beams, Phys. Med. Biol. **37**, 1931–1942 (1992).
- [63] C. E. de Almeida and P. R. Almond, Energy calibration of high energy electrons using a Cerenkov detector and a comparison with different methods, Phys. Med. Biol. **19**, 476–483 (1974).
- [64] L. B. Levy, R. G. Waggener, and A. E. Wright, Measurement of primary bremsstrahlung spectrum from an 8-MeV linear accelerator, Med. Phys. **3**, 173–175 (1976).
- [65] J. Brownridge, S. Samnick, P. Stiles, P. Tipton, J. Veselk, and N. Yeh, Determination of the photon spectrum of a clinical accelerator, Med. Phys. **11**, 794–796 (1984).
- [66] J. J. Battista, *A Magnetic Spectrometer for Betatron Electrons*, M. Sc. Thesis, The University of Western Ontario, London, Canada (1973).
- [67] B. B. Sorcini and S. Rosander, Energy distributions from a racetrack microtron measured with a magnetic spectrometer, Med. Phys. **20**, 695–702 (1993).

- [68] J. J. Livingood, *The Optics of Dipole Magnets*, Academic Press, New York, 1969.
- [69] A. Septier, *Focusing of Charged Particles, Volume I*, Academic Press, 1967.
- [70] P. Lorrain, D. Corson, and F. Lorrain, *Electromagnetic fields and waves*, W. H. Freeman and Company, New York, 1987.
- [71] S. Kowalski and H. A. Enge, RAYTRACE, MIT report, Laboratory for Nuclear Science, Massachusetts Institute of Technology, Cambridge, Massachusetts, 1987.
- [72] D. W. O. Rogers, Low energy electron transport with EGS, Nucl. Inst. Meth. **227**, 535 – 548 (1984).
- [73] M. S. MacPherson and C. K. Ross, A magnetic spectrometer for electron energy calibration, NRC Report PIRS-0617, Ottawa (1998).
- [74] M. Birk, Y. Eisen, and Z. Vager, Compensation for gain variation with rate in a NaI(Tl) scintillation counter, Nucl. Inst. Meth. **108**, 611 – 612 (1973).
- [75] T. Hehl, P. Grabmayr, M. Sauer, and G. J. Wagner, A gain monitoring system for scintillation detectors using ultra bright LEDs, Nucl. Inst. Meth. **A354**, 505–510 (1995).
- [76] M. Yamashita, Method for precision measurement of temperature dependence of scintillation efficiency in NaI(Tl), Rev. Sci. Instrum. **60**, 1203–1205 (1989).
- [77] W. R. Nelson and D. W. O. Rogers, Structure and operation of the EGS4 code system, in *Monte Carlo Transport of Electrons and Photons*, edited by T. Jenkins, W. Nelson, A. Rindi, A. Nahum, and D. Rogers, pages 287 – 306, Plenum Press, New York, 1989.
- [78] A. S. Belousov, Y. A. Vazdik, E. N. Malinovskii, S. V. Rusakov, Y. V. Solv'ev, A. M. Fomenko, and P. N. Shareiko, Stability of scintillation spectrometer with NaI(Tl) crystal and FEU-49 photomultiplier at high count rates, Pribory i Tekhnika Eksperimenta **3**, 49–52 (1986).
- [79] B. A. Faddegon, Pile-up corrections in pulsed-beam spectroscopy, Nucl. Inst. Meth. **51**, 431 – 441 (1990).

- [80] W. R. Nelson, H. Hirayama, and D. W. O. Rogers, The EGS4 Code System, SLAC Report 265, Stanford University, Stanford, California, 1985.
- [81] ISO, *Guide to the Expression of Uncertainty in Measurement*, ISO Report ISO/TAG 4/WG 3, International Organization for Standardization, Geneva, Switzerland, 1992.
- [82] G. X. Ding and D. W. O. Rogers, Energy spectra, angular spread, and dose distributions of electron beams from various accelerators used in radiotherapy, NRC Report PIRS-0439, Ottawa (1995).
- [83] D. W. O. Rogers, Uncertainties in the  $^{60}\text{Co}$  graphite to air stopping-power ratio and a re-evaluation of  $(W/e)_{\text{air}}$  values, NRC Report PIRS-363, Ottawa (1993).
- [84] H. Svensson and A. Brahme, Recent advances in electron and photon dosimetry, Ch 3 in *Radiation Dosimetry* ed by C.G. Orton, Plenum Publishing , 87 – 170 (1986).
- [85] E. Orberg and F. D. Jones, *Machinery's Handbook*, Industrial Press, 1968.
- [86] D. M. Considine, editor, *Van Nostrand's Scientific Encyclopedia*, Van Nostrand and Reinhold, New York, 1989.